Adaptive Marchenko internal multiple attenuation

Adaptive Marchenko internal multiple attenuation

Dissertation

for the purpose of obtaining the degree of doctor
at Delft University of Technology,
by the authority of the Rector Magnificus Prof. dr. ir. T.H.J.J. van der Hagen;
Chair of the Board for Doctorates,
to be defended publicly on
Friday, 25 September 2020 at 12.30 pm

by

Myrna STARING

Master of Science in Applied Geophysics
Delft University of Technology, Netherlands
Eidgenössische Technische Hochschule Zürich, Switzerland
Rheinisch-Westfälische Technische Hochschule, Germany

born in Vlissingen, The Netherlands

This dissertation has been approved by the promotor Prof. dr. ir. C.P.A. Wapenaar.

Composition of the doctoral committee:

Rector Magnificus	chairman
Prof. dr. ir. C.P.A. Wapenaar	Delft University of Technology, promotor

Independent members:

Prof. dr. ir. E.C. Slob	Delft University of Technology
Prof. dr. W.A. Mulder	Delft University of Technology
Prof. dr. A.F. Deuss	Utrecht University
Dr. ir. P.R. Mesdag	CGG
Dr. B. Cox	Hydreco Geomec B.V.
Dr. I.P. Pires de Vasconcelos	Utrecht University

The research in this thesis was funded by the Nederlandse Organisatie voor Wetenschappelijk Onderzoek - domein Toegepaste en Technische Wetenschappen.

Keywords: Marchenko, internal multiples, seismic, adaptive subtraction

Cover illustration: photograph of a Canadian lake by M. Staring

ISBN 978-94-6384-160-3

Print: Ridderprint | www.ridderprint.nl

An electronic version of this dissertation is available at `http://repository.tudelft.nl/`.

For my parents

Tsjeert and Liesbeth

and my mentors

Meneer Theune

Dr. Joe

Andreas Fichtner

Joost van der Neut

Huub Douma

and Kees Wapenaar

"If I have seen a little further it is by standing on the shoulders of Giants"

Isaac Newton, 1676

Summary

Adaptive Marchenko internal multiple attenuation

Curiosity regarding what we cannot see has always driven research. Science has helped us to uncover many of those hidden secrets. In particular, geophysics has helped us to image the inside of the Earth. By sending a seismic signal into the Earth and recording the signal that comes back, geophysicists can characterize the layers of the subsurface. Nowadays, geophysics is used for many purposes, for example, the localization of fossil fuels, the characterization of the subsurface for the construction of wind farms and the evaluation of reservoirs for geothermal energy. In order to decrease the risk and cost involved in these activities, we need images of the subsurface that are as accurate as possible.

These images can only be obtained if we fully understand the propagation of the seismic signal in the subsurface. A long-standing problem in geophysical imaging is the presence of internal multiple reflections. When imaging the subsurface, we assume that the signal only reflects once when there is a contrast in velocity and/or density (for example, when changing from sand to rock). However, in reality, the signal can reflect many times inside the subsurface before being recorded at the surface. When treating the arrivals that have reflected many times as arrivals that have only reflected once, we incorrectly image the subsurface and create ghost reflectors that do not exist. This problem is particularly strong in geological settings that have a complex structure with many strong velocity and/or density contrasts above an area of interest. This may happen, for example, when there is a reservoir of oil below a thick stratified salt layer. In such cases, the image of the area of interest is unreliable due to the presence of many ghost reflectors. Therefore, we have to use knowledge of wave propagation to predict and attenuate the internal multiples in the data prior to imaging.

In this thesis, I further develop the data-driven and wave-equation-based Marchenko method to make it suitable for the attenuation of internal multiples in seismic field data. In addition, I evaluate the performance of suitable methods by applying them to field datasets recorded in different geological settings. I start this evaluation by demonstrating that what we call the conventional Marchenko method is

perhaps not the most suitable Marchenko method for the application to field data. I develop an alternative Marchenko method instead: the adaptive double-focusing method. I show that this method indeed produces improved results compared to the conventional Marchenko method when applying it to a line of 2D data of the Santos Basin, Brazil.

Since the 2D results show promise, I continue with the extension to 3D applications. I first identify the key acquisition parameters that affect the result of our Marchenko method on 3D synthetic data and conclude that the limited crossline aperture and the coarse sail line spacing have the strongest effect on the quality of the result. Based on this evaluation, I interpolate the sail line spacing on 3D field data acquired in the Santos Basin and use the adaptive double-focusing method to predict and subtract internal multiples. I conclude that 3D Marchenko internal multiple attenuation seems to be sufficiently robust for the application to narrow azimuth streamer data in a deep marine setting, provided that there is sufficient aperture in the crossline direction and that the sail lines are interpolated. In addition, the adaptive double-focusing method is suitable for the attenuation of internal multiples generated by a complex overburden and for simultaneously redatuming to a level below this overburden.

Next, I modify the adaptive double-focusing method to obtain an adaptive double dereverberation method that is suitable when only aiming to attenuate internal multiples generated in an overburden without redatuming. Moreover, this method does not require a velocity model. I apply this method to a 2D line of data acquired in the very shallow Arabian Gulf. Also, I assess how to meet the data requirements for the Marchenko method in shallow water environments (e.g., the removal of surface-related multiples, the deconvolution of the source signature) and demonstrate that the state-of-the-art Robust Estimation of Primaries by Sparse Inversion (R-EPSI) method is capable of producing the correct input data for the Marchenko method in such settings.

Subsequently, I discuss the role of the adaptive filter in the application of the Marchenko method to field data. I argue that developments in seismic data processing allow us to predict internal multiples with more accuracy, such that only a conservative adaptive filter is needed to correct for the unavoidable minor amplitude and phase discrepancies between the internal multiples in the data and the predicted internal multiples. I demonstrate this by using a conservative adaptive filter to subtract internal multiples that were predicted by applying an adaptive Marchenko multiple elimination method to a 2D line of field data acquired in the Norwegian North Sea.

Finally, based on the results presented in this thesis, I conclude that the Marchenko method is an effective, data-driven and robust method for the prediction of internal multiples in marine seismic data. Different Marchenko methods are suitable for different purposes. There are two key elements for the successful application of a Marchenko method to field data: 1) the acquisition geometry needs to be sufficiently dense and 2) a careful processing workflow needs to be constructed that accounts for the specifics of the geological setting at hand, with significant emphasis on amplitude and phase preservation.

Samenvatting

Adaptieve Marchenko interne meervoudige reflectie onderdrukking

Nieuwsgierigheid naar het onzichtbare is altijd een belangrijke drijfveer voor onderzoek geweest. De wetenschap heeft ons geholpen om veel van deze verborgen geheimen te ontdekken. Meer specifiek, het vakgebied van de geofysica heeft ons geholpen om de verschillende lagen in de aarde te karakteriseren. Geofysici sturen een seismisch signaal de aarde in en nemen het signaal dat terugkomt op. Tegenwoordig wordt geofysica voor veel doeleinden gebruikt, bijvoorbeeld voor het lokaliseren van fossiele brandstoffen, het karakteriseren van de ondergrond voor de bouw van windmolenparken op zee, en het evalueren van de ondergrond voor geothermie. Om de risico's en de kosten van deze activiteiten te beperken hebben we een zo nauwkeurig mogelijk beeld van de ondergrond nodig.

Een nauwkeurig beeld van de ondergrond kan alleen worden verkregen als we de propagatie en verstrooiïng van het seismische signaal in de ondergrond volledig begrijpen. Een al lang bestaand probleem bij geofysische beeldvorming is de aanwezigheid van interne meervoudige reflecties. Bij beeldvorming van de ondergrond gaat men er standaard van uit dat het signaal slechts één keer reflecteert wanneer er een contrast is in snelheid en/of dichtheid (bijvoorbeeld bij een overgang van zand naar gesteente). In werkelijkheid kan het signaal echter vele malen in de ondergrond reflecteren voordat het aan het oppervlak wordt geregistreerd. Wanneer we een meervoudig gereflecteerd signaal behandelen als een signaal dat maar één keer heeft gereflecteerd, verkrijgen we een onjuist beeld van de ondergrond. Dit probleem is vooral aanwezig in geologische omgevingen met veel sterke snelheids- en/of dichtheidscontrasten boven een interessegebied. Dit komt bijvoorbeeld voor wanneer er zich onder een dikke laag zout een oliereservoir bevindt. In dergelijke gevallen is het verkregen beeld van het interessegebied onbetrouwbaar vanwege de aanwezigheid van veel meervoudige reflecties. Daarom gebruiken we de kennis van golfpropagatie om de interne meervoudige reflecties in de data te voorspellen en te verwijderen voorafgaand aan het beeldvormingsproces.

In dit proefschrift ontwikkel ik de data-gedreven en op de golfvergelijking gebaseerde Marchenko methode om deze geschikt te maken voor de onderdukking

van interne meervoudige reflecties in seismische velddata. Daarnaast evalueer ik de prestaties van deze geschikte methodes door ze toe te passen op velddata die in verschillende geologische omgevingen zijn verkregen. Ik begin deze evaluatie door aan te tonen dat wat we de conventionele Marchenko methode noemen niet altijd de meest geschikte Marchenko methode is voor de toepassing op velddata. Ik stel in plaats daarvan een alternatieve Marchenko methode voor: de adaptieve dubbele focusseringsmethode. Ik laat zien dat deze methode inderdaad betere resultaten oplevert dan de conventionele Marchenko methode bij toepassing op een lijn van 2D data verkregen in het Santos Bekken, Brazilië.

Aangezien de resultaten op 2D data veelbelovend zijn, ga ik door met de uitbreiding naar 3D toepassingen. Ik identificeer eerst de belangrijkste acquisitieparameters die van invloed zijn op het resultaat van de Marchenko methode toegepast op 3D synthetische data en concludeer dat de beperkte dwars-apertuur en de grote afstand tussen de acquisitie-lijnen het sterkste effect hebben op de kwaliteit van het resultaat. Op basis van deze evaluatie interpoleer ik de afstand tussen de acquisitielijnen op 3D velddata verkregen in het Santos Bekken, en gebruik ik de adaptieve dubbele focusseringsmethode om interne meervoudige reflecties te voorspellen en te verwijderen. Ik concludeer dat 3D Marchenko interne meervoudige reflectie onderdrukking voldoende robuust lijkt voor de toepassing op beperkte-hoek data in een diepe mariene omgeving, onder de voorwaarde dat de dwars-apertuur voldoende is en dat er tussen de acquisitie-lijnen geïnterpoleerd is. Daarnaast laat ik zien dat de adaptieve dubbele focusseringsmethode geschikt is voor situaties waarin we interne meervoudige reflecties willen onderdrukken, en tegelijkertijd virtuele bronnen en ontvangers willen creëren op een niveau direct boven het interessegebied.

Vervolgens pas ik de adaptieve dubbele focusseringsmethode aan om een adaptieve dubbele dereverberatiemethode te verkrijgen die geschikt is voor situaties waarin er alleen wordt gestreefd naar het onderdrukken van interne meervoudige reflecties zonder het verplaatsen van de bronnen en ontvangers van het oppervlak naar een interessegebied. Bovendien vereist deze methode geen snelheidsmodel. Ik pas deze methode toe op een lijn van 2D data verkregen in de zeer ondiepe Arabische Golf. Ik kijk ook hoe we kunnen voldoen aan de data vereisten voor de Marchenko methode in een omgeving met ondiep water (bijv. het verwijderen van oppervlaktegerelateerde meervoudige reflecties, de deconvolutie van de bronsignatuur) en laat zien dat de ultramoderne Robust Estimation of Primaries by Sparse Inversion (R-EPSI) methode in staat is om in dergelijke omgevingen de juiste data voor de Marchenko methode te produceren.

Daarna bespreek ik de rol van het adaptieve filter bij de toepassing van de Marchenko methode op velddata. Ik stel dat ontwikkelingen in seismische dataverwerking het mogelijk maken om interne meervoudige reflecties nauwkeuriger te voorspellen, zodat alleen een conservatief adaptief filter nodig is om te corrigeren voor de onvermijdelijke kleine amplitude- en faseverschillen tussen de interne meervoudige reflecties in de data en de voorspelde interne meervoudige reflecties. Ik demonstreer dit door een conservatief adaptief filter te gebruiken om interne meervoudige reflecties te verwijderen die werden voorspeld door een adaptieve Marchenko methode toe te passen op 2D velddata verkregen in de Noorse Noordzee.

Ten slotte concludeer ik op basis van de resultaten in dit proefschrift dat de Marchenko methode een effectieve, data-gedreven en robuuste methode is voor de voorspelling en verwijdering van interne meervoudige reflecties in seismische data verkregen in mariene omgevingen. Verschillende Marchenko methoden zijn geschikt voor verschillende doeleinden. Er zijn twee belangrijke elementen voor het succesvol toepassen van een Marchenko methode op velddata: 1) de acquisitiegeometrie moet voldoende dicht zijn en 2) er moet een zorgvuldige data-verwerkingsprocedure worden opgezet die rekening houdt met de specifieke kenmerken van de geologische omgeving, met voldoende nadruk op amplitude- en fasebehoud.

Contents

1

Introduction

Imagine that you are on the shore of a beautiful lake surrounded by mountains. The water is perfectly still, and the water surface shows a perfect reflection of the mountains. Now pretend that you have no sense of up or down: what are the real mountains and what is just a reflection? And what if we want to see the water in the lake, instead of only seeing the reflection of the mountains?

This is a problem that geophysicists face when making an image of the interior of the Earth. Geophysicists send a signal into the Earth, comparable to the sun that shines on the mountains. They hope to directly receive the signal back, like the light that reflects off the mountains and directly travels to our eyes. However, like the water in the lake reflecting the image of the mountains, there are many layers in the Earth's subsurface that reflect the signal and bounce it around before sending it back to the surface. These layers are created by different materials, for example different types of rock. A change in material causes a contrast that reflects part of the signal. For example, going from sediments to a salt layer causes a strong contrast that results in part of the signal being reflected multiple times before coming back to the surface. These multiple reflections can overlay the actual feature that we wish to see, which gives us an unreliable image of the Earth. How do we know whether what we see is real, or whether it is just a multiple reflection? And how can we find out what the fake image is hiding?

1.1 Seismic imaging for subsurface characterization

■ 1.1.1 The history of seismic imaging

For more than 4000 years, humanity has been using gas, oil, and its derivatives for many aspects in daily life. There are reports of wells being drilled in China as early as 347 BC [*Vogel*, 1993]. With the use of bamboo and a drill bit, Chinese

engineers could already reach depths of 100 m or more. Their wells produced brine and natural gas, which were vital for China's blooming salt industry. Well planning was entirely based on the topology or the location with respect to successful wells, which often resulted in new successful wells, but also frequently resulted in failure. Around the 11th century, deep-drilling was invented in the Sichuan province, four centuries before the Europeans developed a similar technique. Ever since, we have been drilling deeper and deeper to explore more of the subsurface. As a result, the need arose for a tool to optimize the process of exploration, such that well locations could be carefully selected to decrease risk and to optimize cost.

In the beginning of the 19th century, Andrija Mohorovičić, a Kroatian meteorologist and geophysicist, first employed seismic waves from earthquake recordings to make a model of the Earth's interior. Soon afterwards, realization came that there was no need to wait for an earthquake to occur, but that artificial sources (for example, dynamite) could be used to send a signal into the Earth and record what comes back. The first petroleum discoveries using seismic reflection exploration date back to the 1920s [*Telford et al.*, 1990]. After that, developments in both acquisition and processing rapidly followed. Using knowledge of wave propagation, combined with the properties of the different materials that the Earth consists of, we could now create an image of the subsurface. Rather than using the topology or the location with respect to successful wells, well planning became more accurate due to the use of these seismic images, thereby reducing risk and optimizing cost.

1.1.2 Multiples

Figure 1.1 shows some of the paths that seismic waves can take after being sent into the Earth. Figure 1.1a shows what we call a primary reflection, which is the ideal signal that we wish to record. It reflects off a contrast in the subsurface once before being recorded. Figure 1.1b shows an undesired part of the recorded signal: a surface-related multiple. Instead of being recorded directly after reflecting off a contrast, the signal now also reflects at the Earth's surface and reflects again off a contrast in the subsurface before being recorded. In this thesis, we assume that this type of multiple has already been removed from the signal. We focus on the internal multiples as shown in Figure 1.1c. These multiples do not reflect off the Earth's surface, but reflect multiple times at contrasts inside the Earth before being recorded.

Most current imaging methods are based on the assumption that the recorded wavefield only consists of the primary reflections. In reality, there are also internal multiples. Most imaging methods cannot handle internal multiples correctly and will place reflectors at incorrect positions (see Figure 1.2). These incorrect reflectors create artefacts in the image that can interfere with the reflectors that were correctly placed, thereby possibly masking the real structure in the area of interest.

Therefore, the resulting images cannot be completely trusted. Nevertheless, well planning is almost solely based on the interpretation of these incorrect images and therefore still involves a considerable amount of risk. This problem is currently particularly significant, since most of the easily accessible oil and gas has already been found and the remaining resources are more difficult to reach. As a result, the

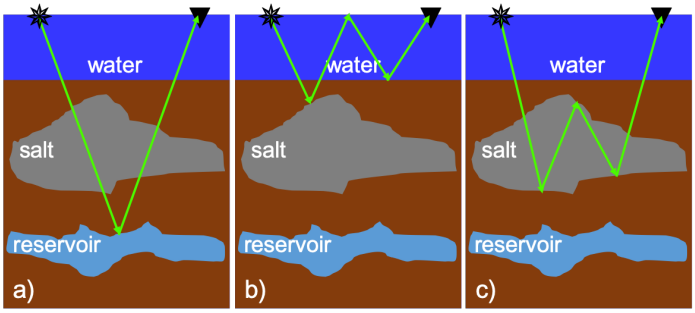

Figure 1.1: *Cartoons showing a geophysical experiment in the ocean. A seismic source (the star) produces a signal that is sent into the Earth through the water layer. It is reflected inside the Earth when properties of the subsurface change from one layer to the other, after which it gets recorded by a receiver (the triangle). The recorded seismic signal has different components: a) primary reflections that have just reflected once in the subsurface, b) surface-related multiples that reflected again at the water-air interface and c) internal multiples that reflected multiple times inside the subsurface.*

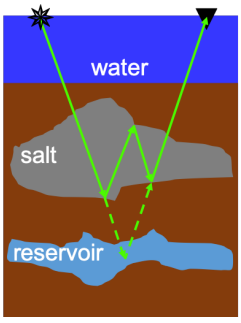

Figure 1.2: *Cartoon showing how most current imaging methods incorrectly handle internal multiple reflections. The methods assume that the wavefield was only reflected once inside the subsurface, such that the internal multiple is incorrectly placed inside the reservoir area.*

complexity and cost of drilling operations is increasing. Having an accurate image of the subsurface, without artefacts due to internal multiples, would be of great aid in decreasing risk and cost in the exploration process.

1.2 The removal of internal multiples

In order to create an accurate image, either a new imaging method that utilizes the internal multiple reflections has to be developed, or internal multiples have to be removed from the reflection response prior to imaging such that the single-reflection

assumption is not violated. The focus of this thesis is on the latter approach, even though extra value could potentially be extracted from internal multiples by the first approach. The attenuation of internal multiples has been extensively studied, resulting in a variety of methods. These methods can be roughly divided into two categories: one that filters the data by using a difference in properties between primary reflections and multiple reflections, and one that uses the wave equation to predict and subtract internal multiples.

1.2.1 Category 1: Filtering methods

The methods of the first category are based on a difference in properties between the primary reflections and the internal multiple reflections. Typically, this difference appears in a particular domain, such as the frequency-wavenumber domain or the τ-p domain. Filtering methods first transform the data into the relevant domain, in which primary reflections and internal multiple reflections occupy different sections of the data, and then apply a simple filter to mute the section that contains the internal multiple reflections [e.g. *Hampson*, 1986; *Foster and Mosher*, 1992; *Zhou and Greenhalgh*, 1994]. Next, these methods perform an inverse-transform to bring the filtered data back into the original domain (the time-space domain). The result is a multiple-free reflection response. Although filtering methods are straightforward and cheap, they are based on an assumption (primaries and internal multiples are separated in some domain) that does not hold in most geological settings (for example, when the subsurface has lateral variations and when velocity inversions are present). These methods typically only work for simple media, where they are preferred due to their low cost, but they are not suitable in most other cases.

1.2.2 Category 2: Wave-equation-based methods

Methods of the second category are based on the wave equation. They use the physics of wave propagation to predict and subtract the internal multiples from the reflection response. By multidimensionally convolving and correlating the data with itself, internal multiples can be predicted [*Berkhout and Verschuur*, 1997; *Weglein et al.*, 1997; *Jakubowicz*, 1998; *Ikelle*, 2006]. Next, these predictions can be subtracted from the data to obtain a multiple-free reflection response that is suitable for imaging. However, some of these methods are recursive, starting at the surface and working their way down to the desired depth level. This causes errors to propagate from the shallow subsurface to the deep subsurface, where our zone of interest lies. Also, these methods often require the identification of multiple generators, thereby introducing bias into the process. Internal multiples that are not obvious might be missed and still cause artefacts in the resulting image. In addition, some of these methods predict kinematically correct internal multiples, but rely on an adaptive filter for obtaining the correct amplitude and/or phase. This poses a risk in highly complex media, where an agressive adaptive filter might be needed to correct for all amplitude and phase errors, thereby making adaptive subtraction without substantial corruption of the primary reflections impossible.

1.3 The Marchenko method

The Marchenko method is also based on the wave equation, but does not require the identification of internal multiple generators. Instead, the method considers the entire overburden as a whole. Also, it does not have a layer-stripping approach that causes error propagation. In addition, the Marchenko method in principle, and on ideal synthetic data, predicts internal multiples with the correct amplitude and phase, such that an adaptive filter is not needed. The method originates from theoretical physics, where the Gelfand-Levitan-Marchenko equation was used to solve the one-dimensional inverse scattering problem. It was rediscovered by the Geophysics community in 2012, when *Broggini et al.* [2012] first showed its use for single-sided focusing in 1D. *Wapenaar et al.* [2013] extended the method to 2D and 3D, which made it suitable for the use on seismic reflection data. The method is data-driven, only needing the reflection response at the acquisition surface and, in some cases, a smooth velocity model of the subsurface.

At the core of the method is a set of equations, the coupled Marchenko equations, that are solved either iteratively or using a direct inversion to retrieve so-called focusing functions. These focusing functions are designed such, that when injected into the medium, they focus on any desired point in the medium and act as a virtual point source or virtual receiver that either emits or records a Green's function. This allows us to create a line or grid of virtual sources and virtual receivers at any desired depth level, for example, directly above our target area or at the acquisition surface. We can then either deconvolve the directionally-decomposed Green's functions to obtain a reflection response without internal multiples generated in an overburden [*Wapenaar et al.*, 2014a], or we can retrieve the focusing functions and Green's functions as a series that contains the internal multiple predictions [*van der Neut et al.*, 2015a]. The latter allows us to use an adaptive filter to subtract the internal multiple predictions from the reflection response. Note that the Marchenko method in principle does not require an adaptive filter, but minor amplitude and phase errors are usually present when predicting internal multiples on field data, caused by imperfect acquisition, imperfect processing and assumptions of the Marchenko method itself. In that case, a conservative adaptive filter can help to correctly attenuate the internal multiples in the reflection response.

After the rediscovery of the Marchenko method by the Geophysics community, theoretical developments followed rapidly. For example, the method was extended to include surface-related multiples [*Singh et al.*, 2015, 2016; *Slob and Wapenaar*, 2017; *Zhang and Slob*, 2019], transmission losses [*Slob*, 2016; *Zhang et al.*, 2019], elastodynamic effects [*Wapenaar*, 2014; *da Costa Filho et al.*, 2014; *Reinicke and Wapenaar*, 2017] and to retrieve primary reflections only [*Meles et al.*, 2016], amongst many others. In theory and on ideal synthetic data, the Marchenko method and its many flavours and extensions work perfectly and show promise. However, when starting this project in 2015, it was uncertain whether the Marchenko method could be applied to field data.

1.4 Aim and outline of this thesis

The aim of this thesis is to enable the application of the Marchenko method on field data. In order to achieve this, I further develop the Marchenko method to make it more suitable for the field data application. In addition, I evaluate the performance of suitable Marchenko methods by applying them to field datasets recorded in different geological settings. This work was carried out in close cooperation with experts from academia and industry.

By building on existing theory and the experience from the first field data application presented by *Ravasi et al.* [2016], chapter 2 introduces a modified version of the Marchenko method: the adaptive double-focusing method. This method is tested and compared to the performance of the conventional Marchenko method [*Wapenaar et al.*, 2014a] on 2D synthetic data and 2D field data of the Santos Basin, Brazil. These tests show that the adaptive double-focusing method is more robust compared to the conventional Marchenko method, which thus makes it more suitable for the field data application. Internal multiples generated in a complex overburden are predicted and subtracted, thereby improving the image of the target area.

Based on the results in chapter 2, I continue the evaluation of the adaptive double-focusing method in chapter 3. I perform a series of 3D synthetic tests to evaluate the key acquisition parameters that have an effect on the result of the adaptive double-focusing method. The limited aperture in the crossline direction and the coarse sail line spacing are the most important parameters that affect the result of the Marchenko method in this particular setting. Unfortunately, the aperture in the crossline direction is a limitation of narrow azimuth (NAZ) streamer acquisition, but we can interpolate for missing sail lines. I carry out this interpolation on 24 lines of 3D NAZ streamer data of the Santos Basin, prior to the application of the adaptive double-focusing method. The method is capable of predicting and subtracting internal multiples from the target area, thereby improving the geological interpretation.

In chapter 4, I propose a modification of the adaptive double-focusing method based on observations in chapter 3. I apply the modified method to ocean bottom cable (OBC) data of the Arabian Gulf, which is well-known for its complex internal multiple problem and therefore considered to be an ultimate test. In addition, challenges related to the preprocessing of the data in a very shallow water environment are addressed. The result of this chapter shows that the Marchenko method can also be applied in geological settings with very shallow water and a complex overburden.

Next, chapter 5 considers the use of adaptive filters for the subtraction of the internal multiple predictions that are obtained using the Marchenko multiple elimination method. I argue that developments in seismic processing in combination with the accurate prediction of internal multiples with a Marchenko method change the role of the adaptive filter. Instead of needing an aggressive adaptive filter to correct for inaccurate internal multiple predictions in combination with an unknown wavelet, we now only need a conservative adaptive filter to take care of minor imperfections in the internal multiple predictions. Using a 2D line of streamer data

from the Vøring basin, I demonstrate that this method is capable of predicting and subtracting all orders of internal multiples from the target area using only a conservative adaptive filter.

The final chapter concludes that the Marchenko method is suitable for the field data application, provided that 1) the acquisition geometry is sufficiently dense and 2) a careful processing workflow is constructed that accounts for the specifics of the geological setting at hand, with emphasis on amplitude and phase preservation. In addition, I address the strengths and limitations of the Marchenko method and provide suggestions for further research. Lastly, I discuss a series of practical considerations for the field data application.

Appendix A presents a monitoring strategy, thereby showing that the Marchenko method can also be used for other purposes apart from internal multiple attenuation. Using the Marchenko method, we can remove the initial target response and replace it with a target response that was modeled for many possible scenario's. For time-lapse applications, this method is more efficient compared to repeated modeling of the complete reflection response.

2

Source-receiver Marchenko redatuming on field data using an adaptive double-focusing method

Abstract In this chapter, we take the first step in analysing the strengths and limitations of Marchenko methods when applied to field data. Typically, the single-focusing Marchenko method is combined with a multidimensional deconvolution (MDD) to achieve redatuming and to attenuate internal multiples generated by an overburden. We call this the conventional Marchenko method. Instead, we propose to replace the MDD step by a second focusing step that naturally complements the single-focusing Marchenko method. We obtain a straightforward and robust method that is less sensitive to imperfections in the data and a sparse acquisition geometry, at the cost of leaving some later arriving internal multiples below the target area behind. In addition, this method is particularly suitable for the application to large data volumes. We apply both the conventional Marchenko method and our proposed Marchenko method to 2D field data of the Santos Basin and evaluate their performance.

Published as: Staring, M., Pereira, R., Douma, H., van der Neut, J., & Wapenaar, K. (2018). Source-receiver Marchenko redatuming on field data using an adaptive double-focusing method. Geophysics, 83(6), S579-S590.
Note that minor changes have been introduced to make the text consistent with the other chapters.

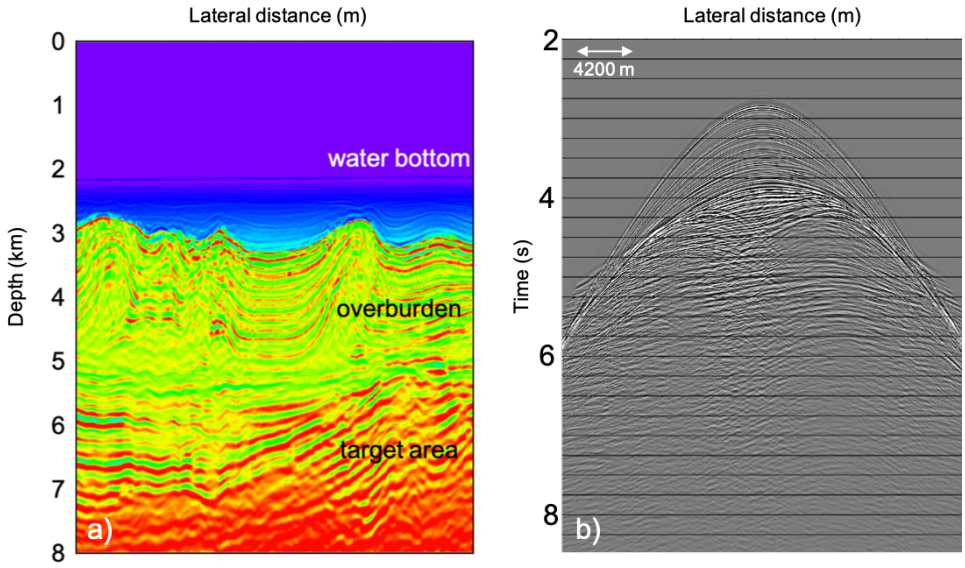

Figure 2.1: *a) A 2D slice of the velocity model of the Santos Basin obtained by an acoustic inversion of 3D field data, and b) a common source gather from the generated realistic synthetic dataset.*

2.1 Introduction

The Santos Basin offshore Brazil is an excellent example of a region where internal multiples hinder accurate imaging [*Cypriano et al.*, 2015]. The region contains pre-salt carbonates that often hold significant amounts of oil. These carbonates are covered by a highly reflective stratified salt layer that generates strong internal multiples. Moreover, the concave shape of the salt focuses the energy and thereby further enhances these multiples.

Most conventional imaging methods, for example the reverse time migration (RTM) method [*Baysal et al.*, 1983], are based on the assumption that the recorded wavefield consists of single-scattered waves. This assumption is not met in reality, which leads to imaging artefacts, especially in areas with a complex overburden that generates strong internal multiples. Figure 2.1a shows a 2D slice of the velocity model of the Santos Basin, obtained from an acoustic inversion of the 3D field data. This slice was used to generate a realistic 2D synthetic dataset (source and receiver spacing 25 m, a common source gather is displayed in figure 2.1b). In order to demonstrate the effect of imaging artefacts in this geological setting, figure 2.2 shows RTM images of this synthetic dataset. The synthetic dataset generated by the velocity model in figure 2.1a produced the image in figure 2.2a, while the synthetic dataset used to create figure 2.2b was generated in the same model that was edited to become homogeneous below the base of salt. As a result, reflections from the

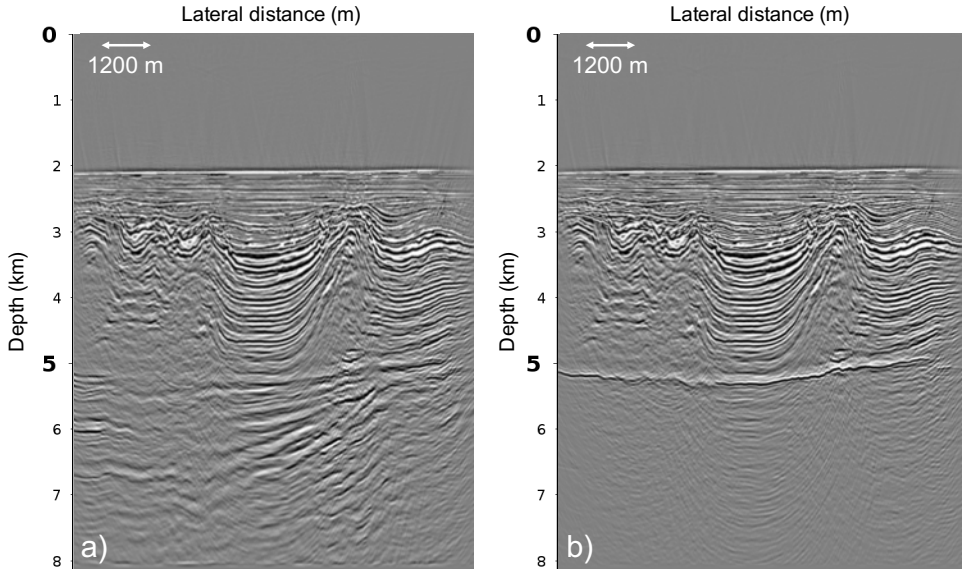

Figure 2.2: *a) RTM image of 2D synthetic data of the Santos Basin, and b) the same image, but the model is homogeneous below the base of salt, such that only internal multiples generated in the overburden are visible below the base of salt.*

reservoir do not exist and only the artefacts due to scattering in the overburden can be observed in the region below the base of the salt. Note that most internal multiples have a half-circle appearance, showing an imprint of the salt above. Based on these images, it is clear that imaging in the Santos Basin, or in similar geological settings, could significantly benefit from the removal of internal multiples.

Various methods exist that aim to predict and remove internal multiples from the reflection response [*Weglein et al.*, 1997; *Jakubowicz*, 1998; *Hung and Wang*, 2012]. Other methods aim to address internal multiples during imaging, such as full waveform imaging [*Davydenko and Verschuur*, 2017]. Our focus is on the Marchenko method, which was reintroduced into the geophysics community by *Broggini and Snieder* [2012], based on the work of *Rose* [2001, 2002]. *Wapenaar et al.* [2013] modified the method and extended it to more dimensions.

The Marchenko method is data-driven, only requiring the reflection response at the acquisition surface and a smooth velocity model of the subsurface. It aims to solve the coupled Marchenko equations, which results in focusing functions. These focusing functions, in turn, relate the wavefield measured at the acquisition surface to directionally-decomposed Green's functions at specified virtual receiver positions (coinciding with the focal points of the focusing functions) inside the medium. These Green's functions contain all orders of internal multiples and can be used to create a redatumed reflection response directly above the target area.

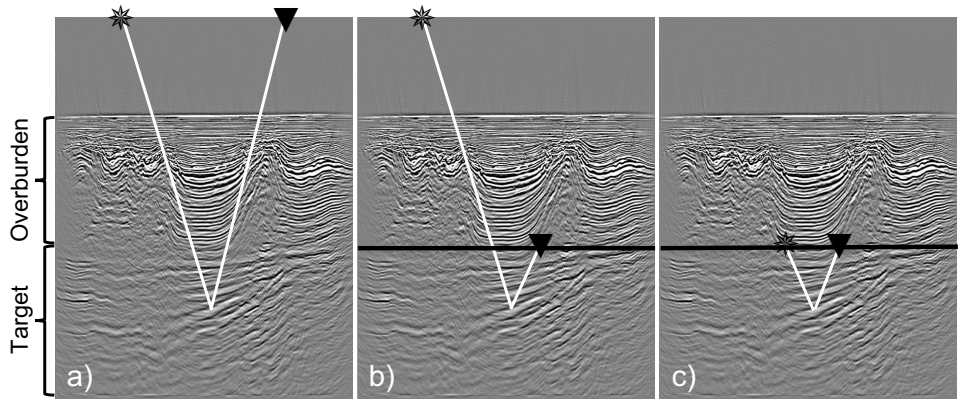

Figure 2.3: *Cartoon illustrating the reflection response a) recorded by sources and receivers at the acquisition surface, b) after receiver redatuming, c) after source-receiver redatuming. The seismic images in the background are only meant to illustrate an inhomogeneous medium, it is the same in all sub-figures.*

There are multiple ways of obtaining a source-receiver redatumed reflection response from the retrieved focusing functions and Green's functions [*van der Neut et al.*, 2018]. Since the Green's functions are already receiver redatumed (see figure 2.3b), the source also needs to be brought down in order to obtain a source-receiver redatumed reflection response (figure 2.3c). Conventionally, a multidimensional deconvolution (MDD) of the retrieved upgoing Green's function with the retrieved downgoing Green's function is used to achieve this [*Wapenaar et al.*, 2014a]. When using this method, the resulting source-receiver redatumed reflection response exists in a truncated medium. The obtained response is free of internal multiples generated in the overburden and can be used to create an image of the target area that is free of artefacts due to these multiples. However, applying the MDD method requires solving a large-scale inverse problem that is fundamentally ill-posed [*Minato et al.*, 2013]. This makes the method sensitive to imperfections in the data (for example, noise or incomplete illumination) and sparse acquisition geometries, which we typically find in field data. Since our aim is to apply source-receiver Marchenko redatuming to field data, we decided to look for an alternative source redatuming approach that is more suitable for our needs.

In this chapter, we present an alternative method to perform source-receiver redatuming: the adaptive double-focusing method. Starting from the preprocessing of the acquired reflection response, we go step-by-step through the theory of the single-focusing Marchenko method to redatum our receivers. After that, we review the MDD method for source redatuming and discuss its advantages and limitations. Based on this evaluation, we introduce the adaptive double-focusing method and explain why this method is more suitable for applying source-receiver Marchenko

redatuming to field data. Next, we bring the theory into practice by performing a series of tests on 2D synthetic data. We compare the performance of the adaptive double-focusing method to the performance of the conventional Marchenko method on 2D synthetic data for three different cases: for a dense acquisition geometry and a known scaling factor, for a dense acquisition geometry and an unknown scaling factor, and for a coarse acquisition geometry and a known scaling factor. The results of these tests clearly show the benefits of the adaptive double-focusing method over the conventional Marchenko method. We conclude this chapter by demonstrating the successful application of the proposed method to 2D field data of the Santos Basin. The adaptive double-focusing method seems to predict and subtract internal multiples, which results in a cleaner image and an improvement of the geological interpretability of the target area.

2.2 Receiver redatuming

We start with reflection response $R(\mathbf{x}_R, \mathbf{x}_S, t)$ that accounts for propagation and scattering from sources $\mathbf{x}_S$ at the acquisition surface $\partial\mathbb{D}_0$ via the inhomogeneous lower half space to receivers $\mathbf{x}_R$ at the acquisition surface $\partial\mathbb{D}_0$. It is assumed that the half space above $\partial\mathbb{D}_0$ is reflection free. This situation is achieved for streamer data by suppressing surface-related multiples, removing noise, horizontally propagating waves and the receiver ghost, and by deconvolving the source signature. For ocean bottom cable (OBC) data, we achieve this situation by applying a multidimensional deconvolution (e.g. *Amundsen et al.* [2001]). For details on the preprocessing of the field data, see section 2.6. Using the preprocessed reflection response R, we introduce operator $\mathcal{R}$:

$$\mathcal{R}P(\mathbf{x}_R, t) = \int_{\partial\mathbb{D}_0} R(\mathbf{x}_R, \mathbf{x}_S, t) * P(\mathbf{x}_S, t) d^2\mathbf{x}_S. \tag{2.2.1}$$

Operator $\mathcal{R}$ performs a multidimensional convolution of the reflection data R with arbitrary wavefield P. We also introduce operator $\mathcal{R}^\star$ that performs a multidimensional correlation of the reflection response R with arbitrary wavefield P:

$$\mathcal{R}^\star P(\mathbf{x}_R, t) = \int_{\partial\mathbb{D}_0} R(\mathbf{x}_R, \mathbf{x}_S, -t) * P(\mathbf{x}_S, t) d^2\mathbf{x}_S. \tag{2.2.2}$$

Next, we use these operators in the Marchenko method. At the core of this method are the directionally-decomposed focusing functions $\hat{f}^+(\mathbf{x}_S, \mathbf{x}_F, t)$ and $\hat{f}^-(\mathbf{x}_S, \mathbf{x}_F, t)$. These functions relate the reflection response $R(\mathbf{x}_R, \mathbf{x}_S, t)$ measured at the acquisition surface $\partial\mathbb{D}_0$ to directionally-decomposed Green's functions $\hat{G}^+(\mathbf{x}_F, \mathbf{x}_S, t)$ and $\hat{G}^-(\mathbf{x}_F, \mathbf{x}_S, t)$ measured at the redatuming level $\partial\mathbb{D}_i$ [*Wapenaar et al.*, 2013; *Slob et al.*, 2014; *van der Neut et al.*, 2015a]:

$$\hat{f}^-(\mathbf{x}_S, \mathbf{x}_F, t) + \hat{G}^-(\mathbf{x}_F, \mathbf{x}_S, t) = \mathcal{R}\hat{f}_0^+(\mathbf{x}_S, \mathbf{x}_F, t) + \mathcal{R}\hat{f}_m^+(\mathbf{x}_S, \mathbf{x}_F, t) \tag{2.2.3}$$

and

$$\hat{f}_0^+(\mathbf{x}_S,\mathbf{x}_F,t)+\hat{f}_m^+(\mathbf{x}_S,\mathbf{x}_F,t)-\hat{G}_d^+(\mathbf{x}_F,\mathbf{x}_S,-t)-\hat{G}_m^+(\mathbf{x}_F,\mathbf{x}_S,-t)=\mathcal{R}^\star\hat{f}^-(\mathbf{x}_S,\mathbf{x}_F,t). \tag{2.2.4}$$

Here the $^+$ and $^-$ represent downgoing and upgoing wavefields recorded at virtual receivers. Vector $\mathbf{x}_F$ denotes the focal points that will become virtual receivers located at the redatuming level $\partial\mathbb{D}_i$. Evanescent waves are neglected in equation 2.2.4. The retrieved Green's functions account for propagation through the inhomogeneous lower half space from a source at the acquisition surface $\mathbf{x}_S$ to a focal point $\mathbf{x}_F$ at the redatuming level, and are thus considered receiver redatumed wavefields (see figure 2.3b). These Green's functions correctly contain all orders of scattering generated in the overburden. Note that the downgoing Green's function $\hat{G}^+$ has a direct part $\hat{G}_d^+$ and a multiple coda $\hat{G}_m^+$. Also the downgoing focusing function consists of a direct part $\hat{f}_0^+$ and a coda $\hat{f}_m^+$. The direct part $\hat{f}_0^+$ is equal to the inverse of the direct arrival of the transmission response of the overburden, which can be estimated from a smooth velocity model [*Broggini et al.*, 2014]. This estimate can be obtained using finite-difference modeling or an Eikonal solver. The wavefield $\hat{f}_0^+$ has been convolved with an user-specified wavelet $\hat{\cdot}$ that covers the finite frequency content of the data, such that a band-limitation is imposed. The coda $\hat{f}_m^+$ follows the direct wave $\hat{f}_0^+$ and accounts for the scattering effects of the overburden. If the overburden were homogeneous, this coda would not exist and the focusing function would only have a direct part.

The key element in solving equations 2.2.3 and 2.2.4 is a causality assumption which presumes that the focusing functions and the Green's functions are separated in the time domain [*Wapenaar et al.*, 2014a]. A Green's function is causal by definition (first arrival at $t=t_d$, followed by the scattering coda), whereas a focusing function is acausal (arriving before $t=t_d$, non-physical). We design a time window $\Theta(\mathbf{x}_F,\mathbf{x}_S,t)$ that separates the causal and acausal wavefields in the time domain:

$$\begin{aligned}\Theta(\mathbf{x}_F,\mathbf{x}_S,t)=\\ (\Theta_0(t+t_d(\mathbf{x}_F,\mathbf{x}_S)-t_\epsilon)-\Theta_0(t-t_d(\mathbf{x}_F,\mathbf{x}_S))+t_\epsilon).\end{aligned} \tag{2.2.5}$$

The truncations applied by this window are tapered Heaviside step functions Θ_0 based on the one-way traveltime t_d from the acquisition surface to the focal point. The term t_ϵ corrects for the finite frequency content of the data. As a rule of thumb, it is equal to half the duration of the user-specified wavelet that was placed on the direct wave $\hat{f}_0^+$ [*Slob et al.*, 2014]. Appendix A explains how to choose t_ϵ such that the time window $\Theta(\mathbf{x}_F,\mathbf{x}_S,t)$ is correctly designed.

We obtain the coupled Marchenko equations by applying time window $\Theta(\mathbf{x}_F,\mathbf{x}_S,t)$ to equations 2.2.3 and 2.2.4:

$$\begin{aligned}\hat{f}^-(\mathbf{x}_S,\mathbf{x}_F,t)=\\ \Theta(\mathbf{x}_F,\mathbf{x}_S,t)\mathcal{R}\hat{f}_0^+(\mathbf{x}_S,\mathbf{x}_F,t)+\Theta(\mathbf{x}_F,\mathbf{x}_S,t)\mathcal{R}\hat{f}_m^+(\mathbf{x}_S,\mathbf{x}_F,t)\end{aligned} \tag{2.2.6}$$

and

$$\hat{f}_m^+(\mathbf{x}_S,\mathbf{x}_F,t) = \Theta(\mathbf{x}_F,\mathbf{x}_S,t)\mathcal{R}^\star \hat{f}^-(\mathbf{x}_S,\mathbf{x}_F,t). \tag{2.2.7}$$

Convolutions and correlations along the time-axis can be efficiently carried out by multiplications in the frequency domain. Conversely, the time-windowing operations are more efficiently carried out in the time domain. When comparing equations 2.2.3 and 2.2.4 to equations 2.2.6 and 2.2.7, the effect of the time window $\Theta(\mathbf{x}_F,\mathbf{x}_S,t)$ becomes clear. The Green's functions $\hat{G}^-$ and $\hat{G}^+$ and the direct downgoing focusing function $\hat{f}_0^+$ have been muted, such that only the coda of the downgoing focusing function $\hat{f}_m^+$ and the upgoing focusing function $\hat{f}^-$ remain on the left-hand side of the equations. The number of unknowns has been reduced to these two focusing functions only, thereby allowing the coupled Marchenko equations to be iteratively solved (given that $\hat{f}_0^+$ is known). The iterative process is initiated by solving equation 2.2.6, using the modeled time-reversed direct transmission $\hat{f}_0^+$ and setting $\hat{f}_m^+ = 0$.

Once initiated, the iterative process alternates between updating the upgoing focusing function $\hat{f}^-$ and the coda of the downgoing focusing function $\hat{f}_m^+$. When converged, the focusing function focuses at the defined focal point which then acts as a virtual source or a virtual receiver. Alternatively, this set of equations can be solved by direct inversion [*Ravasi*, 2017; *Slob and Wapenaar*, 2017].

We apply the time window $\Psi = I - \Theta$ to retrieve the upgoing Green's function $\hat{G}^-$ from equation 2.2.3:

$$\hat{G}^-(\mathbf{x}_F,\mathbf{x}_S,t) = \Psi(\mathbf{x}_F,\mathbf{x}_S,t)\mathcal{R}\hat{f}_0^+(\mathbf{x}_S,\mathbf{x}_F,t) + \Psi(\mathbf{x}_F,\mathbf{x}_S,t)\mathcal{R}\hat{f}_m^+(\mathbf{x}_S,\mathbf{x}_F,t). \tag{2.2.8}$$

However, the time window $\Psi(\mathbf{x}_F,\mathbf{x}_S,t)$ is not sufficient to retrieve the downgoing Green's function $\hat{G}^+$ from equation 2.2.4. When applying this filter to equation 2.2.4, we would not only retrieve $\hat{G}^+$, but also the direct part of the downgoing focusing function $\hat{f}_0^+$. This is due to the fact that the time-reversed direct part of the downgoing Green's function $\hat{G}_d^+$ and the direct part of the downgoing focusing function $\hat{f}_0^+$ overlap in time. To solve this problem, we use the retrieved focusing functions $\hat{f}^-$ and $\hat{f}_0^+$ [*Wapenaar et al.*, 2014a]:

$$\hat{G}^+(\mathbf{x}_F,\mathbf{x}_S,-t) = \hat{f}_0^+(\mathbf{x}_S,\mathbf{x}_F,t) - \Psi\mathcal{R}^\star \hat{f}^-(\mathbf{x}_S,\mathbf{x}_F,t). \tag{2.2.9}$$

This concludes our review of the retrieval of the focusing functions $\hat{f}^+(\mathbf{x}_S,\mathbf{x}_F,t)$ and $\hat{f}^-(\mathbf{x}_S,\mathbf{x}_F,t)$ and the receiver redatumed Green's functions $\hat{G}^+(\mathbf{x}_F,\mathbf{x}_S,t)$ and $\hat{G}^-(\mathbf{x}_F,\mathbf{x}_S,t)$ using the single-focusing Marchenko method. In the following, we use these retrieved wavefields as input for source redatuming.

2.3 Source redatuming: The multidimensional deconvolution

Conventionally, the source redatuming step is achieved by a multidimensional deconvolution (MDD). This method is inherited from seismic interferometry, where it

was used for virtual source redatuming, interferometric imaging, or for retrieving a reflection response from passive seismic data [e.g. *van der Neut et al.*, 2011; *Nakata et al.*, 2014; *Hartstra et al.*, 2017]. The MDD method can also be used as a preprocessing step by removing surface-related multiples, the source signature and ghosts from OBC data [*Amundsen et al.*, 2001]. By (multidimensionally) deconvolving the retrieved Green's functions with one another, we retrieve a redatumed reflection response R:

$$\hat{G}^{-}(\mathbf{x}_F, \mathbf{x}_S, t) = \int_{\partial\mathbb{D}_i} R(\mathbf{x}_F, \mathbf{x}'_F, t) * \hat{G}^{+}(\mathbf{x}'_F, \mathbf{x}_S, t) d^2\mathbf{x}'_F, \tag{2.3.1}$$

where both $\mathbf{x}_F$ and $\mathbf{x}'_F$ indicate focal points, such that redatumed reflection response R accounts for propagation from virtual sources to virtual receivers at the redatuming level $\partial\mathbb{D}_i$. This response is measured in a truncated medium which is reflection-free above the redatuming level (see figure 2.4a). However, we need to solve a large-scale inverse problem to find the redatumed reflection response R that resides inside the integrand. This inverse problem is fundamentally ill-posed [*Minato et al.*, 2013] and has to be stabilized in order to be successfully solved. In field data, we typically have incomplete illumination, a sparse acquisition geometry, a finite aperture and noise. These factors contribute to the instability of the MDD method, thereby making it more difficult to obtain a correct solution to the inverse problem [*van der Neut et al.*, 2011]. Therefore, we decided to look for an alternative method that does not require solving an inverse problem. We remark that the MDD method is successfully used in a range of other applications, and that we simply look for an alternative that is more suitable for our needs.

2.4 An alternative: the adaptive double-focusing method

Solving the coupled Marchenko equations can be considered as a first focusing step (bringing the receivers down), and we now propose to replace the inversion step of the MDD method by a second focusing step (bringing the sources down). Instead of using the directionally-decomposed Green's functions $\hat{G}^{-}$ and $\hat{G}^{+}$ to perform the MDD method, we select the upgoing Green's function $\hat{G}^{-}$ and the downgoing focusing function $\hat{f}^{+}$ for a more simple and straightforward source redatuming scheme. When convolving the downgoing focusing function $\hat{f}^{+}(\mathbf{x}_S, \mathbf{x}'_F, t)$ at a virtual source location with the upgoing Green's function $\hat{G}^{-}(\mathbf{x}_F, \mathbf{x}_S, t)$ at a virtual receiver location, we create downward-radiating virtual sources at the redatuming level [*Wapenaar et al.*, 2016a; *Singh and Snieder*, 2017; *van der Neut et al.*, 2018]:

$$\hat{\tilde{G}}^{-+}(\mathbf{x}_F, \mathbf{x}'_F, t) = \int_{\partial\mathbb{D}_0} \hat{G}^{-}(\mathbf{x}_F, \mathbf{x}_S, t) * \hat{f}^{+}(\mathbf{x}_S, \mathbf{x}'_F, t) d^2\mathbf{x}_S. \tag{2.4.1}$$

$\hat{\tilde{G}}^{-+}(\mathbf{x}_F, \mathbf{x}'_F, t)$ is the redatumed reflection response measured by virtual receivers at $\mathbf{x}_F$ due to downgoing virtual sources at $\mathbf{x}'_F$. The virtual sources have to be located slightly above the virtual receivers for this relation to hold. Note that the redatumed response $\hat{\tilde{G}}^{-+}$ has to be deconvolved of one user-specified wavelet.

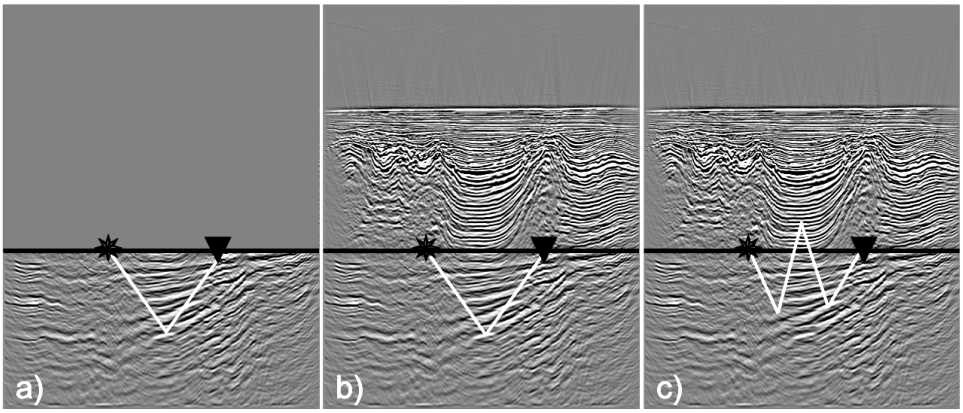

Figure 2.4: *Cartoons illustrating a) the result of source-receiver redatuming in a truncated medium using the conventional Marchenko method (the single-focusing Marchenko method combined with the MDD method), b) the result of source-receiver redatuming in the physical medium using the adaptive double-focusing method, and c) the remaining interactions with the overburden that result from redatuming in the physical medium instead of in the truncated medium. The seismic images in the background are only meant to illustrate an inhomogeneous (truncated) medium.*

The convolution in equation 2.4.1 results in a wavefield that exists in the physical medium as opposed to the truncated medium that is obtained with the MDD method (see figures 2.4a and 2.4b). Therefore, this operation removes internal multiples generated by the overburden, but leaves some later arriving internal multiples behind. Since we created downward radiating sources and upward measuring receivers at the redatuming level, waves that propagate from the virtual source downwards into the reservoir, reflect back up into the overburden, reflect back down into the target, and then reflect up again until sensed by the virtual receiver will remain (figure 2.4c). These remnant multiples can be an issue depending on the geology of the area (for example, the structure of the overburden and the depth and the thickness of the reservoir). Awareness of this potential limitation is important and we advice to test this method on synthetic data that closely resembles the field data if suspecting that this might be a problem. In the Santos Basin, we performed tests on synthetic data and observed that these remaining internal multiples arrive later than the reservoir. Note that source-receiver redatuming in the physical medium also has an advantage: the resulting redatumed reflection response can serve as input for further processing, for example, a target-oriented velocity analysis [*Mildner et al.*, 2017] or to create target-enclosed extended images [*van der Neut et al.*, 2017].

We can now achieve source redatuming without the need for an inversion (and its accompanying stabilization). This should make the double-focusing method less sensitive to imperfections that are typically found in field data. In addition, double-focusing is computationally cheaper, easier to implement and can be parallelized by

pairs of focal points due to the integral over the acquisition surface $\partial\mathbb{D}_0$. This is particularly useful when dealing with large volumes of field data. In contrast, the MDD method requires inverting an integral over the redatuming level $\partial\mathbb{D}_i$, such that it does not allow for this parallelization. Also, the double-focusing method can be implemented adaptively by writing the iterative retrieval of the wavefields $\hat{f}^+$ and $\hat{G}^-$ as a series:

$$\hat{f}^+(\mathbf{x}_S, \mathbf{x}'_F, t) = \sum_{i=0}^{\infty} \hat{f}_i^+(\mathbf{x}_S, \mathbf{x}'_F, t) = \sum_{i=0}^{\infty} \{\Theta\mathcal{R}^\star\Theta\mathcal{R}\}^i \hat{f}_0^+(\mathbf{x}_S, \mathbf{x}'_F t), \tag{2.4.2}$$

and

$$\begin{aligned} \hat{G}^-(\mathbf{x}_F, \mathbf{x}_S, t) &= \sum_{j=0}^{\infty} \hat{G}_j^-(\mathbf{x}_F, \mathbf{x}_S, t) \\ &= \Psi\mathcal{R} \sum_{j=0}^{\infty} \hat{f}_j^+(\mathbf{x}_S, \mathbf{x}_F, t) = \Psi\mathcal{R} \sum_{j=0}^{\infty} \{\Theta\mathcal{R}^\star\Theta\mathcal{R}\}^j \hat{f}_0^+(\mathbf{x}_S, \mathbf{x}_F, t), \end{aligned} \tag{2.4.3}$$

where i and j denote the iteration numbers. When studying the physical interpretation of the individual terms of the wavefields $\hat{G}^-$ and $\hat{f}^+$ that we obtain throughout the iterations, we see why the double-focusing method is suitable for adaptive subtraction. The upgoing Green's function $\hat{G}^-$ consists of an initial wavefield $\hat{G}_0^-$ and updates $\hat{G}_1^-$, $\hat{G}_2^-$, etc. The initial wavefield $\hat{G}_0^-$ is the standard receiver redatumed Green's function that contains all primaries and all orders of internal multiples. The first update $\hat{G}_1^-$ contains a first-order estimate of the receiver-side overburden internal multiples with opposite polarity (so-called counter-events). However, the amplitudes of the counter-events in $\hat{G}_1^-$ are not correct yet. Following iterations will provide higher-order updates to correct the amplitude of these counter-events until they completely match the ampitudes of the original events, ensuring a complete removal of the internal multiples. We observe a similar story for the individual terms of the downgoing focusing function $\hat{f}^+$. The wavefield $\hat{f}_0^+$ that is used to initiate the scheme already contains all physical information. The term $\hat{f}_1^+$ gives the first-order estimate of the coda $\hat{f}_m^+$ that is needed to compensate for the inhomogeneous overburden. Its first estimate $\hat{f}_1^+$ already contains the most important events, but with incorrect amplitude. More updates, as provided by next iterations, modify these amplitudes until they are correct.

When convolving the series in equation 2.4.2 and 2.4.3 according to equation 2.4.1, we can write the double-focusing method as a series:

$$
\begin{aligned}
&\hat{\hat{G}}^{-+}(\mathbf{x}_F, \mathbf{x}'_F, t) = \\
&\sum_{j=0}^{\infty}\sum_{i=0}^{\infty}\int_{\partial\mathbb{D}_0}\hat{G}_j^{-}(\mathbf{x}_F, \mathbf{x}_S, t) * \hat{f}_i^{+}(\mathbf{x}_S, \mathbf{x}'_F, t)d^2\mathbf{x}_S \\
&\approx \int_{\partial\mathbb{D}_0}\hat{G}_0^{-}(\mathbf{x}_F, \mathbf{x}_S, t) * \hat{f}_0^{+}(\mathbf{x}_S, \mathbf{x}'_F, t)d^2\mathbf{x}_S \\
&+ \int_{\partial\mathbb{D}_0}\hat{G}_1^{-}(\mathbf{x}_F, \mathbf{x}_S, t) * \hat{f}_0^{+}(\mathbf{x}_S, \mathbf{x}'_F, t)d^2\mathbf{x}_S \\
&+ \int_{\partial\mathbb{D}_0}\hat{G}_0^{-}(\mathbf{x}_F, \mathbf{x}_S, t) * \hat{f}_1^{+}(\mathbf{x}_S, \mathbf{x}'_F, t)d^2\mathbf{x}_S \\
&+ \int_{\partial\mathbb{D}_0}\hat{G}_1^{-}(\mathbf{x}_F, \mathbf{x}_S, t) * \hat{f}_1^{+}(\mathbf{x}_S, \mathbf{x}'_F, t)d^2\mathbf{x}_S \\
&+ \ldots.
\end{aligned}
\tag{2.4.4}
$$

Here the first term resembles the result of conventional redatuming by using the wavefield $\hat{f}_0^+$ for both receiver and source redatuming. This wavefield contains all primaries and all internal multiples. The second and third term contain first-order estimates of receiver-side and source-side overburden internal multiples. The fourth term contains a first-order estimate of source-and-receiver-side overburden internal multiples, and so forth. Note that the Marchenko method does not require the use of an adaptive filter in theory or on ideal synthetic data. However, the preprocessed field data usually has minor amplitude and phase errors due to imperfect acquisition, attenuation, and/or inaccurate removal of the source signature, such that also the internal multiple predictions are not entirely accurate [*van der Neut and Wapenaar*, 2016]. Therefore, we use an adaptive filter to ensure the correct and complete attenuation of the internal multiples from field data. The adaptive subtraction can be applied in the image domain or in the redatumed data domain, such that the result can be either an image or a redatumed reflection response that can be used as input for further processing. Since we use an adaptive filter, we do not need the amplitude updates that are normally provided by computing many terms of the series in equation 2.4.4, but we only require the terms that contain new events. The number of terms required depends on the geological setting. An estimate of this number can be obtained by testing the method on synthetic data that closely resembles the field data.

We remark that the MDD method can be similarly written as a series to make it suitable for adaptive subtraction [*van der Neut and Wapenaar*, 2016]. However, the computation of this series is still expensive due to the need for a densely sampled array of focal points at the redatuming level $\partial\mathbb{D}_i$, which is often unnecessary for following processing steps (for example migration). In contrast, the double-focusing method requires integration over the acquisition level $\partial\mathbb{D}_0$, which gives us the freedom to select our focal points based on the requirements for further processing and the selection of the area of interest.

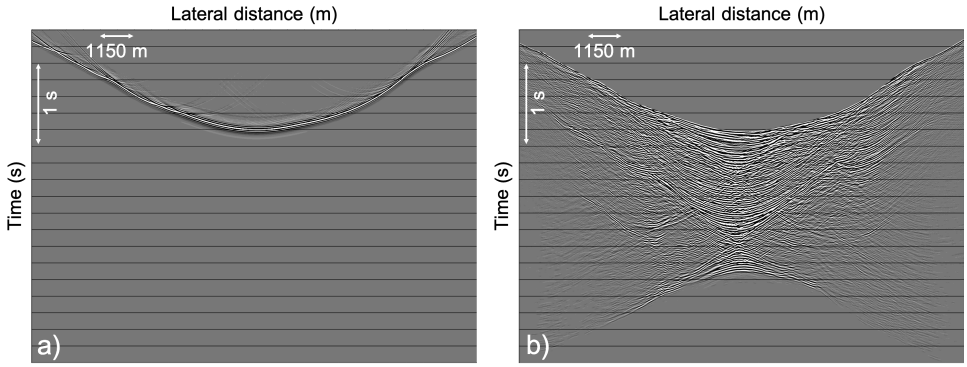

Figure 2.5: *Common source gathers of a) the direct downgoing focusing function $\hat{f}_0^+$ and b) the first-order estimate of its coda $\hat{f}_1^+$.*

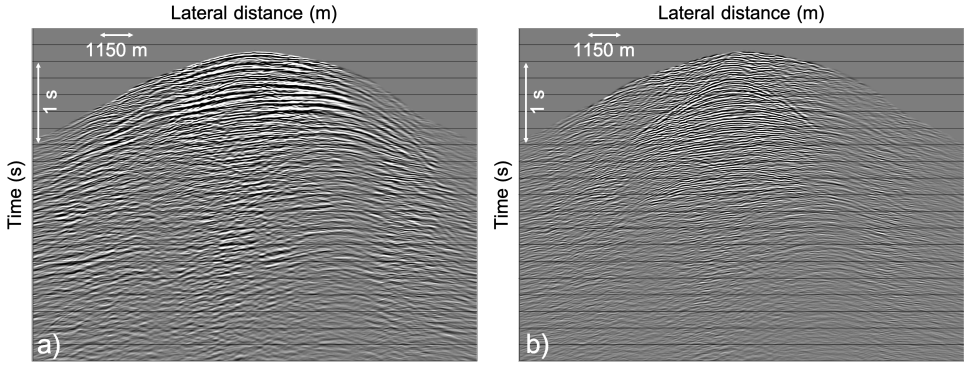

Figure 2.6: *Common source gathers of a) the initial receiver redatumed upgoing Green's function $\hat{G}_0^-$ containing primaries and internal multiples and b) $\hat{G}_1^-$ containing a first-order estimate of receiver-side overburden internal multiples.*

2.5 Application to 2D synthetic data

In order to demonstrate the concept of the adaptive double-focusing method, tests on synthetic data and field data were performed. Both the synthetic data and the field data used in this chapter are from the Santos Basin in Brazil. To make the synthetic tests as realistic as possible, and thus to predict the behaviour of our method on field data as accurately as possible, data were generated in a velocity model and a density model obtained from an acoustic inversion of the field data (see figure 2.1a). The reflection response was modeled using 601 co-located sources and receivers with a spacing of 25 m. Figure 2.1b shows a common source gather of the synthetic dataset and figure 2.2a displays its RTM image.

The first step is modeling the direct downgoing focusing function $\hat{f}_0^+$ from the acquisition surface to our redatuming level just above the base of salt (see lines in figure 2.4) and designing the time window $\Theta(\mathbf{x}_F, \mathbf{x}_S, t)$. We modeled the direct downgoing focusing function $\hat{f}_0^+$ using an Eikonal solver and a smooth velocity model, and convolved it with an Ormsby wavelet with a central frequency of 35 Hz to simulate a band-limitation. The result is visible in figure 2.5a. The design of the time window $\Theta(\mathbf{x}_F, \mathbf{x}_S, t)$ is described in section 2.8. A correctly designed windowing function is crucial for the correct implementation of the adaptive double-focusing method.

After performing multiple iterations of the Marchenko scheme with a correct time window, we obtain the individual terms of $\hat{G}^-$ and $\hat{f}^+$. Figure 2.5 shows common source gathers of $\hat{f}_0^+$ and $\hat{f}_1^+$, while figure 2.6 displays common source gathers of $\hat{G}_0^-$ and $\hat{G}_1^-$. The first update of the downgoing focusing function, $\hat{f}_1^+$, already shows a complex wavefield. The first update of the receiver redatumed upgoing Green's function, $\hat{G}_1^-$, clearly contains counter-events for events in $\hat{G}_0^-$.

Next, we convolve the individual terms of $\hat{G}^-$ and $\hat{f}^+$ with each other according to equation 2.4.4. The first 3 terms of this series ($\hat{G}_0^- * \hat{f}_0^+$, $\hat{G}_1^- * \hat{f}_0^+$ and $\hat{G}_0^- * \hat{f}_1^+$) are displayed in figure 2.7. Remember that the first term contains both primaries and all orders of internal multiples, while the second and third terms contain first-order predictions of receiver-side and source-side internal multiples generated by the overburden.

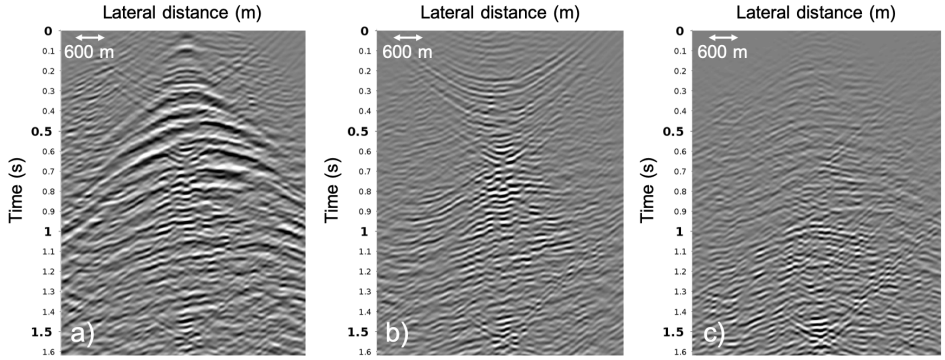

Figure 2.7: *Common source gathers showing a) redatumed reflection response $\hat{G}_0^- * \hat{f}_0^+$ with primaries and internal multiples, b) first-order counter-events for receiver-side internal multiples in $\hat{G}_1^- * \hat{f}_0^+$ and c) first-order counter-events for source-side internal multiples in $\hat{G}_0^- * \hat{f}_1^+$.*

After the retrieval of the individual terms, we add the internal multiple predictions in figures 2.7b and 2.7c to the redatumed response in figure 2.7a, which results

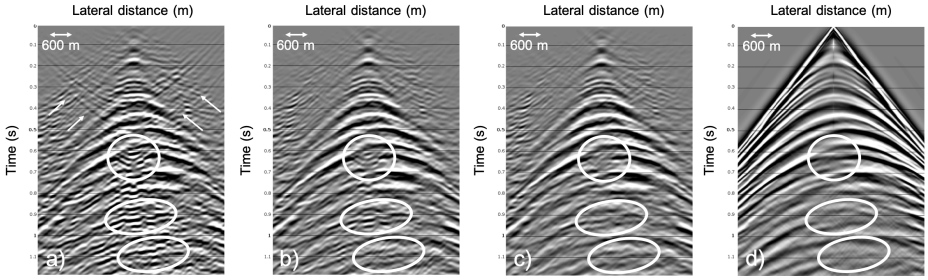

Figure 2.8: *Common source gathers showing the redatumed upgoing Green's function a)* $\hat{G}_0^- * \hat{f}_0^+$ *including both primaries and internal multiples, b) with attenuated internal multiples due to adding internal multiple estimates* $\hat{G}_1^- * \hat{f}_0^+$ *and* $\hat{G}_0^- * \hat{f}_1^+$ *c) with attenuated internal multiples due to adding* $\hat{G}_1^- * \hat{f}_0^+$ *and* $\hat{G}_0^- * \hat{f}_1^+$ *and 6 more terms, d) modeled in a truncated medium. The white ellipses highlight areas in which changes are clearly visible.*

in figure 2.8b. When comparing this result to the modeled response without internal multiples in figure 2.8d, especially in the areas indicated by the white ellipses, it is clear that the 2 terms somewhat attenuated the internal multiples in the redatumed reflection response. However, remnants are visible. Figure 2.8c shows the redatumed response that results when adding 6 more terms of the series in equation 2.4.4 to the redatumed reflection response in figure 2.8. These 6 terms have provided amplitude updates for the internal multiple predictions, thereby attenuating the internal multiples in the reflection response more completely.

We continue by testing the effect of adaptive subtraction on the retrieval of the redatumed wavefield $\hat{\hat{G}}^{-+}(\mathbf{x}_F, \mathbf{x}'_F, t)$. This can be done in multiple domains. Figure 2.9 shows the comparison of subtracting 2 terms of internal multiple predictions using an adaptive filter in time-space (filter length: 3, window size: 300 ms by 30 traces) and an adaptive filter in the curvelet domain (window size: 768 ms by 256 traces) [*Herrmann et al.*, 2008; *Wu and Hung*, 2015]. The result in figure 2.9c after subtracting the internal multiples using a filter in the curvelet domain more closely resembles the modeled response in figure 2.9b compared to the result in figure 2.9a that was obtained using an adapive filter in time-space. The adaptive filter in the curvelet domain provides an extra degree of freedom in terms of dip separation that can make a difference in distinguishing between primaries and internal multiples. The curvelet domain handles both curved and linear events better, particularly when a primary and a multiple overlap in time and space, but not in dip. In addition, the filter in the curvelet domain seems to attenuate noise in addition to the internal multiples. In the following, we will be using an adaptive filter in the curvelet domain. We found that no new events were predicted beyond the third term in equation 2.4.4, so we only use the terms $\hat{G}_1^- * \hat{f}_0^+$ and $\hat{G}_0^- * \hat{f}_1^+$ for the prediction of internal multiples in this particular setting. Naturally, care has to be taken not to damage the primary reflections.

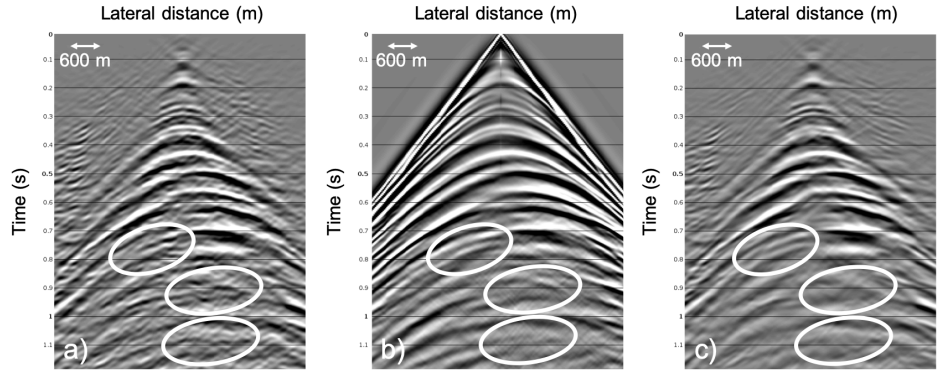

Figure 2.9: *Common source gathers showing the result of adding internal multiple estimates* $\hat{G}_1^- * \hat{f}_0^+$ *and* $\hat{G}_0^- * \hat{f}_1^+$ *to* $\hat{G}_0^- * \hat{f}_0^+$ *using a) an adaptive filter in the time-space domain, b) the modeled upgoing Green's function in a truncated medium for comparison, and c) an adaptive filter in the curvelet domain. The white ellipses highlight areas in which differences are clearly visible.*

Figure 2.10b and 2.10c show the source-receiver redatumed reflection responses that result from applying the conventional Marchenko method and the adaptive double-focusing method to 2D synthetic data of the Santos Basin. Both the conven-

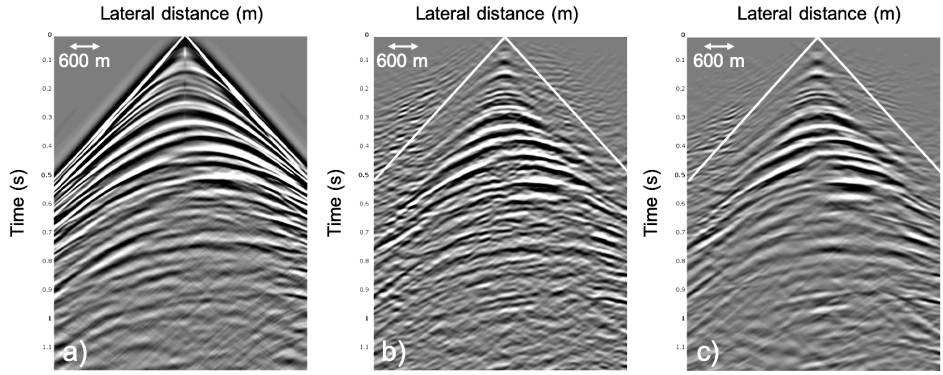

Figure 2.10: *Common source gathers of a) data modeled in a medium that is homogeneous above the redatuming level, b) the result of the conventional Marchenko method, c) the result of the adaptive double-focusing method. Both the conventional Marchenko method and the adaptive double-focusing method use wavefields acquired after two iterations of the single-focusing Marchenko method.*

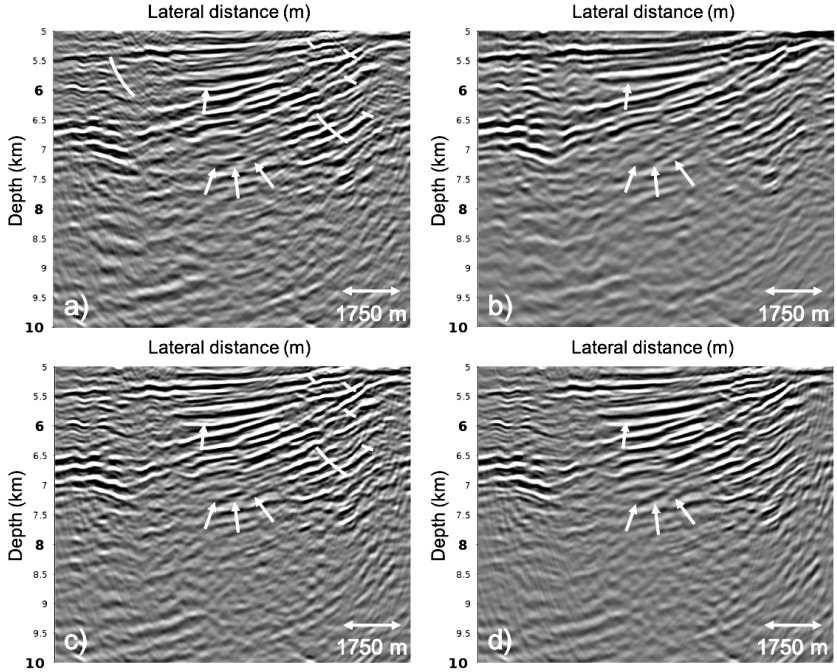

Figure 2.11: *RTM images of a) data at the acquisition surface, zoomed in at the target area, b) the modeled redatumed reflection response, obtained in a medium that is homogeneous above the redatuming level, c) the result of the conventional Marchenko method, d) the result of the adaptive double-focusing method.*

tional Marchenko method and the adaptive double-focusing method use wavefields that result from 2 iterations of the single-focusing Marchenko method. Figure 2.10a shows the modeled redatumed reflection response for comparison. It has been obtained in a medium that is homogeneous above the redatuming level, such that the overburden does not exist. The white lines indicate the mute that is applied to remove the acausal wavefields. When comparing the results of both the conventional Marchenko method and the adaptive double-focusing method to the modeled reflection response, it is clear that the adaptive double-focusing method delivers a reflection response that resembles the modeled response more closely. The conventional Marchenko method seems to suffer from high-frequency remnants of multiples or high frequency noise due to the required inversion. We remark that the result of the conventional Marchenko method can be improved by using more iterations of the single-focusing Marchenko method. However, this comes at a cost. Using the

same amount of iterations, the adaptive double-focusing method provides a cleaner redatumed reflection response. Despite not having achieved a full medium truncation, internal multiples originating from remaining interactions between the target area and the overburden (as depicted in figure 2.4c) are not visible.

Figure 2.11b, 2.11c and 2.11d show the images obtained after applying the RTM method to the redatumed reflection responses in figure 2.10. In addition, figure 2.11a contains an image of directly applying the RTM method to the reflection response at the acquisition surface $\partial\mathbb{D}_0$. The artefacts in the image due to internal multiples can be seen in the shape of half-circles (indicated by white circle segments) as spotted earlier in figure 2.2b. The white arrows point to artefacts that are no longer present in the RTM images after applying the conventional Marchenko method and the adaptive double-focusing method. Both methods remove internal multiples well, but the adaptive double-focusing method produces a slightly cleaner image that resembles the image of the modeled reflection response more closely.

2.5.1 Sensitivity to an unknown scaling factor

Next, we continue by verifying whether the proposed method is less sensitive to imperfections in the (preprocessed) data than the conventional Marchenko method. A typical shortcoming of field data is an unknown scaling of the source strength [*Ravasi et al.*, 2016]. So far, we have assumed that $R(\mathbf{x}_R, \mathbf{x}_S, t)$ is the real reflection response of the subsurface, but this is not the case in reality. We only have access to a reflection response that is scaled by an unknown factor that depends on the acquisition and the preprcocessing (for example, the deconvolution of the (unknown) source signature). We compare the performance of the conventional Marchenko method and the adaptive double-focusing method for the most simple error in scaling: a reflection response multiplied by a single scalar. We test values of 0.5 and 2.0. The resulting redatumed responses can be found in figure 2.12.

When scaling the reflection response by a factor 0.5, the conventional Marchenko method has problems to remove internal multiples (figure 2.12b). In contrast, the adaptive filter used in the double-focusing method corrects for this error in scaling (figure 2.12e). When multiplying the amplitudes of the reflection response by a factor 2.0, the conventional Marchenko method starts adding multiples instead of removing them (figure 2.12c). Again, the adaptive filter corrects for the erroneous scaling factor (figure 2.12f). This shows that the adaptive double-focusing method is more robust and less sensitive to imperfections in the preprocessed data. In theory, the result of the conventional Marchenko method can be improved by using other methods that estimate the unknown scaling factor [*Brackenhoff*, 2016]. However, these methods do not always result in the correct answer and only provide an estimate at additional computational cost. In contrast, the adaptive double-focusing method implicitly takes care of issues related to an unknown scaling factor.

2.5.2 Sensitivity to a less dense source and receiver spacing

In reality, a perfect acquisition geometry does not exist. Therefore, it is important that the adaptive double-focusing method is capable of obtaining an acceptable

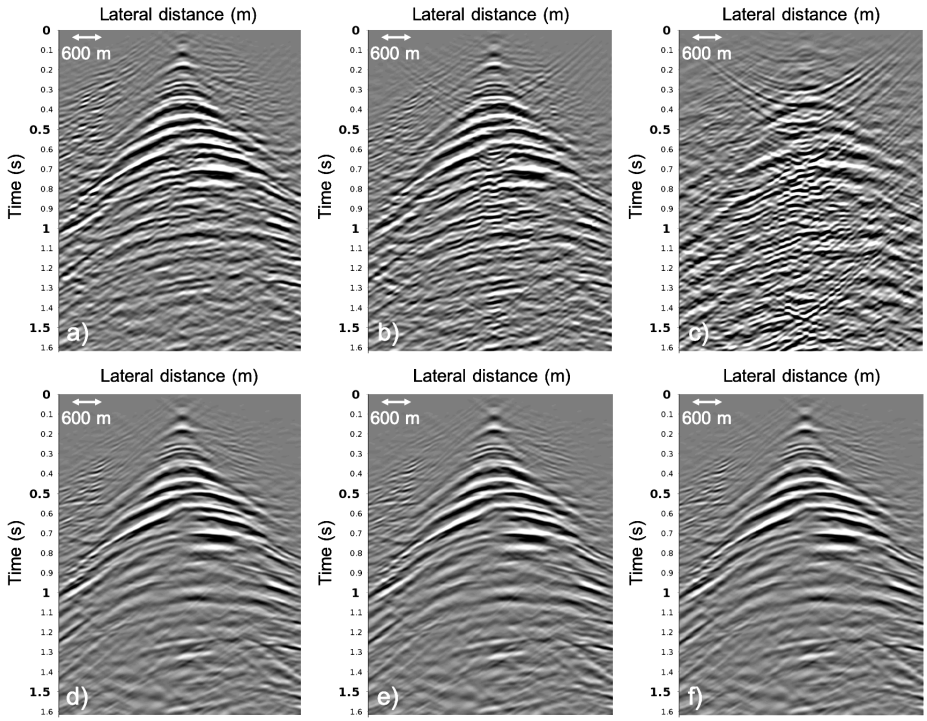

Figure 2.12: *Comparison of the conventional Marchenko method (top row) and the adaptive double-focusing method (bottom row) for an unknown scaling of source strength. Redatumed reflection response resulting from the conventional Marchenko method using a) the correct scaling factor, b) the correct scaling factor multiplied by 0.5, c) the correct scaling factor multiplied by 2.0. Redatumed reflection response resulting from the adaptive double-focusing method using d) the correct scaling factor, e) the correct scaling factor multiplied by 0.5, f) the correct scaling factor multiplied by 2.0.*

result when the source and receiver spacing is coarser than the 25 m used to generate the synthetic data. Figure 2.13 shows the redatumed reflection responses obtained by applying both the conventional Marchenko method and the adaptive double-focusing method to reflection responses modeled with spacings of 25 m, 50 m and 100 m. The conventional Marchenko method greatly suffers and has problems to recover primary signal with a coarser acquisition geometry. The adaptive double-focusing method also suffers, but still manages to obtain a reasonable amount of primary energy.

Figure 2.14 shows a comparison of the RTM images of the conventional Marchenko method and the adaptive double-focusing method with a source and receiver spacing of 50 m. The adaptive double-focusing method has removed significantly more artefacts due to internal multiples than the conventional Marchenko method. By

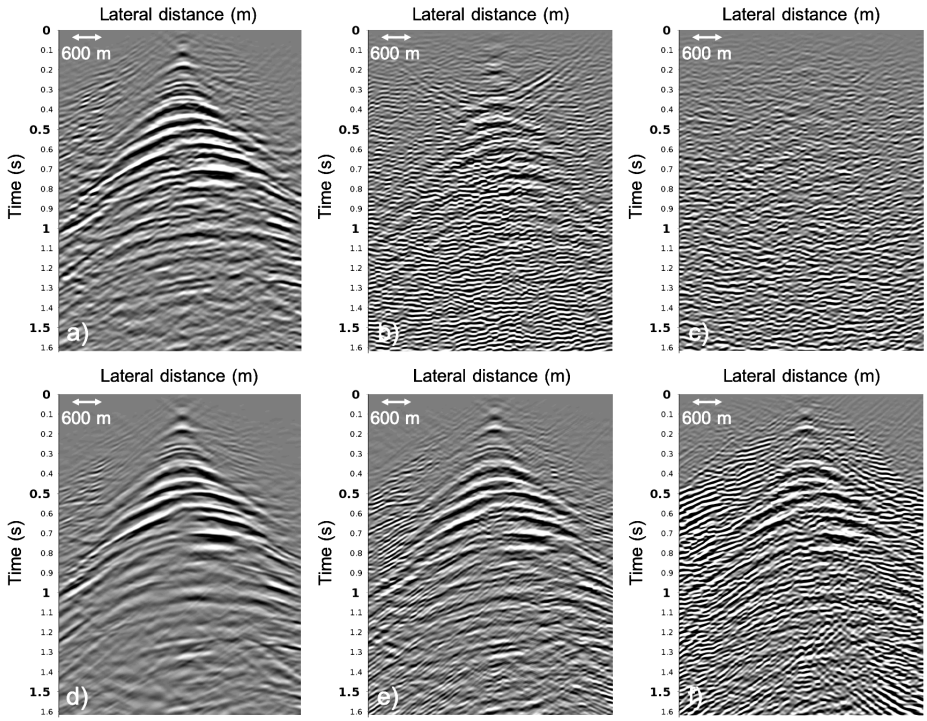

Figure 2.13: *Comparison of the conventional Marchenko method (top row) and the adaptive double-focusing method (bottom row) applied to data modeled with different source and receiver spacings. Redatumed reflection response resulting from the conventional Marchenko method using a) a spacing of 25 m, b) a spacing of 50 m, c) a spacing of 100 m. Redatumed reflection response resulting from the adaptive double-focusing method using d) a spacing of 25 m, e) a spacing of 50 m, f) a spacing of 100 m. Both methods suffer, but adaptive double-focusing is less sensitive.*

replacing the MDD method by a second focusing step, we have created a redatuming method that is more capable of handling a sparse acquisition geometry.

2.6 Application to 2D field data

We continue by applying the adaptive double-focusing method to 2D field data. The data were acquired in the same region as covered by the synthetic data. Acquisition was performed with 6 streamers, having a cable spacing of 150 m and a cable length of 6000 m (covering offsets from 250 m to 6250 m). To satisfy the assumptions underlying the Marchenko scheme, the data were preprocessed using denoise, designature, deghosting and surface-related multiple attenuation. We performed deghosting in the f-p domain [*Wang et al.*, 2013] and used a designature filter retrieved from the

water bottom reflection. A partial normal moveout (NMO) correction of traces per common depth point (CDP) [e.g. *Dragoset et al.*, 2010] was used to reconstruct shots and near offsets. Next, we selected a single inline and interpolated shot and receiver positions to obtain a line with a source and receiver spacing of 25 m. The RTM image in figure 2.15a was created using the reflection response acquired at the acquisition surface $\partial\mathbb{D}_0$, zoomed in at the target area. We call this the result of conventional imaging. Internal multiples from the overburden create artefacts in the target zone, as indicated by the ellipse and the stripes. Figure 2.15b shows the RTM image of the first term of the adaptive double-focusing method: the redatumed reflection response. This term includes both primaries and artefacts due to internal multiples from the overburden and is similar to the RTM image from the reflection response at the acquisition surface. Figure 2.15c shows the result of applying the conventional Marchenko method. It did not succeed in removing the internal multiples, but seems to have boosted their amplitudes instead. This is comparable to what we observed in figure 2.12 and 2.13. Figure 2.15d shows the result of applying the adaptive double-focusing method to this dataset. The ellipse highlights the most significant improvement in the image: the application of our method has improved the geological interpretability in the area. The half-circles due to multiples that we first encountered in the synthetic data (figure 2.2b) have given the elliptical section in the other images of figure 2.15 a different appearance, thereby masking the real structure below. This masked structure, visible in the velocity model in figure 2.1a, becomes visible after application of the adaptive double-focusing method.

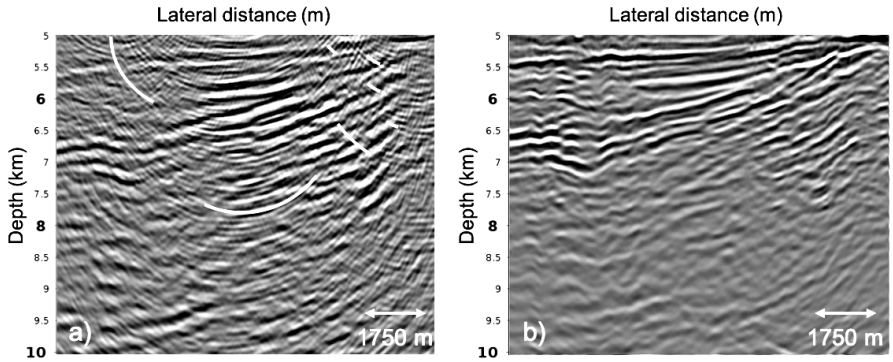

Figure 2.14: *RTM images of the conventional Marchenko method and the adaptive double-focusing method for a source and receiver spacing of 50 m. The image of the result of the conventional Marchenko method shows many artefacts, while the adaptive double-focusing method has still managed to remove a significant amount of these artefacts despite the coarse acquisition geometry.*

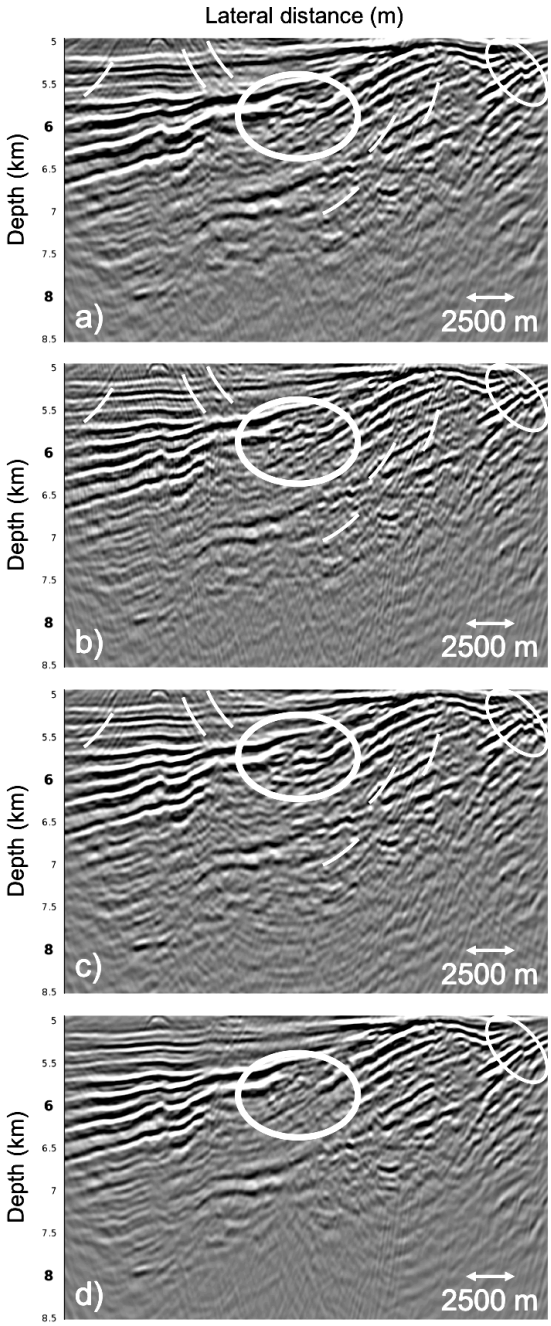

Figure 2.15: *RTM images resulting from a) data at the acquisition surface, zoomed in at the target, b) the first term of the adaptive double-focusing method, c) the result of the conventional Marchenko method, d) the result of the adaptive double-focusing method.*

2.7 Conclusion

We presented the adaptive double-focusing method as an alternative for conventional Marchenko redatuming that is more suitable for applying source-receiver redatuming to field data. Instead of using a multidimensional deconvolution as a second focusing step, the double-focusing method uses a simple and straightforward convolution that naturally complements the first focusing step of the single-focusing Marchenko method, at the cost of leaving some later arriving internal multiples behind. Not only is this method less sensitive to imperfections in the data and the acquisition geometry than the conventional Marchenko method, it is also computationally much cheaper and allows for parallelization over pairs of focal points, thereby making it suitable for the application to large data volumes. Furthermore, it produces improved results when using wavefields resulting from the same amount of single-focusing Marchenko iterations. This was clearly visible when applying our method to field data of the Santos Basin, where the adaptive double-focusing method managed to predict and subtract internal multiples originating from the overburden, thereby improving the geologic interpretability in the target area despite using field data. Based on the synthetic and field data evaluations in this chapter, we conclude that the adaptive double-focusing method is an effective tool for applying source-receiver Marchenko redatuming to field data.

2.8 Appendix: Design of the time window Θ for the adaptive double-focusing method

The first step of the adaptive double-focusing method, single-focusing by iteratively solving the coupled Marchenko equations, requires designing a time window $\Theta(\mathbf{x}_F, \mathbf{x}_S, t)$ to correctly retrieve the wavefields needed for source redatuming. This window is designed by choosing parameters t_d and t_ϵ (see equation 2.2.5). The choice of t_d is based on the smooth velocity model, but the choice of t_ϵ is not that straightforward. We will explain how the choice of t_ϵ affects the adaptive double-focusing method and how we can make a correct choice.

A rule of thumb is to set t_ϵ equal to half the duration of the wavelet convolved with the direct wave $\hat{f}_0^+$. This holds for synthetic data in 1D, but it does not always hold for 2D and 3D data with a finite aperture. If using the rule of thumb, we estimate a t_ϵ of 14.3 ms for the 2D synthetic data of the Santos Basin. When taking a t_ϵ that is smaller than this estimation, we retrieve the wavefields in figure 2.16. Note that the first term should contain primaries and all orders of internal multiples, while the second and third terms should only contain counter-events for the most dominant internal multiples generated in the overburden. However, when looking closely at the events in all three terms, the second and third terms have events that appear to be the result of 'primary leakage'. They seem to contain a copy of the correct events in the first term that should remain intact. If we use these incorrectly retrieved wavefields for adaptive subtraction, the damage of the primary will be severe: the second and third terms will remove the primaries together with the multiples.

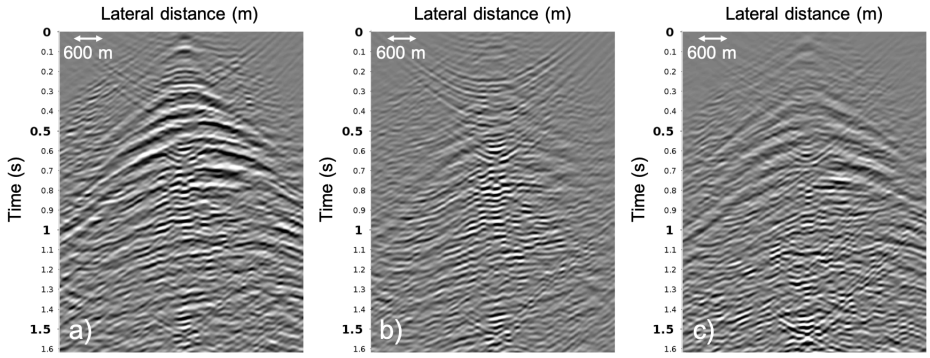

Figure 2.16: *Common source gathers of the individual terms in equation 2.4.4 retrieved using an erroneously small t_ϵ: a) redatumed reflection response $\hat{G}_0^- * \hat{f}_0^+$ with primaries and internal multiples, b) counter-events for receiver-side internal multiples in $\hat{G}_1^- * \hat{f}_0^+$ and c) counter-events for source-side internal multiples in $\hat{G}_0^- * \hat{f}_1^+$.*

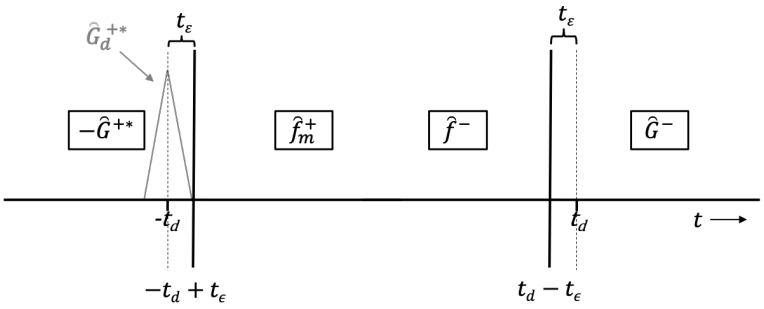

Figure 2.17: *Illustration of the truncations imposed by the filter Θ in the Marchenko method for a focusing depth that is sufficiently far away from a reflector.*

We will now show that the apparent 'primary leakage' is actually the result of an incorrect choice of t_ϵ, and can thus be avoided. Figure 2.17 shows the truncations in the time-domain during the two steps that comprise a single iteration of the Marchenko scheme (equations 2.2.3 and 2.2.4). When looking at the wavefields that result from evaluating equation 2.2.3, the upgoing focusing function $\hat{f}^-$ can be found before t_d (the traveltime of the direct wavefield from the focal point to the acquisition surface) and the upgoing Green's function $\hat{G}^-$ can be found after t_d. The actual truncation applied by time window $\Theta(\mathbf{x}_F, \mathbf{x}_S, t)$ in equation 2.2.6 is made at $t_d - t_\epsilon$, so slightly before t_d.

The evaluation of equation 2.2.4 results in the coda of the polarity- and time-reversed downgoing Green's function $\hat{G}_m^+$ before $-t_d$ and the coda of the downgoing

focusing function $\hat{f}_m^+$ after $-t_d$. However, the updates of the direct wave of the downgoing Green's function $\hat{G}_d^+(-t)$ arrive exactly at $-t_d$ (see the gray-coloured arrival in figure 2.17). In this situation, the time window $\Theta(\mathbf{x}_F, \mathbf{x}_S, t)$ in equation 2.2.7 is applied slightly after $-t_d$, at $-t_d + t_\epsilon$.

When now studying the retrieval of the individual terms $\hat{G}_0^-$, $\hat{G}_1^-$ and $\hat{f}_1^+$ from equation 2.4.4 in detail, while keeping figure 2.17 in mind, the issue becomes clear. Note that $\hat{f}_0^+$ is a known that is unaffected by the truncations. The wavefield $\hat{G}_0^-$ is retrieved during the first iteration by computing $\hat{G}_0^- = \Psi\mathcal{R}\hat{f}_0^+$. No matter how small t_ϵ is chosen, the truncation will never be placed later than t_d, and will thus never incorrectly place parts of the upgoing focusing function $\hat{f}^-$ into this Green's function. Therefore, our first term, containing both $\hat{G}_0^-$ and $\hat{f}_0^+$, should not suffer from a t_ϵ that was chosen too small.

The story is different for the second and third terms in equation 2.4.4. The third term contains the wavefield $\hat{f}_1^+$ that is retrieved by evaluating $\hat{f}_1^+ = \Theta\mathcal{R}^\star\hat{f}_0^-$. Now the truncation does matter, since a t_ϵ that is chosen too small will result in an $\hat{f}_1^+$ that also contains part of the update of the direct downgoing Green's function $\hat{G}_d^+(-t)$ (see figure 2.17). This update arrives at the exact same time as wavefield $\hat{f}_0^+$ and will therefore act as a scaled version of this wavefield. As a result, we do not retrieve $\hat{f}_1^+$, but we obtain $\hat{f}_1^+ + \alpha\hat{f}_0^+$ for a t_ϵ that is too small. When then performing the convolution of $\hat{G}_0^-$ and $\hat{f}_1^+$ to compute the third term, we obtain $\hat{G}_0^- * (\hat{f}_1^+ + \alpha\hat{f}_0^+)$ instead, which is equal to adding a scaled version of the first term to the third term. As a result, we see the same primaries as found in the first term also in the third term for an erroneously small t_ϵ.

When now continuing with our incorrectly retrieved $\hat{f}_1^+$, such that it is actually $\hat{f}_1^+ + \alpha\hat{f}_0^+$, the next step is the retrieval of the wavefield $\hat{G}_1^-$. This is the first update of the wavefield $\hat{G}_0^-$, which can be written as $\hat{G}_1^- = \Psi\mathcal{R}\hat{f}_1^+$ (see equation 2.2.8). Using our incorrect $\hat{f}_1^+ = \hat{f}_1^+ + \alpha\hat{f}_0^+$, we now obtain $\hat{G}_1^- = \Psi R * (\hat{f}_1^+ + \alpha\hat{f}_0^+) = \hat{G}_1^- + \alpha\hat{G}_0^-$. Therefore, the retrieved $\hat{G}_1^-$ has an imprint of $\hat{G}_0^-$, which explains the 'primary leakage' that is also observed in the second term.

Thus, finding a correct t_ϵ is essential for the successful application of adaptive subtraction in the double-focusing method. It would seem straightforward to just choose a very large value for t_ϵ, but this can unfortunately result in an incomplete solution. The choice of t_ϵ defines the smallest period of internal multiple that can be resolved. The shorter the period of the internal multiples, the closer the coda $\hat{f}_m^+$ will follow the direct wave $\hat{f}_0$. Thus, the larger the choice of t_ϵ, the higher the risk of incorrectly muting part of the focusing functions. When incorrectly muted, not all internal multiples will be constructed, and they cannot be subtracted. This is something that should not be taken lightly, since this is the purpose of applying source-receiver redatuming to the reflection response.

Instead of using trial and error to find a suitable value for t_ϵ, the auto-correlation of the reflection response R can serve as an indication. Figure 2.18 shows the auto-correlation of the synthetic reflection response. The auto-correlation of the individual events can be found on the zero-lag. Correlations of different events with each other can be found elsewhere in time. The correlation of a short period

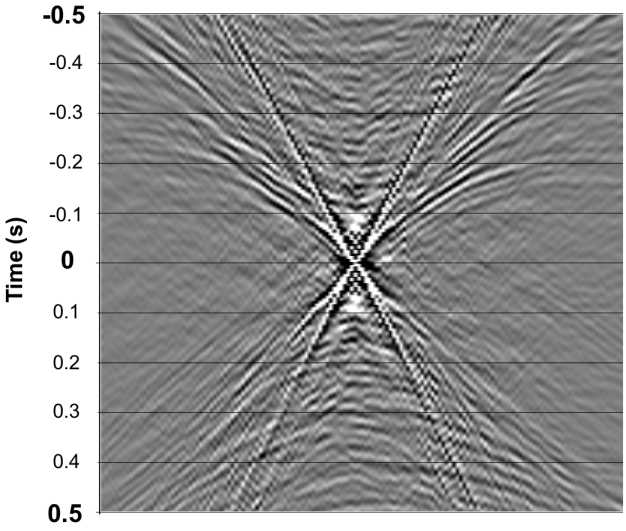

Figure 2.18: *Auto-correlation of the synthetic reflection response of the Santos basin.*

internal multiple with a primary generated by the same reflector will appear close to the zero-lag, since there is only a small difference in travel time. Therefore, the time in-between the arrival at the zero-lag and the next arrival is an indication of the shortest period internal multiples that are present in the data. This can be used as a guide to define an upper bound for t_ϵ, while visual inspection for 'primary leakage' can be used to set a lower bound. When the upper bound is below the lower bound, short-period internal multiples may have to be sacrificed in order to ensure a correct adaptive subtraction. Note that the auto-correlation of the reflection response R should only have a single source signature, otherwise this method is not reliable. We also remark that this explanation holds for the first-order internal multiples as observed in the data of the Santos Basin, where we have strong reflectors from the salt with weaker reflectors below. The explanation might not hold when more (strong) reflectors are involved.

3

3D Marchenko internal multiple attenuation on narrow azimuth streamer data of the Santos Basin

Abstract

Based on the results of the previous chapter, we leave conventional Marchenko redatuming behind and continue the analysis of the adaptive double-focusing method in 3D. First, we perform a series of synthetic tests to identify the key acquisition parameters that affect the result of 3D Marchenko internal multiple prediction and subtraction using an adaptive double-focusing method. Starting from a wide azimuth dense grid of sources and receivers, a series of decimation tests is performed until a narrow azimuth streamer geometry remains. We evaluate the effect of the removal of sail lines, near offsets, far offsets and outer cables on the result of the adaptive double-focusing method. Based on these tests, we define an interpolation strategy and use it for the field data application. Finally, we apply our method to the narrow azimuth streamer field data from the Santos Basin, Brazil. Internal multiples are predicted and adaptively subtracted, thereby improving the geological interpretation of the target area. These results imply that our adaptive double-focusing method is sufficiently robust for the application to 3D field data, although the key acquisition parameters and limitations will naturally differ in other geological settings and for other types of acquisition.

Published as: Staring, M. and K. Wapenaar, 3D Marchenko internal multiple attenuation on narrow azimuth streamer data of the Santos Basin, Brazil.
Note that minor changes have been introduced to make the text consistent with the other chapters.

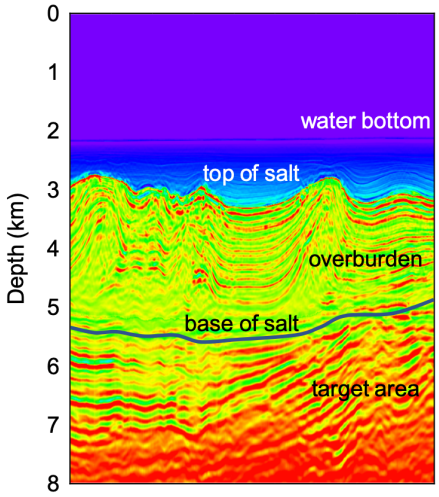

Figure 3.1: *A 2D slice of the velocity model of the Santos Basin, Brazil.*

3.1 Introduction

The Santos Basin in Brazil is known for its oil-bearing carbonate reservoirs below a highly reflective stratified salt layer (see figure 3.1). The salt layer generates strong internal multiples that pose a problem for seismic imaging [*Cypriano et al.*, 2015]. Most imaging methods assume that the recorded wavefield was only reflected once and thus incorrectly interpret internal multiples as primaries from deeper reflectors. As a result, these methods create ghost reflectors that do not exist in reality. These ghost reflectors can interfere with the real reflectors in the target area and thereby corrupt the image. Therefore, we wish to attenuate internal multiples in order to obtain a reliable image of the target area.

The attenuation of internal multiples is a challenge. Various methods have been proposed, ranging from filtering methods [e.g. *Hampson*, 1986; *Foster and Mosher*, 1992; *Zhou and Greenhalgh*, 1994] that transform the reflection response to an alternative domain in which the primaries and the internal multiples separate, to wave-equation-based methods that aim to predict the internal multiples by convolving and correlating the reflection response with itself [e.g. *Jakubowicz*, 1998; *Weglein et al.*, 1997]. The application of filtering methods is often challenging in settings with a complex overburden, since there is usually no distinct difference in properties between the primary reflections from the target area and the (strong) internal multiples generated by the overburden. Also, the application of wave-equation-based methods is not undisputed. Some wave-equation-based methods require the manual identification of internal multiple generators, thereby introducing bias and the risk of not correctly capturing all internal multiple generators into the process. In addition, some wave-equation-based methods predict internal multiples with incor-

rect amplitudes or use a layer stripping approach that results in error accumulation from shallow to deep reflectors. In order to attenuate internal multiples in a complex setting such as the Santos Basin, an alternative method is needed.

Marchenko methods [*Ware and Aki*, 1969; *Broggini et al.*, 2012; *Wapenaar et al.*, 2014a] are data-driven and wave-equation-based methods that do not have these drawbacks. They have the ability to consider the entire overburden as a whole, instead of having to identify all individual internal multiple generators separately. In addition, Marchenko methods allow us to retrieve Green's functions including primaries as well as all orders of internal multiples at any desired depth level without having to resolve overlying layers first. When writing the retrieval of Green's functions using the coupled Marchenko equations as a Neumann series, Marchenko methods can be used for the prediction of internal multiples [*van der Neut et al.*, 2015b]. These predictions in principle have the correct amplitude and phase. However, minor amplitude and phase differences are usually present when applying the method to field data due to imperfect acquisition or preprocessing. A mild adaptive filter can be used to correct for these minor differences. We previously reported on the successful application of an adaptive Marchenko method (the adaptive double-focusing method) to 2D synthetic data and a 2D line of streamer data of the Santos Basin in Brazil [*Staring et al.*, 2018a]. Internal multiples were predicted and adaptively subtracted from the target area, which improved the geological interpretation. In addition, we found that the adaptive double-focusing method was relatively robust for a sparse acquisition geometry in 2D and suitable for the application to large data volumes. In the hope that these properties also hold in 3D, we use this adaptive Marchenko method for the prediction and adaptive subtraction of internal multiples from 3D narrow azimuth streamer data acquired in the Santos Basin.

The extension from 2D to 3D Marchenko methods may seem trivial in theory, but it is not the case in practice. Some aspects are similar, such as the data preparation requirements that include noise suppression, signature deconvolution, deghosting and the removal of surface-related multiples. However, aspects related to the sampling of the acquired data are different. In addition to the inline direction in 2D, there is in 3D also a crossline direction that typically has a limited aperture and less densely spaced sources and receivers. Also, streamers usually do not record responses at negative offsets, near offsets and far offsets in the inline direction. A thorough understanding of the effect of these acquisition limitations on the result of Marchenko internal multiple attenuation would allow us to estimate whether the application to any particular dataset is feasible. In addition, it would aid us in defining an interpolation strategy. Even though some researchers already applied a Marchenko method to 3D field data [*Staring et al.*, 2018b; *Pereira et al.*, 2018], they did not address the acquisition requirements and limitations of 3D Marchenko methods in detail. The objective of this chapter is to gain a better understanding of the key acquisition parameters and limitations that affect the application of the adaptive double-focusing method to 3D data.

In this chapter, we first revise the theory of the adaptive Marchenko double-focusing method. Second, we perform a series of 3D synthetic tests to study the effect of the acquisition parameters on the result of internal multiple prediction and

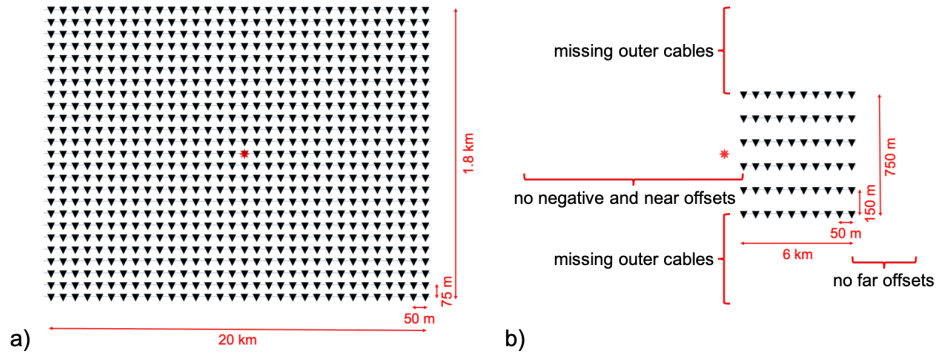

Figure 3.2: *Cartoons showing a) the starting acquisition geometry and b) the final acquisition geometry for the synthetic decimation tests in this chapter. The final acquisition geometry is based on our narrow azimuth streamer data. The stars represent sources and the triangles represent receivers.*

adaptive subtraction using this method. Starting from a grid spacing of 50 m (inline direction) by 75 m (crossline direction) co-located sources and receivers with positive and negative offsets, near offsets, far offsets and a crossline aperture of 1.8 km (figure 3.2a), we step-by-step decimate the acquisition down to a narrow azimuth streamer geometry on which our 3D field data were acquired (figure 3.2b). Based on these tests, we identify the key limiting acquisition parameters and use these to design an interpolation strategy for the field data application. Next, we test the proposed interpolation strategy on 3D synthetic data. Finally, we apply the adaptive double-focusing method to 3D narrow azimuth streamer data. In the following discussion and conclusion section, we evaluate the performance of the adaptive double-focusing method.

3.2 Marchenko internal multiple attenuation by adaptive double-focusing

The adaptive Marchenko double-focusing method requires a preprocessed reflection response $R(\mathbf{x}_R, \mathbf{x}_S, t)$ acquired on a sufficiently dense grid of sources $\mathbf{x}_S$ and receivers $\mathbf{x}_R$ at the acquisition surface $\partial\mathbb{D}_0$. A smooth velocity model of the subsurface is needed to obtain the direct wave of the downgoing focusing function $\hat{f}_0^+$. The direct wave is obtained by modeling and time-reversing the response from sources at the redatuming level $\partial\mathbb{D}_i$ to receivers at the acquisition surface $\partial\mathbb{D}_0$ using finite-difference modeling or an Eikonal solver (see figure 3.3). The $\hat{\cdot}$ symbol indicates an user-specified wavelet that is convolved with the modeled wavefield. The direct downgoing focusing function $\hat{f}_0^+$ initiates the iterative scheme that solves the coupled Marchenko equations. If the overburden were homogeneous, this initial wavefield would be sufficient to create a focus at the desired focal point at $\partial\mathbb{D}_i$. Otherwise,

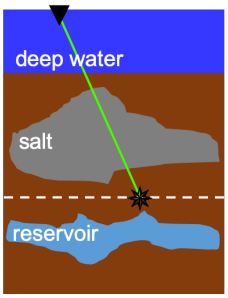

Figure 3.3: *Cartoon illustrating the direct wave $\hat{f}_0^+$, which we obtain using a smooth velocity model and an Eikonal solver.*

a coda for the downgoing focusing function has to be retrieved using the following series [*van der Neut et al.*, 2015a]:

$$\hat{f}^+(\mathbf{x}_S,\mathbf{x}'_F,t)=\sum_{i=0}^{\infty}\hat{f}_i^+(\mathbf{x}_S,\mathbf{x}'_F,t)=\sum_{i=0}^{\infty}\{\Theta\mathcal{R}^\star\Theta\mathcal{R}\}^i\hat{f}_0^+(\mathbf{x}_S,\mathbf{x}'_F,t), \tag{3.2.1}$$

where i is the iteration number. Symbol $\mathbf{x}'_F$ denotes focal points at the redatuming level $\partial\mathbb{D}_i$ that become virtual sources. Operators $\mathcal{R}$ and $\mathcal{R}^\star$ perform a multidimensional convolution or correlation of the reflection response R with the wavefield that it acts upon. Window functions Θ are tapered Heaviside step functions that separate the causal and the acausal wavefields (i.e. Green's functions and focusing functions) in time. See section 2.8 for details on the design of window function Θ. The first update of the coda of the downgoing focusing function $\hat{f}_1^+$ already contains many of the correct events to compensate for the inhomogeneous overburden, but with incorrect amplitudes. Higher-order estimates ($i=2,3,4,etc.$) are needed to obtain the correct amplitudes.

Using the downgoing focusing function $\hat{f}^+$, we can also retrieve the receiver redatumed upgoing Green's function:

$$\begin{aligned}\hat{G}^-(\mathbf{x}_F,\mathbf{x}_S,t)&=\sum_{j=0}^{\infty}\hat{G}_j^-(\mathbf{x}_F,\mathbf{x}_S,t)\\&=\Psi\mathcal{R}\hat{f}^+(\mathbf{x}_S,\mathbf{x}_F,t)=\Psi\mathcal{R}\sum_{j=0}^{\infty}\{\Theta\mathcal{R}^\star\Theta\mathcal{R}\}^j\hat{f}_0^+(\mathbf{x}_S,\mathbf{x}_F,t),\end{aligned} \tag{3.2.2}$$

where mute $\Psi=I-\Theta$ now selects the causal wavefield and symbol $\mathbf{x}_F$ represents focal points at the redatuming level $\partial\mathbb{D}_i$ that become virtual receivers. The iteration number is given by j. Initial estimate $\hat{G}_0^-$ is the standard receiver-redatumed upgoing Green's function at $\mathbf{x}_F$. The first update $\hat{G}_1^-$ contains a first-order estimate

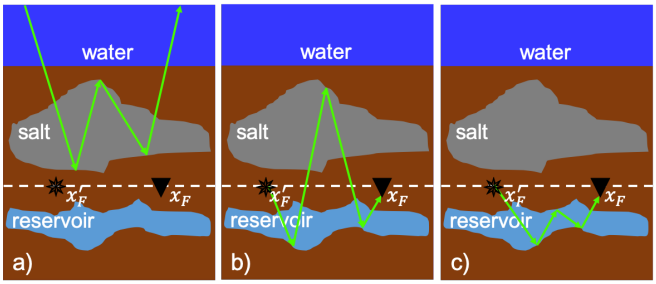

Figure 3.4: *Cartoons illustrating the redatumed sources at $\boldsymbol{x}'_F$ and the redatumed receivers at $\boldsymbol{x}_F$ resulting from the adaptive double-focusing method. Internal multiples a) generated by the overburden have been removed by double-focusing, while b) later arriving internal multiples generated by interactions between the target area and the overburden and c) later arriving internal multiples generated by the target area remain.*

of the receiver-side internal multiples generated in the overburden with incorrect amplitude. Next updates ($\hat{G}_2^-$, $\hat{G}_3^-$, etc.) contain higher-order estimates that are necessary to obtain the correct amplitudes. An additional step is needed to also remove source-side and source-and-receiver-side internal multiples generated by the overburden.

The retrieval of the upgoing Green's function $\hat{G}^-$ with a grid of sources at the acquisition surface $\partial\mathbb{D}_0$ and a grid of virtual receivers at the redatuming level $\partial\mathbb{D}_i$ is a single-focusing step. By creating double-focusing we also remove other internal multiples generated by the overburden. To this end, we convolve the upgoing Green's function $\hat{G}^-$ at virtual receivers with the downgoing focusing function $\hat{f}^+$ at virtual sources [*Wapenaar et al.*, 2016a; *van der Neut et al.*, 2018; *Staring et al.*, 2018a]:

$$\hat{\hat{G}}^{-+}(\mathbf{x}_F, \mathbf{x}'_F, t) = \int_{\partial\mathbb{D}_0} \hat{G}^-(\mathbf{x}_F, \mathbf{x}_S, t) * \hat{f}^+(\mathbf{x}_S, \mathbf{x}'_F, t) d^2\mathbf{x}_S. \tag{3.2.3}$$

By applying this for many positions $\mathbf{x}_F$ and $\mathbf{x}'_F$ at redatuming level $\partial\mathbb{D}_i$, a grid of downward radiating virtual sources and virtual receivers that measure the upgoing wavefield is created. The result is a redatumed Green's function $\hat{\hat{G}}^{-+}$ in the physical medium. Internal multiples generated by the overburden (figure 3.4a) have been removed, but later arriving internal multiples generated by interactions between the target area and the overburden (figure 3.4b) and internal multiples generated by the target area (figure 3.4c) remain. According to *Cypriano et al.* [2015], the main internal multiples that contaminate the image of the target area in the Santos Basin are generated between the water bottom and the top of salt (see figure 3.1). By using double-focusing, we remove these internal multiples, while leaving some internal multiples below the target area behind. Note that one user-specified wavelet $\hat{\cdot}$ has to be deconvolved from the redatumed Green's function $\hat{\hat{G}}^{-+}$. Also note that the integral over the acquisition surface $\partial\mathbb{D}_0$ allows us to parallelize the implementation

of the double-focusing method per pair of focal points, which makes this method particularly suitable for the application to large 3D data volumes.

Using equations 3.2.1 and 3.2.2, we can write equation 3.2.3 as a series:

$$
\begin{aligned}
&\hat{\hat{G}}^{-+}(\mathbf{x}_F, \mathbf{x}'_F, t) = \\
&\sum_{j=0}^{\infty}\sum_{i=0}^{\infty}\int_{\partial\mathbb{D}_0} \hat{G}_j^-(\mathbf{x}_F, \mathbf{x}_S, t) * \hat{f}_i^+(\mathbf{x}_S, \mathbf{x}'_F, t) d^2\mathbf{x}_S \\
&\approx \int_{\partial\mathbb{D}_0} \hat{G}_0^-(\mathbf{x}_F, \mathbf{x}_S, t) * \hat{f}_0^+(\mathbf{x}_S, \mathbf{x}'_F, t) d^2\mathbf{x}_S \\
&- \int_{\partial\mathbb{D}_0} -\hat{G}_1^-(\mathbf{x}_F, \mathbf{x}_S, t) * \hat{f}_0^+(\mathbf{x}_S, \mathbf{x}'_F, t) d^2\mathbf{x}_S \\
&- \int_{\partial\mathbb{D}_0} -\hat{G}_0^-(\mathbf{x}_F, \mathbf{x}_S, t) * \hat{f}_1^+(\mathbf{x}_S, \mathbf{x}'_F, t) d^2\mathbf{x}_S \\
&- \int_{\partial\mathbb{D}_0} -\hat{G}_1^-(\mathbf{x}_F, \mathbf{x}_S, t) * \hat{f}_1^+(\mathbf{x}_S, \mathbf{x}'_F, t) d^2\mathbf{x}_S \\
&- \ldots
\end{aligned}
\tag{3.2.4}
$$

The first term $\hat{G}_0^- * \hat{f}_0^+$ is the standard source-and-receiver redatumed Green's function including primaries and internal multiples. The second term $-\hat{G}_1^- * \hat{f}_0^+$ contains first-order predictions of receiver-side internal multiples generated by the overburden, while the third term $-\hat{G}_0^- * \hat{f}_1^+$ contains first-order predictions of source-side internal multiples generated by the overburden and the fourth term $-\hat{G}_1^- * \hat{f}_1^+$ contains first-order predictions of source-and-receiver-side internal multiples generated by the overburden. Subsequent terms contain higher-order estimates of the predicted internal multiples that are needed to obtain the correct amplitude and phase. Note that Marchenko methods in principle do not rely on an adaptive filter to accurately attenuate internal multiples. However, instead of retrieving all terms in the series in equation 3.2.4 by correlating and convolving the data with itself many times (see equations 3.2.1 and 3.2.2), we propose to retrieve only a few updates and use an adaptive filter as a substitute for higher-order corrections. Also, an adaptive filter can correct for any minor amplitude and phase differences that are present in the internal multiple predictions due to imperfections in the data acquisition and/or preprocessing. The number of terms needed to obtain predictions of all overburden internal multiples depend on the geological setting. In our case, new internal multiples were not predicted beyond the third term in equation 3.2.4, so we only use the terms $-\hat{G}_1^- * \hat{f}_0^+$ and $-\hat{G}_0^- * \hat{f}_1^+$ for the prediction of internal multiples in this particular setting. These predictions are treated as individual internal multiple predictions, which are orthogonalized to the data prior to simultaneous adaptive subtraction. We have chosen for an adaptive filter in the curvelet domain [*Herrmann et al.*, 2008; *Wu and Hung*, 2015], since it can distinguish between primaries and internal multiples in space, time and dip. Naturally, care has to be taken not to subtract the primary reflections together with the internal multiples.

3.3 Sensitivity tests on 3D synthetic data

We perform a series of 3D synthetic tests to identify the key acquisition parameters that affect the result of the adaptive double-focusing method. In order to generate synthetic data that represent the geological contrasts in the area as realistically as possible, we use a velocity model (see a 2D slice in figure 3.1) and a density model that are obtained from an acoustic inversion of field data based on the original seismic image and migration velocity. The grid size of these models is 18.75 m by 18.75 m by 10 m. Co-located sources and receivers are positioned with a spacing of 50 m in the inline direction and a spacing of 75 m in the crossline direction (see figure 3.2a), thereby simulating an inline spacing of 50 m and a sail line spacing of 75 m. The inline aperture is 20 km (offsets from -10 km to 10 km) and the crossline aperture is 1.8 km. An acoustic finite-difference algorithm is used to model data up to 30 Hz, such that the dominant wavelength at the receivers is 50 m. The recording time is 8.5 s. Also, we generate an initial focusing function $\hat{f}_0^+$ in the smooth velocity model using an Eikonal solver. Geometrical spreading is part of the simulation. In addition, we convolve the response with an Ormsby wavelet with tapers at the low and the high ends.

Starting from 24 lines of data modeled on this dense acquisition grid, we step-by-step decimate down to a realistic streamer acquisition geometry with a cable spacing of 150 m, a sail line spacing of 450 m and a cable length of 6 km. The inline source and receiver spacing remain 50 m. Inline offsets range from 250 m to 6250 m and the crossline aperture is 0.75 km (see figure 3.2b). Throughout the decimation tests, we use the Marchenko double-focusing method to redatum to a grid of co-located virtual sources and virtual receivers below the overburden with a spacing of 25 m by 37.5 m. We have chosen the redatuming level to be just above the base of salt. The base of salt is the top of our reservoir and is therefore part of the target area. The main internal multiple generators in this geological setting, the water bottom and the top of salt, are part of the overburden. Internal multiple predictions are obtained by convolving the individual updates of the wavefields G_j^- and $\hat{f}_i^+$ with one another. We orthogonalize the predictions and the data before subtraction, but do not use a global least-squares filter for pre-conditioning. Next, the internal multiple predictions are simultaneously subtracted from the data using a 3D curvelet filter [*Wu and Hung*, 2015]. Parameters that need to be set are the number of scales in the transform, the number of angles in the transform, the window size and some sparsity parameters that control the inversion. We extensively test different filter settings and obtain the best results (the least damage of the primary reflections) using 7 scales, 8 angles and tapered windows of 768 ms by 256 traces. These settings are used for all synthetic examples shown here.

■ 3.3.1 The complete data set

First, we apply the adaptive double-focusing method to synthetic data generated on the dense grid in figure 3.2a. Figure 3.5 shows redatumed common source gathers before and after internal multiple prediction and subtraction ($\hat{G}_0^- * \hat{f}_0^+$ and $\hat{\hat{G}}^{-+}$

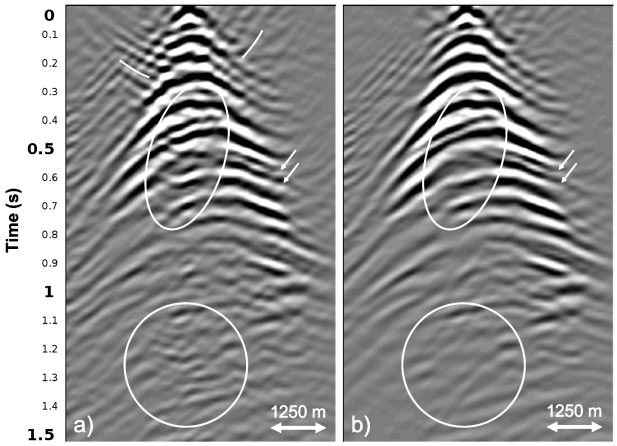

Figure 3.5: *Redatumed common source gathers showing the result of the adaptive double-focusing method applied to 3D synthetic data modeled on the dense acquisition grid in figure 3.2a. The gathers show: a) the redatumed Green's function $\hat{G}_0^- * \hat{f}_0^+$ including primaries and internal multiples and b) the redatumed Green's function $\hat{\hat{G}}^{-+}$ after prediction and adaptive subtraction of internal multiples. The white ellipses, stripes and arrows indicate areas in which internal multiple attenuation is most visible.*

from equation 3.2.4). The common source gathers are from a virtual source in the middle of the grid of focal points, as indicated by the red star in figure 3.2a. A difference is visible, especially in the white ellipses, at the arrows and along the white lines. It seems that conflicting seismic events were resolved, resulting in a better continuity of the primary events.

Next, we deconvolve an user-specified wavelet $\hat{\cdot}$ and migrate the result. Figure 3.6 shows RTM images of the reflection response $\hat{R}$ at the acquisition surface (note that this image was truncated at the base of salt for comparison), the redatumed Green's function including primaries and internal multiples $G_0^- * \hat{f}_0^+$ and the redatumed Green's function $\hat{G}^{-+}$ after internal multiple prediction and subtraction. Figures 3.6a and 3.6b are comparable, thereby demonstrating that source-receiver redatuming was correctly performed (according to the standard primary approach). A comparison between figure 3.6b and figure 3.6c shows a distinct difference. Internal multiples in the white ellipses and indicated by the white curved stripe in figures 3.6a and 3.6b are no longer visible in figure 3.6c. Overall, the continuity of the reflectors has improved. Below the vertical RTM images are depth slices of the 3D RTM volume at 5900 m depth, where the internal multiples are present in figures 3.6a and 3.6b, but have been attenuated in figure 3.6c. Based on these results, we conclude that adaptive double-focusing performs well in terms of redatuming and predicting and subtracting internal multiples when applying it to the initial dense acquisition geometry. Note that the image in figure 3.6c appears to

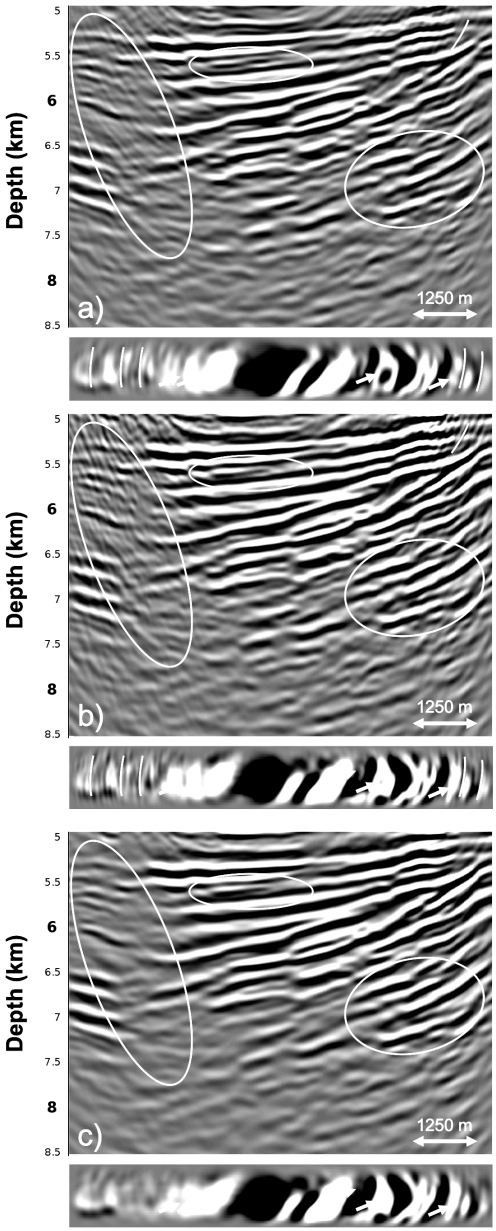

Figure 3.6: *RTM images showing the result of the adaptive double-focusing method applied to 3D synthetic data modeled on the dense acquisition grid in figure 3.2a. The images show: a) the migrated reflection response $\hat{R}$, b) the redatumed and migrated Green's function $G_0^- * \hat{f}_0^+$ including primaries and internal multiples, and c) the redatumed and migrated Green's function $\hat{G}^{-+}$ after prediction and adaptive subtraction of internal multiples. Below the RTM images are depth slices at 5900 m. The white ellipses, line and arrows indicate areas in which internal multiple attenuation is most visible.*

have a lower frequency content compared to the images in figures 3.6a and 3.6b. It seems that the internal multiple reflections favor the high frequencies, possibly due to the generation mechanism in the stratified salt. The resulting images in other papers on internal multiple attenuation in the Santos Basin [e.g. *Griffiths et al.*, 2011; *Cypriano et al.*, 2015] confirm this observation.

In the following, we continue with synthetic data without negative offsets and use source-receiver reciprocity for reconstruction before applying the adaptive double-focusing method.

3.3.2 A coarser sail line spacing

Since a sail line spacing of 75 m is not realistic, we study the effect of coarser sail line spacings on the result of our adaptive double-focusing method. Starting from the result in figure 3.6c with 75 m sail line spacing (here figure 3.7a), we compare RTM images showing the result of adaptive double-focusing when using a sail line spacing of 150 m (figure 3.7b), 300 m (figure 3.7c) and finally 450 m (figure 3.7d). The result obtained from data with a sail line spacing of 150 m looks very similar to the result obtained with 75 m sail line spacing, there are only some minor amplitude differences indicated by the arrows. A more significant difference becomes visible when decimating from 150 m sail line spacing to 300 m sail line spacing. Some internal multiples at the top of the image are no longer predicted and subtracted, probably because the traces that are necessary for the reconstruction of these multiples are missing. The realistic scenario of 450 m sail line spacing shows more internal multiples that could not be predicted and subtracted, now in the deeper part of the image as well. The depth slices confirm these observations: there is little difference between the results obtained with 75 m and 150 m sail line spacing, but internal multiple attenuation becomes less effective when moving to a sail line spacing of 300 m and 450 m. Based on these tests, we conclude that the sail line spacing is a key acquisition parameter that affects our adaptive double-focusing method. Ideally, interpolation from 450 m sail line spacing to 150 m sail line spacing would be applied prior to the field data application in this geological setting. We remark that although we expect that the sail line spacing will also be a key acquisition parameter that affects the result of our adaptive double-focusing methods in other geological settings, the exact spacing at which the result is still acceptable will be different for every setting. In the following synthetic tests, we continue with a sail line spacing of 150 m, thereby assuming that the interpolation from 450 m sail line spacing to 150 m sail line spacing can be carried out correctly.

3.3.3 The removal of the near offsets

The responses at near offsets are typically not recorded by streamers, so we study the effect of removing the first 250 m of inline offsets. Figure 3.8 shows a comparison of RTM images with and without near offsets, both after internal multiple prediction and subtraction. The removal of the near offsets deteriorates the result somewhat in terms of a few remnant internal multiples (at the arrows, the stripe and the ellipse), but not as much as expected. The depth of the first reflector influences how much

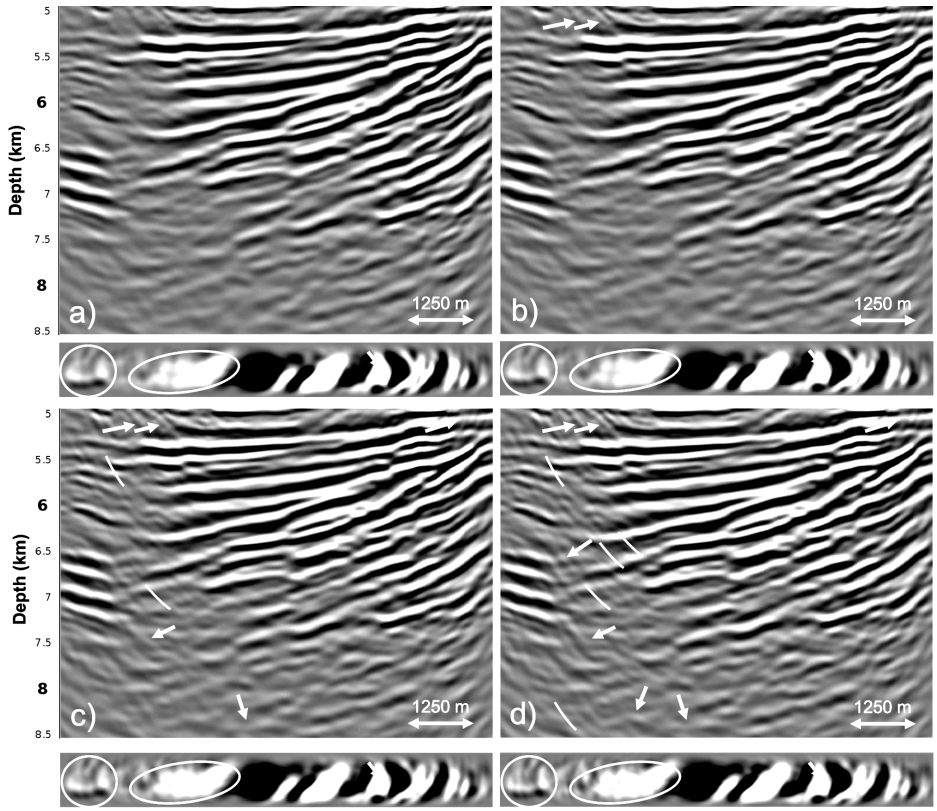

Figure 3.7: *RTM images obtained from the Green's function $\hat{G}^{-+}$ after internal multiple prediction and subtraction for a reflection response modeled with: a) 75 m sail line spacing, b) 150 m sail line spacing, c) 300 m sail line spacing and d) 450 m sail line spacing. Below the RTM images are depth slices at 5900 m. The results using 75 m and 150 m sail line spacing are similar, but the image starts to deteriorate when moving to 300 m sail line spacing.*

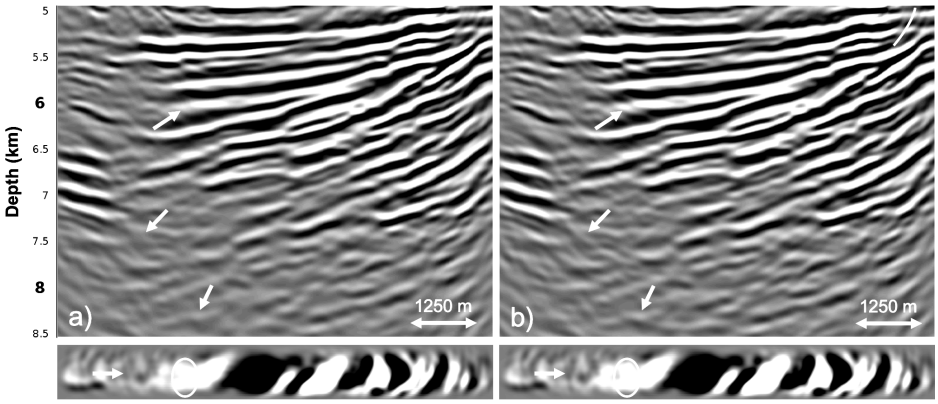

Figure 3.8: *RTM images obtained from the Green's function $\hat{G}^{-+}$ after internal multiple prediction and subtraction for a reflection response modeled with: a) near offsets (0-250 m) and b) without near offsets. Below the RTM images are depth slices at 5900 m. Only a slight difference is visible at the arrows, possibly due to the depth of the target zone.*

the near offset responses contribute to the image. Since the water bottom in this setting is very deep (see figure 3.1), most reflections originating from this depth would have simply not been recorded by the first 250 m of receivers. Even though the near offset responses do not have a large effect on the result of internal multiple prediction and removal in this very deep marine setting, we will interpolate the field data for the missing offsets in order to predict as many internal multiples as accurately as possible.

■ 3.3.4 The removal of the far offsets

Next, we assume that we could correctly reconstruct the responses at near offsets and we study the effect of removing the far offsets (the inline offsets 6250-10000 m). Figure 3.9 shows the RTM images of the result of internal multiple prediction and subtraction using adaptive double-focusing, where figure 3.9a shows the result when including far offsets in the reflection response and figure 3.9b shows the result when excluding far offsets from the reflection response. Only minor differences in amplitude are visible at the arrows. Surprisingly, the far offsets seem to have little impact on the result of adaptive double-focusing, similar to the near offsets. *Verschuur* [2013] reports that missing offsets have a particularly large effect on multiple prediction methods in a shallow water setting. Since we are in a very deep marine setting, missing offsets seem to only have a minor effect.

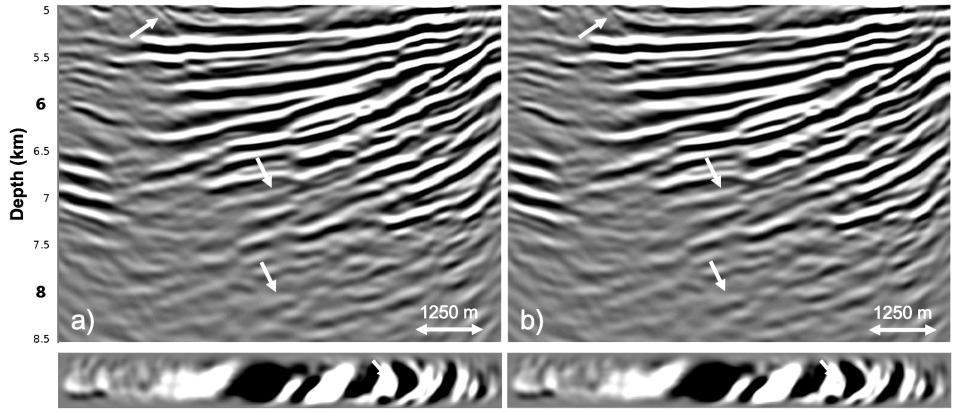

Figure 3.9: *RTM images obtained from the Green's function $\hat{G}^{-+}$ after internal multiple prediction and subtraction for a reflection response modeled with: a) far offsets (6250-10000 m) and b) without far offsets. Below the RTM images are depth slices at 5900 m. Only minor differences are visible at the arrows, mostly in terms of amplitude.*

■ 3.3.5 The removal of the outer cables

Lastly, we study the effect of removing the outer cables. Instead of a crossline aperture of 1800 m, as used in the previous tests, we now use a crossline aperture of 750 m. The RTM images in figure 3.10 show that removing the outer cables has a significant effect on the adaptive double-focusing result. The quality of the image in figure 3.10b has deteriorated and some internal multiples were not predicted and subtracted. Although the missing outer cables have a large effect on the result of adaptive double-focusing, the image in figure 3.10b is still of acceptable quality. This becomes especially clear when comparing it to the standard redatumed Green's function in figure 3.6b, which is constructed from a dense and wide azimuth grid of sources and receivers at the acquisition surface. Compared to this image, figure 3.10b still shows a significant reduction in internal multiple energy. This is promising for the field data application, since we cannot compensate for missing outer cables during preprocessing. We remark that the effect of removing the outer cables is expected to become more severe in geological settings with strongly dipping reflectors in the crossline direction. In those cases, the missing outer cables can be a limiting factor that hinders the application of the adaptive double-focusing method. This observation is supported by reports on the performance of similar multiple prediction and removal methods [*Wang and Hung*, 2014; *Moore and Dragoset*, 2008].

■ 3.3.6 The combination of all effects

Although the results of the synthetic tests in the previous sections are encouraging, they do not provide an indication on the feasibility of the application of the

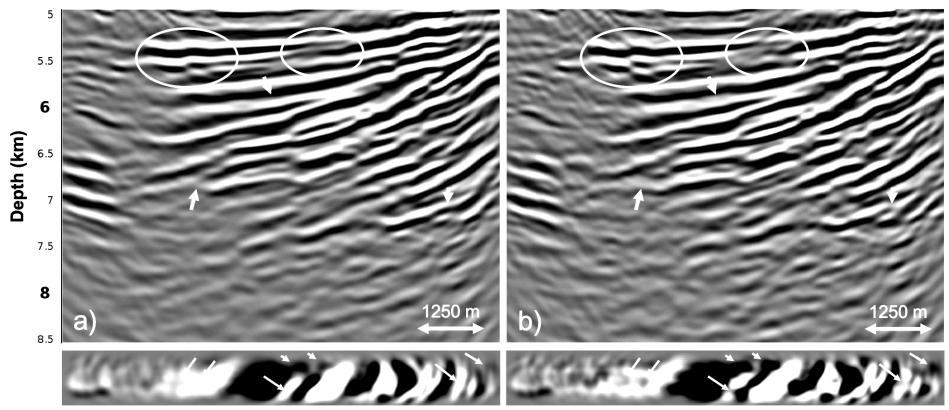

Figure 3.10: *RTM images obtained from the Green's function $\hat{G}^{-+}$ after internal multiple prediction and subtraction for a reflection response modeled: a) with outer cables (1.8 km crossline aperture) and b) without outer cables (0.75 km crossline aperture). Below the RTM images are depth slices at 5900 m. The image considerably deteriorates when removing the outer cables, as indicated by the white ellipses and arrows.*

adaptive double-focusing method to our field dataset, where all acquisition restrictions are imposed simultaneously. The negative offsets, the near offsets, the far offsets, some sail lines and the outer cables are all missing. Therefore, we model 32 lines of 3D synthetic data based on the acquisition geometry of our narrow azimuth streamer data (figure 3.2b). Next, we reconstruct the negative offsets (by applying source-receiver reciprocity) and the near offsets (by interpolation) and perform interpolation for the sail line spacing (from 450 m to 150 m). Figure 3.11 shows the RTM images of the reflection response $\hat{R}$, the standard redatumed Green's function $G_0^- * \hat{f}_0^+$ with primaries and internal multiples and the redatumed Green's function $\hat{G}^{-+}$ after internal multiple prediction and subtraction, zoomed in at the target area. We observe an unexpected difference in illumination when comparing figure 3.11a and figure 3.11b, especially on the right side of the images. Figure 3.11a is constructed by applying an RTM method to the reflection response $\hat{R}$, which uses a finite-difference method to back-propagate the wavefield from the acquisition surface to the redatuming level. In contrast, figure 3.11b is constructed by first back-propagating the reflection response R using convolutions with the modeled direct downgoing focusing function, according to $f_0^+ * \Psi\mathcal{R} * \hat{f}_0^+$ (see equation 3.2.3), to obtain $G_0^- * \hat{f}_0^+$, which is subsequently back-propagated from the redatuming level into the target using the RTM method. In principle, back-propagation using a multidimensional convolution is equivalent to back-propagation using an RTM method [*Esmersoy and Oristaglio*, 1988]. However, in practice, these are only equivalent when the same numerical method is used. We use an Eikonal solver to model the direct wave $\hat{f}_0^+$, which is different from the finite-difference method used in the RTM method. As a result, there are slight differences in illumination between the two

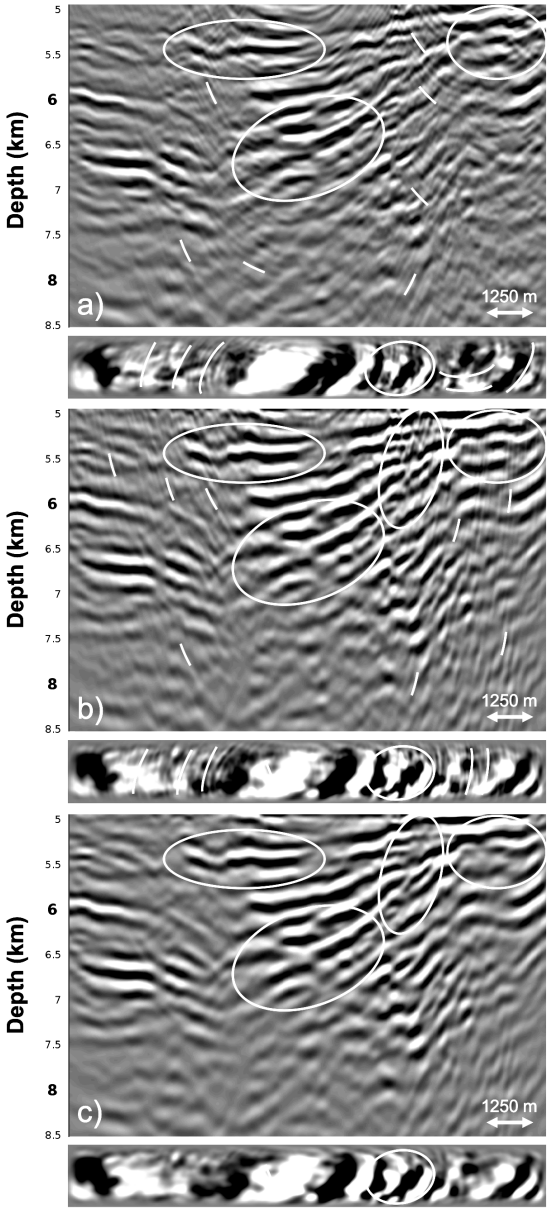

Figure 3.11: *RTM images of the result after applying the adaptive double-focusing method to 3D synthetic data based on the field data acquistion geometry. The images show: a) the migrated reflection response $\hat{R}$, b) the redatumed and migrated Green's function $G_0^- * \hat{f}_0^+$ including primaries and internal multiples, and c) the redatumed and migrated Green's function $\hat{G}^{-+}$ after prediction and adaptive subtraction of internal multiples. Below the RTM images are depth slices at 5900 m.*

images.

Next, we evaluate the effectiveness of internal multiple attenuation. A comparison of figures 3.11b and 3.11c shows that the adaptive double-focusing method succeeded in predicting and subtracting internal multiples from the standard redatumed Green's function. Especially inside the white ellipses, the internal multiple energy is significantly reduced, resulting in a better continuity of the reflectors. Again, we observe that the internal multiples seem to mainly have a high frequency content. We conclude that the adaptive double-focusing method appears to be sufficiently robust for the prediction and adaptive subtraction of internal multiples from narrow azimuth streamer data in this geological setting.

3.4 The 3D field data application

Based on the results of the synthetic tests, we continue with the field data application. We have 24 lines of narrow azimuth streamer data, acquired using 6 flat streamers with a cable spacing of 150 m and a sail line spacing of 450 m. The length of the cables is 6000 m, covering offsets from 250 to 6250 m. The source and receiver spacing is 50 m in the inline direction. The crossline aperture is 750 m. Deghosting is performed in the f-p domain [*Wang et al.*, 2013] and a designature filter is obtained from the water bottom reflection. Shot and near offset reconstruction are performed using a partial normal moveout (NMO) correction of traces per common depth point (CDP) [e.g. *Dragoset et al.*, 2010]. In addition, the data are projected on a regular grid using a $\tau - p$ transform [*Wang and Nimsaila*, 2014]. We also remove surface-related multiples, the evanescent wavefield and noise. After preprocessing, we obtain a dataset with a sail line spacing of 150 m. Similar to the synthetic tests, we have chosen the redatuming level just above the base of salt. A smoothed version of the velocity model in figure 3.1 and an Eikonal solver are used to model our direct downgoing focusing function $\hat{f}_0^+$ (including geometerical spreading), which we subsequently convolve with a 30 Hz Ormsby wavelet. Convergence is tracked by computing the L_2 norm of the updates of the downgoing focusing function $\hat{f}_i^+$.

After convolving the individual updates of the wavefields $\hat{f}_i^+$ and G_j^- and migrating them, we obtain the internal multiple predictions in the image domain. Extensive testing shows us that primary reflections are better preserved when subtracting the internal multiple predictions in the image domain instead of in the redatumed domain. Prior to subtraction, the predictions are orthogonalized. We use the full curvelet transform (for all scales) and tapered windows of 768 ms by 256 traces.

Figure 3.12 and figure 3.13 show the result of applying the adaptive double-focusing method to predict and adaptively subtract internal multiples. First, we observe that there is still a slight illumination difference between the RTM migrated image of the reflection response in figure 3.12a and the image of the RTM migrated redatumed reflection response in figure 3.12b (see the white circle in the top right), which has been explained earlier. However, the difference is not as pronounced as in figure 3.11. Second, a clear difference is visible between figures 3.12b and figure 3.12c, indicating that the adaptive double-focusing method succeeded in predicting

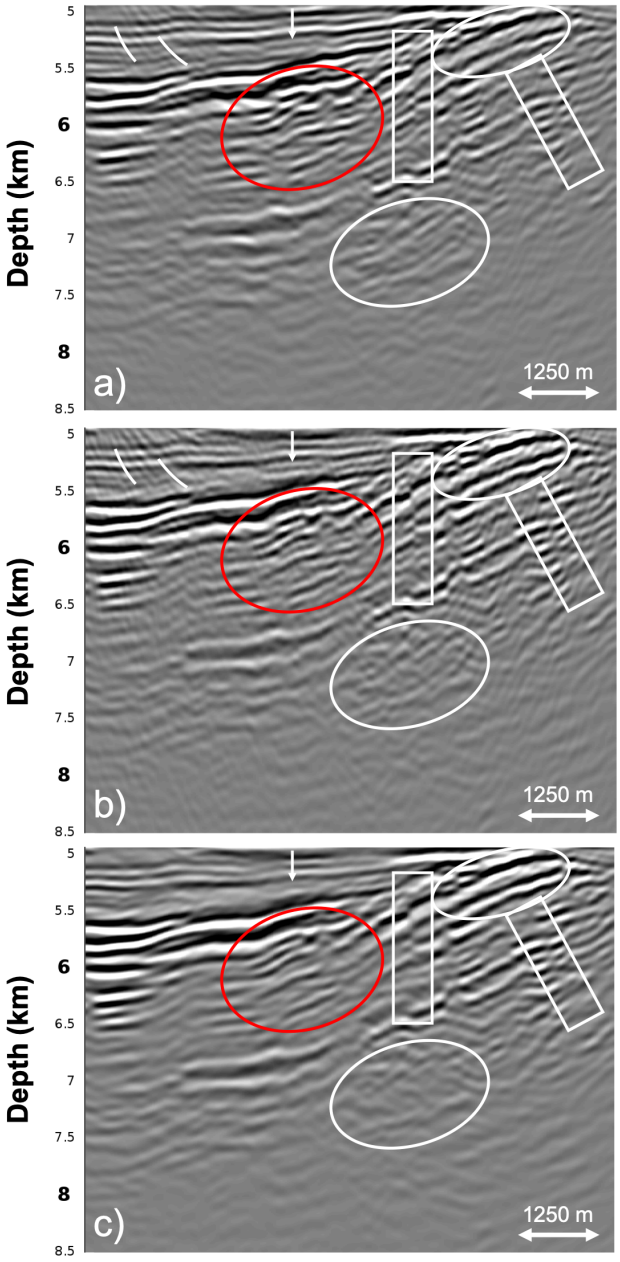

Figure 3.12: *RTM images of the result after applying the adaptive double-focusing method to 3D NAZ streamer data of the Santos Basin, Brazil. The images show: a) the migrated reflection response $\hat{R}$, b) the redatumed and migrated Green's function $G_0^- * \hat{f}_0^+$ including primaries and internal multiples, and c) the redatumed and migrated upgoing Green's function $\hat{G}^{-+}$ after prediction and adaptive subtraction of internal multiples. Internal multiples were predicted and subtracted, resulting in an improved image of the target area.*

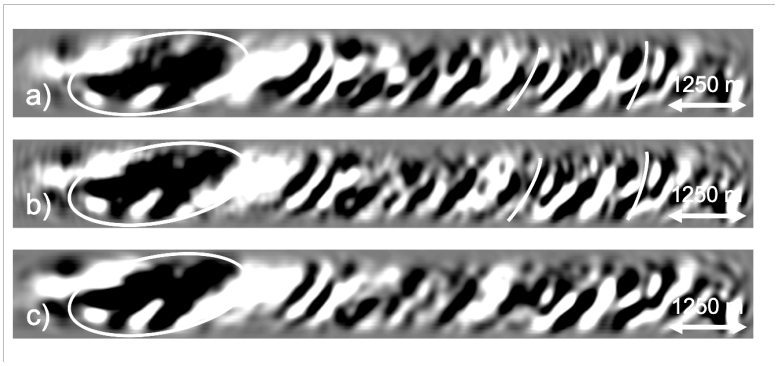

Figure 3.13: *Depth slices corresponding to the RTM images in figure 3.12 at 5900 m. The slices show: a) the migrated reflection response $\hat{R}$, b) the redatumed and migrated Green's function $G_0^- * \hat{f}_0^+$ including primaries and internal multiples, and c) the redatumed and migrated upgoing Green's function $\hat{G}^{-+}$ after prediction and adaptive subtraction of internal multiples.*

and adaptively subtracting events which are likely internal multiples. The arrow, the ellipses and the lower white circle indicate areas in which events were attenuated, while the white boxes indicate what we interpret to be an improvement in fault definition. The red ellipse shows conflicting events that are being resolved, but it also shows events that we believe to be remnant internal multiples. These were most likely generated by the base of salt, which is not part of our overburden. In order to also remove these events, we can obtain additional internal multiple predictions by repeating our procedure while placing the redatuming level just below the base of salt. The RTM depth slices in figure 3.13 demonstrate the attenuation of events in the form of ellipses. This example shows that the adaptive double-focusing method is sufficiently robust for the application to our 3D narrow azimuth streamer dataset. Naturally, this result can be improved by the use of more lines of data.

3.5 Discussion and Conclusion

In this paper, we identified the key acquisition parameters that affect the application of our adaptive Marchenko internal multiple attenuation method to narrow azimuth streamer data. Tests on 3D synthetic data evaluated the effect of removing sail lines, near offsets, far offsets and the outer cables. The results of these tests show that the aperture in the crossline direction and the sail line spacing have the strongest effect on the quality of the result. Typically, the sail line spacing can be interpolated, but the aperture in the crossline direction can possibly be a limiting factor for our method. Surprisingly, the missing near offsets and the far offsets only had a modest effect on the result of our method, possibly due to the very deep target area. In addition, we found that the responses at the negative offsets and the near offsets could be accurately reconstructed. We remark that these tests are only

valid for this particular dataset, but they give an impression of the possibilities and limitations of the adaptive Marchenko double-focusing method. For an Ocean Bottom Node (OBN) acquisition geometry, these tests imply that our method will be most sensitive to the node separation (especially in the direction of the strongest geological variation).

Based on the decimation tests, we defined an interpolation strategy that was first tested on a realistic synthetic dataset. We reconstructed the negative offsets and the near offsets, and interpolated the sail line spacing from 450 m to 150 m. When applying the 3D adaptive double-focusing method, an important aspect that was not visible in earlier 2D applications became visible, thereby showing that the extension of a method from 2D to 3D is not always trivial. In 3D, when using an Eikonal solver for the modeling of the direct wave and a finite-difference-based RTM method, a slight difference in illumination between the RTM image of the reflection response and the RTM image of the redatumed response occurs. Nevertheless, the double-focusing method predicted and adaptively subtracted internal multiples, thereby improving the image of the target area.

Next, we applied the adaptive double-focusing method to 24 lines of narrow azimuth streamer data. We reconstructed the negative and the near offsets and interpolated the sail line spacing. We interpret that internal multiples were predicted and adaptively subtracted, which resulted in an improved geological interpretation of the target area. Therefore, we conclude that 3D Marchenko internal multiple attenuation using an adaptive double-focusing method is sufficiently robust for the application to narrow azimuth streamer data in a deep marine setting, provided that there is sufficient aperture in the crossline direction and that the sail lines are interpolated.

Note that redatuming is optional for Marchenko methods. The adaptive double-focusing method used in this paper includes source-receiver redatuming, which is particularly useful when the aim is to attenuate internal multiples in the target area and at the same time reducing the data volume for a next processing step (for example, a target-oriented full waveform inversion). However, when the aim is to only attenuate internal multiples without redatuming, the adaptive double-focusing method might not be the Marchenko method of choice. A direct quality check of the input common source gathers and the redatumed common source gathers is not possible, which is a disadvantage in a general processing workflow. In addition, a quality check on the resulting images is only possible when the same numerical method is used to obtain the direct wave for the Marchenko method as for the migration of the original data. Therefore, for the purpose of internal multiple elimination only, we propose the use of other Marchenko methods that do not include redatuming and thus allow for an easier quality check. An example is the adaptive overburden elimination method [*van der Neut and Wapenaar*, 2016], as shown in papers by *Pereira et al.* [2018], *Krueger et al.* [2018] and *Pereira et al.* [2019]. A modified version of the adaptive double-focusing method is presented by *Staring et al.* [2019]. Other alternatives are the Marchenko multiple elimination scheme [*Zhang and Staring*, 2018] and the primary-only method proposed by *Meles et al.* [2016].

The Marchenko method used in this paper is acoustic. The synthetic data are acoustic, but naturally the field data are elastic. A suggestion for further research is to evaluate the effect of the presence of mode conversions on the acoustic Marchenko method in this geological setting, as was done by *Reinicke et al.* [2019] for the offshore Middle East. By applying an acoustic Marchenko method to elastic synthetic data, and comparing it to the result of applying an acoustic Marchenko method to acoustic synthetic data, *Reinicke et al.* [2019] evaluated whether the acoustic approximation is valid for structural imaging in the region. They concluded that the acoustic approximation may be sufficient when used for structural imaging in 1.5D geological settings.

4

R-EPSI and Marchenko-based workflow for multiple attenuation in the case of a shallow water layer and a complex overburden: A 2D case study in the Arabian Gulf

Abstract The previous chapter has shown the application of the adaptive double-focusing method to 3D streamer data. The results show that the adaptive double-focusing method is well-suited when wishing to redatum, but that it is perhaps not the method of choice when only wishing to predict and subtract internal multiples while keeping sources and receivers at the acquisition surface. Therefore, we formulate a new Marchenko method, the double dereverberation method, that does not require redatuming and does not require model information. Next, we test this new method on OBC data acquired in the Arabian Gulf. This is a challenging geological setting due to very shallow water and a finely layered medium with strong contrasts. Instead of only having the challenge of removing numerous and strong internal multiples, there is also the challenge of the attenuation of surface-related multiples and the estimation of the source wavelet. To address these issues, we design a workflow that combines the Robust Estimation of Primaries by Sparse Inversion (R-EPSI) method for the suppression of surface-related multiples and the estimation of an effective source signature with the novel Marchenko method for the attenuation of internal multiples generated by the complex overburden. As part of this workflow, we introduce a simple yet effective method to obtain data with the correct scaling as input for the Marchenko method. Finally, we apply the workflow to field data and manage to predict and subtract a complex interference pattern of internal multiples, thereby significantly improving the image of the target area.

Under review: Staring, M., M. Dukalski, M. Belonosov, R. H. Baardman, J. Yoo, R. F. Hegge, R. van Borselen and K. Wapenaar, R-EPSI and Marchenko equation-based workflow for multiple suppression in the case of a shallow water layer and a complex overburden: A 2D case study in the Arabian Gulf.

4.1 Introduction

The combination of a shallow water layer and a complex overburden, for example, in Norway [*Rønholt et al.*, 2014], in the West Central Graben of the North Sea [*Yanez et al.*, 2018] and in the Middle East [*El-Emam et al.*, 2011], present a challenge for seismic processing. Typically, many orders of strong surface-related multiples and internal multiples are generated and interfere with the primary reflections from the target area. When not correctly suppressing these multiples before migration, an inaccurate image of the target area is obtained that cannot be used for geological interpretation. We present a processing workflow that is specifically designed for shallow water environments in combination with a complex overburden. We use the R-EPSI method [*Lin and Herrmann*, 2013] for the simultaneous estimation of the source wavelet and the suppression of surface-related multiples and a double dereverberation method (a novel Marchenko method) for the suppression of internal multiples.

Most commonly, surface-related multiples are predicted and adaptively subtracted using either model-based methods [*Lokshtanov*, 1999] that require prior knowledge of the subsurface, or data-driven methods, for example surface-related multiple elimination (SRME) [*Berkhout and Verschuur*, 1997] and its numerous modifications [e.g. *Castelan et al.*, 2016]. *Hargreaves* [2006], *Hung et al.* [2010] and *Barnes et al.* [2014] report that SRME methods produce poor results in shallow water environments, because the different orders of surface-related multiples strongly interfere with the primary events. This makes adaptive subtraction without substantial corruption of the primaries impossible. Alternatively, there are Marchenko methods that address surface-related multiples in addition to internal multiples [*Ware and Aki*, 1969; *Singh et al.*, 2016; *Ravasi*, 2017], but currently available results illustrate a poor convergence of these methods [*Dukalski and de Vos*, 2017]. To address the surface-related multiples, we propose to use the Robust Estimation of Primaries by Sparse Inversion (R-EPSI) method [*Lin and Herrmann*, 2013], since field data tests illustrate that it performs well in a shallow water regime [*Belonosov and van Borselen*, 2017; *Belonosov et al.*, 2019]. This method retrieves surface-related multiples of all orders from the input data only, using a large-scale and automatic inversion process. In addition, the output reflection response (i.e., the response without the predicted surface-related multiples) has been deconvolved by an estimated source wavelet, which is otherwise difficult to obtain in a shallow water environment. In the following, we call the deconvolved reflection response without surface-related multiples the Green's function.

After suppression of the surface-related multiples by the R-EPSI method, the next step is the prediction and subtraction of internal multiples. A range of internal multiple prediction methods exists, but most are not suitable for the prediction of internal multiples generated in a complex overburden. Internal multiple prediction methods that rely on the interpretation of an image to identify multiple generators, for example *Jakubowicz* [1998], are hampered by the complexity of the overburden. Filtering methods, that rely on a difference in properties between primaries and internal multiples in an alternative domain (for example, the τ-p or the FK domain), are also not suitable since there is usually no clear difference in properties between

the internal multiple reflections and the primary reflections [*Griffiths et al.*, 2011; *Lesnikov et al.*, 2011; *Brookes*, 2011]. In contrast, Marchenko methods are well-suited for the prediction of a complex interference pattern, because they consider the entire overburden at once without needing to identify individual multiple generators. Moreover, they do not rely on a difference in properties between primaries and internal multiples. Marchenko methods solve an inverse problem to obtain an inverse transmission response through the overburden including primaries and internal multiples, given only reflection data and a smooth model of the overburden [*Wapenaar et al.*, 2014a]. The retrieved transmission response can be used to create virtual sources and virtual receivers anywhere inside the subsurface [*Wapenaar et al.*, 2018]. Alternatively, the Marchenko equations can be written as a nested series in order to predict overburden borne reverberations [*van der Neut et al.*, 2015a; *van der Neut and Wapenaar*, 2016; *Staring et al.*, 2018a]. We modify the approach from *van der Neut and Wapenaar* [2016] using the approach from *Staring et al.* [2018a] to obtain a more practical and efficient Marchenko method that is capable of predicting internal multiples generated by a complex overburden.

After the selection of the R-EPSI method and an adaptive Marchenko method, it is key to design a workflow that correctly prepares the data and makes the two methods compatible. Our proposed workflow (figure 4.1) consists of three stages that each have their own objective: preprocessing, R-EPSI-based surface-related multiple suppression and Marchenko internal multiple attenuation. Table 4.1 shows an overview of the reflection responses and Green's functions that we obtain from the different stages. Although our Marchenko method (stage 3) predicts internal multiples with the correct amplitude and phase in theory, an adaptive filter is needed to correct for minor amplitude and phase differences between the internal multiple predictions and the internal multiples in the data due to imperfections in data acquisition and processing. When not paying sufficient attention to amplitude and phase fidelity in the first and second stage of the workflow, amplitude and phase differences might be enhanced, such that the internal multiples predicted in the third stage are significantly different from the internal multiples in the data. In that case, a more agressive adaptive filter would be needed for the subtraction of the predicted internal multiples, which increases the risk of damaging the primaries. Therefore, we have carefully selected the methods in the first and second stage of our workflow based on the preservation of amplitude and phase fidelity (for details, see figure 4.1). Next, we have to ensure that the second and third stage correctly match each other. The Green's function without surface-related multiples that results from the R-EPSI method is a suitable input for our Marchenko method. However, the R-EPSI method has an inherent scaling ambiguity that is caused by deconvolving an effective wavelet from the reflection response [*Lin and Herrmann*, 2013]. Therefore, a scaling factor has to be determined at the beginning of the third stage. The proposed workflow is suitable for OBC, OBN and streamer data (in the latter case negative and near offset data need to be reconstructed during the first stage of the workflow).

In this chapter, we begin with the theory of the proposed Marchenko method, since the main novelty of the workflow is stage 3. We combine the approaches from

Symbol	Meaning
$\mathcal{R}$	raw reflection response
R	reflection response after preprocessing
R_0	reflection response without surface-related multiples
s	the estimated source wavelet
M	predicted surface-related multiples
G	Green's function, equal to R_0 deconvolved by s
v^+	projected Marchenko focusing function
U^-	upgoing wavefield without receiver-side overburden internal multiples
$\mathcal{U}^{-+}$	upgoing Green's function without overburden internal multiples

Table 4.1: *Table accompanying the workflow in figure 4.1, showing symbols and their meaning.*

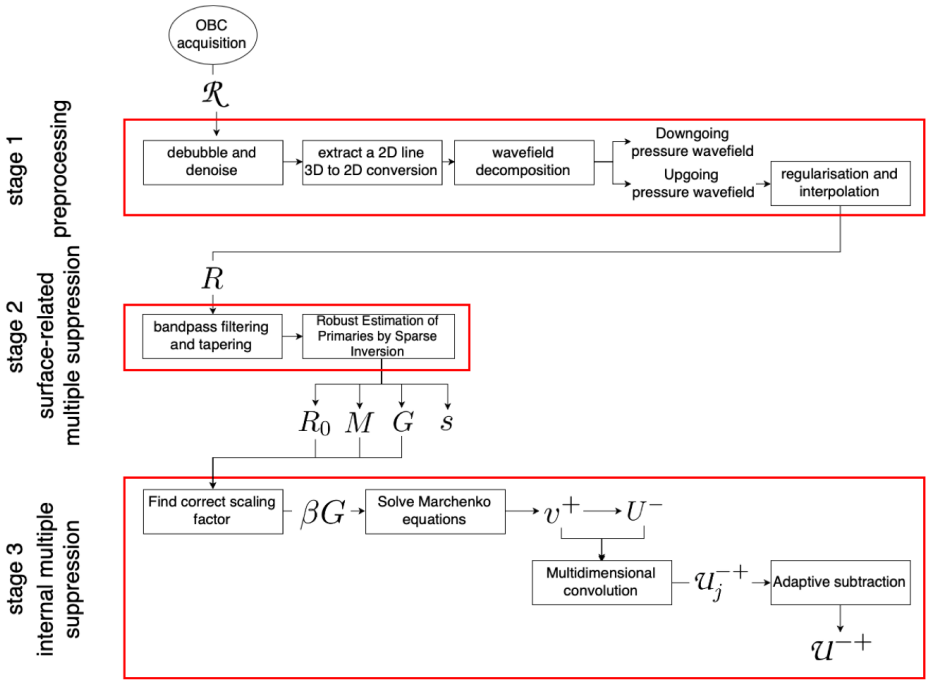

Figure 4.1: *Workflow designed for the processing of a seismic dataset acquired in a shallow water environment with a complex overburden.*

van der Neut and Wapenaar [2016] and *Staring et al.* [2018a] to obtain a double dereverberation method that is well-suited for our purpose. Next, as a case study,

we apply our workflow to a 2D line of OBC data from the Arabian Gulf. We discuss the application of our workflow step-by-step and show intermediate results. In addition, we present a method to find the correct scaling factor to compensate for the scaling ambiguity in the R-EPSI method. Finally, we discuss the result of the entire workflow, where a complex interference pattern of internal multiples was subtracted from the target area.

4.2 Theory of stage 3: the double dereverberation method

Since the R-EPSI method is well-established in the literature [*Van Groenestijn and Verschuur*, 2009a; *Lin and Herrmann*, 2013; *Belonosov and van Borselen*, 2017; *Belonosov et al.*, 2019], the novelty in our work is the incorporation of an adaptive Marchenko method for the prediction and adaptive subtraction of internal multiples generated in a complex overburden. This method requires as input a Green's function G acquired by a sufficiently dense grid of co-located dipole sources and monopole receivers. This Green's function should not be contaminated by noise, ghosts, source signature and surface-related multiples. These requirements are similar to many routinely used internal multiple prediction methods, for example, *Jakubowicz* [1998]. We use the pressure-normalized equivalent of the flux-normalized approach proposed by *van der Neut and Wapenaar* [2016] to retrieve the following nested series:

$$\hat{v}^{+} = \sum_{i=0}^{N} \hat{v}_i^{+} = \sum_{i=0}^{N} \{\Theta_{t_0}^{t_2} \mathcal{G}^{\star} \Theta_{t_0}^{t_2} \mathcal{G}\}^i \hat{\delta} \text{ and} \tag{4.2.1}$$

$$\hat{U}^{-} = \sum_{j=0}^{P} \hat{U}_j^{-} = \Theta_{t_2}^{\infty} \mathcal{G} \sum_{j=0}^{P} \hat{v}_j^{+}. \tag{4.2.2}$$

The symbol $\hat{\cdot}$ denotes that the wavefield is convolved with a user-specified wavelet that simulates a band-limitation. The symbols i and j indicate the iteration number that ranges from 1 to N and from 1 to P respectively. $\hat{v}^{+}$ is the Marchenko focusing function f^{+} projected to the acquisition surface, and $\hat{U}^{-}$ denotes an upgoing wavefield with sources and receivers at the acquisition surface. Symbol $\hat{\delta}$ represents a band-limited spatio-temporal delta function. Operators $\mathcal{G}^{\star}$ and $\mathcal{G}$ perform multidimensional correlations and convolutions of the Green's function G with the wavefield that it acts upon, and $\Theta_{t_0}^{t_2}$ and $\Theta_{t_2}^{\infty}$ are tapered Heaviside muting functions. The two-way traveltime curve t_2 separates the overburden response from that of the target area and t_0 is a curve that depends on the finite temporal and spatial frequency content of the data. These curves can either be modeled in a smooth velocity model or picked from the wavelet-dressed Green's function, provided that there is a strong reflector above the target area. If picking is possible, our approach is data-driven and can be used in the workflow before velocity model building. We explain how to pick boundaries t_0 and t_2 in the application section of this chapter.

The upgoing wavefield $\hat{U}^{-}$ is free from receiver-side internal multiples that have a final reflection point in the overburden (figure 4.2a). Other internal multiples, as depicted in figure 4.2b and 4.2c, are still part of the retrieved upgoing wavefield. An

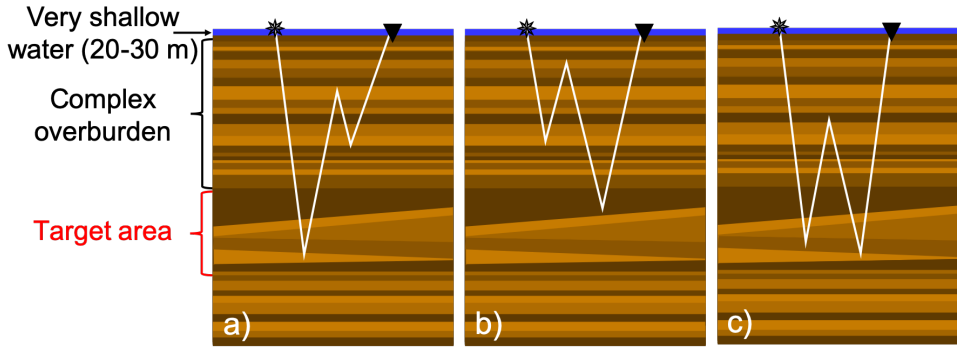

Figure 4.2: *Cartoons illustrating different types of internal multiples: a) an internal multiple with a final reflection point in the overburden, b) an internal multiple with an initial reflection point in the overburden, and c) an internal multiple with initial and final reflection points below the overburden.*

additional processing step is needed to remove other overburden internal multiples. Instead of performing a multidimensional deconvolution of $\hat{U}^-$ and $\hat{U}^+$ as suggested by *van der Neut and Wapenaar* [2016], we propose a more straightforward step that follows the adaptive double-focusing method introduced by *Staring et al.* [2018a]. We convolve upgoing wavefield U^- with the projected Marchenko focusing function v^+ to create a double dereverberation method:

$$\begin{aligned}\hat{u}^{-+} &= \hat{U}^- * v^+ = \sum_{j=0}^{P}\sum_{i=0}^{N} \hat{U}_j^- * v_i^+ \\ &= \hat{U}_0^- + (\hat{U}_1^- + \hat{U}_0^- * v_1^+ + \hat{U}_1^- * v_1^+ + ...) \\ &\equiv \hat{u}_0^{-+} - \sum_{k=1}^{Q} \hat{u}_k^{-+},\end{aligned} \tag{4.2.3}$$

where $\hat{u}_0^{-+} = \hat{U}_0^-$, $\hat{u}_1^{-+} = -\hat{U}_1^-$, $\hat{u}_2^{-+} = -\hat{U}_0^- * v_1^+$, etc. Furthermore, $v_0^+ = \delta$ and k indicates the iteration number that ranges from 1 to Q. The user-specified wavelet was deconvolved from the projected Marchenko focusing function v^+ prior to convolution with upgoing wavefield $\hat{U}^-$. The first term of the series $\hat{u}_0^{-+} = \Theta_{t_2}^{\infty}\mathcal{G}\hat{\delta}$ is the muted wavelet-dressed Green's function, while later terms $\hat{u}_j^{-+}$ contain predictions of internal multiples. These predictions are subtracted directly from the Green's function, thereby making a quality check straightforward. A single adaptive filter α is used to compensate for (unavoidable) minor amplitude and phase differences:

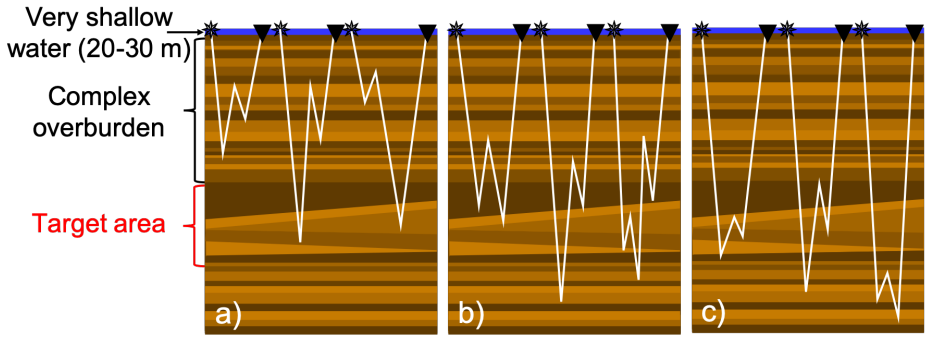

Figure 4.3: *Cartoons illustrating different types of internal multiples: a) internal multiples generated by the overburden, b) internal multiples generated by interactions between the target area and the overburden, c) internal multiples generated by the target area and below the target area.*

$$\hat{\mathcal{U}}^{-+} \approx \hat{\mathcal{U}}_0^{-+} - \alpha \sum_{k=1}^{Q} \hat{\mathcal{U}}_k^{-+}. \tag{4.2.4}$$

Note that the individual terms in $\sum_{k=1}^{Q} \hat{\mathcal{U}}_k^{-+}$ are summed without adaptive filter, showing the importance of amplitude and phase fidelity in our workflow. The retrieved wavelet-dressed Green's function $\hat{\mathcal{U}}^{-+}$ is the reflection response that has sources and receivers at the acquisition surface and does not contain internal multiples generated by the overburden (figure 4.3a). Note that later arriving internal multiples (which would be imaged deeper) generated by interactions of the target area with the overburden (figure 4.3b) and internal multiples generated by the target area or below the target area (figure 4.3c) are not suppressed by this convolution. Hence, equation 4.2.4 addresses internal multiples that contaminate the target area, while leaving some internal multiples arriving later than the primaries of the target area unaddressed.

4.3 Case Study: the Arabian Gulf

In this section, we apply the workflow in figure 4.1 to an OBC dataset acquired in the Arabian Gulf with a grid of receivers at the sea bottom (20-30 m deep) and lines of sources just below the sea level. Figure 4.4 shows the acquisition geometry. The subsurface contains many fine layers of anhydrites, carbonates and clastics with strong acoustic impedance contrasts [*Alá'i et al.*, 2002; *Owusu et al.*, 2016]. The very shallow water generates many orders of strong surface-related multiples and the abundance of subsurface layers generates many orders of strong internal multiples that do not appear as separate events, but make up a complex interference

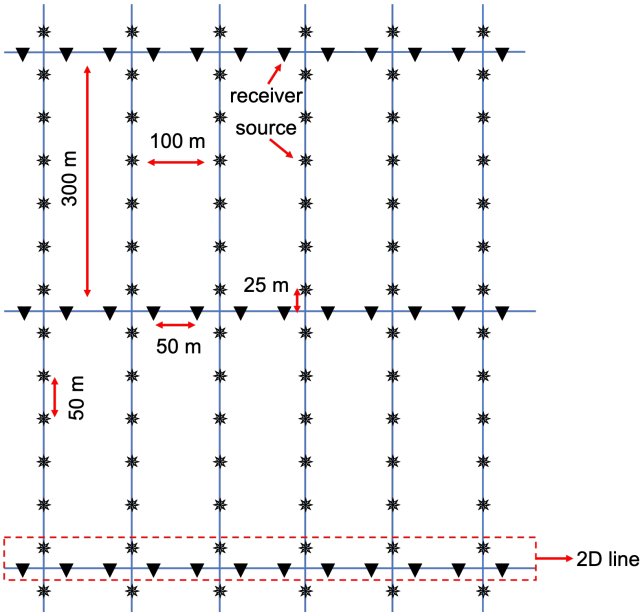

Figure 4.4: *The OBC acquisition geometry used to acquire the data from the Arabian Gulf. Note that receivers reside at the sea bottom, while sources reside just below the sea level.*

pattern where also higher-order internal multiples are of importance. In addition, the geology is relatively flat, which makes it difficult to distinguish the primary reflections from the multiple reflections. The complexity of the multiple problem in this setting makes it an ideal test-case for our workflow.

■ 4.3.1 Stage 1: Preprocessing

Our starting point is the raw reflection response $\mathcal{R}$. Figure 4.5a shows a 2D subset of a 3D common source gather, where strong ground roll dominates the reflections. Following our workflow in figure 4.1, we apply debubbling and static corrections for the water column, remove anomalous amplitude noise, strong mudrolls and amplitude outliers, and attenuate linear noise. A 2D line with 50 m receiver spacing and 100 m source spacing was extracted from the 3D dataset (as indicated by the dotted red box in figure 4.4). The use of a 2D line instead of a 3D volume is not a serious limitation in this geological setting, since the subsurface of the Arabian Gulf has a 1.5D character (due to the nearly flat layering). In addition, the dense receiver spacing of the line is beneficial for our proposed method. Next, 3D to 2D correction was applied [*Wapenaar et al.*, 1992] and the data were decomposed into downgoing and upgoing wavefields [*Soubaras*, 1996]. We select the upgoing pressure wavefield to make this workflow also suitable for single component data. Figure 4.5b shows a common source gather of this wavefield, where the reflections are better visible

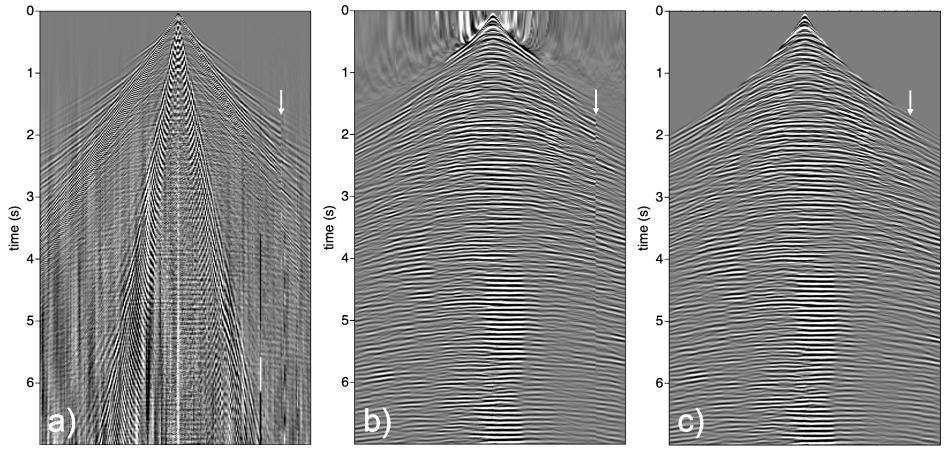

Figure 4.5: *Common source gathers containing: a) the raw reflection response $\mathcal{R}$, b) the upgoing wavefield after debubble, denoise and decomposition, c) the reflection response R after regularization and interpolation. A time-dependent gain $t^{1.5}$ was applied to the data for display purposes. The white arrows indicate an acquisition gap that is being closed.*

compared to figure 4.5a. Note an acquisition gap on the right side of the gather, indicated by a white arrow. We apply 2D interpolation and regularization to obtain a line of unaliased data with 25 m spacing. Figure 4.5c shows a common source gather of the reflection response R, where the acquisition gap has now been closed.

4.3.2 Stage 2: The estimation of the source wavelet and the suppression of surface-related multiples

Next, we apply a bandpass filter (2-6-38-42 Hz) to the reflection response R to avoid aliasing in subsequent processing steps. Also, we place a taper on the common source gathers to avoid edge effects (see figure 4.6a). Next, we apply the R-EPSI method to retrieve the reflection response R_0 without all orders of surface-related multiples M. In addition, we obtain the corresponding Green's function G without the estimated effective source signature s. Data extrapolation through the water layer is a component of R-EPSI for OBC data, such that sources and receivers now reside just below the sea level. The common source gather in figure 4.6a was also extrapolated for comparison. Figure 4.6b shows a common source gather of the reflection response R_0, where a clear difference with figure 4.6a is visible due to the suppression of surface-related multiples. Primary events that were not visible before have emerged and the continuity of the reflections has improved. Figure 4.6c shows the suppressed surface-related multiples M. When studying the FK spectra in figure 4.7, it seems that surface-related multiples between 20 Hz and 32 Hz are absent due to some unexplained property of the subsurface or due to destructive interference of

the (short-period) surface-related multiples with each other. Most surface-related multiples seem to have frequencies between 8 Hz and 18 Hz, with a main peak around 14 Hz. Figure 4.8 shows the depth migrated images (obtained by applying a reverse time migration (RTM) method [*Kim et al.*, 2013]) that correspond to figure 4.6. Figure 4.8b shows the RTM image of the reflection response R_0 that results from R-EPSI. The image of the target area (in the white box) has significantly improved compared to figure 4.8a by the suppression of the surface-related multiples M in figure 4.8c. Note in figure 4.8c that the migrated surface-related multiples seem to increase in amplitude in the deeper parts of the image (not just due to the gain), something that can also be noticed in the common source gather in figure 4.6c. It seems that higher-order surface-related multiples have stronger amplitudes compared to lower orders or that the many orders start to constructively interfere with each other at later times. As a result, the image after surface-related multiple suppression (figure 4.8b) seems more balanced in terms of amplitude.

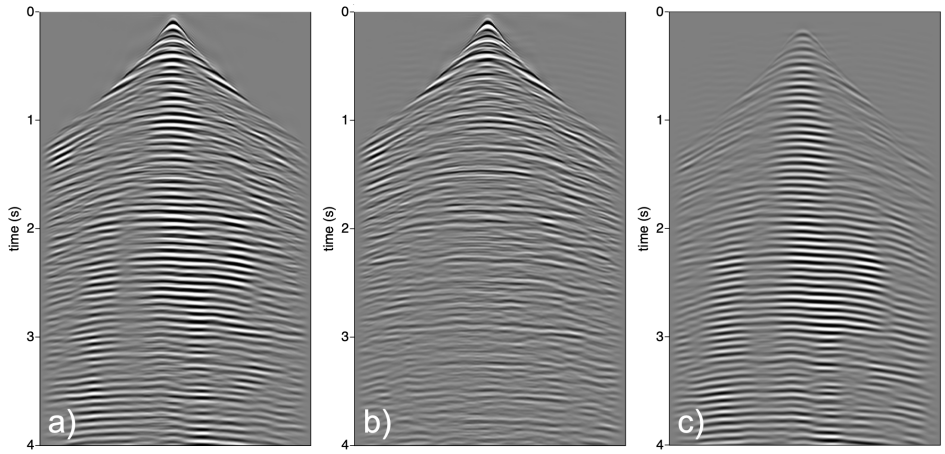

Figure 4.6: *Shot gathers containing: a) the bandpass filtered and tapered reflection response R before R-EPSI, b) the reflection response R_0 after R-EPSI, and c) the suppressed surface-related multiples. Figure a) has been brought to the same datum (just below sea level) as figures b) and c) for easier comparison. A time-dependent gain $t^{1.5}$ was applied for display purposes.*

■ 4.3.3 Stage 3: The prediction and adaptive subtraction of internal multiples

Finding a scaling factor

The third stage of our workflow requires the correctly scaled Green's function G that results from the R-EPSI method as input. The Green's function G is obtained

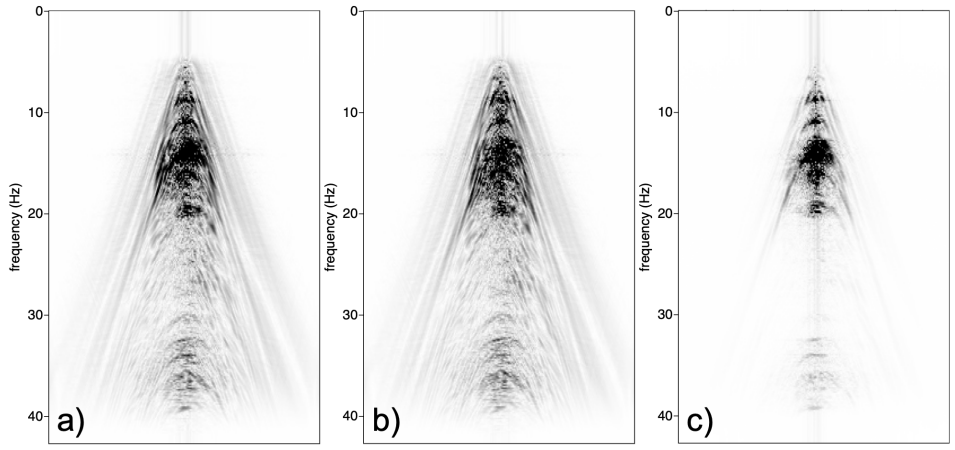

Figure 4.7: *FK spectra of the common source gathers in figure 4.6.*

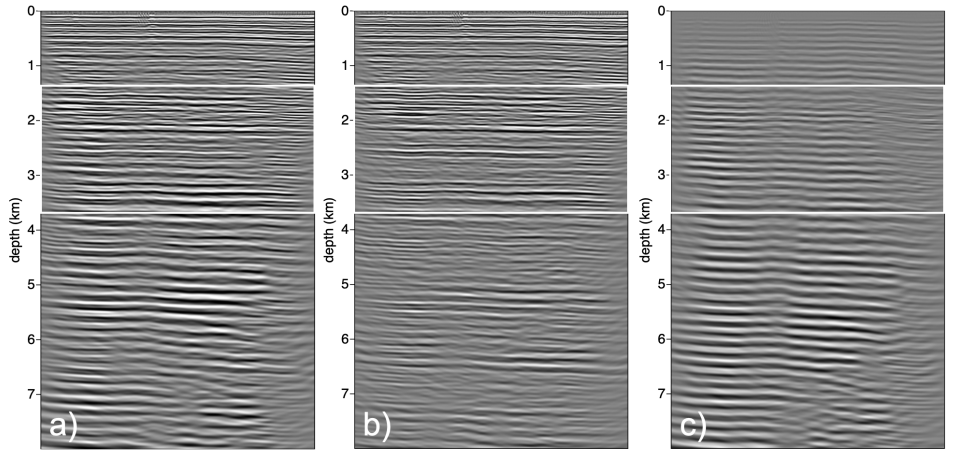

Figure 4.8: *RTM images obtained from: a) the reflection response R before R-EPSI, b) the reflection response R_0 after R-EPSI, and c) the suppressed surface-related multiples.*

by deconvolving the effective wavelet s from the reflection response R_0, thereby introducing a scaling ambiguity β. The missing scaling factor can be found by cleverly making use of the surface-related multiples M that were predicted from the reflection response R during the second stage of our workflow. We can repredict each order l of surface-related multiples by convolving G the right number of times with R_0 (i.e. $\sum_l (G^l) * R_0$) and compare them to the surface-related multiples

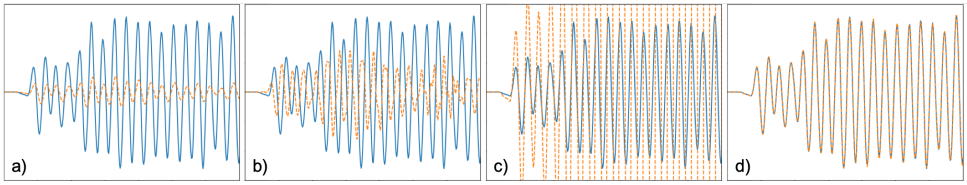

Figure 4.9: *Plots with surface-related multiples as found in the data (solid blue line) and the repredicted surface-related multiples (dashed orange line). The Green's function used for reprediction is: a) the result of R-EPSI, b) the result of R-EPSI multiplied by k_z, c) the result of R-EPSI multiplied with $\sqrt{i\omega}$, d) the result of R-EPSI multiplied by $\sqrt{i\omega}$ and a scaling factor of 0.396.*

M predicted by the R-EPSI method. If the repredicted and predicted surface-related multiples match, then the Green's function G should be a suitable input for Marchenko methods that also use convolutions (and correlations). Otherwise, the scaling and/or phase of the Green's function has to be adjusted until predicted and repredicted surface-related multiples match.

Figure 4.9 shows the comparison of the predicted surface-related multiples M (in solid blue) with the surface-related multiples that were repredicted by convolving the Green's function G up to 20 times ($l = 20$) with the reflection response R_0 (in dashed orange). Figure 4.9a shows the result of simply using the output Green's function G of the R-EPSI method without any additional phase shift or scaling factor to repredict surface-related multiples. Both amplitude and phase of the repredicted surface-related multiples do not match the predicted surface-related multiples M, indicating that this is not the corrrect Green's function. In order to check whether we have the correct type of Green's function (dipole sources, monopole receivers), we tested whether multiplying the data by a factor k_z would improve the match. Figure 4.9b shows that this only worsened it. Next, we tried applying a half time-differentiation to the data in figure 4.9c. When looking back at our R-EPSI implementation, it indeed follows that we need this phase shift. The result shows a slightly better match, but the convolutions seem to diverge, which indicates an incorrect scaling factor. When scaling the Green's function by a factor 0.396, we obtain a near perfect match in figure 4.9d. Note that the R-EPSI method provides output data with an arbitrary scaling factor because it deconvolves an effective wavelet from the data. Therefore, the scaling factor will be different for every dataset. This demonstrates the importance of performing such a quality check. Furthermore, it shows that repredicting surface-related multiples is a useful tool to find the correct input Green's function for Marchenko methods. We remark that this method can be automatized based on minimizing the difference between repredicted and actual surface-related multiples (find β which minimizes $\|M - \sum_l (\beta G^l) * R_0\|$).

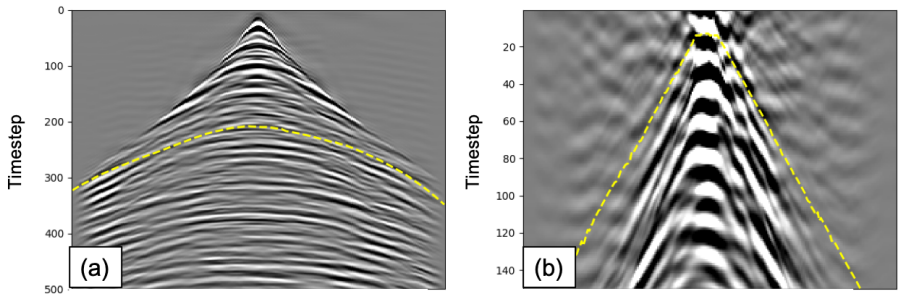

Figure 4.10: *a) Common source gather from the middle of the 2D line, showing the picked t_2 traveltime curve in dashed yellow and b) common source gather of the auto-correlated reflection response, showing the picked t_0 in dashed yellow.*

The application of the double dereverberation method

The application of our double dereverberation method starts by convolving the Green's function G with an user-specified wavelet to simulate the operation $\mathcal{G}\hat{\delta}$ in equation 4.2.1. For example, we could use a Ricker wavelet with a maximum frequency that matches the frequency spectrum of the data. To be able to compare our results throughout the workflow, we have chosen our user-specified wavelet to be the effective wavelet s estimated by the R-EPSI method, so that we can use reflection response R_0 as input (figure 4.11a).

Next, traveltime curve t_2 is picked from reflection response R_0. The two-way traveltime curve t_2 separates the overburden from the target area and is picked directly from the common source gathers. If a strong reflector is present above the target area, it can be tracked for every common source gather and smoothing is applied to correct for jumps in the traveltime curve between sources. The curve should be shifted back in time by a small time step ϵ, which is approximately equal to half the duration of the user-specified wavelet, to exclude the event itself from the truncation. Figure 4.10a shows the t_2 curve in a common source gather from the middle of our 2D line. If a strong reflector above the target area is not present, the t_2 curve can also be modeled in a smooth velocity model.

Having obtained curve t_2, the tapered spatio-temporal Heaviside muting function $\Theta_{t_2}^{\infty}$ can be constructed. Tapering is needed to avoid Gibb's phenomena by sudden truncations. Using this muting function, we retrieve the muted reflection response $\Theta_{t_2}^{\infty} R_0$ from equation 4.2.2 (see figure 4.11b). This is the first term $\hat{\mathcal{U}}_0^{-+}$ in equation 4.2.4 from which the predicted internal multiples are going to be adaptively subtracted. Figure 4.14b shows the effect of the mute in the image domain, which seems to be following the flat layering of the subsurface.

In order to construct muting function $\Theta_{t_0}^{t_2}$, we need curve t_0. We obtain curve t_0 by first constructing operator $\mathcal{G}$ used in equation 4.2.1 by taking our correctly

Figure 4.11: *Common source gathers containing: a) the reflection response R_0 after R-EPSI (same as figure 4.6b), b) the muted reflection response $\hat{\mathcal{U}}_0{}^{-+} = \Theta_{t_0}^{t_2} R_0$, c) the resulting reflection response after internal multiple suppression using equation 4.2.3 and d) the subtracted internal multiples. A time-dependent gain $t^{1.5}$ was applied to the data for display purposes.*

scaled Green's function G. Next, we perform a multidimensional crosscorrelation of the muted reflection response $\Theta_{t_2}^{\infty} R_0$ with operator $\mathcal{G}$. The t_0 curve can be picked in this result for each common source gather (see figure 4.10b). If short-period interbed multiples are present, they appear as events close to the event at zero-lag, or even intersecting with this event. Ideally, curve t_0 would be picked such that it separates the event at zero-lag from the other events, but a clear separation is usually not present in field data. Cutting into the event at zero-lag results in primary leakage [*Staring et al.*, 2018a]. Alternatively, cutting into the events close to the event at zero-lag results in the exclusion of short-period internal multiples from the predictions. A practical approach is to select t_0 at the zero-offset trace at approximately half the duration of the user-specified wavelet and then pick a moveout according to the data. If there is no primary leakage in the internal multiple predictions, then this curve was correctly chosen. Unfortunately, this approach results in not predicting some short-period internal multiples. For more details on t_0 and t_2, see *van der Neut and Wapenaar* [2016]. Having obtained curve t_0, we contruct the tapered spatio-temporal Heaviside muting function $\Theta_{t_0}^{t_2}$.

All ingredients that are needed to evaluate equation 4.2.1 are now available. The number of iterations N can be chosen based on convergence, which can be tracked by computing the L_2 norm of individual terms of $\hat{v}^+$. When using a correctly scaled Green's function for operator $\mathcal{G}$, this quantity is expected to decrease continuously until at some point it is so small that it is no longer relevant. The required number of iterations to achieve convergence is different for every medium. Since the subsurface of the Arabian Gulf generates a highly complex interference pattern, convergence is of the utmost importance to avoid missing important amplitude and phase updates and thus to ensure the internal multiple predictions match the data. An idea of the convergence rate can be obtained by applying the double dereverberation method to a realistic synthetic dataset. The dashed blue line and the solid green line in figure 4.12 show the convergence rate based on synthetic tests in a model created from a well-log. The actual convergence rate of our method when applied to the field data, depicted in dotted red, closely resembles the convergence rate of the synthetic data. This provides confidence in the result of the field data application. Note the slow convergence rate, especially when comparing it to *Staring et al.* [2018a] who only needed two iterations to predict internal multiples for a target area in deep water Brazil. Other synthetic studies from the Middle East support this slow convergence rate [*Elison et al.*, 2019]. The reason can perhaps be found in the complexity of the internal multiple problem in this setting.

After having retrieved the projected Marchenko focusing function $\hat{v}^+$, equation 4.2.2 is used to obtain upgoing wavefield $\hat{U}^-$. Subsequently, we retrieve internal

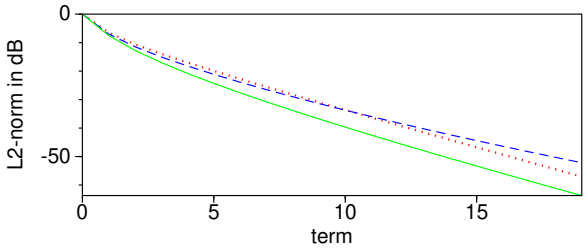

Figure 4.12: *L_2 norm of the individual terms in the series of equation 4.2.1. Convergence curve for acoustic synthetic data in dashed blue, for elastic synthetic data in continuous green and for the Arabian Gulf field data in dotted red.*

multiple predictions $\hat{u}_k^{-+}$ by performing equation 4.2.3 (see figure 4.11d). Instead of distinct events, we observe a complex interference pattern of internal multiples. It matches the pattern in the data closely, such that only a mild adaptive filter α (filter length of 5 samples, windows of 100 samples by 25 traces for the L_2 minimization) was needed to subtract the predictions from the muted reflection response $\hat{u}_0{}^{-+}$. A range of filter lengths led to very similar results, thereby showing the robustness of the method. Figure 4.11c shows the result after adaptive subtraction of the internal multiple predictions. When looking at a common source gather of the predicted internal multiples in figure 4.11d, there are areas where internal multiples constructively interfere with themselves and areas where they destructively interfere, thereby creating a patchy pattern in which it seems as if there are areas with no internal multiples at all. This confirms that we are not dealing with separate events, but with a complex interference pattern created by internal multiples.

When studying the FK spectra in figure 4.13, the effect of the subtraction of the internal multiples is also visble. Most internal multiples seem to have frequencies between 12 Hz and 20 Hz, indicating that this complex overburden may have the property that it mainly generates low frequency internal multiples.

The RTM images in figure 4.14 show the effect of internal multiple prediction and subtraction in the image domain. The white boxes indicate the target area, where a clear difference can be observed. Note that a difference is also visible below the target area. Although this area is likely to have remnant internal multiples generated by the target area or by interactions between the target area and the overburden (figures 4.3b and 4.3c), internal multiples generated by the overburden have been subtracted. Figures 4.15a, 4.15b and 4.15c show a zoom of the target area to study the details. A significant reduction of internal multiples is visible in the yellow circles. Also, conflicting seismic events have been resolved, leading to improved visibility of known horizons (the green circles). In addition, the images now have a better definition of faulty structures (the red circles).

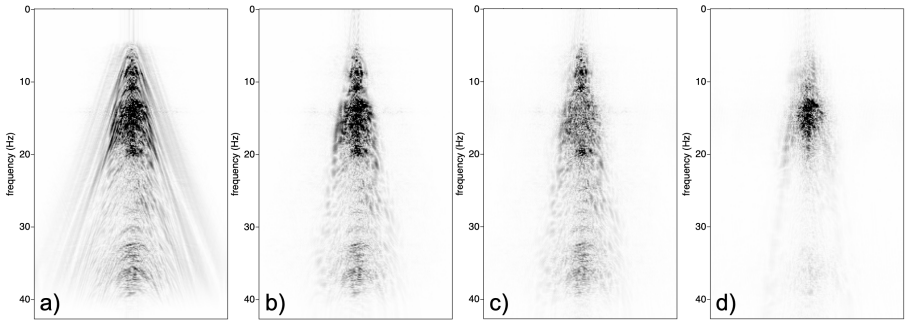

Figure 4.13: *FK spectra of the common source gathers in figure 4.11.*

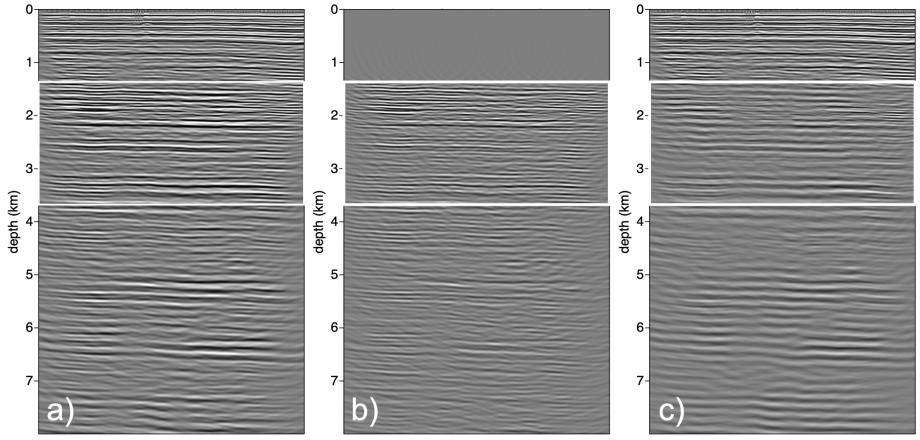

Figure 4.14: *RTM images: a) before internal multiple prediction and subtraction, b) after internal multiple prediction and subtraction, and c) their difference, showing the overburden primaries and the internal multiples that were subtracted.*

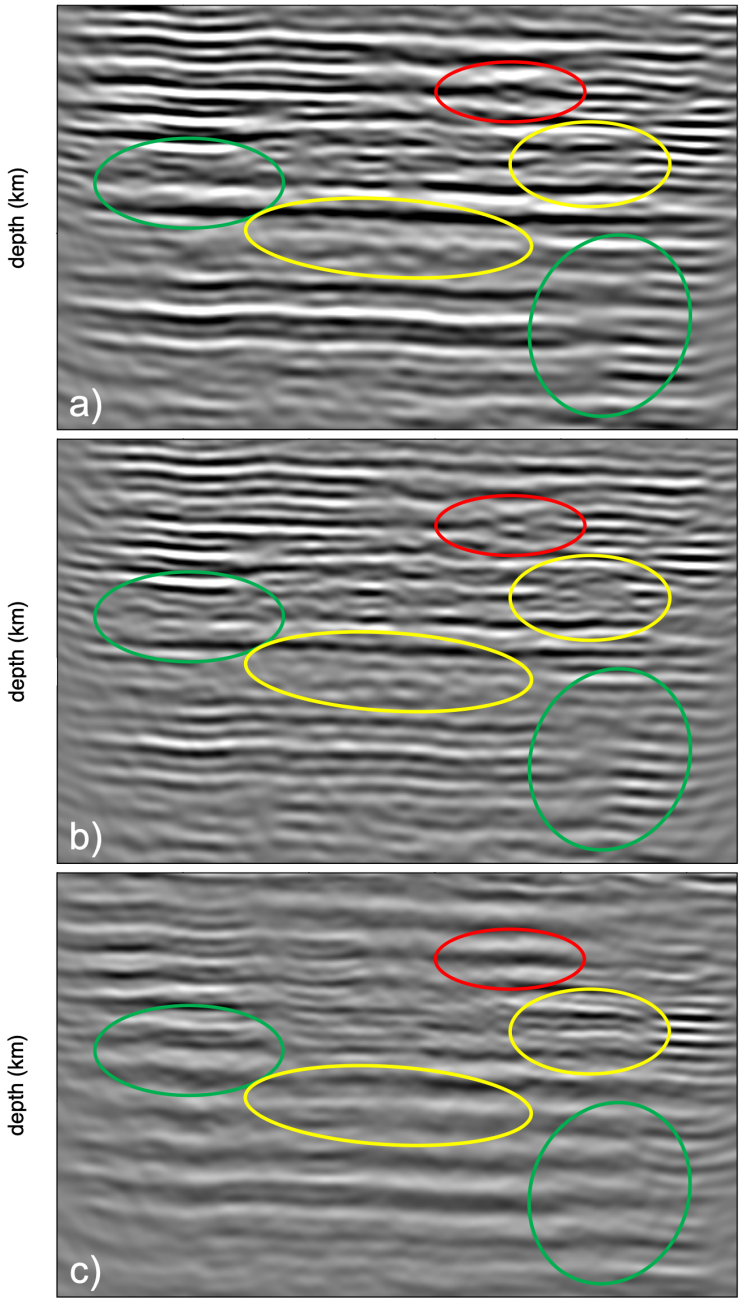

Figure 4.15: *RTM images only showing the target area: a) before internal multiple prediction and subtraction, b) after internal multiple prediction and subtraction, and c) their difference, showing the internal multiples that were subtracted.*

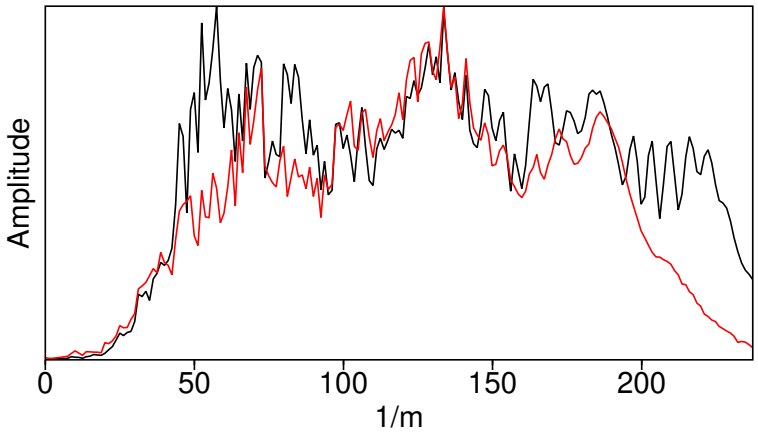

Figure 4.16: *Spectral analysis of vertical wavenumbers for the zoomed area of RTMs of data before and after Marchenko in red and black, respectively.*

When looking at the image of the internal multiples that were subtracted from the target area (figure 4.15c) in more detail, we observe again a complex interference pattern. The pattern looks almost monochromatic and appears to mainly contain low frequencies, as also observed in figure 4.13d. In order to check whether the low frequency narrow-band internal multiple predictions are indeed a property of this particular overburden, we studied the normalized stacked amplitude spectra of the RTM images before and after internal multiple suppression in figure 4.16. The amplitude spectrum of the image in figure 4.15a is in black and the amplitude spectrum of the image in figure 4.15b is in red. These spectra confirm that the removed interference pattern mainly had low frequencies, but that also some higher frequencies were attenuated (that are not so easily observed by visual inspection of the RTM images). This observation is supported by detailed synthetic controlled experiments [*Elison et al.*, 2019].

4.4 Discussion

Although the processing carried out in this chapter was performed to the best of our abilities, there are always details that can be improved. In this section, we go through our workflow in figure 4.1 and provide suggestions for improvement or further research.

In the first phase of the workflow, we performed wavefield decomposition and

continued with the upgoing pressure wavefield only. One could argue that both upgoing and downgoing pressure wavefields could have been used to perform a multidimensional deconvolution [*Wapenaar et al.*, 2000; *Amundsen et al.*, 2001; *Ravasi et al.*, 2016] instead, which would remove ghosts, surface-related multiples and the source signature in a single inversion step. However, this method requires both the up- and the downgoing wavefield and relative hydrophone and geophone amplitude calibration. Additionally, this scheme in a shallow water setting might be more difficult to implement due to limited (or saturated) dynamic range of the receivers by the direct (downgoing) wave. Therefore, we have chosen to only select the upgoing pressure wavefield and use the R-EPSI method to estimate the source wavelet and to remove surface-related multiples in a phase and amplitude preserving manner. Furthermore, only using the upgoing pressure wavefield also makes this workflow suitable for acquisition geometries in which only the upgoing wavefield is measured.

In the second phase of the workflow, we apply the R-EPSI method. The R-EPSI method is data-driven and only needs the reflection response and an indication of the noise floor. We tested a small range of noise floor settings and selected the best. However, a more extensive study that would test the effect of different noise floors in the R-EPSI method on the final result (i.e. after the double dereverberation method in stage 3) would be useful.

In the third phase of the workflow, we apply our proposed Marchenko internal multiple prediction method. In preparation for the application, we picked the traveltime curve t_2 from common source gathers of the reflection response R_0. Figure 4.14b shows that our target boundary is approximately horizontal, but there is currently no consensus on whether it actually needs to be near horizontal. We tested multiple boundaries for estimating t_2 and did not observe any significant differences. Another ambiguity related to the t_2 curve concerns the separation of the picked event. In an environment with many fine layers, for example, in the Arabian Gulf, it is impossible for curve t_2 not to cut into any other events. We anticipated that this could generate strong artefacts in the internal multiple predictions. Fortunately, we observed that sufficient tapering of the muting functions provides a remedy, but more research is needed to properly evaluate the effect of the t_2 curves cutting into other events.

Note that our proposed method is an acoustic Marchenko method, while our data also contains elastic effects. Although ground roll and most other elastic effects were removed during preprocessing, some elastic effects might remain, especially in terms of offset-dependent amplitude. In order to correctly handle these effects, a Marchenko method that includes elastic effects should ideally be applied. Such methods are currently being developed [*Wapenaar*, 2014; *da Costa Filho et al.*, 2014; *Reinicke and Wapenaar*, 2019].

4.5 Conclusion

We presented a workflow for the suppression of surface-related multiples and internal multiples in an environment with a shallow water layer and a complex overburden. The nucleus of this workflow is a double dereverberation method (a novel Marchenko

method) for the prediction and adaptive subtraction of internal multiples. Building on the approach introduced by *van der Neut and Wapenaar* [2016], we introduced a more efficient and straightforward approach to remove internal multiples that contaminate the target area, at the cost of leaving some later arriving internal multiples behind. This method requires, much like other internal multiple suppression methods, that the amplitude and phase of the data remain intact during the processing workflow. If this is correctly done, the predicted internal multiples will have similar amplitude and phase as the internal multiples in the data and, as a consequence, only a mild adaptive filter will be needed for the subtraction. In environments with fine layering, this becomes particularly important, since the risk of damaging the primaries quickly increases with the agressiveness of the adaptive filter. For this reason, we carefully designed a workflow to ensure that amplitude and phase were preserved.

Our designated workflow consists of three stages: preprocessing, surface-related multiple suppression and internal multiple suppression. The first stage preprocesses the data by debubbling, denoising, decomposition and interpolation, while the second stage tackles challenges related to a shallow water environment (deconvolution of the source signature and surface-related multiple suppression) by applying the R-EPSI method. Prior to the third stage, we introduced a simple but effective method for retrieving a missing scaling factor. After retrieval of this scaling factor, we obtained a correctly scaled Green's function that is suitable as input for the internal multiple prediction and subtraction using our proposed Marchenko method.

We applied our workflow to an OBC dataset acquired in the Arabian Gulf. The R-EPSI method simultaneously suppressed surface-related multiples and deconvolved an estimated effective source signature. The double dereverberation method accurately predicted the internal multiples, such that only a mild adaptive filter was needed to correct for unavoidable minor amplitude and phase differences. We observed that the internal multiple predictions consisted of a complex interference pattern of events, rather than individual events, thereby demonstrating the complexity of the internal multiple problem in this geological setting. Also, the predicted complex wavefield mainly contained low frequencies, which appears to be a property of this particular overburden. Based on this case study, we conclude that a key element in the field data application of any Marchenko method is the use of a processing workflow that is carefully designed, accounting for the specifics of the geological setting at hand and with emphasis on amplitude and phase preservation.

5

A different role for adaptive filters in Marchenko methods for the attenuation of internal multiples

Abstract This chapter was written based on discussions on the use of adaptive filtering for the attenuation of internal multiples during the 2019 SEG/KOC workshop on multiples. During the workshop, it became clear that the use of an adaptive filter for the attenuation of internal multiples is often considered to be a necessary evil. In this chapter, we look at modern seismic data processing methods and question whether this is still the case. We start by providing a quick review of advances in seismic processing and reflect on how these can aid us in obtaining more accurate internal multiple predictions. Our method of choice for internal multiple prediction is the Marchenko method, which has undergone many developments in the past years to make it completely data-driven. This method in principle predicts internal multiples with the correct amplitude and phase. However, on field data, this method predicts internal multiples with minor errors in amplitude and phase due to imperfections in the acquisition and the preprocessing of the data. We argue that by carefully constructing a workflow that aims to preserve the amplitude and phase of the data as well as possible, we can eventually obtain internal multiple predictions that are as close to the internal multiples in the data as possible. As such, only a very conservative adaptive filter would be needed for subtraction, thereby considerably reducing the risk of damaging the primary reflections. We demonstrate this on a 2D line of field data recorded in a deep water environment. In addition, we observe that an adaptive filter can be used as a feedback mechanism to improve the seismic processing workflow.

5.1 Introduction

The use of adaptive filters for internal multiple attenuation is not an undisputed topic in geophysics. Opponents argue that the use of such filters can damage the primary reflections, especially when users give an adaptive filter too much freedom (e.g. long filters applied in small windows). In the worst case scenario, the imprudent use of adaptive filters can result in a reflection response that is not representative of the subsurface. On the other hand, proponents argue that a complete attenuation of internal multiples without adaptive filtering is not realistic. The field data used as input for the prediction of internal multiples has minor amplitude and phase errors caused by imperfect acquisition and preprocessing, for example, imperfectly reconstructed near offsets and inaccurate deconvolution of the source signature. As a result, even the most precise internal multiple prediction method might not be able to predict internal multiples that exactly match the internal multiples in the field data. When not using an adaptive filter to correct for the mismatch, it can potentially result in an incorrect image and incorrect interpretation of a target area.

Fortunately, there have been improvements in the accuracy of the prediction of internal multiples. The phenomenon of multiples was first observed in seismic recordings in the late 1940s [*Ellsworth*, 1948; *Hansen and Johnson*, 1948; *Dix*, 1948; *Waterman*, 1948]. Initial ideas on how to remove these observed multiple reflections were proposed in the 1950s and 1960s, such as the predictive deconvolution [*Robinson*, 1957; *Peacock and Treitel*, 1969] and moveout filtering [*Schneider et al.*, 1965]. These methods are only effective when primaries and multiples have a difference in periodicity (for the predictive deconvolution) or when they have a difference in moveout (for the moveout filtering), which is often not the case in practice. In the 1970s and 1980s, wave-equation-based modeling methods [*Loewenthal et al.*, 1974; *Hampson*, 1986; *Wiggins*, 1988], and filtering methods that exploit more pronounced differences between primaries and multiples in alternative domains [*Kennett*, 1979; *Taner*, 1980; *Hampson*, 1987] were proposed. Some of these methods [e.g. *Griffiths et al.*, 1977] already used adaptive filtering to match the inaccurate multiple predictions to the actual multiples in the data. In the 1990s came the first data-driven and wave-equation-based methods for the prediction of internal multiples [*Berkhout and Verschuur*, 1997; *Weglein et al.*, 1997; *Jakubowicz*, 1998]. The feedback method of *Berkhout and Verschuur* [1997] uses the concept that internal multiples are made up of two components, and predict internal multiples by downward extrapolating predicted surface-related multiples to an interface in the subsurface. In contrast, *Weglein et al.* [1997] and *Jakubowicz* [1998] presented methods in which internal multiples are reconstructed using 3 components. These methods can be used to obtain kinematically correct internal multiple predictions without velocity model, but require the identification of multiple generators and strongly rely on adaptive filters to attenuate the actual multiples in field data (often along with the unknown source signature). More developments rapidly followed that predict internal multiples with greater accuracy [e.g. *ten Kroode*, 2002; *Ikelle*, 2006; *Wapenaar et al.*, 2014a]. The paper of *ten Kroode* [2002] modified the work of *Weglein et al.* [1997] by truncating integrals in time instead of depth, thereby creating a method that

is easier to implement. The method proposed by *Ikelle* [2006] no longer requires a velocity model or the identification of individual multiple generators. Recently, we have seen many developments related to Marchenko methods for the attenuation of internal multiples [*Wapenaar et al.*, 2020]. These wave-equation-based methods initially required a smooth velocity model [*Wapenaar et al.*, 2014a], but developed into methods that do not require any model information [*van der Neut and Wapenaar*, 2016; *Zhang and Staring*, 2018]. These new Marchenko methods in principle predict internal multiples with the correct amplitude and phase and thus only need a conservative adaptive filter to account for imperfections in the acquisition and the preprocessing of the data. In this paper, we will use a Marchenko method for the prediction of internal multiples. The increase in accuracy of internal multiple prediction obviates the need for aggressive adaptive filters and thereby lowers the risk of damaging the primary reflections.

In addition, there have been improvements in the preprocessing of the data, thereby making it easier to preserve amplitude and phase during data preparation and provide the desired input data to internal multiple attenuation methods. Three important prerequisites for data-driven internal multiple prediction methods are the reconstruction of missing offsets (in particular the near offsets for streamer data), the removal of surface-related multiples and the deconvolution of the source signature. The reconstruction of missing offsets was originally performed by prediction of dips of events in the data [*Larner et al.*, 1981; *Bardan*, 1987; *Spitz*, 1991], but this is not effective for crossing events. More robust and recent advances include the parabolic Radon transform [*Kabir and Verschuur*, 1995], differential offset continuation [*Fomel*, 2003] and interferometric interpolation [*Wang et al.*, 2009]. Next, surface-related multiples should be removed. Typically, these multiples are removed by surface-related multiple elimination (SRME) [*Berkhout and Verschuur*, 1997]. However, this method suffers in shallow water environments [*Hargreaves*, 2006; *Hung et al.*, 2010; *Barnes et al.*, 2014], in which case a much less reliable predictive deconvolution is typically used to attenuate surface-related multiples [*Hung et al.*, 2010]. Next, the source signature has to be deconvolved, for example, by means of a predictive deconvolution (spiking deconvolution) [*Robinson*, 1957; *Leinbach*, 1995] or as part of the adaptive subtraction of predicted surface-related multiples [*Verschuur et al.*, 1992; *Ikelle et al.*, 1997; *Kelamis and Verschuur*, 2000]. The predictive deconvolution method makes assumptions about the reflectivity of the subsurface and the phase of the wavelet, such that a correct result is not always obtained. Fortunately, a recent advancement in seismic processing can tackle all 3 requirements robustly and simultaneously: the (Robust) Estimation of Primaries by Sparse Inversion (R-EPSI or EPSI) solves a large scale inversion problem for the primaries, the source signature and the missing offsets [*Van Groenestijn and Verschuur*, 2009a; *Lin and Herrmann*, 2013]. It removes all orders of surface-related multiples and deconvolves an estimated source signature from the input data, without the need for adaptive subtraction. This method also performs well in geological settings in which wavelet estimation and surface-related multiple suppression typically fail, for example in very shallow water environments [*Van Groenestijn and Verschuur*, 2009b; *Belonosov and van Borselen*, 2017]. Using such a method to preprocess the field

data results in an input reflection response for internal multiple attenuation that has as little imperfections as possible, which in turn might result in more accurate internal multiple predictions.

Also, the adaptive filters themselves have improved. Initial shaping filters for the suppression of multiples were constructed using the L_2 norm [e.g. *Verschuur et al.*, 1992; *Jakubowicz*, 1998]. The use of the L_2 norm comes with the assumption that the signal after adaptive filtering has minimal energy and is orthogonal to the noise (the internal multiples), which does not always hold. *Guitton and Verschuur* [2004] have shown that these filters can even introduce spurious events when the internal multiple predictions are weak compared to the primary reflections. Therefore, alternative approaches that do not make these assumptions, such as pattern-based filtering [*Spitz*, 1999] and the use of a hybrid L_1/L_2 norm [*Guitton and Verschuur*, 2004] were introduced. In addition, *Fomel* [2009] proposed the use of non-stationary adaptive filters, thereby capturing the non-stationary character of the seismic signal without needing to split the data into windows. Another approach is the use of a transform to subtract the predicted internal multiples in an alternative domain, for example, a combination of the Radon transform and the orthogonal polynomial transform which better preserves the AVO information of the primary reflections [*Xue et al.*, 2016]. Also, adaptive subtraction can be performed in the curvelet domain [*Herrmann et al.*, 2008; *Wu and Hung*, 2015], such that events can be separated in terms of time, space an dip. These developments have resulted in adaptive filters that are more capable of preserving the primary reflections while subtracting the predicted internal multiples.

In this chapter, we will use a field dataset to show how the use of more accurate preprocessing, more accurate internal multiple prediction and more accurate adaptive filters have altered the role of adaptive subtraction for the attenuation of internal multiples. We start by briefly introducing the theory behind the internal multiple prediction method that we will be using: the adaptive Marchenko multiple elimination (MME) method. Next, we compare the performance of two methods for the suppression of surface-related multiples: the conventionally used SRME method and the state-of-the-art EPSI method. This evaluation will show us the importance of designing a preprocessing workflow based on the dataset and the geological setting in which it was recorded. Subsequently, we apply our adaptive MME method to the field data and obtain internal multiple predictions. We evaluate the use of different adaptive filters (using the L_2 norm and a hybrid L_1/L_2 norm). Finally, we show that only a conservative adaptive filter is required to correct for minor amplitude and phase differences in the internal multiple predictions, thereby improving the internal multiple attenuation on field data. Based on these results, we argue that it is no longer a choice of using an aggressive adaptive filter or not using an adaptive filter, but rather on how adaptive filters can provide support in straightening out the final details.

5.2 Theory: an adaptive Marchenko multiple elimination method

The starting point of the Marchenko method is the preprocessed reflection response R acquired by dipole sources and monopole receivers and without evanescent waves, noise, receiver ghost, suface-related multiples and deconvolved from its source signature. Note that the Marchenko method requires a preprocessing workflow that preserves the amplitude and phase of the data as well as possible. Next, either the coupled Marchenko equations as introduced by *Wapenaar et al.* [2013] or the projected coupled Marchenko equations as introduced by *van der Neut and Wapenaar* [2016] are solved to retrieve focusing functions, which can in turn be used to retrieve Green's functions between any two points in the subsurface or at the surface. In this paper, we use the projected Marchenko equations for a model independent Marchenko method. The projected downgoing focusing funtion is retrieved using the following operations [*van der Neut and Wapenaar*, 2016]:

$$\hat{v}^{+} = \sum_{i=0}^{M} \hat{v}_i^{+} = \sum_{i=0}^{M} (\Theta_{t_0}^{t_2} \mathcal{R}^{\star} \Theta_{t_0}^{t_2} \mathcal{R})^i \hat{\delta}, \tag{5.2.1}$$

where $\mathcal{R}$ and $\mathcal{R}^{\star}$ are operators that perform a multidimensional convolution and a multidimensional correlation of the reflection response with the wavefield that it acts upon. An user-specified wavelet that represents the band-limitation in the data is represented by the symbol $\hat{\ }$. The symbol i indicates the iteration number in the Marchenko algorithm that ranges from 1 to M. The total number of iterations M that is required until convergence is achieved depends on the dataset. The L_2 norm of the individual updates $\hat{v}_i^{+}$ can be tracked and plotted to monitor the progress of the iterative scheme. In successive iterations, the updates $\hat{v}_i^{+}$ should become smaller until negligible. If time permits, it is useful to first test a Marchenko method on realistic synthetic data that closely resembles the field data to obtain an estimate of the convergence and the number of iterations M that is required. Symbol $\hat{\delta}$ represents a band-limited spatio-temporal delta function. A tapered Heaviside muting function $\Theta_{t_0}^{t_2}$ is applied in the time domain and is constructed based on the finite temporal and spatial frequency content of the data (t_0) and based on the two-way traveltime curve t_2 that separates the overburden response from the target area response (see *van der Neut and Wapenaar* [2016] and chapter 4). Having retrieved the projected downgoing focusing function, we can also obtain the projected upgoing Green's function $\hat{U}^{-}$:

$$\hat{U}^{-} = \sum_{j=0}^{N} \hat{U}_j^{-} = \Theta_{t_2}^{\infty} \mathcal{R} \sum_{j=0}^{N} \hat{v}_j^{+}. \tag{5.2.2}$$

The Heaviside muting function $\Theta_{t_2}^{\infty}$ is based on the two-way traveltime curve t_2 and infinity ∞, which in practice is the maximum time in our recording. The retrieved wavefield $\hat{U}^{-}$ has sources and receivers at the acquisition surface and is without receiver-side internal multiples with a final reflection point in the overburden. More internal multiples can be removed by performing a multidimensional deconvolution of this wavefield with the projected downgoing Green's function $\hat{U}^{+}$

[*van der Neut and Wapenaar*, 2016] or by using a double dereverberation method [*Staring et al.*, 2020].

When introducing wavefield $\hat{U}^-$, *van der Neut and Wapenaar* [2016] noted connections with other internal multiple attenuation methods, for example, the inverse scattering series [*Weglein et al.*, 1997], work by *ten Kroode* [2002], the method of Jakubowicz [*Jakubowicz*, 1998] and source-receiver interferometry [*Löer et al.*, 2016]. Based on the strong connection of the Marchenko wavefield $\hat{U}^-$ with the work of *ten Kroode* [2002] and *Löer et al.* [2016], *van der Neut and Wapenaar* [2016] could retrieve a method that attenuates all orders of internal multiples for a particular two-way traveltime t_2:

$$\hat{R}_t = \mathcal{R}\hat{v}^+ = \mathcal{R}\hat{\delta} - \alpha(x,t)\sum_{k=1}^{P} -\mathcal{R}(\theta_{t_0}^{t_2}\mathcal{R}^\star\theta_{t_0}^{t_2}\mathcal{R})^k\hat{\delta}. \tag{5.2.3}$$

By evaluating equation 5.2.3 for each timestep $t_2 = t - t_0$ (t_0 depends on the band-limitation in the data [*Slob et al.*, 2014; *Staring et al.*, 2018a]) and only saving the sample at timestep t, we obtain a new reflection response $\hat{R}_t$ that contains only primaries. We call this method the Marchenko multiple elimination method [*Zhang and Staring*, 2018]. This method is not a layer-stripping approach, since we can apply it to any timestep without needing to resolve overlying layers first. Note that equation 5.2.3 is equal to equation 5.2.2 apart from the application of a final muting function (which does not change the result at time t). While *van der Neut and Wapenaar* [2016] assumed that the application of muting function $\theta_{t_0}^{t_2}$ required the construction of two-way traveltime curves for each timestep, *Zhang and Staring* [2018] have shown that the truncations at t_0 and t_2 can simply be constant in equation 5.2.3. As such, this method is completely data-driven and model independent. Naturally, evaluating this series for every timestep is computationally expensive, but *Zhang and Slob* [2020a] introduced a method that can speed up this process considerably.

In principle, and on ideal synthetic data, this method predicts all orders of internal multiples with the correct amplitude and phase. However, this is not the case in practice. An imperfect acquisition and imperfect preprocessing (for example, an inaccurate deconvolution of the source signature) cause minor amplitude and/or phase errors in the input reflection response for the Marchenko method, such that the internal multiple predictions (obtained after convolving and correlating the data with itself multiple times) do not entirely match the internal multiples in the data. Therefore, we will use adaptive filter α for the subtraction of the sum of the internal multiple predictions from the data. The individual terms of the series are summed without adaptive filter, thereby making it very important that the scaling of the reflection response R is correct. Chapter 4 of this thesis presents a simple method that can be used to obtain the correct scaling factor of the reflection response R.

5.3 Surface-related multiple suppression

We use a 2D line of streamer data acquired by Equinor in a deep water area of the Norwegian Sea. We obtained the dataset after 3D to 2D amplitude conversion, the

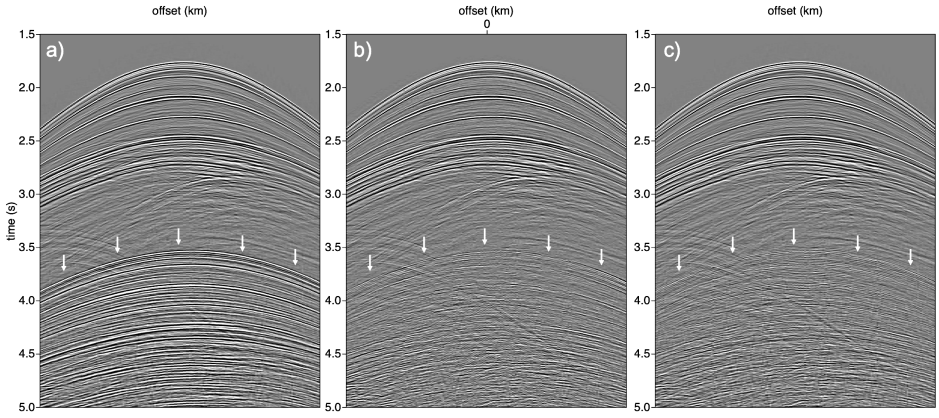

Figure 5.1: *Common source gather of the reflection response a) after interpolation, b) after applying the SRME method and c) after applying the EPSI method. The white arrows indicate that differences are mainly visible after 3.5 s.*

reconstruction of near offsets (according to *Kabir and Verschuur* [1995]) and the regularization of both source and receiver spacing to 25 m in a split-spread geometry. In addition, two surface-related multiple suppression methods (the conventionally used SRME method [*Berkhout and Verschuur*, 1997] and the state-of-the-art EPSI method [*Van Groenestijn and Verschuur*, 2009a]) were applied to a subsection of this dataset to evaluate their performance. *Van Groenestijn and Verschuur* [2009b] have shown that the EPSI method provides similar results to the SRME method when near offsets can be accurately reconstructed and primary reflections and surface-related multiples are well-separated (for example, in deep water environments). However, the EPSI method provides superior results when near offsets cannot be reliably reconstructed and primaries and surface-related multiples are not well-separated (for example, in shallow water environments, as shown in *Baardman et al.* [2010]). Therefore, we expect the SRME method and the EPSI method to give similar results when applied to our dataset recorded in a deep water environment.

And indeed, figures 5.1, 5.2, 5.3 and 5.4 show that both the SRME method and the EPSI method have a very similar performance on this dataset. Figure 5.1 shows that the surface-related multiples mainly contaminate the later part (after 3.5 s) of the reflection response. When zooming in on the area after 3.5 s, figure 5.2 shows the surface-related multiples that were subtracted by both methods. The multiples seem very similar, although minor differences in terms of amplitude and high-frequency events are visible. When studying the FK spectra in figure 5.3, it becomes clear that some of these differences can be attributed to the EPSI multiples containing higher frequencies (up to 70 Hz) compared to the SRME multiples (up to 50 Hz). Also, the EPSI result seems to contain more spatial aliasing, possibly due to a subsampled Fresnel zone.

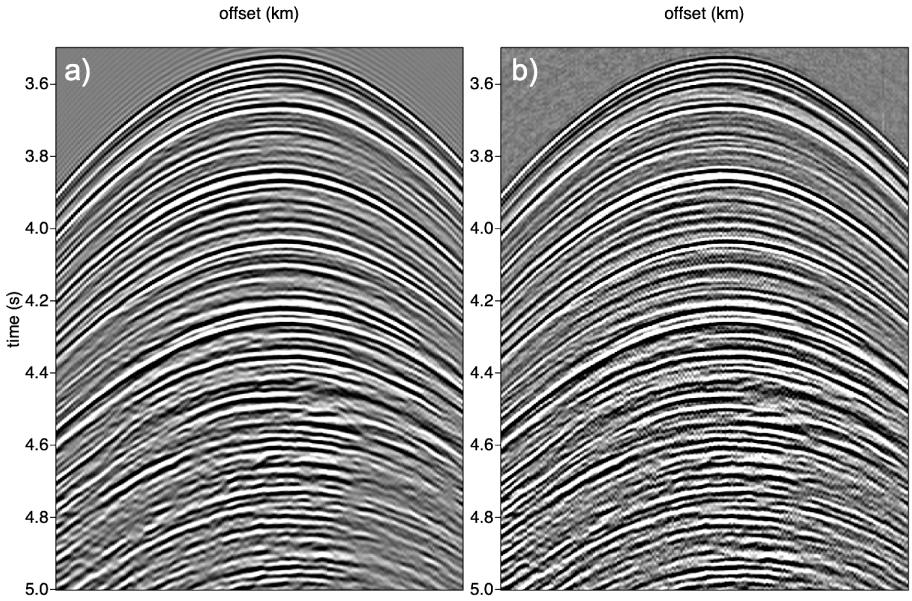

Figure 5.2: *Common source gathers of the subtracted surface-related multiples a) using the SRME method, b) using the EPSI method. The subtracted multiples are very similar.*

We obtain figure 5.4 when migrating the data using a one-way wave equation migration. These images show no difference between the result of the SRME method and the EPSI method. Since the SRME method is considerably cheaper compared to the EPSI method, we decided to continue by applying the SRME method to the full dataset. This example shows that we need to be critical of our data and of the methods that we apply to it. We can play safe and apply the more expensive state-of-the-art method to any dataset at additional computational cost, but this is not always necessary.

5.4 Internal multiple attenuation using the adaptive MME method

After applying the SRME method to the entire dataset and deconvolving the source signature, we apply the adaptive Marchenko multiple elimination method to predict internal multiples. *Zhang and Slob* [2020b] have already applied the MME method without adaptive subtraction to this dataset and obtained promising results. Figure 5.5 shows common source gathers of the data after applying the SRME method, the data after applying 6 iterations ($P = 6$ in equation 5.2.3) of the MME method without adaptive filter (the same as in *Zhang and Slob* [2020b]) and the internal multiple predictions. The white arrows show events that were somehwat attenuated, but not entirely. The FK spectra in figure 5.6a and 5.6b show that attenuation of internal

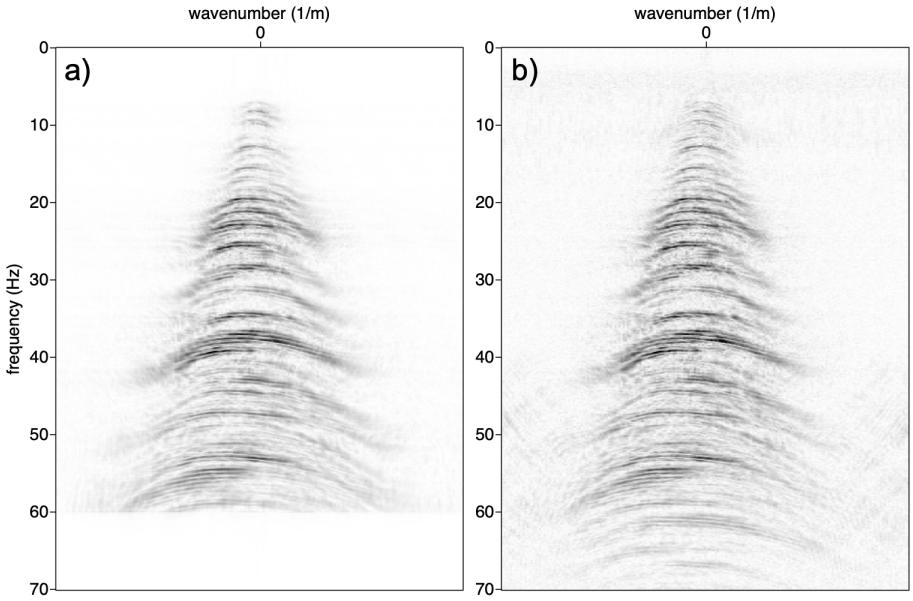

Figure 5.3: *FK spectra of the subtracted surface-related multiples in figure 5.2 by using a) the SRME method and b) the EPSI method.*

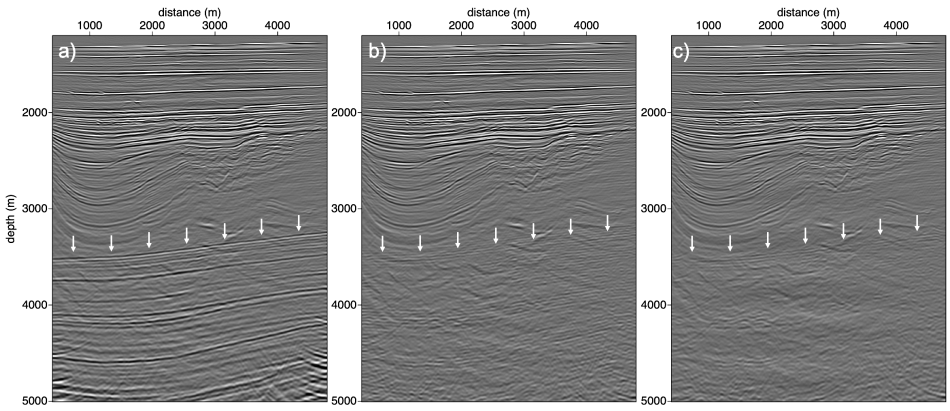

Figure 5.4: *Images of the reflection response a) after interpolation, b) after applying the SRME method and c) after applying the EPSI method. The white arrows indicate the start of the area in which differences are visible.*

multiples only very slightly alters the spectrum of the reflection response. Figure

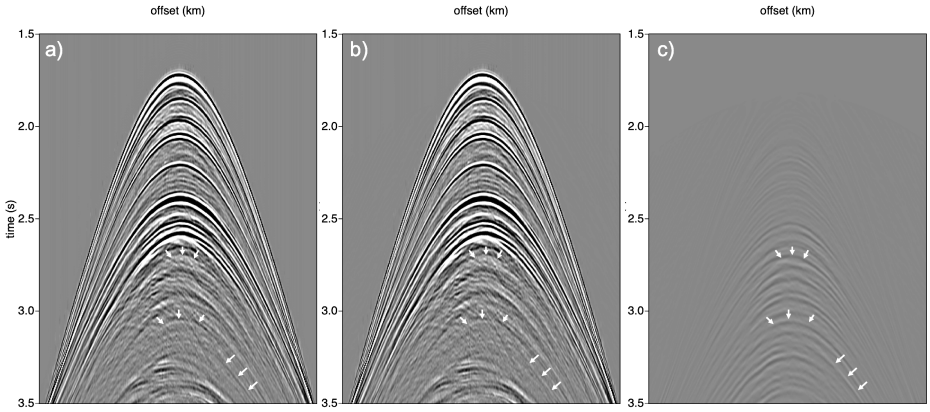

Figure 5.5: *Common source gather of the reflection response a) after applying the SRME method, b) after applying the non-adaptive MME method and c) the predicted internal multiples. The white arrows indicate differences due to internal multiple attenuation.*

5.6c shows that the predicted internal multiples constructively and destructively interfere with one another in some frequency bands. Next, figure 5.7 shows the corresponding images after one-way wave equation migration. Numbers 1 and 4 show arrows that indicate the (incomplete) attenuation of what we expect to be internal multiples. Numbers 2, 3 and 5 have ellipses and an arrow to indicate the better visibility of primary reflections after internal multiple attenuation. However, the attenuation of the internal multiples seems incomplete, since remnants of internal multiples seem to be present. These remnants are unavoidable, since the Marchenko multiple elimination method was given imperfect data (regarding acquisition, near offset reconstruction, regularization and interpolation, surface-related multiple elimination and source signature deconvolution) and thus predicted imperfect internal multiples. We will show how the use of a conservative adaptive filter can improve this result.

Next, there is the choice for a type of adaptive filter. Do we want to simply apply it in the space-time domain? Or in an alternative domain, such as the curvelet domain? And do we use L_2 or L_1 norm minimization? Application in the curvelet domain seems to be mainly useful when primary reflections and internal multiples have a distinct difference in dip (see *Staring et al.* [2018a]), but this does not seem to be the case here. Therefore, we have chosen for an adaptive filter in the space-time domain. The L_1 norm is known to perform better compared to the L_2 norm when the internal multiples are much weaker compared to the primary reflections [*Guitton and Verschuur*, 2004]. Also, the L_1 norm is more robust to amplitude anomalies and outliers. Since the predicted multiples in figure 5.5c seem very weak, we expect the L_1 to perform better, but we test the application of both the L_2 and L_1 norm. We use a modified verion of the hybrid L_1/L_2 norm as introduced in *Guitton and*

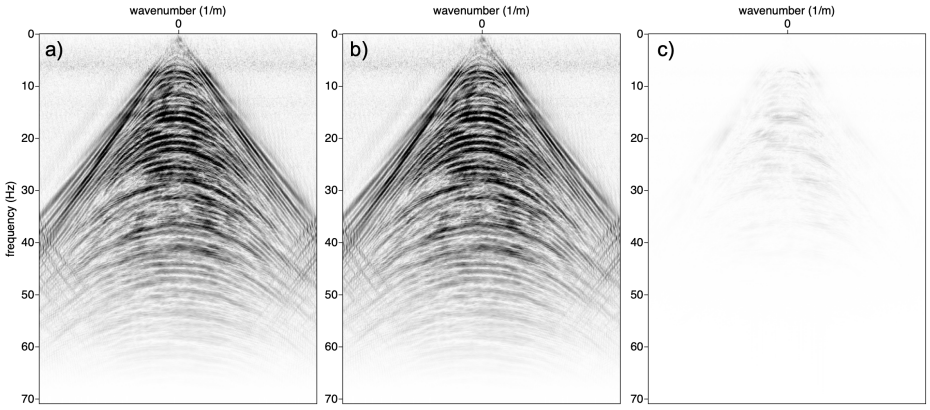

Figure 5.6: *FK spectra of the reflection response a) after applying the SRME method, b) after applying the non-adaptive MME method and c) the predicted internal multiples.*

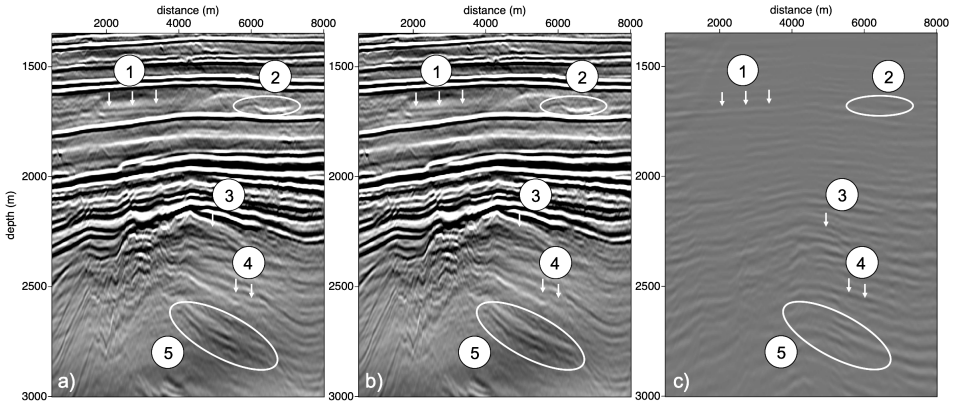

Figure 5.7: *Images of the reflection response a) after applying the SRME method, b) after applying the non-adaptive MME method and c) the predicted internal multiples. The white arrows and ellipses indicate some interesting differences.*

Verschuur [2004] to treat large residuals with the L_1 norm and small residuals with the L_2 norm. In addition, the L_1 norm is not continuous and differentiable in all places, in contrast to the hybrid L_1/L_2 norm.

Figure 5.8 shows the predicted internal multiples using the Marchenko multiple elimination method, the adjusted multiples after application of a filter using the L_2 norm and the adjusted multiples after application of a filter using the hybrid L_1/L_2 norm. The adaptive filter using the L_2 norm seems to find events where there are none (as indicated by the white arrows of figure 5.8b), while the adaptive

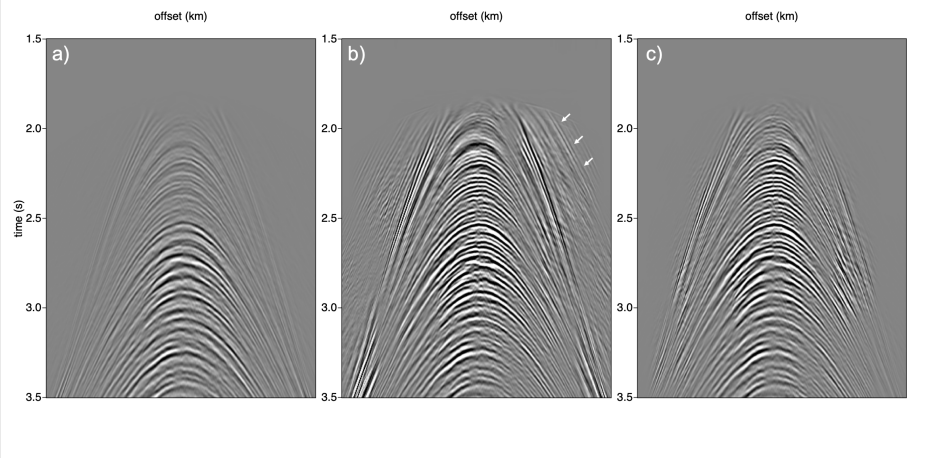

Figure 5.8: *Common source gather of the predicted internal multiples a) before applying an adaptive filter, b) after applying an adaptive filter using the L_2 norm and c) after applying an adaptive filter using the L_1 norm.*

filter using the hybrid L_1/L_2 norm stays close to the original predictions. The FK spectra in figure 5.9 confirm this, and show that the filter using the L_2 norm puts more emphasis on the diagonal lines that originate at $k = 0$. The high angles have a high amplitude in the shot record and significantly contribute to the minimization of the L_2 norm. The same events are very weak in the predicted multiples. Based on these tests, we decide to chose for the adaptive filter using the hybrid L_1/L_2 norm.

We test a range of filter settings and window sizes and finally select the filter that is capable of attenuating most internal multiples without damaging the primary reflections. A filter can be applied globally, such that the window size encompasses the entire shot, or locally, such that the non-stationary character of the data can be captured by smaller windows. A commonly used approach is to first apply a global adaptation to precondition the data, after which more localized filters (with overlap to ensure a smooth transition) are used to subtract the preconditioned predictions from the data. The filter length defines how much the predictions are allowed to shift within their window. A filter length of 3 means that the predictions can shift by 1 sample each way, while a filter length of 5 means that the predictions have the freedom to have a maximum shift of 2 samples each way. We use a filter length of 3, such that the data can be shifted one sample up or one sample down within its window to correct for minor phase differences. Our window size is 200 timesamples (0.8 s) by 50 space samples (1250 m). We consider this to be a conservative adaptive filter, since we have large windows in which we do not allow the internal multiple predictions to shift much. The filter mainly adjusts the amplitudes of the predicted internal multiples, as can be seen in figure 5.8c. This indicates that the scaling of the input data might not have been optimal. We can use this observation as a

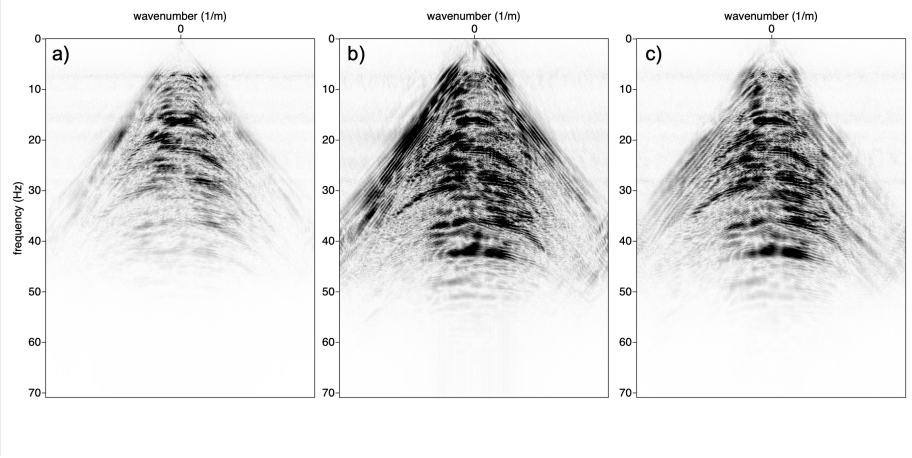

Figure 5.9: *FK spectra of the predicted internal multiples a) before applying an adaptive filter, b) after applying an adaptive filter using the L_2 norm and c) after applying an adaptive filter using the L_1 norm.*

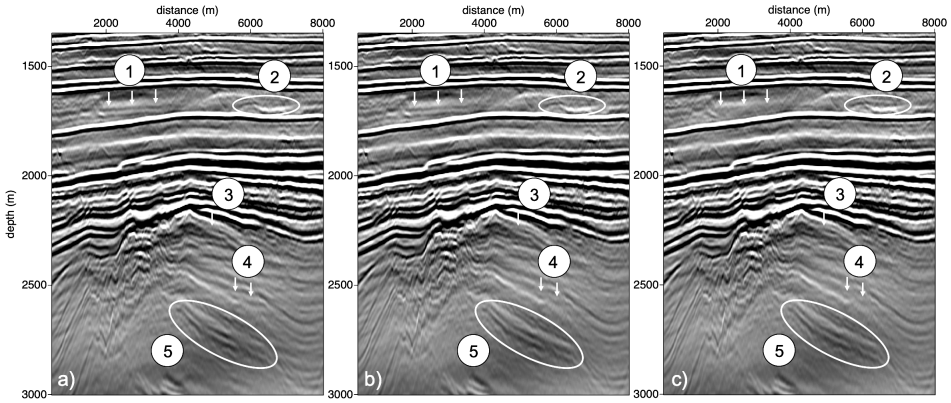

Figure 5.10: *Images of the reflection response a) after applying the SRME method, b) after applying the non-adaptive MME method and c) after applying the adaptive MME method. The white arrows and ellipses indicate some interesting differences.*

feedback mechanism to improve our processing workflow. Perhaps the amplitude and phase of the data can be better preserved throughout the workflow, or perhaps the scaling of the data prior to application of the MME method simply needs to be adjusted. Note that we did not use any preconditioning.

Finally, we migrate the result and compare it to the non-adaptive result. Figure 5.10a and 5.10b are repetitions of figures 5.7a and 5.7b, while figure 5.10c shows

the image of the result using the adaptive filter. The adaptive result shows a more complete attenuation of internal multiples at numbers 1 and 4 compared to the non-adaptive result. In addition, numbers 2, 3 and 5 indicate how primary reflections are becoming better visible after the more complete subtraction of the multiple reflections. Notice that an improvement is obtained without using aggressive adaptive filters. This illustrates that it is no longer a debate on whether to use an aggressive adaptive filter or not to use an adaptive filter, but that modern processing methods allow us to use a conservative adaptive filter to straighten out the last details that could not be accounted for during oreprocessing.

5.5 Conclusion and discussion

The aim of this chapter was to add to the debate on the use of adaptive filters for the attenuation of internal multiples. We discussed recent advances in seismic processing that (sometimes indirectly) improve the accuracy with which internal multiples are predicted. Instead of either using an aggressive adaptive filter or using no adaptive filter at all, these advances allow us to use a conservative adaptive filter to straighten out the last details. In addition, we argued that a conservative adaptive filter can be used as a feedback mechanism to improve the preprocessing of the data and thereby provide more suitable input for internal multiple attenuation.

To substantiate these arguments, we applied a workflow for surface-related multiple attenuation and internal multiple attenuation to a 2D line of field data acquired in a deep water environment. We tested two methods to remove surface-related multiples: the conventionally used SRME method and the more recently developed and robust EPSI method. These methods provided almost the exact same result on our dataset, thereby showing that an awareness of which method to use (or which method is not necessary to use) in which situation is very important. We decided to continue with the SRME method, since it provided very similar results at less computational cost compared to the EPSI method. Next, we applied the Marchenko multiple elimination method to the data without surface-related multiples. The non-adaptive MME method attenuated what we believe to be internal multiples. However, remnants seemed to be present. The adaptive MME method removed these remnants with the use of a conservative adaptive filter. We tested adaptive filters with L_2 and a hybrid L_1/L_2 norm minimization and concluded that the filter with the hybrid L_1/L_2 minimization provided superior results. This can be explained by the fact that our data do not meet the assumptions of the L_2 norm minimization, namely that primaries and multiples have an equally strong amplitude distribution and are orthogonal. Using a simple and conservative adaptive filter in space-time with a hybrid L_1/L_2 norm minimization has helped us to correct for minor amplitude and phase differences in the internal multiple predictions that were unavoidable due to imperfect acquisition and processing. In addition, the adjusted internal multiple predictions indicated that the amplitude and phase preservation throughout the workflow can be improved. Based on the evaluation of these results, we conclude that the adaptive filter has a new role: it straightens out unavoidable amplitude and/or phase errors in the internal multiple predictions and it can act as

a feedback mechanism to indicate whether the amplitude and phase preservation of the data throughout the workflow has to be improved.

A topic that we did not yet touch upon is the choice of subtraction in the data domain (on shot gathers) or in the image domain (on migrated sections). Unfortunately, the adaptive filter used in this paper was not capable of subtracting the internal multiple predictions in the image domain. However, in our experience [*Staring et al.*, 2018a; *Staring and Wapenaar*, 2020], adaptive subtraction in the image domain is often more robust compared to adaptive subtraction in the data domain, simply because internal multiples tend to have a better separation from primary reflections in that domain.

Another important topic to discuss are the limitations of the Marchenko method. We state that the Marchenko method in principle predicts internal multiples with the correct amplitude and phase, but that it predicts internal multiples with minor amplitude and/or phase errors due to imperfections in the acquisition and the preprocessing. Other reasons for imperfections in the Marchenko result are the presence of mode conversions (we used an acoustic implementation here), evanescent waves, the presence of short-period internal multiples (depending on the frequency content of the data) and transmission losses. Also note that we applied the Marchenko method to a 2D line of data while it was acquired in a 3D subsurface, such that out-of-plane effects are not taken into account.

6

Conclusions and recommendations

In this final chapter, I reflect on the results obtained in this thesis and present recommendations for further research. First, I present a quick summary of the work presented in the other chapters and provide a general conclusion. Next, I address each strength and limitation of the Marchenko method individually and provide suggestions for further research. Lastly, I discuss a series of practical considerations.

6.1 Introduction

The aim of the research described in this thesis is to enable the application of the Marchenko method on field data. Prior to starting this PhD project in 2015, the Marchenko method had only been tested on ideal synthetic data and it was uncertain whether the method would be applicable to field data. Therefore, I further developed the Marchenko method to make it suitable for the field data application in different geological settings.

I started with the development of the adaptive double-focusing method. This Marchenko method is less sensitive to imperfections in the data and the acquisition geometry than the conventional Marchenko method. Next, I tested the performance of both the conventional Marchenko method and the adaptive double-focusing method on 2D synthetic data and a 2D line of field data recorded in the Santos Basin, Brazil. I observed that the adaptive double-focusing method is indeed more robust than the conventional Marchenko method and could predict and subtract internal multiples generated in the complex overburden. Next, I used 3D synthetic data to learn which acquisition parameters have an effect on the result of the adaptive double-focusing method. I found that the limited aperture in the crossline direction and the coarse sail line spacing in narrow azimuth data have a significant effect on the result of the adaptive double-focusing method. Based on this evaluation, I interpolated the sail line spacing of the 3D narrow azimuth streamer dataset prior to applying the adaptive double-focusing method. I observed that this method could predict and subtract internal multiples from the interpolated dataset,

thereby improving the geological interpretation of the target area.

Next, I developed a Marchenko method that does not require redatuming and that is model independent: the double dereverberation method. Instead of using data recorded in a deep water environment, I now used a dataset acquired in a very shallow water environment. I showed that the processing challenges related to a shallow water environment (the removal of surface-related multiples and the estimation of the source signature) can be overcome using the state-of-the-art R-EPSI method and that internal multiples can be attenuated using the double dereverberation method.

Lastly, I investigated the role of the adaptive filter in the application of Marchenko methods on field data. I used a data-driven and model-independent Marchenko multiple elimination method to show that only a conservative adaptive filter is needed to subtract the internal multiple predictions.

Based on the results in this thesis, I conclude that, in general, the Marchenko method is an effective, data-driven and robust method for the attenuation of internal multiples in marine seismic data, provided that 1) the acquisition geometry is sufficiently dense and 2) a careful processing workflow is constructed that accounts for the specifics of the geological setting at hand, with significant emphasis on amplitude and phase preservation. Ideally, VSP data are available to check the quality of the result after internal multiple prediction and subtraction.

In the following, I discuss the strengths and limitations of the Marcenko method in more detail.

6.2 A strength: the versatility of the Marchenko method

A strength of the Marcheno method is its versatility. There is a range of Marchenko methods that are suitable for different purposes. I studied four Marchenko methods in this thesis: the conventional Marchenko method (chapter 2), the adaptive double-focusing method (chapters 2 and 3), the double dereverberation method (chapter 4) and the Marchenko multiple elimination method (chapter 5). In addition, there are many more Marchenko methods for internal multiple attenuation that were not discussed in this thesis, for example, the Transmission-compensated Marchenko multiple elimination [*Zhang et al.*, 2019], Rayleigh-Marchenko redatuming [*Ravasi*, 2017] and virtual plane wave imaging [*Meles et al.*, 2018]. Each method aims to tackle a slightly different problem. When aiming to attenuate internal multiples generated in an overburden and simultaneously redatum (for example, to reduce the data volume for a target-oriented FWI), the adaptive double-focusing method is most suitable. When aiming to attenuate internal multiples generated in an overburden without redatuming or when aiming to attenuate internal multiples without needing a velocity model as input, the adaptive double dereverberation method is most suitable. When not minding computational cost and aiming to attenuate internal multiples for all multiple generators in the subsurface without velocity model, the adaptive Marchenko multiple elimination method is most suitable. It appears that there is a Marchenko method for every internal multiple problem, and the development of new methods or modifications of existing methods is currently work

in progress. In addition, there are other applications of the Marchenko method beyond internal multiple attenuation, such as target replacement for monitoring (see appendix A), homogeneous Green's function retrieval [*Wapenaar et al.*, 2016b] and virtual seismology [*Brackenhoff et al.*, 2019]. This demonstrates the versatility and wide applicability of the Marchenko method.

6.3 A strength: the accuracy of internal multiple prediction

The most important strength of the Marchenko method is the accurate prediction of internal multiples. In principle, and on ideal synthetic data, the wave-equation-based and data-driven Marchenko method predicts internal multiples with the correct amplitude and phase. Moreover, the Marchenko method does not require the identification of individual multiple generators and is not a layer stripping approach, such that it does not suffer from error propagation from shallow to deep layers. Instead, the Marchenko method considers the entire overburden at once. It only requires the construction of a single time windowing function which is retained throughout the prediction process. The combination of these factors results in a robustness and prediction accuracy that is not always found in internal multiple prediction methods. Naturally, the Marchenko method cannot predict internal multiples that perfectly match the internal multiples in field data, mainly due to imperfect acquisition, imperfect preprocessing and assumptions made by the Marchenko method itself (for example, the acoustic approximation). Despite these imperfections, the Marchenko method is capable of predicting internal multiples with only minor amplitude and phase errors on field data, as demonstrated in this thesis. Particularly, chapter 5 demonstrates that only a conservative adaptive filter is needed to subtract the predicted internal multiples from field data. Ideally, we would like to be able to perfectly predict internal multiples on field data and not need an adaptive filter at all, but the Marchenko method allows us to get close. As the Marchenko method is further developed to include more propagation effects (for example, mode conversions) in combination with developments in dense acquisition (for example, fiber optic technology) and developments in seismic processing (for example, related to machine learning), we might be able to get even closer.

6.4 A limitation or perhaps a strength: the data requirements of the Marchenko method

The data requirements of the Marchenko method are often described as stringent. These requirements concern the acquisition and the preprocessing of the seismic data. In terms of acquisition, the Marchenko method requires a reflection response acquired by a sufficiently dense grid of co-located sources and receivers as input. But what is sufficiently dense? Chapter 3 shows a series of decimation tests on 3D synthetic data for the evaluation of the key acquisition parameters that affect the result of the Marchenko method when applied to narrow azimuth streamer data in a deep water environment. In this particular situation, the limited aperture in the crossline direction and the coarse sail line spacing had the strongest effect.

The aperture in the crossline direction was limited but sufficient, and the sail line spacing was interpolated to become sufficient. However, this might be different in other geological settings. Interpolation can correct for missing offsets, missing shots and a coarse spacing, but only up to a certain level. Interpolation cannot correct for the crossline aperture and the inline far offsets. Therefore, there may be some combinations of geological setting and sparse acquisition geometry that might prove too challenging for the Marchenko method. I remark that the geological setting (for example, target depth, water depth) is usually considered in the acquisition design. If an image of the target area can be constructed, we can predict internal multiples and subtract them from this image using a Marchenko method.

In addition, the Marchenko method requires input data that have been preprocessed. Noise, surface waves, the receiver ghost and surface-related multiples need to be removed. In addition, the data have to be deconvolved for the source wavelet and missing offsets and missing shots have to be reconstructed. These requirements might seem strict, but are again similar to many routinely used convolution-and-correlation-based internal multiple prediction methods, for example, the method presented by *Jakubowicz* [1998]. Consequently, when another convolution-and-correlation-based internal multiple prediction method has already been applied to a dataset, the Marchenko method can also be applied.

We remark that the data requirements of the Marchenko method can also be seen as an opportunity. This amplitude sensitive method can predict accurate internal multiples and requires correctly preprocessed input data. This forces us to put sufficient care into the design and execution of the workflow. Of course, we could decide not to deconvolve the source signature prior to the application of a Marchenko method and obtain inaccurate internal multiple predictions that need to be subtracted using an aggressive adaptive filter, thereby resulting in significant damage of the primary reflections. But this is not what we have set out to achieve. When carefully selecting and using the seismic processing methods that are available, the Marchenko method has the potential to predict accurate internal multiples on field data.

Also, note that there are Marchenko methods that aim to solve the coupled Marchenko equations as a direct inversion. Some of these methods, for example, Rayleigh-Marchenko redatuming [*Ravasi*, 2017], also include the unknown source signature and surface-related multiples into this inversion. However, an analysis by *Dukalski and de Vos* [2017] suggests that these methods do not always converge. If the convergence issue can be addressed, this line of research can have potential. Perhaps the Robust Estimation of Primaries by Sparse Inversion (R-EPSI) method that is capable of simultaneously reconstructing missing offsets, attenuating surface-related multiples and obtaining an estimate of the source signature can be used as a starting point, or can be extended to also include internal multiples.

Another recommendation for further research is to evaluate the effect of incorrect input data on the result of internal multiple attenuation using the Marchenko method. What is the effect of the presence of noise? What is the effect of remnant surface-related multiples? What is the effect of incorrect regularization? How crucial is the correct deconvolution of the source signature? And what is the effect of

poorly reconstructing the missing offsets?

6.5 A limitation: the acoustic approximation

The Marchenko methods developed in this thesis are acoustic and do not take mode conversions into account. *Reinicke et al.* [2019] have shown that the acoustic approximation is valid for structural imaging of 1.5D media, but more research is needed to evaluate the limits of validity of the acoustic approximation for structural imaging in 2D and 3D media. The E&P industry is moving towards fully elastic processing and it could potentially benefit the accuracy of the internal multiple predictions if the Marchenko method would be able to join this trend.

6.6 A limitation: the reflection response should only contain reflection events

Another limitation is that the Marchenko method assumes that all events in the reflection response are reflection events. For example, it does not incorporate refracted waves and scattered waves related to point scatterers [*Zhang et al.*, 2019]. Moreover, spurious events can be generated if these effects are not properly accounted for prior to the application of the Marchenko method. Therefore, another suggestion for future research is to study how to correctly incorporate these currently unwanted events into the Marchenko method.

6.7 A limitation: the applicability to land data

This thesis has investigated the application of Marchenko methods on marine data, but not on land data. This is partially due to a limitation of the Marchenko method itself, because it currently cannot handle the elastic effects that are abundant in land data. Also, this is partially due to a limitation of the acquisition and preprocessing caused by near surface issues, for example, the lower quality of the data, source and receiver coupling and the challenge of applying static corrections [*Keho and Kelamis*, 2012]. A range of issues related to the near surface have to be solved first before we can even consider applying the Marchenko method to land data, whether in an acoustic form or an elastic form.

6.8 A limitation: short-period internal multiples

Currently, the period of the internal multiples that can be predicted is still restricted by the band-limitation in the data. *Zhang et al.* [2019] show that the Marchenko method perceives a layer that is thinner than the data resolution as a single reflector with complicated behaviour. It would be beneficial for thinly layered media, for example, in the Middle East, if we could incorporate short-period internal multiples into the Marchenko method. *Elison et al.* [2019] present an augmented Marchenko method that is also capable of attenuating short-period internal multiples. This

method shows promise when applied to 2D synthetic data, but has not been proven yet to work on field data. It is important that this method and other methods aimed at incorporating short-period internal multiples into the Marchenko method are further developed.

6.9 Practical remarks

Based on the experience of performing the work shown in this thesis, I would like to provide some practical remarks that might be helpful for other researchers or seismic processors that would like to apply a Marchenko method to field data.

First, gather information about the dataset. It is important to know as much as possible about the acquisition and the preprocessing of the data in order to understand what needs to be done to obtain the correct input data for a Marchenko method. For example, if it would not be communicated that a half time-differentiation is missing from the data, the application of a Marchenko method to that dataset will result in inaccurate internal multiple predictions (see figure 4.9). Of course, the quality check introduced in chapter 4 is able to detect such errors, but being aware of missing or additional factors on the data in advance can speed up the process considerably.

Second, it is of utmost importance that the processing workflow is carefully designed to account for the specifics of the geological setting at hand and with emphasis on amplitude and phase preservation. Processing methods that do not preserve the amplitude fidelity of the data, for example, a spiking deconvolution (that artificially balances the amplitude spectrum) for the removal of an unknown wavelet can have a negative effect on an amplitude sensitive method such as the Marchenko method. Therefore, it is important to be aware of the effect that an applied processing method has on the data.

Third, the importance of proper tapering should not be underestimated. The use of time windowing in Marchenko methods is an important limitation. We apply the time windowing to avoid creating copies of primary reflections, comparable to the lower-higher-lower criterion in the inverse scattering series (ISS) method [*Weglein et al.*, 1997]. In this thesis, the effect of an incorrectly placed truncation can be observed in figure 2.16, where copies of the primary reflections are part of our internal multiple predictions. But even if we manage to truncate the data such that copies of primary reflections are not obtained, we potentially cut through events. An abrupt truncation is unnatural and will create artefacts (Gibb's phenomena) if not properly alleviated through tapering.

Fourth, it is important to track the convergence of the Marchenko method during application by plotting the L_2 norm of the updates of the downgoing focusing function or the projected downgoing focusing function (depending on which Marchenko method you are using). It serves as an important quality check, since convergence indicates whether the resulting internal multiple predictions are reliable. If the L_2 norm of the updates diverges, the result of the Marchenko method will be incorrect. If convergence is very slow, or if it plateaus very quickly, then something might also be wrong. In those cases, the data might not have been correctly processed or

scaled.

Fifth, the use of synthetic data. When given a field dataset and a Marchenko method, and when time permits, it is helpful to first perform a test on realistic synthetic data. Ideally, a realistic velocity and density model are used to generate synthetic data that closely resemble the field data. For example, in chapters 2 and 3, I generated synthetic data using a velocity and a density model obtained from an acoustic inversion of the field data. Synthetic testing provides an estimate of the expected convergence rate, which can be used as a quality check for the field data application (see figure 4.12). In addition, synthetic tests help to evaluate whether a certain Marchenko method is indeed suitable for application to a particular dataset. For example, the adaptive double-focusing method and the adaptive double dereverberation method do not address internal multiples generated by interactions between the target area and the overburden (see figure 4.3b). These remnant internal multiples typically arrive later than the primaries from the target area, but it is helpful to verify that this is indeed the case on synthetic data in order to foresee any problems on field data.

Finally, I strongly recommend spending time on quality checking the preprocessing and the scaling of the data prior to the application of the Marchenko method. Chapter 4 introduces a simple and straightforward method to check the quality of the data after preprocessing. By convolving the potential input data for the Marchenko method with itself multiple times, we can repredict each order of surface-related multiple which should have been present in the data prior to surface-related multiple elimination. When these repredicted surface-related multiples are equal to the surface-related multiples that were removed from the data, the potential input data for the Marchenko method has the correct scaling and phase. Otherwise, the data has to be adjusted (for example, by adjusting the scaling, deconvolving for a source wavelet, applying a half time-differentiation) until removed and repredicted surface-related multiples match.

When carefully designing a workflow that accounts for the specifics of the geological setting at hand, with emphasis on amplitude and phase preservation, and when keeping these practical aspects in mind, it should be possible to predict internal multiples on marine field data using the Marchenko method.

A

Marchenko-based target replacement, accounting for all orders of multiple reflections

Abstract In seismic monitoring, one is usually interested in the response of a changing target zone, embedded in a static inhomogeneous medium. We introduce an efficient method which predicts reflection responses at the earth's surface for different target-zone scenarios, from a single reflection response at the surface and a model of the changing target zone. The proposed process consists of two main steps. In the first step, the response of the original target zone is removed from the reflection response, using the Marchenko method. In the second step, the modelled response of a new target zone is inserted between the overburden and underburden responses. The method fully accounts for all orders of multiple scattering and, in the elastodynamic case, for wave conversion. For monitoring purposes, only the second step needs to be repeated for each target-zone model. Since the target zone covers only a small part of the entire medium, the proposed method is much more efficient than repeated modelling of the entire reflection response.

Published as: Wapenaar, K., and M. Staring, (2018), Marchenko-based target replacement, accounting for all orders of multiple reflections, Journal of Geophysical Research: Solid Earth, 123(6), 4942–4964.
Note that minor changes have been introduced to make the text consistent with the other chapters.

A.1 Introduction

In seismic modelling, inversion, and monitoring one is often interested in the response of a relatively small target zone, embedded in a larger inhomogeneous medium. Yet, to obtain the seismic response of a target zone at the earth's surface, the entire medium enclosing the target should be involved in the modelling process. This may become very inefficient when different scenarios for the target zone need to be evaluated, or when a target that changes over time needs to be monitored, for example to follow fluid flow in an aquifer, subsurface storage of waste products, or production of a hydrocarbon reservoir. Through the years, several efficient methods have been developed for modelling successive responses of a medium in which the parameters change only in a target zone. *Robertsson and Chapman* [2000] address this problem with the following approach. First they model the wave field in the full medium, define a boundary around the target zone in which the changes take place, and evaluate the field at this boundary. Next, they numerically inject this field from the same boundary into different models of the target zone. Because the target zone usually covers only a small part of the full medium, this injection process takes only a fraction of the time that would be needed to model the field in the full medium. This method is very well suited to model different time-lapse scenarios of a specific subsurface process in an efficient way. A limitation of the method is that multiple scattering between the changed target and the embedding medium is not taken into account. The method was adapted by *van Manen et al.* [2007] to account for this type of interaction, by modifying the field at the boundary around the changed target at every time-step of the simulation. Wave field injection methods are not only useful for efficient numerical modelling of wave fields in a changing target zone, they can also be used to physically inject a field from a large numerical environment into a finite-size physical model [*Vasmel et al.*, 2013].

Instead of numerically modelling the field at the boundary enclosing the target, *Elison et al.* [2016] propose to use the Marchenko method to derive this field from reflection data at the surface. Hence, to obtain the wave field in a changing target zone, they need a measured reflection response at the surface of the original medium and a model of the target. Their method exploits an attractive property of the Marchenko method, namely that "redatumed" reflection responses of a target zone from above ($\mathbf{R}^{\cup}$) and from below ($\mathbf{R}^{\cap}$) can both be obtained from single-sided reflection data at the surface and an estimate of the direct arrivals between the surface and the target zone [*Wapenaar et al.*, 2014a].

In most of the methods discussed above, the wave fields are derived inside the changing target. Here we discuss a method which predicts reflection responses (including all multiples) at the earth's surface for different target-zone scenarios, from a single reflection response at the surface and a model of the changing target zone. The proposed method, which we call "target replacement", consists of two main steps. In the first step, which is analogous to the method proposed by *Elison et al.* [2016], we use the Marchenko method to remove the response of the target zone from the original reflection response. In the second step we insert the response of a new target zone, yielding the desired reflection response at the surface for the

particular target-zone scenario. Both steps fully account for multiple scattering between the target and the embedding medium. Note that, to model different reflection responses for different target models, only the second step needs to be repeated. Hence, this process is particularly efficient when reflection responses at the surface are needed for many target-zone scenarios. Also note that, unlike the model-driven methods of *Robertsson and Chapman* [2000] and *van Manen et al.* [2007], our method as well as that of *Elison et al.* [2016] only needs a smooth model of the overburden and no model of the underburden. The required detailed information of the over- and underburden comes from the measured reflection response.

Similar as the other methods discussed in this introduction, we assume that the target zone is the only region in which changes occur; the over- and underburden are assumed to remain unchanged. However, changes in a reservoir may lead to changes in the embedding medium [*Hatchell and Bourne*, 2005; *Herwanger and Horne*, 2009]. When this is the case, the target zone should not be restricted to the reservoir, but it should also include the part of the embedding medium in which the changes have a noticeable effect on the waves propagating through it. Of course the larger the target zone, the smaller the efficiency gain.

The setup of this paper is as follows. In Section A.2, we derive a representation of the seismic reflection response at the earth's surface (including all orders of multiple scattering), which explicitly distinguishes between the response of the target zone and that of the embedding medium. Next, based on this representation, in Section A.3, we discuss how to remove the response of the target zone from the reflection response at the surface. In Section A.4, we discuss how the response of a changed target zone can be inserted into the reflection response at the surface. The proposed method is illustrated with numerical examples in Section A.5. We end the paper with a discussion (Section A.6) and conclusions (Section A.7).

A.2 Representation of the reflection response

We derive a representation for the reflection response at the earth's surface, which distinguishes between the response of the target zone and that of the embedding medium. We start by dividing the subsurface into three units. The first unit, indicated as unit a in Figure A.1, covers the region between the earth's surface and boundary $\mathbb{S}_1$, the latter defining the upper boundary of the target zone. The earth's surface (indicated by the solid line) may be considered either as a free or as a transparent surface (the latter after surface-related multiple elimination). The earth's surface is included in unit a. A transparent boundary $\mathbb{S}_0$ (indicated by the upper dashed line) is defined at an infinitesimal distance below the earth's surface (in the following we abbreviate "an infinitesimal distance above/below" as "just above/below"). Unit a, i.e., the region above the target zone, is called the overburden. The second unit, indicated as unit b in Figure A.1, represents the target zone and is enclosed by boundaries $\mathbb{S}_1$ and $\mathbb{S}_2$. The third unit, indicated as unit c in Figure A.1, represents the region below the lower boundary of the target zone, $\mathbb{S}_2$. Unit c, i.e., the region below the target zone, is called the underburden.

We assume that the media inside the units are arbitrary inhomogeneous, lossless

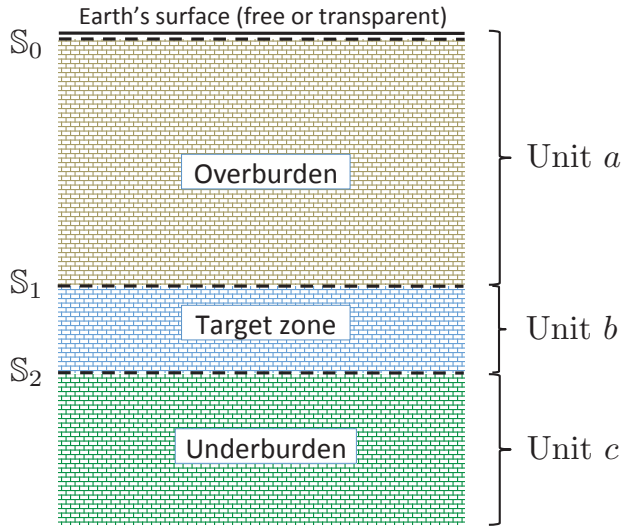

Figure A.1: *Subdivision of the inhomogeneous subsurface into three units: an overburden (unit a), a target zone (unit b) and an underburden (unit c). Note that unit a includes the earth's surface just above* $\mathbb{S}_0$*. This surface may be considered either as a free or as a transparent surface.*

media. Furthermore, we assume that the boundaries $\mathbb{S}_1$ and $\mathbb{S}_2$ do not coincide with interfaces, or in other words, we consider these boundaries to be transparent for downgoing and upgoing waves incident to these boundaries. The representation derived below could be extended to account for scattering at these boundaries, but that would go at the cost of clarity. By allowing some flexibility in the definition of the target zone, it will often be possible to choose boundaries $\mathbb{S}_1$ and $\mathbb{S}_2$ that are (close to) transparent.

The starting point for the derivation of the representation and the target replacement method is formed by the following one-way reciprocity theorems in the space-frequency domain

$$\int_{\mathbb{S}_m} \{(\mathbf{p}_A^+)^t \mathbf{p}_B^- - (\mathbf{p}_A^-)^t \mathbf{p}_B^+\} \mathrm{d}\mathbf{x} = \int_{\mathbb{S}_n} \{(\mathbf{p}_A^+)^t \mathbf{p}_B^- - (\mathbf{p}_A^-)^t \mathbf{p}_B^+\} \mathrm{d}\mathbf{x} \tag{A.2.1}$$

and

$$\int_{\mathbb{S}_m} \{(\mathbf{p}_A^+)^\dagger \mathbf{p}_B^+ - (\mathbf{p}_A^-)^\dagger \mathbf{p}_B^-\} \mathrm{d}\mathbf{x} = \int_{\mathbb{S}_n} \{(\mathbf{p}_A^+)^\dagger \mathbf{p}_B^+ - (\mathbf{p}_A^-)^\dagger \mathbf{p}_B^-\} \mathrm{d}\mathbf{x} \tag{A.2.2}$$

[*Wapenaar and Grimbergen*, 1996]. Here $\mathbb{S}_m$ and $\mathbb{S}_n$ can stand for any of the boundaries $\mathbb{S}_0$, $\mathbb{S}_1$ and $\mathbb{S}_2$. Subscripts A and B refer to two independent states. Superscripts $+$ and $-$ stand for downward and upward propagation, respectively.

Superscript t in equation (A.2.1) denotes the transpose and superscript $\dagger$ in equation (A.2.2) the adjoint (i.e., the complex conjugate transpose). The vectors $\mathbf{p}_A^{\pm}$ and $\mathbf{p}_B^{\pm}$ represent flux-normalised one-way wave fields in states A and B. For the elastodynamic situation they are defined as

$$\mathbf{p}_A^{\pm}(\mathbf{x},\omega) = \begin{pmatrix} \Phi_A^{\pm} \\ \Psi_A^{\pm} \\ \Upsilon_A^{\pm} \end{pmatrix}(\mathbf{x},\omega), \quad \mathbf{p}_B^{\pm}(\mathbf{x},\omega) = \begin{pmatrix} \Phi_B^{\pm} \\ \Psi_B^{\pm} \\ \Upsilon_B^{\pm} \end{pmatrix}(\mathbf{x},\omega), \tag{A.2.3}$$

where $\Phi_{A,B}^{\pm}$, $\Psi_{A,B}^{\pm}$ and $\Upsilon_{A,B}^{\pm}$ represent P, $S1$ and $S2$ waves, respectively. For the acoustic situation, $\mathbf{p}_A^{\pm}(\mathbf{x},\omega)$ and $\mathbf{p}_B^{\pm}(\mathbf{x},\omega)$ reduce to scalar functions. The Cartesian coordinate vector $\mathbf{x}$ is defined as $\mathbf{x} = (x_1, x_2, x_3)$ (the x_3-axis pointing downward) and ω denotes angular frequency. An underlying assumption for both reciprocity theorems is that the medium parameters in states A and B are identical in the domain enclosed by boundaries $\mathbb{S}_m$ and $\mathbb{S}_n$. Outside this domain the medium parameters in state A may be different from those in state B, a property that we will make frequently use of throughout this paper. Another assumption is that there are no sources between $\mathbb{S}_m$ and $\mathbb{S}_n$. Finally, an assumption that holds specifically for equation (A.2.2) is that evanescent waves are neglected at boundaries $\mathbb{S}_m$ and $\mathbb{S}_n$. For a more detailed discussion of these one-way reciprocity theorems, including their extensions for the situation that the domain between $\mathbb{S}_m$ and $\mathbb{S}_n$ contains sources and the medium parameters in the two states are different in this domain, see *Wapenaar and Grimbergen* [1996].

In the following derivations, equations (A.2.1) and (A.2.2) will frequently be applied, each time to a combination of independent wave states in two media that are identical in the domain between $\mathbb{S}_m$ and $\mathbb{S}_n$. Figure A.2 shows six media that will be used in different combinations. Media a, b and c in the left column contain the units a (the overburden), b (the target zone) and c (the underburden) of the actual medium, each embedded in a homogeneous background. The grey areas indicate the inhomogeneous units (as depicted in Figure A.1), whereas the white areas represent the homogeneous embedding. Reflection and transmission responses are also indicated in Figure A.2. Reflection responses from above and from below are denoted by $\mathbf{R}^{\cup}$ and $\mathbf{R}^{\cap}$, respectively, and the transmission responses by $\mathbf{T}^{+}$ and $\mathbf{T}^{-}$. The subscripts a, b and c refer to the units to which these responses belong. The rays are simplifications of the actual responses, which contain all orders of multiple scattering and, in the elastodynamic case, mode conversion. When the earth's surface just above $\mathbb{S}_0$ is a free surface, then the responses in unit a also include multiple scattering related to the free surface. Media A, B and C in the right column in Figure A.2 consist of one to three units, as indicated (note that medium A is identical to medium a, whereas medium C represents the entire medium). The reflection and transmission responses of these media are indicated by capital subscripts A, B and C. In addition, the Green's functions $\mathbf{G}^{+,+}$ and $\mathbf{G}^{-,+}$ in these media between $\mathbb{S}_0$ and the top boundary of the deepest unit are shown (the superscripts will be explained later). Again, all responses contain all orders of multiple scattering (and mode conversion), including surface-related multiples when there is a free surface just above $\mathbb{S}_0$.

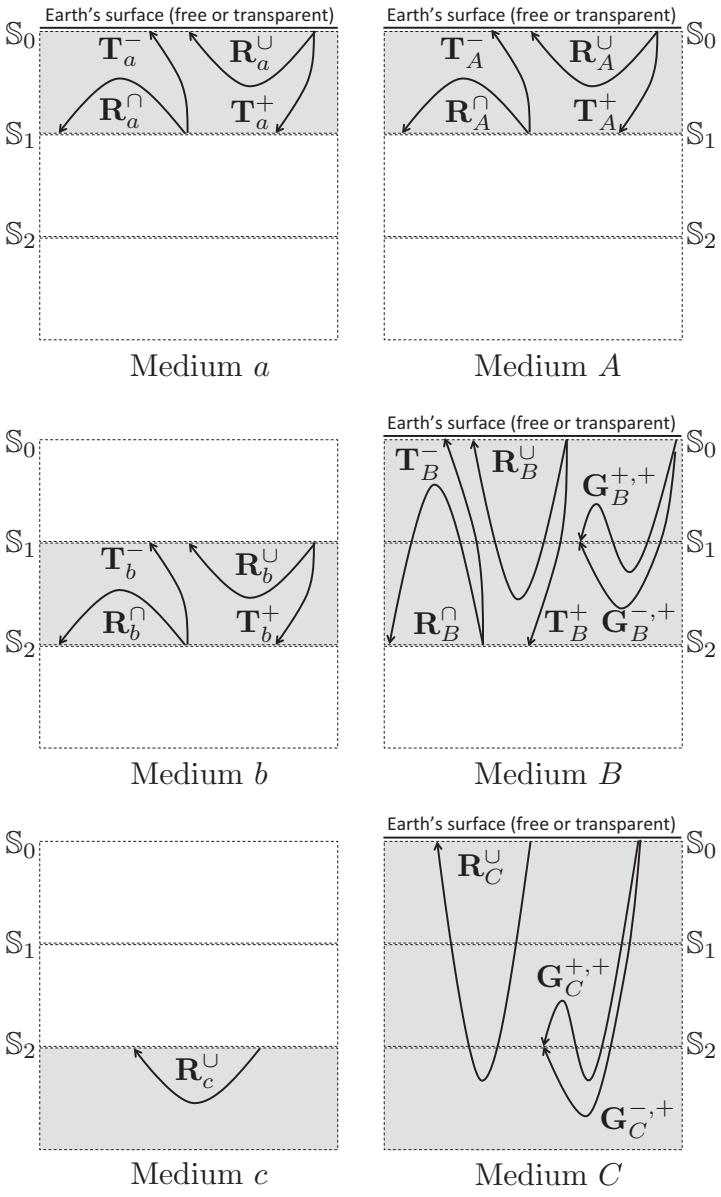

Figure A.2: *Six media with their responses. Grey areas represent the inhomogeneous units (and combinations thereof) of Figure A.1. Media A (=a), B and C include the earth's surface just above $\mathbb{S}_0$, which may be considered either as a free or as a transparent surface. The rays stand for the full responses, including all orders of multiple scattering and, in the elastodynamic case, mode conversion.*

Table A.1: *Quantities to derive a representation for* $\mathbf{R}_B^{\cup}$.

	State A: Medium A Source at $\mathbf{x}_R$ just above $\mathbb{S}_0$	State B: Medium B Source at $\mathbf{x}_S$ just above $\mathbb{S}_0$
$\mathbb{S}_0$	$\mathbf{p}_A^+(\mathbf{x},\omega) \rightarrow \mathbf{I}\delta(\mathbf{x}_{\mathrm{H}}-\mathbf{x}_{\mathrm{H},R})$ $+\mathbf{r}^{\cap}\mathbf{R}_A^{\cup}(\mathbf{x},\mathbf{x}_R,\omega)$	$\mathbf{p}_B^+(\mathbf{x},\omega) \rightarrow \mathbf{I}\delta(\mathbf{x}_{\mathrm{H}}-\mathbf{x}_{\mathrm{H},S})$ $+\mathbf{r}^{\cap}\mathbf{R}_B^{\cup}(\mathbf{x},\mathbf{x}_S,\omega)$
	$\mathbf{p}_A^-(\mathbf{x},\omega) \rightarrow \mathbf{R}_A^{\cup}(\mathbf{x},\mathbf{x}_R,\omega)$	$\mathbf{p}_B^-(\mathbf{x},\omega) \rightarrow \mathbf{R}_B^{\cup}(\mathbf{x},\mathbf{x}_S,\omega)$
$\mathbb{S}_1$	$\mathbf{p}_A^+(\mathbf{x},\omega) \rightarrow \mathbf{T}_A^+(\mathbf{x},\mathbf{x}_R,\omega)$	$\mathbf{p}_B^+(\mathbf{x},\omega) \rightarrow \mathbf{G}_B^{+,+}(\mathbf{x},\mathbf{x}_S,\omega)$
	$\mathbf{p}_A^-(\mathbf{x},\omega) \rightarrow \mathbf{O}$	$\mathbf{p}_B^-(\mathbf{x},\omega) \rightarrow \mathbf{G}_B^{-,+}(\mathbf{x},\mathbf{x}_S,\omega)$

Our aim is to derive a representation for the reflection response of the entire medium, $\mathbf{R}_C^{\cup}$, in terms of the reflection responses of media A $(= a)$, b and c. We start by deriving a representation for $\mathbf{R}_B^{\cup}$ in terms of the reflection responses of media A and b. To this end, we substitute the quantities of Table 1 into equation (A.2.1). Let us first discuss these quantities one by one. In state B, the downgoing and upgoing fields in medium B for $\mathbf{x}$ at $\mathbb{S}_1$ are given by

$$\mathbf{p}_B^{\pm}(\mathbf{x},\omega) \rightarrow \mathbf{G}_B^{\pm,+}(\mathbf{x},\mathbf{x}_S,\omega). \tag{A.2.4}$$

Here $\mathbf{G}_B^{\pm,+}(\mathbf{x},\mathbf{x}_S,\omega)$ is the Green's one-way wave field matrix in medium B in the space-frequency domain [*Wapenaar*, 1996]. The source is at $\mathbf{x}_S$, which is chosen just above $\mathbb{S}_0$. The second superscript $+$ indicates that this source is downward radiating. The receiver is at $\mathbf{x}$ at $\mathbb{S}_1$. The first superscript $\pm$ indicates the propagation direction at the receiver ($+$ for downgoing and $-$ for upgoing). Analogous to equation (A.2.3), the general Green's one-way wave field matrix can, for the elastodynamic situation, be written as

$$\mathbf{G}^{\pm,\pm}(\mathbf{x},\mathbf{x}',\omega) = \begin{pmatrix} G_{\phi,\phi}^{\pm,\pm} & G_{\phi,\psi}^{\pm,\pm} & G_{\phi,\upsilon}^{\pm,\pm} \\ G_{\psi,\phi}^{\pm,\pm} & G_{\psi,\psi}^{\pm,\pm} & G_{\psi,\upsilon}^{\pm,\pm} \\ G_{\upsilon,\phi}^{\pm,\pm} & G_{\upsilon,\psi}^{\pm,\pm} & G_{\upsilon,\upsilon}^{\pm,\pm} \end{pmatrix} (\mathbf{x},\mathbf{x}',\omega). \tag{A.2.5}$$

Each column corresponds to a specific type of source at $\mathbf{x}'$ and each row to a specific type of receiver at $\mathbf{x}$ (where subscripts ϕ, ψ and υ refer to flux-normalised P, $S1$ and $S2$ waves, respectively). For the acoustic situation, $\mathbf{G}^{\pm,\pm}(\mathbf{x},\mathbf{x}',\omega)$ reduces to a scalar function. The following reciprocity relations hold for the general Green's matrix

$$\mathbf{G}^{-,+}(\mathbf{x}',\mathbf{x},\omega) = \{\mathbf{G}^{-,+}(\mathbf{x},\mathbf{x}',\omega)\}^t, \tag{A.2.6}$$

$$\mathbf{G}^{+,-}(\mathbf{x}',\mathbf{x},\omega) = \{\mathbf{G}^{+,-}(\mathbf{x},\mathbf{x}',\omega)\}^t, \tag{A.2.7}$$

$$\mathbf{G}^{-,-}(\mathbf{x}',\mathbf{x},\omega) = -\{\mathbf{G}^{+,+}(\mathbf{x},\mathbf{x}',\omega)\}^t, \tag{A.2.8}$$

[*Haines*, 1988; *Kennett et al.*, 1990; *Wapenaar*, 1996]. In state B, the upgoing field for $\mathbf{x}$ at $\mathbb{S}_0$ in Table 1 is given by

$$\mathbf{p}_B^-(\mathbf{x},\omega) \rightarrow \mathbf{G}_B^{-,+}(\mathbf{x},\mathbf{x}_S,\omega) = \mathbf{R}_B^{\cup}(\mathbf{x},\mathbf{x}_S,\omega). \tag{A.2.9}$$

Note that $\mathbf{G}^{-,+}(\mathbf{x},\mathbf{x}',\omega)$ represents a reflection response from above, denoted by $\mathbf{R}^{\cup}(\mathbf{x},\mathbf{x}',\omega)$, whenever the source and receiver are situated at (or just above) the same depth level. From equations (A.2.6) and (A.2.9), we find

$$\mathbf{R}^{\cup}(\mathbf{x}',\mathbf{x},\omega) = \{\mathbf{R}^{\cup}(\mathbf{x},\mathbf{x}',\omega)\}^t. \tag{A.2.10}$$

Similarly, $\mathbf{G}^{+,-}(\mathbf{x},\mathbf{x}',\omega)$ represents a reflection response from below, denoted by $\mathbf{R}^{\cap}(\mathbf{x},\mathbf{x}',\omega)$, whenever the source and receiver are situated at (or just below) the same depth level. From equations (A.2.7) and (A.2.9) we find

$$\mathbf{R}^{\cap}(\mathbf{x}',\mathbf{x},\omega) = \{\mathbf{R}^{\cap}(\mathbf{x},\mathbf{x}',\omega)\}^t. \tag{A.2.11}$$

In state B, the downgoing field for $\mathbf{x}$ at $\mathbb{S}_0$ in Table 1 is given by

$$\begin{aligned}\mathbf{p}_B^+(\mathbf{x},\omega) \rightarrow \mathbf{G}_B^{+,+}(\mathbf{x},\mathbf{x}_S,\omega) =& \mathbf{I}\delta(\mathbf{x}_{\mathrm{H}}-\mathbf{x}_{\mathrm{H},S}) \\ &+ \mathbf{r}^{\cap}\mathbf{R}_B^{\cup}(\mathbf{x},\mathbf{x}_S,\omega).\end{aligned} \tag{A.2.12}$$

Since $\mathbf{x}_S$ was chosen just above $\mathbb{S}_0$, the direct contribution of the flux-normalised Green's matrix $\mathbf{G}_B^{+,+}(\mathbf{x},\mathbf{x}_S,\omega)$ consists of a spatial delta function $\delta(\mathbf{x}_{\mathrm{H}}-\mathbf{x}_{\mathrm{H},S})$, with $\mathbf{x}_{\mathrm{H}} = (x_1,x_2)$ and $\mathbf{x}_{\mathrm{H},S} = (x_{1,S},x_{2,S})$, hence, the singularity occurs at the lateral position of the source. This delta function is multiplied by $\mathbf{I}$, which is a 3×3 identity matrix for the elastodynamic situation, to acknowledge the matrix character of $\mathbf{G}_B^{+,+}(\mathbf{x},\mathbf{x}_S,\omega)$, as defined in equation (A.2.5). For the acoustic situation $\mathbf{I}=1$. The second term in equation (A.2.12), $\mathbf{r}^{\cap}\mathbf{R}_B^{\cup}(\mathbf{x},\mathbf{x}_S,\omega)$, accounts for the earth's surface just above $\mathbb{S}_0$. Here $\mathbf{r}^{\cap}$ is the reflection operator of the earth's surface from below. It turns the reflection response $\mathbf{R}_B^{\cup}(\mathbf{x},\mathbf{x}_S,\omega)$ into a downgoing field which, according to equation (A.2.12), is added to the direct downgoing field. When the earth's surface is transparent, we may simply set $\mathbf{r}^{\cap} = \mathbf{O}$, where $\mathbf{O}$ is a 3×3 zero matrix for the elastodynamic situation and $\mathbf{O}=0$ for the acoustic situation. When the earth's surface is a free surface, $\mathbf{r}^{\cap}$ is a pseudo-differential operator for the elastodynamic situation. We introduce its transpose, $\{\mathbf{r}^{\cap}\}^t$, and adjoint, $\{\mathbf{r}^{\cap}\}^\dagger$, via the following integral relations

$$\int_{\mathbb{S}_0}\{\mathbf{r}^{\cap}\mathbf{f}(\mathbf{x})\}^t\mathbf{g}(\mathbf{x})\mathrm{d}\mathbf{x} = \int_{\mathbb{S}_0}\{\mathbf{f}(\mathbf{x})\}^t\{\mathbf{r}^{\cap}\}^t\mathbf{g}(\mathbf{x})\mathrm{d}\mathbf{x} \tag{A.2.13}$$

and

$$\int_{\mathbb{S}_0}\{\mathbf{r}^{\cap}\mathbf{f}(\mathbf{x})\}^\dagger\mathbf{g}(\mathbf{x})\mathrm{d}\mathbf{x} = \int_{\mathbb{S}_0}\{\mathbf{f}(\mathbf{x})\}^\dagger\{\mathbf{r}^{\cap}\}^\dagger\mathbf{g}(\mathbf{x})\mathrm{d}\mathbf{x}, \tag{A.2.14}$$

respectively. The following properties hold [*Kennett et al.*, 1990; *Wapenaar et al.*, 2004]

$$\{\mathbf{r}^{\cap}\}^t = \mathbf{r}^{\cap}, \tag{A.2.15}$$

$$\{\mathbf{r}^{\cap}\}^\dagger\mathbf{r}^{\cap} = \mathbf{I}. \tag{A.2.16}$$

Table A.2: *Quantities to derive a representation for* $\mathbf{G}_B^{-,+}$.

	State A: Medium b Source at $\mathbf{x}'$ just above $\mathbb{S}_1$	State B: Medium B Source at $\mathbf{x}_S$ just above $\mathbb{S}_0$
$\mathbb{S}_1$	$\mathbf{p}_A^+(\mathbf{x},\omega) \rightarrow \mathbf{I}\delta(\mathbf{x}_{\mathrm{H}} - \mathbf{x}'_{\mathrm{H}})$	$\mathbf{p}_B^+(\mathbf{x},\omega) \rightarrow \mathbf{G}_B^{+,+}(\mathbf{x},\mathbf{x}_S,\omega)$
	$\mathbf{p}_A^-(\mathbf{x},\omega) \rightarrow \mathbf{R}_b^{\cup}(\mathbf{x},\mathbf{x}',\omega)$	$\mathbf{p}_B^-(\mathbf{x},\omega) \rightarrow \mathbf{G}_B^{-,+}(\mathbf{x},\mathbf{x}_S,\omega)$
$\mathbb{S}_2$	$\mathbf{p}_A^+(\mathbf{x},\omega) \rightarrow \mathbf{T}_b^+(\mathbf{x},\mathbf{x}',\omega)$	$\mathbf{p}_B^+(\mathbf{x},\omega) \rightarrow \mathbf{T}_B^+(\mathbf{x},\mathbf{x}_S,\omega)$
	$\mathbf{p}_A^-(\mathbf{x},\omega) \rightarrow \mathbf{O}$	$\mathbf{p}_B^-(\mathbf{x},\omega) \rightarrow \mathbf{O}$

For the acoustic situation we simply have $\mathbf{r}^{\cap} = -1$.

In state A, the downgoing field in medium A for $\mathbf{x}$ at $\mathbb{S}_1$ in Table 1 is given by

$$\mathbf{p}_A^+(\mathbf{x},\omega) \rightarrow \mathbf{G}_A^{+,+}(\mathbf{x},\mathbf{x}_R,\omega) = \mathbf{T}_A^+(\mathbf{x},\mathbf{x}_R,\omega). \tag{A.2.17}$$

This time the source is at $\mathbf{x}_R$, again just above $\mathbb{S}_0$. The receiver is at $\mathbf{x}$ at $\mathbb{S}_1$. Note that $\mathbf{G}^{+,+}(\mathbf{x},\mathbf{x}',\omega)$ represents a downgoing transmission response, denoted by $\mathbf{T}^+(\mathbf{x},\mathbf{x}',\omega)$, whenever the source and receiver are situated above and below an inhomogeneous slab. Similarly, $\mathbf{G}^{-,-}(\mathbf{x}',\mathbf{x},\omega)$ represents an upgoing transmission response, denoted by $-\mathbf{T}^-(\mathbf{x}',\mathbf{x},\omega)$ (note the minus sign), whenever the source and receiver are situated below and above an inhomogeneous slab. From equation (A.2.8), we find

$$\mathbf{T}^-(\mathbf{x}',\mathbf{x},\omega) = \{\mathbf{T}^+(\mathbf{x},\mathbf{x}',\omega)\}^t. \tag{A.2.18}$$

In state A, the upgoing field for $\mathbf{x}$ at $\mathbb{S}_1$ in Table 1 is zero because medium A is homogeneous below $\mathbb{S}_1$. The downgoing and upgoing fields in state A for $\mathbf{x}$ at $\mathbb{S}_0$ are defined in a similar way as in state B.

Now that we have discussed all quantities in Table 1, we substitute them into equation (A.2.1). Despite the different media (medium A in state A and medium B in state B), this is justified, because between $\mathbb{S}_0$ and $\mathbb{S}_1$ these media are the same in both states (see Figure A.2). Here and in the remainder of this paper, the operator $\mathbf{r}^{\cap}$ is the same in both states (zero and thus obeying equation (A.2.15) when the earth's surface is considered transparent, or non-zero and obeying equations (A.2.15) and (A.2.16) when the earth's surface is considered a free surface). Using equations (A.2.10), (A.2.13), (A.2.15) and (A.2.18), setting $m = 0$ and $n = 1$ in equation (A.2.1), we obtain

$$\begin{aligned}\mathbf{R}_B^{\cup}(\mathbf{x}_R,\mathbf{x}_S,\omega) =& \mathbf{R}_A^{\cup}(\mathbf{x}_R,\mathbf{x}_S,\omega) \\ &+ \int_{\mathbb{S}_1} \mathbf{T}_A^-(\mathbf{x}_R,\mathbf{x},\omega)\mathbf{G}_B^{-,+}(\mathbf{x},\mathbf{x}_S,\omega)\mathrm{d}\mathbf{x},\end{aligned} \tag{A.2.19}$$

for $\mathbf{x}_S$ and $\mathbf{x}_R$ just above $\mathbb{S}_0$, see Figure A.3.

Next, we derive a representation for $\mathbf{G}_B^{-,+}(\mathbf{x},\mathbf{x}_S,\omega)$ in equation (A.2.19). Substituting the quantities of Table 2 into equation (A.2.1), using equation (A.2.10)

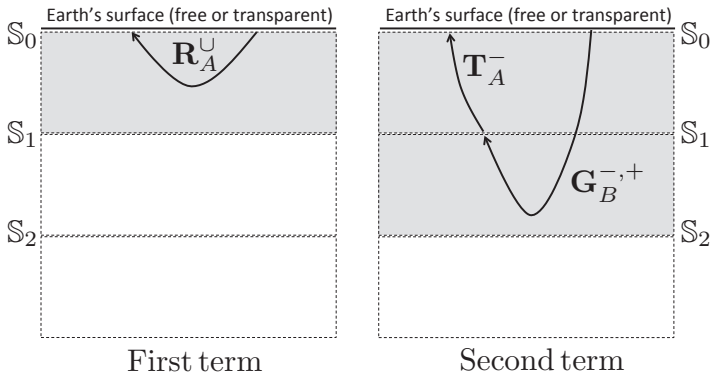

Figure A.3: *Visualization of the first an second term in the representation of equation (A.2.19).*

and setting $m = 1$ and $n = 2$, gives

$$\mathbf{G}_B^{-,+}(\mathbf{x}', \mathbf{x}_S, \omega) = \int_{\mathbb{S}_1} \mathbf{R}_b^{\cup}(\mathbf{x}', \mathbf{x}, \omega)\mathbf{G}_B^{+,+}(\mathbf{x}, \mathbf{x}_S, \omega)\mathrm{d}\mathbf{x}, \tag{A.2.20}$$

for $\mathbf{x}_S$ just above $\mathbb{S}_0$ and $\mathbf{x}'$ just above $\mathbb{S}_1$. Because $\mathbb{S}_1$ is transparent (i.e., it does not coincide with an interface), equation (A.2.20) does not alter if we take $\mathbf{x}'$ at $\mathbb{S}_1$ instead of just above it. Thus, taking $\mathbf{x}'$ at $\mathbb{S}_1$, substituting equation (A.2.20) into equation (A.2.19) (with $\mathbf{x}$ in equation (A.2.19) replaced by $\mathbf{x}'$), we obtain

$$\begin{aligned}\mathbf{R}_B^{\cup}(\mathbf{x}_R, \mathbf{x}_S, \omega) =& \mathbf{R}_A^{\cup}(\mathbf{x}_R, \mathbf{x}_S, \omega) \\ &+ \int_{\mathbb{S}_1}\int_{\mathbb{S}_1} \mathbf{T}_A^{-}(\mathbf{x}_R, \mathbf{x}', \omega)\mathbf{R}_b^{\cup}(\mathbf{x}', \mathbf{x}, \omega)\mathbf{G}_B^{+,+}(\mathbf{x}, \mathbf{x}_S, \omega)\mathrm{d}\mathbf{x}\mathrm{d}\mathbf{x}',\end{aligned} \tag{A.2.21}$$

for $\mathbf{x}_S$ and $\mathbf{x}_R$ just above $\mathbb{S}_0$. This is the sought representation for $\mathbf{R}_B^{\cup}$. In a similar way we find the following representation for $\mathbf{R}_C^{\cup}$

$$\begin{aligned}\mathbf{R}_C^{\cup}(\mathbf{x}_R, \mathbf{x}_S, \omega) =& \mathbf{R}_B^{\cup}(\mathbf{x}_R, \mathbf{x}_S, \omega) \\ &+ \int_{\mathbb{S}_2}\int_{\mathbb{S}_2} \mathbf{T}_B^{-}(\mathbf{x}_R, \mathbf{x}', \omega)\mathbf{R}_c^{\cup}(\mathbf{x}', \mathbf{x}, \omega)\mathbf{G}_C^{+,+}(\mathbf{x}, \mathbf{x}_S, \omega)\mathrm{d}\mathbf{x}\mathrm{d}\mathbf{x}',\end{aligned} \tag{A.2.22}$$

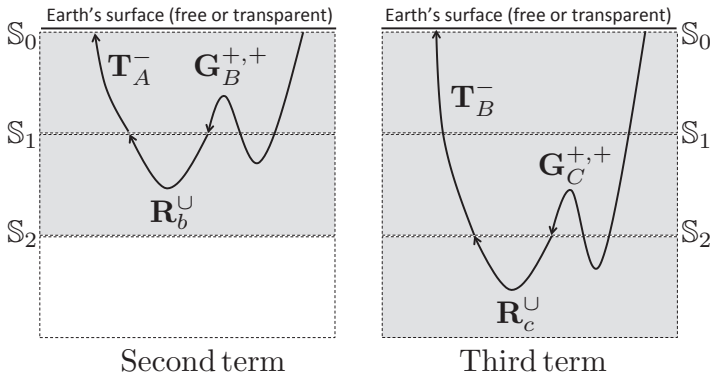

Figure A.4: *Visualization of the second an third term in the representation of equation (A.2.23).*

or, upon substitution of equation (A.2.21),

$$\begin{aligned}\mathbf{R}_C^{\cup}(\mathbf{x}_R,\mathbf{x}_S,\omega) =&\mathbf{R}_A^{\cup}(\mathbf{x}_R,\mathbf{x}_S,\omega)\\ &+\int_{\mathbb{S}_1}\int_{\mathbb{S}_1}\mathbf{T}_A^-(\mathbf{x}_R,\mathbf{x}',\omega)\mathbf{R}_b^{\cup}(\mathbf{x}',\mathbf{x},\omega)\mathbf{G}_B^{+,+}(\mathbf{x},\mathbf{x}_S,\omega)\mathrm{d}\mathbf{x}\mathrm{d}\mathbf{x}'\\ &+\int_{\mathbb{S}_2}\int_{\mathbb{S}_2}\mathbf{T}_B^-(\mathbf{x}_R,\mathbf{x}',\omega)\mathbf{R}_c^{\cup}(\mathbf{x}',\mathbf{x},\omega)\mathbf{G}_C^{+,+}(\mathbf{x},\mathbf{x}_S,\omega)\mathrm{d}\mathbf{x}\mathrm{d}\mathbf{x}',\end{aligned} \tag{A.2.23}$$

for $\mathbf{x}_S$ and $\mathbf{x}_R$ just above $\mathbb{S}_0$. The first term on the right-hand side is the reflection response of the overburden (Figure A.2, medium A $(= a)$). The second and third terms on the right-hand side contain the reflection responses of the target zone and the underburden, respectively (media b and c in Figure A.2). These terms are visualised in Figure A.4.

Note that, if the subsurface would be divided into more and thinner units, the recursive derivation process could be continued, leading to additional terms on the right-hand side of equation (A.2.23). In the limiting case (for infinitesimally thin units), the reflection responses under the integrals could be replaced by local reflection operators, the Green's functions $\mathbf{G}^{+,+}$ by transmission responses $\mathbf{T}^+$, and the sum in the right-hand side would become an integral along the depth coordinate. The resulting expression would be the so-called "generalised primary representation" [*Kennett*, 1974; *Hubral et al.*, 1980; *Resnick et al.*, 1986; *Fishman et al.*, 1987; *Wapenaar*, 1996; *Haines and de Hoop*, 1996].

The representation of equation (A.2.23) is not meant as a recipe for numerical modelling. However, it is a suited starting point for the derivation of a scheme for target replacement. In equation (A.2.23), $\mathbf{R}_b^{\cup}(\mathbf{x}',\mathbf{x},\omega)$ represents the reflection response from above of the target zone (unit b in Figure A.1). Let $\bar{\mathbf{R}}_b^{\cup}(\mathbf{x}',\mathbf{x},\omega)$ denote the reflection response of a changed target zone (which we denote as unit

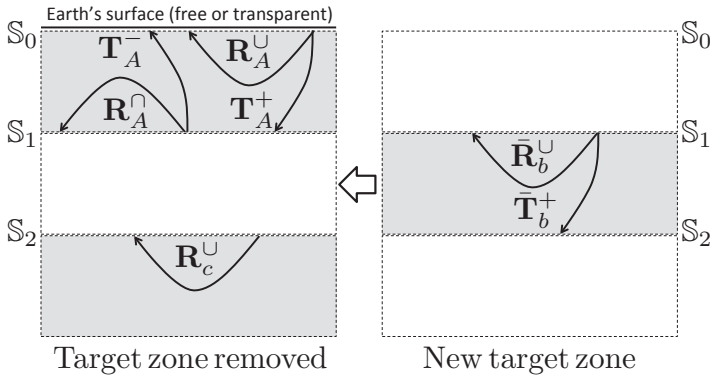

Figure A.5: *Left: overburden and underburden responses, obtained from the reflection response $\mathbf{R}_C^\cup$, using the Marchenko method. Right: modelled responses of the new target zone, to be inserted between the overburden and underburden responses.*

$\bar{b}$). The reflection response of the entire medium, with the changed target zone, is given by the following representation

$$\begin{aligned}\bar{\mathbf{R}}_C^\cup(\mathbf{x}_R,\mathbf{x}_S,\omega) =& \mathbf{R}_A^\cup(\mathbf{x}_R,\mathbf{x}_S,\omega)\\ &+\int_{\mathbb{S}_1}\int_{\mathbb{S}_1}\mathbf{T}_A^-(\mathbf{x}_R,\mathbf{x}',\omega)\bar{\mathbf{R}}_b^\cup(\mathbf{x}',\mathbf{x},\omega)\bar{\mathbf{G}}_B^{+,+}(\mathbf{x},\mathbf{x}_S,\omega)\mathrm{d}\mathbf{x}\mathrm{d}\mathbf{x}'\\ &+\int_{\mathbb{S}_2}\int_{\mathbb{S}_2}\bar{\mathbf{T}}_B^-(\mathbf{x}_R,\mathbf{x}',\omega)\mathbf{R}_c^\cup(\mathbf{x}',\mathbf{x},\omega)\bar{\mathbf{G}}_C^{+,+}(\mathbf{x},\mathbf{x}_S,\omega)\mathrm{d}\mathbf{x}\mathrm{d}\mathbf{x}'.\end{aligned} \tag{A.2.24}$$

Note that, although it is assumed that the overburden and underburden are unchanged, all quantities on the right-hand side that contain a propagation path through the target zone are influenced by the changes, which is indicated by the bars. In the following two sections, we discuss the target replacement in detail. First, in Section A.3 we discuss the removal of the target zone response from the original reflection response $\mathbf{R}_C^\cup(\mathbf{x}_R,\mathbf{x}_S,\omega)$. Next, in Section A.4 we discuss how to insert the response of the changed target into the new reflection response $\bar{\mathbf{R}}_C^\cup(\mathbf{x}_R,\mathbf{x}_S,\omega)$.

A.3 Removing the target zone from the original reflection response

Given the reflection response of the entire medium, $\mathbf{R}_C^\cup$, our aim is to resolve the responses of the media A (= a) and c (i.e., the overburden and underburden, Figure A.5). If $\mathbf{R}_C^\cup$ contained only primary P-wave reflections, we could apply simple time-windowing in the time domain to separate the reflection responses of the different units. However, because of multiple scattering (possibly including surface-related

multiples) and wave conversion, the responses of the different units overlap and cannot be straightforwardly separated by time-windowing. Here we show that so-called "focusing functions", recently introduced for Marchenko imaging [*Wapenaar et al.*, 2013; *Slob et al.*, 2014], can be used to obtain the responses of media A (= a) and c.

We start by defining the focusing function $\mathbf{F}^{+}_{1,A}(\mathbf{x},\mathbf{x}',\omega)$ in medium A, with or without free surface just above $\mathbb{S}_0$ (Figure A.6). Here, $\mathbf{x}'$ defines a focal point at boundary $\mathbb{S}_1$, i.e., the lower boundary of unit a. Hence, $\mathbf{x}' = (x'_1, x'_2, x_{3,1})$, with $x_{3,1}$ denoting the depth of $\mathbb{S}_1$. The coordinate $\mathbf{x}$ is a variable in medium A. The superscript + refers to the propagation direction at $\mathbf{x}$ (which is downgoing in this case). The focusing function is emitted from all $\mathbf{x}$ at $\mathbb{S}_0$ into medium A. Due to scattering in the inhomogeneous medium it gives rise to an upgoing function $\mathbf{F}^{-}_{1,A}(\mathbf{x},\mathbf{x}',\omega)$. The focusing conditions for $\mathbf{x}$ at $\mathbb{S}_1$ can be formulated as

$$\{\mathbf{F}^{+}_{1,A}(\mathbf{x},\mathbf{x}',\omega)\}_{x_3=x_{3,1}} = \mathbf{I}\delta(\mathbf{x}_{\mathrm{H}}-\mathbf{x}'_{\mathrm{H}}), \tag{A.3.1}$$

$$\{\mathbf{F}^{-}_{1,A}(\mathbf{x},\mathbf{x}',\omega)\}_{x_3=x_{3,1}} = \mathbf{O}, \tag{A.3.2}$$

with $\mathbf{x}'_{\mathrm{H}} = (x'_1, x'_2)$. Equation (A.3.1) defines the convergence of $\mathbf{F}^{+}_{1,A}(\mathbf{x},\mathbf{x}',\omega)$ to the focal point $\mathbf{x}'$ at $\mathbb{S}_1$, whereas equation (A.3.2) states that the focusing function contains no upward scattered components at $\mathbb{S}_1$, because for medium A the half-space below this boundary is homogeneous. In practical situations evanescent waves are neglected to avoid instability of the focusing function, hence, the delta function in equation (A.3.1) should be interpreted as a band-limited spatial impulse.

The focusing functions $\mathbf{F}^{+}_{1,A}(\mathbf{x},\mathbf{x}',\omega)$ and $\mathbf{F}^{-}_{1,A}(\mathbf{x},\mathbf{x}',\omega)$ for $\mathbf{x}$ at $\mathbb{S}_0$ and $\mathbf{x}'$ at $\mathbb{S}_1$ can be obtained from the reflection response $\mathbf{R}^{\cup}_{C}(\mathbf{x}_R,\mathbf{x},\omega)$ for $\mathbf{x}_R$ just above $\mathbb{S}_0$, using the Marchenko method. We only outline the main features. In Appendix A.8.1, the following relations between $\mathbf{R}^{\cup}_{C}(\mathbf{x}_R,\mathbf{x},\omega)$, $\mathbf{F}^{\pm}_{1,A}(\mathbf{x},\mathbf{x}',\omega)$ and $\mathbf{G}^{\pm,+}_{C}(\mathbf{x}',\mathbf{x}_R,\omega)$ are derived

$$\begin{aligned}\{\mathbf{G}^{-,+}_{C}(\mathbf{x}',\mathbf{x}_R,\omega)\}^{t} + \mathbf{F}^{-}_{1,A}(\mathbf{x}_R,\mathbf{x}',\omega)\\ = \int_{\mathbb{S}_0}\mathbf{R}^{\cup}_{C}(\mathbf{x}_R,\mathbf{x},\omega)\mathbf{F}^{+}_{1,A}(\mathbf{x},\mathbf{x}',\omega)\mathrm{d}\mathbf{x},\end{aligned} \tag{A.3.3}$$

and

$$\begin{aligned}\{\mathbf{G}^{+,+}_{C}(\mathbf{x}',\mathbf{x}_R,\omega)\}^{t} - \{\mathbf{F}^{+}_{1,A}(\mathbf{x}_R,\mathbf{x}',\omega)\}^{*}\\ = -\int_{\mathbb{S}_0}\mathbf{R}^{\cup}_{C}(\mathbf{x}_R,\mathbf{x},\omega)\{\mathbf{F}^{-}_{1,A}(\mathbf{x},\mathbf{x}',\omega)\}^{*}\mathrm{d}\mathbf{x},\end{aligned} \tag{A.3.4}$$

(with $\mathbf{x}_R$ just above $\mathbb{S}_0$ and $\mathbf{x}'$ at $\mathbb{S}_1$) for the situation that the earth's surface is transparent. For the acoustic case, these equations can be solved for $\mathbf{F}^{+}_{1,A}(\mathbf{x},\mathbf{x}',\omega)$ and $\mathbf{F}^{-}_{1,A}(\mathbf{x},\mathbf{x}',\omega)$ using the multidimensional Marchenko method [*Wapenaar et al.*, 2014a; *Slob et al.*, 2014; *van der Neut et al.*, 2015a; *Ravasi et al.*, 2016]. The main assumption is that, in addition to $\mathbf{R}^{\cup}_{C}(\mathbf{x}_R,\mathbf{x},\omega)$, an estimate of the direct arrival of $\mathbf{F}^{+}_{1,A}(\mathbf{x},\mathbf{x}',\omega)$ is available. This can be defined in a smooth model of the overburden. The Marchenko method uses causality arguments to separate the Green's functions

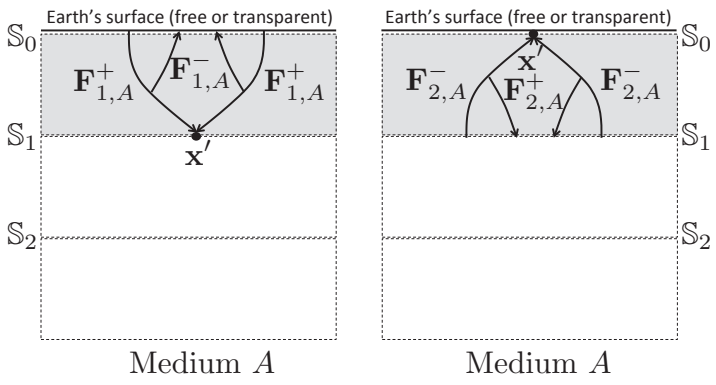

Figure A.6: *Focusing functions* $\mathbf{F}^{\pm}_{1,A}(\mathbf{x},\mathbf{x}',\omega)$ *and* $\mathbf{F}^{\pm}_{2,A}(\mathbf{x},\mathbf{x}',\omega)$ *in medium A. The rays stand for the full focusing functions, including all orders of multiple scattering and, in the elastodynamic case, mode conversion.*

from the focusing functions in the left-hand sides of the time-domain versions of equations (A.3.3) and (A.3.4). The multidimensional Marchenko method also holds for the elastodynamic case, except that in this case an estimate of the direct arrival plus the forward scattered events of $\mathbf{F}^{+}_{1,A}(\mathbf{x},\mathbf{x}',\omega)$ needs to be available [*Wapenaar et al.*, 2014a].

For the situation that the earth's surface is a free surface, equations (A.3.3) and (A.3.4) have been modified by *Singh and Snieder* [2017], *Slob and Wapenaar* [2017] and *Ravasi* [2017], to account for the surface-related multiple reflections. In these approaches, the surface-related multiples are present in the reflection response, but not in the focusing functions. For the target replacement procedure discussed in this paper it is more convenient to use focusing functions that include surface-related multiples. From the derivation in Appendix A.8.1 it follows that for this situation equation (A.3.3) remains valid (but with all quantities now including the surface-related multiples), and that equation (A.3.4) needs to be replaced by

$$\begin{aligned}&\{\mathbf{G}^{+,+}_{C}(\mathbf{x}',\mathbf{x}_R,\omega)\}^t - \{\mathbf{F}^{+}_{1,A}(\mathbf{x}_R,\mathbf{x}',\omega) + \mathbf{r}^{\cap}\mathbf{F}^{-}_{1,A}(\mathbf{x}_R,\mathbf{x}',\omega)\}^*\\ &= \int_{\mathbb{S}_0} \mathbf{R}^{\cup}_{C}(\mathbf{x}_R,\mathbf{x},\omega)\mathbf{r}^{\cap}\{\mathbf{F}^{+}_{1,A}(\mathbf{x},\mathbf{x}',\omega)\}^*\mathrm{d}\mathbf{x}\end{aligned} \tag{A.3.5}$$

(with $\mathbf{x}_R$ just above $\mathbb{S}_0$ and $\mathbf{x}'$ at $\mathbb{S}_1$). The set of equations (A.3.3) and (A.3.5) for the situation with free surface can be solved in a similar way as the set of equations (A.3.3) and (A.3.4) for the situation without free surface. A further discussion of the multidimensional Marchenko method to resolve $\mathbf{F}^{\pm}_{1,A}(\mathbf{x},\mathbf{x}',\omega)$ from the reflection response $\mathbf{R}^{\cup}_{C}(\mathbf{x}_R,\mathbf{x},\omega)$ is beyond the scope of this paper.

Assuming the focusing functions $\mathbf{F}^{+}_{1,A}(\mathbf{x},\mathbf{x}',\omega)$ and $\mathbf{F}^{-}_{1,A}(\mathbf{x},\mathbf{x}',\omega)$ have been found, we use these to resolve the responses of medium A. In Appendix A.8.1, we show that the response to focusing function $\mathbf{F}^{+}_{1,A}(\mathbf{x},\mathbf{x}',\omega)$, when emitted from

$\mathbb{S}_0$ into medium A, can be quantified as follows

$$\mathbf{I}\delta(\mathbf{x}''_{\mathrm{H}} - \mathbf{x}'_{\mathrm{H}}) = \int_{\mathbb{S}_0} \mathbf{T}^+_A(\mathbf{x}'', \mathbf{x}, \omega)\mathbf{F}^+_{1,A}(\mathbf{x}, \mathbf{x}', \omega)\mathrm{d}\mathbf{x}, \tag{A.3.6}$$

for $\mathbf{x}'$ and $\mathbf{x}''$ at $\mathbb{S}_1$, and

$$\mathbf{F}^-_{1,A}(\mathbf{x}_R, \mathbf{x}', \omega) = \int_{\mathbb{S}_0} \mathbf{R}^{\cup}_A(\mathbf{x}_R, \mathbf{x}, \omega)\mathbf{F}^+_{1,A}(\mathbf{x}, \mathbf{x}', \omega)\mathrm{d}\mathbf{x}, \tag{A.3.7}$$

for $\mathbf{x}_R$ just above $\mathbb{S}_0$ and $\mathbf{x}'$ at $\mathbb{S}_1$. Equation (A.3.6) describes the transmission response of medium A to the focusing function. The response at $\mathbb{S}_1$ is a (band-limited) spatial impulse (consistent with the focusing condition of equation (A.3.1)). Equation (A.3.7) describes the reflection response of medium A to the focusing function. The response at $\mathbb{S}_0$ is the upgoing part of the focusing function. Both equations (A.3.6) and (A.3.7) hold for the situation with or without free surface just above $\mathbb{S}_0$. Inverting these equations yields the transmission response $\mathbf{T}^+_A(\mathbf{x}'', \mathbf{x}, \omega)$ (which, according to equation (A.3.6) is the inverse of the focusing function $\mathbf{F}^+_{1,A}(\mathbf{x}, \mathbf{x}', \omega)$) and the reflection response $\mathbf{R}^{\cup}_A(\mathbf{x}_R, \mathbf{x}, \omega)$ of medium A, the overburden (Figure A.5).

To derive the response of medium A from below, we introduce a second focusing function $\mathbf{F}^-_{2,A}(\mathbf{x}, \mathbf{x}', \omega)$ in medium A, with or without free surface just above $\mathbb{S}_0$ (Figure A.6). This time $\mathbf{x}'$ defines a focal point at boundary $\mathbb{S}_0$, i.e., the upper boundary of unit a. Hence, $\mathbf{x}' = (x'_1, x'_2, x_{3,0})$, with $x_{3,0}$ denoting the depth of $\mathbb{S}_0$. The coordinate $\mathbf{x}$ is a variable in medium A. The superscript $-$ refers to the propagation direction at $\mathbf{x}$ (which is upgoing in this case). The focusing function is emitted from all $\mathbf{x}$ at $\mathbb{S}_1$ into medium A. Due to scattering in the inhomogeneous medium, it gives rise to a downgoing function $\mathbf{F}^+_{2,A}(\mathbf{x}, \mathbf{x}', \omega)$. The focusing conditions for $\mathbf{x}$ at $\mathbb{S}_0$ can be formulated as

$$\{\mathbf{F}^-_{2,A}(\mathbf{x}, \mathbf{x}', \omega)\}_{x_3=x_{3,0}} = \mathbf{I}\delta(\mathbf{x}_{\mathrm{H}} - \mathbf{x}'_{\mathrm{H}}), \tag{A.3.8}$$

$$\{\mathbf{F}^+_{2,A}(\mathbf{x}, \mathbf{x}', \omega)\}_{x_3=x_{3,0}} = \mathbf{r}^{\cap}\mathbf{I}\delta(\mathbf{x}_{\mathrm{H}} - \mathbf{x}'_{\mathrm{H}}). \tag{A.3.9}$$

Equation (A.3.8) defines the convergence of $\mathbf{F}^-_{2,A}(\mathbf{x}, \mathbf{x}', \omega)$ to the focal point $\mathbf{x}'$ at $\mathbb{S}_0$, whereas equation (A.3.9) accounts for the downward reflection of the upgoing focusing function at $\mathbb{S}_0$. This term vanishes when the earth's surface is transparent. In Appendix A.8.1, we show that the response to focusing function $\mathbf{F}^-_{2,A}(\mathbf{x}, \mathbf{x}', \omega)$, when emitted from $\mathbb{S}_1$ into medium A, can be quantified as follows

$$\mathbf{I}\delta(\mathbf{x}''_{\mathrm{H}} - \mathbf{x}'_{\mathrm{H}}) = \int_{\mathbb{S}_1} \mathbf{T}^-_A(\mathbf{x}'', \mathbf{x}, \omega)\mathbf{F}^-_{2,A}(\mathbf{x}, \mathbf{x}', \omega)\mathrm{d}\mathbf{x}, \tag{A.3.10}$$

for $\mathbf{x}'$ and $\mathbf{x}''$ at $\mathbb{S}_0$, and

$$\mathbf{F}^+_{2,A}(\mathbf{x}'', \mathbf{x}', \omega) = \int_{\mathbb{S}_1} \mathbf{R}^{\cap}_A(\mathbf{x}'', \mathbf{x}, \omega)\mathbf{F}^-_{2,A}(\mathbf{x}, \mathbf{x}', \omega)\mathrm{d}\mathbf{x}, \tag{A.3.11}$$

for $\mathbf{x}''$ just below $\mathbb{S}_1$ and $\mathbf{x}'$ at $\mathbb{S}_0$. Inverting these equations yields the transmission response $\mathbf{T}^-_A(\mathbf{x}'', \mathbf{x}, \omega)$ (which, according to equation (A.3.10) is the inverse of the

focusing function $\mathbf{F}^-_{2,A}(\mathbf{x},\mathbf{x}',\omega)$) and the reflection response $\mathbf{R}^{\cap}_A(\mathbf{x}'',\mathbf{x},\omega)$ of medium A from below (Figure A.5). In Appendix A.8.1 we show that the focusing functions $\mathbf{F}^+_{2,A}$ and $\mathbf{F}^-_{2,A}$ are related to the focusing functions $\mathbf{F}^+_{1,A}$ and $\mathbf{F}^-_{1,A}$, according to

$$\mathbf{F}^+_{1,A}(\mathbf{x}'',\mathbf{x}',\omega) = \{\mathbf{F}^-_{2,A}(\mathbf{x}',\mathbf{x}'',\omega)\}^t, \tag{A.3.12}$$

and

$$\mathbf{F}^-_{1,A}(\mathbf{x}'',\mathbf{x}',\omega) = -\{\mathbf{F}^+_{2,A}(\mathbf{x}',\mathbf{x}'',\omega)\}^\dagger \tag{A.3.13}$$

(with $\mathbf{x}''$ at $\mathbb{S}_0$ and $\mathbf{x}'$ at $\mathbb{S}_1$) for the situation that the earth's surface is transparent. For the situation that the earth's surface is a free surface, equation (A.3.12) remains valid, and equation (A.3.13) needs to be replaced by

$$(\mathbf{r}^{\cap})^*\mathbf{F}^+_{1,A}(\mathbf{x}'',\mathbf{x}',\omega) = \{\mathbf{F}^+_{2,A}(\mathbf{x}',\mathbf{x}'',\omega)\}^\dagger \tag{A.3.14}$$

(with $\mathbf{x}''$ at $\mathbb{S}_0$ and $\mathbf{x}'$ at $\mathbb{S}_1$).

Next we discuss how to obtain the response of unit c, the underburden, from $\mathbf{R}^{\cup}_C$. We consider again equations (A.3.3) and (A.3.4) (or (A.3.5)), this time with $\mathbf{x}'$ at $\mathbb{S}_2$ and $\mathbf{F}^{\pm}_{1,A}(\mathbf{x},\mathbf{x}',\omega)$ replaced by $\mathbf{F}^{\pm}_{1,B}(\mathbf{x},\mathbf{x}',\omega)$. The focusing functions in medium B can be obtained from the reflection response $\mathbf{R}^{\cup}_C(\mathbf{x}_R,\mathbf{x},\omega)$, using the multidimensional Marchenko method, under the same assumptions as outlined above. Once these focusing functions have been found, they can be substituted into the modified equations (A.3.3) and (A.3.4) (or (A.3.5)), yielding the Green's functions $\mathbf{G}^{\pm,+}_C(\mathbf{x}',\mathbf{x}_R,\omega)$, with $\mathbf{x}_R$ just above $\mathbb{S}_0$ and $\mathbf{x}'$ at $\mathbb{S}_2$. Analogous to equation (A.2.20), these Green's function are mutually related via

$$\mathbf{G}^{-,+}_C(\mathbf{x}',\mathbf{x}_R,\omega) = \int_{\mathbb{S}_2} \mathbf{R}^{\cup}_c(\mathbf{x}',\mathbf{x},\omega)\mathbf{G}^{+,+}_C(\mathbf{x},\mathbf{x}_R,\omega)\mathrm{d}\mathbf{x}. \tag{A.3.15}$$

Inversion of equation (A.3.15) yields the reflection response $\mathbf{R}^{\cup}_c(\mathbf{x}',\mathbf{x},\omega)$ for $\mathbf{x}$ and $\mathbf{x}'$ at $\mathbb{S}_2$ (Figure A.5).

We summarise the steps discussed in this section. Starting with the reflection response of the entire medium, $\mathbf{R}^{\cup}_C(\mathbf{x}_R,\mathbf{x},\omega)$, use the Marchenko method to derive the focusing functions $\mathbf{F}^{\pm}_{1,A}(\mathbf{x},\mathbf{x}',\omega)$ and $\mathbf{F}^{\pm}_{2,A}(\mathbf{x},\mathbf{x}',\omega)$ for medium A. Resolve the responses of the overburden, $\mathbf{T}^+_A(\mathbf{x}'',\mathbf{x},\omega)$, $\mathbf{R}^{\cup}_A(\mathbf{x}_R,\mathbf{x},\omega)$, $\mathbf{T}^-_A(\mathbf{x}'',\mathbf{x},\omega)$ and $\mathbf{R}^{\cap}_A(\mathbf{x}'',\mathbf{x},\omega)$, by inverting equations (A.3.6), (A.3.7), (A.3.10) and (A.3.11). Next, use the Marchenko method to derive the Green's functions $\mathbf{G}^{\pm,+}_C(\mathbf{x}',\mathbf{x}_R,\omega)$, for $\mathbf{x}'$ at $\mathbb{S}_2$. Resolve the reflection response of the underburden, $\mathbf{R}^{\cup}_c(\mathbf{x}',\mathbf{x},\omega)$, by inverting equation (A.3.15). The resolved responses are free of an imprint of unit b, the target zone.

A.4 Inserting a new target zone into the reflection response

Given the retrieved responses of the overburden (medium A) and underburden (unit c) and a model of the changed target zone (unit $\bar{b}$), our aim is to obtain the reflection response $\bar{\mathbf{R}}^{\cup}_C(\mathbf{x}_R,\mathbf{x}_S,\omega)$ of the entire medium with the new target zone (medium $\bar{C}$). The procedure starts by numerically modelling the reflection and transmission

responses of the new target zone, $\bar{\mathbf{R}}_b^{\cup}(\mathbf{x}', \mathbf{x}, \omega)$ and $\bar{\mathbf{T}}_b^{+}(\mathbf{x}', \mathbf{x}, \omega)$ (Figure A.5). Next, the response $\bar{\mathbf{R}}_C^{\cup}(\mathbf{x}_R, \mathbf{x}_S, \omega)$ is built up step by step, using equation (A.2.24) as the underlying representation. Analogous to equations (A.2.21) and (A.2.22), we rewrite equation (A.2.24) as a cascade of two representations, as follows

$$\begin{aligned}\bar{\mathbf{R}}_B^{\cup}(\mathbf{x}_R, \mathbf{x}_S, \omega) =& \mathbf{R}_A^{\cup}(\mathbf{x}_R, \mathbf{x}_S, \omega) \\ &+ \int_{\mathbb{S}_1}\int_{\mathbb{S}_1} \mathbf{T}_A^{-}(\mathbf{x}_R, \mathbf{x}', \omega)\bar{\mathbf{R}}_b^{\cup}(\mathbf{x}', \mathbf{x}, \omega)\bar{\mathbf{G}}_B^{+,+}(\mathbf{x}, \mathbf{x}_S, \omega)\mathrm{d}\mathbf{x}\mathrm{d}\mathbf{x}',\end{aligned} \tag{A.4.1}$$

followed by

$$\begin{aligned}\bar{\mathbf{R}}_C^{\cup}(\mathbf{x}_R, \mathbf{x}_S, \omega) =& \bar{\mathbf{R}}_B^{\cup}(\mathbf{x}_R, \mathbf{x}_S, \omega) \\ &+ \int_{\mathbb{S}_2}\int_{\mathbb{S}_2} \bar{\mathbf{T}}_B^{-}(\mathbf{x}_R, \mathbf{x}', \omega)\mathbf{R}_c^{\cup}(\mathbf{x}', \mathbf{x}, \omega)\bar{\mathbf{G}}_C^{+,+}(\mathbf{x}, \mathbf{x}_S, \omega)\mathrm{d}\mathbf{x}\mathrm{d}\mathbf{x}',\end{aligned} \tag{A.4.2}$$

for $\mathbf{x}_S$ and $\mathbf{x}_R$ just above $\mathbb{S}_0$. Quantities in these representations that still need to be determined are $\bar{\mathbf{G}}_B^{+,+}(\mathbf{x}, \mathbf{x}_S, \omega)$, $\bar{\mathbf{G}}_C^{+,+}(\mathbf{x}, \mathbf{x}_S, \omega)$ and $\bar{\mathbf{T}}_B^{-}(\mathbf{x}_R, \mathbf{x}', \omega)$.

In Appendix A.8.2, we derive the following equation for the unknown $\bar{\mathbf{G}}_B^{+,+}(\mathbf{x}, \mathbf{x}_S, \omega)$

$$\mathbf{T}_A^{+}(\mathbf{x}'', \mathbf{x}_S, \omega) = \int_{\mathbb{S}_1} \bar{\mathbf{C}}_{Ab}(\mathbf{x}'', \mathbf{x}, \omega)\bar{\mathbf{G}}_B^{+,+}(\mathbf{x}, \mathbf{x}_S, \omega)\mathrm{d}\mathbf{x}, \tag{A.4.3}$$

with

$$\begin{aligned}\bar{\mathbf{C}}_{Ab}(\mathbf{x}'', \mathbf{x}, \omega) =& \mathbf{I}\delta(\mathbf{x}''_{\mathrm{H}} - \mathbf{x}_{\mathrm{H}}) \\ &- \int_{\mathbb{S}_1} \mathbf{R}_A^{\cap}(\mathbf{x}'', \mathbf{x}', \omega)\bar{\mathbf{R}}_b^{\cup}(\mathbf{x}', \mathbf{x}, \omega)\mathrm{d}\mathbf{x}',\end{aligned} \tag{A.4.4}$$

for $\mathbf{x}_S$ just above $\mathbb{S}_0$, and $\mathbf{x}$ and $\mathbf{x}''$ at $\mathbb{S}_1$. Since $\mathbf{T}_A^{+}$, $\mathbf{R}_A^{\cap}$ and $\bar{\mathbf{R}}_b^{\cup}$ are known, $\bar{\mathbf{G}}_B^{+,+}(\mathbf{x}, \mathbf{x}_S, \omega)$ can be resolved by inverting equation (A.4.3). Substituting this into equation (A.4.1), together with the other quantities that are already known, yields $\bar{\mathbf{R}}_B^{\cup}(\mathbf{x}_R, \mathbf{x}_S, \omega)$.

Similarly $\bar{\mathbf{G}}_C^{+,+}(\mathbf{x}, \mathbf{x}_S, \omega)$ can be resolved by inverting

$$\bar{\mathbf{T}}_B^{+}(\mathbf{x}'', \mathbf{x}_S, \omega) = \int_{\mathbb{S}_2} \bar{\mathbf{C}}_{Bc}(\mathbf{x}'', \mathbf{x}, \omega)\bar{\mathbf{G}}_C^{+,+}(\mathbf{x}, \mathbf{x}_S, \omega)\mathrm{d}\mathbf{x}, \tag{A.4.5}$$

with

$$\begin{aligned}\bar{\mathbf{C}}_{Bc}(\mathbf{x}'', \mathbf{x}, \omega) =& \mathbf{I}\delta(\mathbf{x}''_{\mathrm{H}} - \mathbf{x}_{\mathrm{H}}) \\ &- \int_{\mathbb{S}_2} \bar{\mathbf{R}}_B^{\cap}(\mathbf{x}'', \mathbf{x}', \omega)\mathbf{R}_c^{\cup}(\mathbf{x}', \mathbf{x}, \omega)\mathrm{d}\mathbf{x}',\end{aligned} \tag{A.4.6}$$

for $\mathbf{x}_S$ just above $\mathbb{S}_0$, and $\mathbf{x}$ and $\mathbf{x}''$ at $\mathbb{S}_2$. This requires expressions for $\bar{\mathbf{T}}_B^{+}(\mathbf{x}'', \mathbf{x}_S, \omega)$ and $\bar{\mathbf{R}}_B^{\cap}(\mathbf{x}'', \mathbf{x}', \omega)$.

In Appendix A.8.2 we derive the following representation for $\bar{\mathbf{T}}_B^+(\mathbf{x}'', \mathbf{x}_S, \omega)$

$$\bar{\mathbf{T}}_B^+(\mathbf{x}'', \mathbf{x}_S, \omega) = \int_{\mathbb{S}_1} \bar{\mathbf{T}}_b^+(\mathbf{x}'', \mathbf{x}, \omega)\bar{\mathbf{G}}_B^{+,+}(\mathbf{x}, \mathbf{x}_S, \omega)\mathrm{d}\mathbf{x}, \tag{A.4.7}$$

for $\mathbf{x}_S$ just above $\mathbb{S}_0$ and $\mathbf{x}''$ at $\mathbb{S}_2$. Note that $\bar{\mathbf{T}}_B^-(\mathbf{x}_R, \mathbf{x}', \omega)$, needed in equation (A.4.2), follows by applying equation (A.2.18).

In Appendix A.8.2, we derive the following equation for the unknown $\bar{\mathbf{R}}_B^{\cap}(\mathbf{x}, \mathbf{x}', \omega)$

$$\begin{aligned}\int_{\mathbb{S}_2} \{\bar{\mathbf{T}}_B^-(\mathbf{x}_S, \mathbf{x}, \omega)\}^* \bar{\mathbf{R}}_B^{\cap}(\mathbf{x}, \mathbf{x}', \omega)\mathrm{d}\mathbf{x} = \\ - \int_{\mathbb{S}_0} \{\bar{\mathbf{R}}_B^{\cup}(\mathbf{x}_S, \mathbf{x}, \omega)\}^* \bar{\mathbf{T}}_B^-(\mathbf{x}, \mathbf{x}', \omega)\mathrm{d}\mathbf{x},\end{aligned} \tag{A.4.8}$$

(with $\mathbf{x}_S$ just above $\mathbb{S}_0$ and $\mathbf{x}'$ at $\mathbb{S}_2$) for the situation that the earth's surface is transparent. For the situation that the earth's surface is a free surface, this equation needs to be replaced by

$$\int_{\mathbb{S}_2} \{\bar{\mathbf{T}}_B^-(\mathbf{x}_S, \mathbf{x}, \omega)\}^* \bar{\mathbf{R}}_B^{\cap}(\mathbf{x}, \mathbf{x}', \omega)\mathrm{d}\mathbf{x} = \mathbf{r}^{\cap}\bar{\mathbf{T}}_B^-(\mathbf{x}_S, \mathbf{x}', \omega), \tag{A.4.9}$$

(with $\mathbf{x}_S$ just above $\mathbb{S}_0$ and $\mathbf{x}'$ at $\mathbb{S}_2$). Since $\bar{\mathbf{R}}_B^{\cup}$ and $\bar{\mathbf{T}}_B^-$ are known, $\bar{\mathbf{R}}_B^{\cap}(\mathbf{x}, \mathbf{x}', \omega)$ can be resolved by inverting either equation (A.4.8) or (A.4.9).

We summarise the steps discussed in this section. Starting with a model of the new target zone, determine its responses $\bar{\mathbf{R}}_b^{\cup}(\mathbf{x}', \mathbf{x}, \omega)$ and $\bar{\mathbf{T}}_b^+(\mathbf{x}', \mathbf{x}, \omega)$ by numerical modelling. Next, resolve the Green's function of medium $\bar{B}$, $\bar{\mathbf{G}}_B^{+,+}(\mathbf{x}, \mathbf{x}_S, \omega)$, by inverting equation (A.4.3). Substitute this, together with $\bar{\mathbf{R}}_b^{\cup}(\mathbf{x}', \mathbf{x}, \omega)$, into equation (A.4.1), which yields the reflection response of medium $\bar{B}$, $\bar{\mathbf{R}}_B^{\cup}(\mathbf{x}_R, \mathbf{x}_S, \omega)$. Resolve $\bar{\mathbf{R}}_B^{\cap}(\mathbf{x}, \mathbf{x}', \omega)$ by inverting equation (A.4.8) or (A.4.9). Substitute this into equation (A.4.6) and, subsequently, substitute the result $\bar{\mathbf{C}}_{Bc}(\mathbf{x}'', \mathbf{x}, \omega)$ into equation (A.4.5). Resolve $\bar{\mathbf{G}}_C^{+,+}(\mathbf{x}, \mathbf{x}_S, \omega)$ by inverting equation (A.4.5). Substitute this, together with the other quantities that are already known, into equation (A.4.2), which yields the sought reflection response $\bar{\mathbf{R}}_C^{\cup}(\mathbf{x}_R, \mathbf{x}_S, \omega)$.

A.5 Numerical examples

We illustrate the proposed method with two numerical examples. Although the method holds for vertically and laterally inhomogeneous media, for simplicity we consider laterally invariant media in the following examples.

In the first example, we consider the acoustic plane-wave response of a horizontally layered medium, without free surface (which is the situation after surface-related multiple elimination). Figure A.7 shows the horizontally layered medium. The velocities are given in m/s, the mass densities in kg/m^3, and the depth of the interfaces (denoted by the solid lines) in m. To emphasise internal multiples, the mass densities have the same numerical values as the propagation velocities. The layer between 1200 m and 1400 m represents a reservoir (hence, this is the layer in

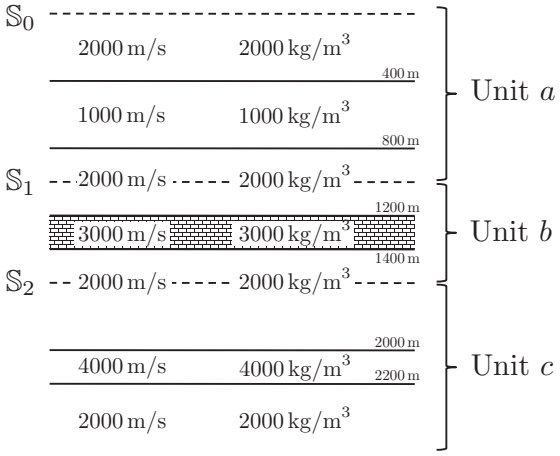

Figure A.7: *Horizontally layered medium for the plane-wave experiment, with the three units indicated. The earth's surface is considered transparent.*

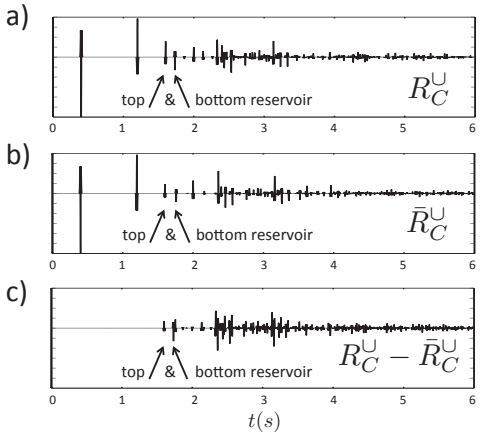

Figure A.8: *(a) Numerically modelled reflection response of the model of Figure A.7. (b) Numerically modelled time-lapse response. (c) The difference of the responses in (a) and (b).*

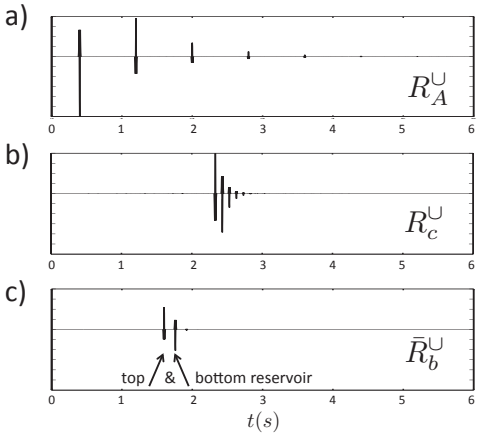

Figure A.9: *(a) The response of medium A (the overburden), retrieved from $R_C^{\cup}(t)$. (b) The response of unit c (the underburden), retrieved from $R_C^{\cup}(t)$. (c) Numerically modelled response of unit $\bar{b}$ (the new target zone).*

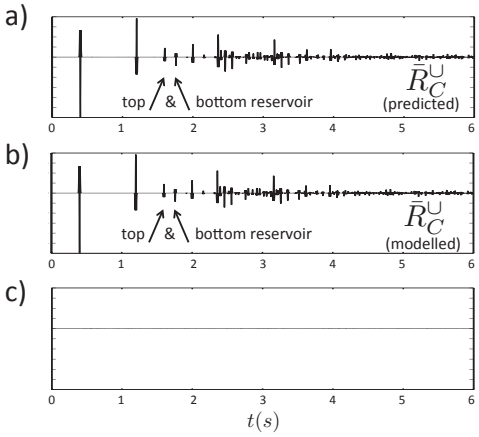

Figure A.10: *(a) The predicted time-lapse response $\bar{R}_C^{\cup}(t)$, constructed from the responses in Figure A.9. (b) For comparison, the numerically modelled time-lapse response. (c) The difference of the responses in (a) and (b).*

which changes will take place). The target zone (unit b) includes this reservoir layer (the remainder of the target zone will, however, not undergo any changes). Figure A.8(a) shows the numerically modelled plane-wave reflection response $R^{\cup}_C(t)$ at $\mathbb{S}_0$ in the time domain, convolved with a Ricker wavelet with a central frequency of 50 Hz (note that we replaced the boldface symbol $\mathbf{R}$ by a plain R, because the acoustic response is a scalar function; moreover, we replaced ω by t because the response is shown in the time domain). The reflections from the top and bottom of the reservoir are indicated by arrows. We consider a time-lapse scenario, in which the velocity in the reservoir is changed from 3000 m/s to 2500 m/s (and a similar change is applied to the mass density). Figure A.8(b) shows the numerically modelled time-lapse reflection response $\bar{R}^{\cup}_C(t)$ and Figure A.8(c) shows the difference $R^{\cup}_C(t) - \bar{R}^{\cup}_C(t)$. Note the significant multiple coda, following the difference response of the reservoir. Our aim is to show that the time-lapse response (Figure A.8(b)) can be predicted from the original response (Figure A.8(a)) by target replacement.

Following the procedure discussed in Section A.3 (simplified for the 1D situation), we remove the response of the target zone from the reflection response $R^{\cup}_C(t)$. The overburden response $R^{\cup}_A(t)$, resolved from equation (A.3.7), is shown in the time domain in Figure A.9(a). Note that it contains the first two events of $R^{\cup}_C(t)$ and a coda due to the internal multiples in the low-velocity layer in the overburden. The underburden response $R^{\cup}_c(t)$, resolved from equation (A.3.15), is shown in Figure A.9(b). For display purposes it has been shifted in time, so that the travel times correspond with those in Figure A.8(a).

Following the procedure discussed in Section A.4 (simplified for the 1D situation), we predict the time-lapse response. To this end, we first model the response of the new target zone, $\bar{R}^{\cup}_b(t)$. This is shown in Figure A.9(c). For display purposes, it has been shifted in time so that the travel time to the top of the reservoir corresponds with that in Figure A.8(a). The predicted time-lapse reflection response at the surface, $\bar{R}^{\cup}_C(t)$, obtained with the representations of equations (A.4.1) and (A.4.2), is shown in the time domain in Figure A.10(a). The numerically modelled response of Figure A.8(b), is once more shown (as a reference) in Figure A.10(b). The difference of the predicted and modelled responses is shown in Figure A.10(c) and appears to be practically zero. This confirms that the new reflection response $\bar{R}^{\cup}_C(t)$ has been very accurately predicted by the proposed method.

For the next example, we consider a 2D acoustic point-source response of a horizontally layered medium. The medium is shown in Figure A.11. Note that the overburden and underburden contain more layers than in the previous example. Figure A.12(a) shows the numerically modelled response $R^{\cup}_C(\mathbf{x}_R, \mathbf{x}_S, t)$ at the surface $\mathbb{S}_0$ in the time domain, for a fixed source at $\mathbf{x}_S = (0, 0)$ and variable receivers at $\mathbf{x}_R = (x_{1,R}, 0)$. Because the medium is horizontally layered, the responses to sources at other positions at $\mathbb{S}_0$ are simply laterally shifted versions of the response in Figure A.12(a). In the time-lapse scenario, the velocity in the reservoir layer is changed from 3000 m/s to 2500 m/s (and a similar change is applied to the mass density). Figure A.12(b) shows the difference of the numerically modelled responses $R^{\cup}_C(\mathbf{x}_R, \mathbf{x}_S, t)$ and $\bar{R}^{\cup}_C(\mathbf{x}_R, \mathbf{x}_S, t)$. The responses in this and the following figures are displayed with a small time-dependent gain of $\exp(0.5 * t)$ to emphasise the internal multiples.

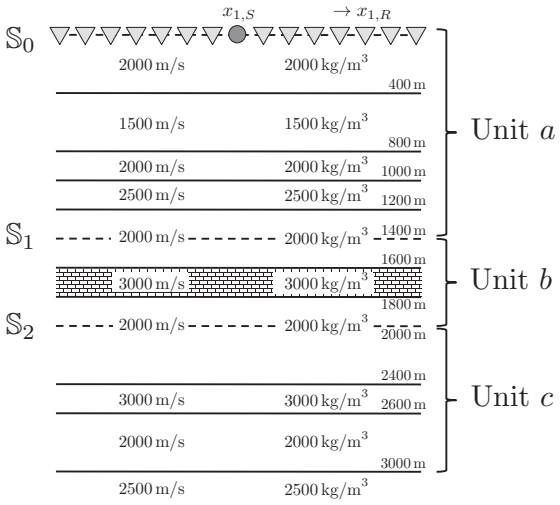

Figure A.11: *Horizontally layered medium for the 2D experiment.*

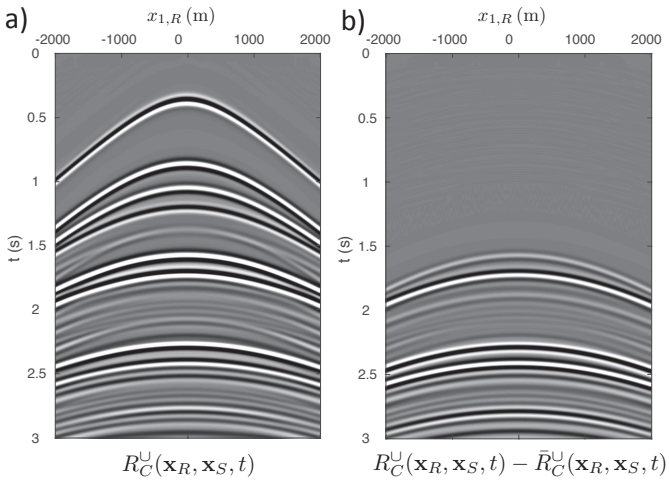

Figure A.12: *(a) Numerically modelled 2D reflection response. (b) Numerically modelled difference response.*

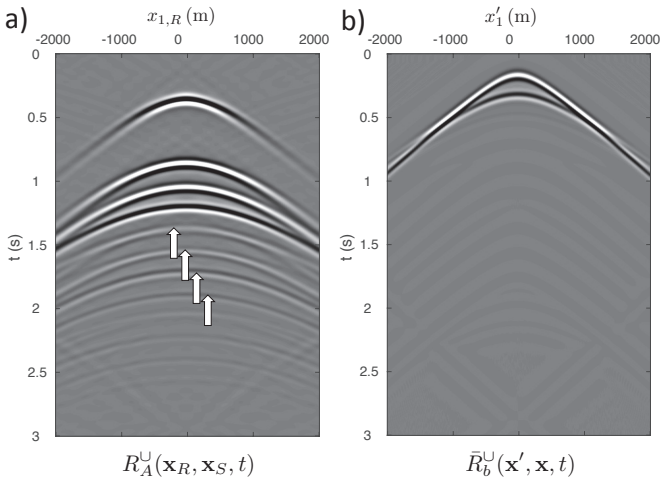

Figure A.13: *(a) The response of medium A (the overburden), retrieved from $R_C^{\cup}(\mathbf{x}_R, \mathbf{x}_S, t)$. (b) Numerically modelled response of the new target zone.*

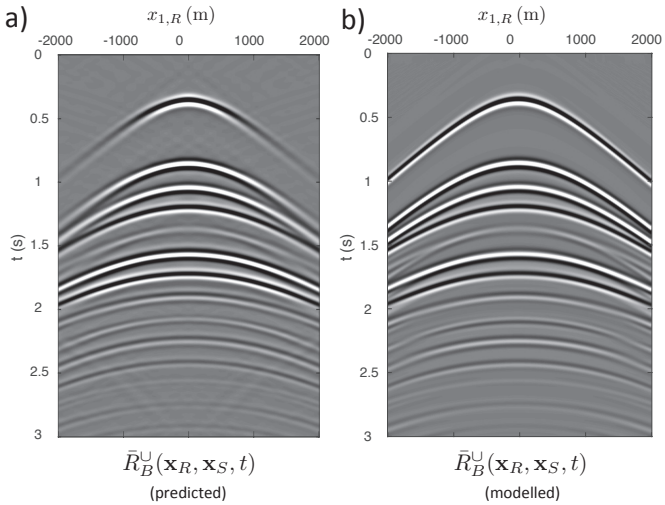

Figure A.14: *(a) The predicted time-lapse response $\bar{R}_B^{\cup}(\mathbf{x}_R, \mathbf{x}_S, t)$, constructed from the responses in Figure A.13. (b) For comparison, the numerically modelled time-lapse response.*

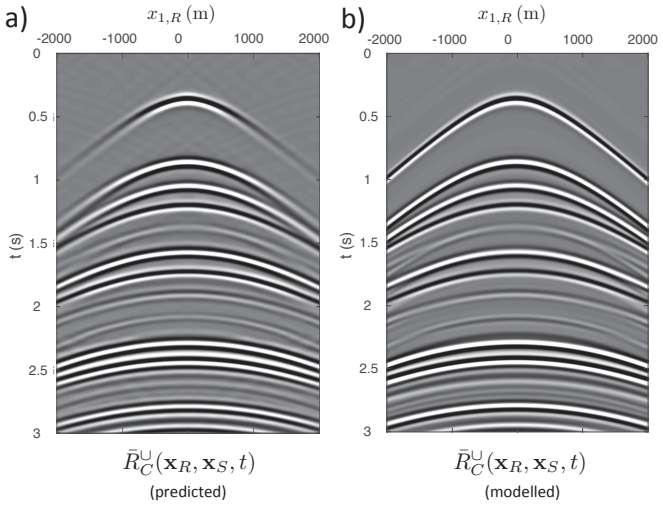

Figure A.15: *(a) The predicted time-lapse response $\bar{R}^{\cup}_{C}(\mathbf{x}_R, \mathbf{x}_S, t)$, constructed from $\bar{R}^{\cup}_{B}(\mathbf{x}_R, \mathbf{x}_S, t)$ and the response of the underburden. (b) For comparison, the numerically modelled time-lapse response.*

We use our standard implementation of the Marchenko method [*Thorbecke et al.*, 2017] for the estimation of the focusing functions. Next, because the medium is horizontally layered, we efficiently carry out the layer replacement method in the wavenumber-frequency domain (hence, all integrals from equation (A.3.6) onward reduce to straightforward products of the transformed quantities). Figure A.13(a) shows the overburden response $R^{\cup}_{A}(\mathbf{x}_R, \mathbf{x}_S, t)$, resolved from equation (A.3.7) in the wavenumber-frequency domain and transformed back to the space-time domain. Note that the internal multiples of the overburden, indicated by the arrows, have been recovered from behind the reflection response of the reservoir layer. The modelled response of the new target zone, $\bar{R}^{\cup}_{b}(\mathbf{x}', \mathbf{x}, t)$ at $\mathbb{S}_1$, is shown in Figure A.13(b), for a fixed source at $\mathbf{x} = (0, 1400)$ m and variable receivers at $\mathbf{x}' = (x'_1, 1400)$ m. The predicted time-lapse reflection response at the surface of the overburden and target zone, $\bar{R}^{\cup}_{B}(\mathbf{x}_R, \mathbf{x}_S, t)$, obtained with the representation of equation (A.4.1) in the wavenumber-frequency domain, is shown in Figure A.14(a). The numerically modelled time-lapse response is shown (as a reference) in Figure A.14(b). Next, the response of the underburden is included, using the representation of equation (A.4.2) in the wavenumber-frequency domain. This yields the predicted time-lapse reflection response at the surface of the entire medium, $\bar{R}^{\cup}_{C}(\mathbf{x}_R, \mathbf{x}_S, t)$, see Figure A.15(a). The numerically modelled time-lapse response of the entire medium is shown in Figure A.15(b). Although the match is not as perfect as in the 1D example (Figure A.10(c)), Figure A.15 shows that the 2D time-lapse response has been accurately predicted. We used dip-filtering to suppress artefacts related to the finite aperture and the negligence of evanescent waves. This explains the diminishing

amplitudes of the early reflections at large offsets.

A.6 Discussion

The numerical examples in the previous section show that under ideal circumstances the proposed method accurately predicts the time-lapse responses. Hence, these examples validate the theory. In practice there will be several factors that limit the accuracy. First, the direct arrivals of the focusing function $\mathbf{F}^{\pm}_{1,A}$, needed to initiate the Marchenko scheme, are in practice defined in estimated models of the medium. Hence, the amplitudes and traveltimes of these direct arrivals will not be exact. The Marchenko method is robust to small-to-moderate errors in the direct arrival, in the sense that it predicts the multiples in the focusing functions and Green's functions, but these predicted multiples will exhibit similar amplitude and travel time errors as the direct arrival [*Wapenaar et al.*, 2014b; *Broggini et al.*, 2014]. The errors in $\mathbf{F}^{+}_{1,A}$ and $\mathbf{F}^{-}_{1,A}$ largely compensate each other in the inversion of equation (A.3.7), to obtain the overburden response $\mathbf{R}^{\cup}_{A}$. Hence, $\mathbf{R}^{\cup}_{A}$ will be retrieved very accurately, despite the errors in the direct arrival (it has been previously observed that the Marchenko method for obtaining data at the surface is very robust [*Meles et al.*, 2016; *van der Neut and Wapenaar*, 2016]). This implies that multiples generated in the overburden are accurately separated from the response of deeper layers. The response of the overburden from below, $\mathbf{R}^{\cap}_{A}$, is obtained by inverting equation (A.3.11). Here the amplitude errors in $\mathbf{F}^{+}_{2,A}$ and $\mathbf{F}^{-}_{2,A}$ largely compensate each other, but travel time errors will result in an overall time shift of $\mathbf{R}^{\cap}_{A}$. A similar remark holds for the underburden response $\mathbf{R}^{\cup}_{c}$. These errors will propagate into the predicted time-lapse response. We expect that the errors in the predicted primaries and low order multiples will be of the same order as the errors in the direct arrivals and that these errors will grow for higher order multiples.

The accuracy of the predicted time-lapse response will further be limited by losses in the medium, inaccuracies in the deconvolution for the source wavelet, the finite length of the acquisition aperture and incomplete sampling (particularly for 3D applications). Currently much research is going on to improve the Marchenko method to address these issues [*van der Neut and Wapenaar*, 2016; *Ravasi et al.*, 2016; *Slob*, 2016; *Staring et al.*, 2017]. The proposed target replacement scheme will benefit from these developments.

The computational costs of the proposed method depend on the implementation. For the numerical examples in the previous section we took advantage of the fact that the medium is horizontally layered. We implemented the 2D layer replacement in the wavenumber-frequency domain. This implies that the inversion of the various integral equations is replaced by a straightforward scalar inversion per wavenumber-frequency combination. For laterally varying media, the integral equations should be solved in the space-frequency domain. After discretisation, this comes to a matrix inversion for each frequency component. In several cases (equations (A.4.3) and (A.4.5)) the matrix inversion can efficiently be replaced by a series expansion, which can be terminated after a few terms, depending on the number of multiples that need

to be taken into account. All at all, removing the target zone (section A.3) requires applying the Marchenko method at two depth levels ($\mathbb{S}_1$ and $\mathbb{S}_2$) and five matrix inversions (per frequency component) to solve integral equations (A.3.6), (A.3.7), (A.3.10), (A.3.11) and (A.3.15). Inserting the new target zone (section A.4) requires numerical modelling of the target zone response and three matrix inversions (per frequency component) to solve integral equations (A.4.3), (A.4.5) and (A.4.8). The costs for substituting the results into equations (A.4.1) and (A.4.2) are negligible in comparison with the matrix inversions. Despite the significant number of steps for the entire process, the total costs should be seen in perspective with other methods. In comparison with numerically modelling the entire time-lapse reflection response, our method requires numerical modelling of the target zone response only. The additional costs for the Marchenko method and the matrix inversions are significant but not excessive. For example, applying the Marchenko method at two depth levels is feasible, considering the fact that some Marchenko imaging methods apply this method for a large range of depth levels in an image volume [*Broggini et al.*, 2014; *Behura et al.*, 2014]. The trade-off between the cost reduction for the numerical modelling and the cost increase related to the Marchenko method and the matrix inversions depends on the implementation details and needs further investigation.

A.7 Conclusions

We have proposed an efficient two-step process to replace the response of a target zone in a reflection response at the earth's surface. In the first step, the response of the original target zone is removed from the reflection response, using the Marchenko method. In the second step, the modelled response of a new target zone is inserted between the overburden and underburden responses. The method holds for vertically and laterally inhomogeneous lossless media. It fully accounts for all orders of multiple scattering and, in the elastodynamic case, for wave conversion. It can be employed to predict the time-lapse reflection response for a range of target-zone scenarios. For this purpose, the first step needs to be carried out only once. Only the second step needs to be repeated for each target-zone model. Since the target zone covers only a small part of the entire medium, repeated modelling of the target-zone response (and inserting it each time between the same overburden and underburden responses) is a much more efficient process than repeated modelling of the entire reflection response, but there are also additional costs related to the Marchenko method and several matrix inversions. This method may find applications in time-lapse full wave form inversion, for example to monitor fluid flow in an aquifer, subsurface storage of waste products, or production of a hydrocarbon reservoir. Since all multiples are taken into account, the coda following the response of the target zone may be employed in the inversion. Because of the high sensitivity of the coda for changes in the medium [*Snieder et al.*, 2002], this may ultimately improve the resolution of the inverted time-lapse changes. Finally, when medium changes are not restricted to a reservoir, the target zone should be taken sufficiently large to include those parts of the embedding medium in which changes take place.

Table A.3: *Quantities to derive Marchenko representations.*

	State A: Medium C Source at $\mathbf{x}_R$ just above $\mathbb{S}_0$	State B: Medium A Focus at $\mathbf{x}'$ at $\mathbb{S}_1$
$\mathbb{S}_0$	$\mathbf{p}_A^+(\mathbf{x},\omega) \rightarrow \mathbf{I}\delta(\mathbf{x}_{\mathrm{H}} - \mathbf{x}_{\mathrm{H},R})$ $+\mathbf{r}^{\cap}\mathbf{R}_C^{\cup}(\mathbf{x},\mathbf{x}_R,\omega)$ $\mathbf{p}_A^-(\mathbf{x},\omega) \rightarrow \mathbf{R}_C^{\cup}(\mathbf{x},\mathbf{x}_R,\omega)$	$\mathbf{p}_B^+(\mathbf{x},\omega) \rightarrow \mathbf{F}_{1,A}^+(\mathbf{x},\mathbf{x}',\omega)$ $+\mathbf{r}^{\cap}\mathbf{F}_{1,A}^-(\mathbf{x},\mathbf{x}',\omega)$ $\mathbf{p}_B^-(\mathbf{x},\omega) \rightarrow \mathbf{F}_{1,A}^-(\mathbf{x},\mathbf{x}',\omega)$
$\mathbb{S}_1$	$\mathbf{p}_A^+(\mathbf{x},\omega) \rightarrow \mathbf{G}_C^{+,+}(\mathbf{x},\mathbf{x}_R,\omega)$ $\mathbf{p}_A^-(\mathbf{x},\omega) \rightarrow \mathbf{G}_C^{-,+}(\mathbf{x},\mathbf{x}_R,\omega)$	$\mathbf{p}_B^+(\mathbf{x},\omega) \rightarrow \mathbf{I}\delta(\mathbf{x}_{\mathrm{H}} - \mathbf{x}'_{\mathrm{H}})$ $\mathbf{p}_B^-(\mathbf{x},\omega) \rightarrow \mathbf{O}$

This will of course have a limiting effect on the efficiency gain.

A.8 Appendices

A.8.1 Derivations for Section A.3

Representations for Marchenko method

We derive relations between $\mathbf{R}_C^{\cup}$, $\mathbf{F}_{1,A}^{\pm}$ and $\mathbf{G}_C^{-,\pm}$. State A in Table A.1 is defined in a similar way as state B in Table 1, except that here we consider medium C, and we choose a source at $\mathbf{x}_R$, just above $\mathbb{S}_0$. State B in Table A.1 represents the focusing function, which is defined in medium A. At $\mathbb{S}_0$, the downgoing field consists of the emitted focusing function $\mathbf{F}_{1,A}^+(\mathbf{x},\mathbf{x}',\omega)$, plus the downward reflected upgoing part of the focusing function. The latter term is absent when the earth's surface is transparent. The upgoing field at $\mathbb{S}_0$ is given by the upgoing part of the focusing function. The quantities at $\mathbb{S}_1$ in state B represent the focusing conditions, formulated by equations (A.3.1) and (A.3.2).

We substitute the quantities of Table A.1 into equation (A.2.1). Using equations (A.2.10) and (A.2.15), setting $m = 0$ and $n = 1$, this gives

$$\begin{aligned}\{\mathbf{G}_C^{-,+}(\mathbf{x}',\mathbf{x}_R,\omega)\}^t + \mathbf{F}_{1,A}^-(\mathbf{x}_R,\mathbf{x}',\omega)& \\ = \int_{\mathbb{S}_0} \mathbf{R}_C^{\cup}(\mathbf{x}_R,\mathbf{x},\omega)\mathbf{F}_{1,A}^+(\mathbf{x},\mathbf{x}',\omega)\mathrm{d}\mathbf{x},&\end{aligned} \tag{A.8.1}$$

for $\mathbf{x}_R$ just above $\mathbb{S}_0$ and $\mathbf{x}'$ at $\mathbb{S}_1$. Next, we substitute the quantities of Table A.1 into equation (A.2.2). Using equations (A.2.10) and (A.2.15), setting $m = 0$ and

Table A.4: *Quantities to derive the response to* $\mathbf{F}^+_{1,A}$.

	State A: Medium A Source at $\mathbf{x}''$ just below $\mathbb{S}_1$	State B: Medium A Focus at $\mathbf{x}'$ at $\mathbb{S}_1$
$\mathbb{S}_0$	$\mathbf{p}^+_A(\mathbf{x},\omega) \rightarrow \mathbf{r}^{\cap}\mathbf{T}^-_A(\mathbf{x},\mathbf{x}'',\omega)$	$\mathbf{p}^+_B(\mathbf{x},\omega) \rightarrow \mathbf{F}^+_{1,A}(\mathbf{x},\mathbf{x}',\omega)$ $+\mathbf{r}^{\cap}\mathbf{F}^-_{1,A}(\mathbf{x},\mathbf{x}',\omega)$
	$\mathbf{p}^-_A(\mathbf{x},\omega) \rightarrow \mathbf{T}^-_A(\mathbf{x},\mathbf{x}'',\omega)$	$\mathbf{p}^-_B(\mathbf{x},\omega) \rightarrow \mathbf{F}^-_{1,A}(\mathbf{x},\mathbf{x}',\omega)$
$\mathbb{S}_1$	$\mathbf{p}^+_A(\mathbf{x},\omega) \rightarrow \mathbf{R}^{\cap}_A(\mathbf{x},\mathbf{x}'',\omega)$ $\mathbf{p}^-_A(\mathbf{x},\omega) \rightarrow \mathbf{I}\delta(\mathbf{x}_{\mathrm{H}}-\mathbf{x}''_{\mathrm{H}})$	$\mathbf{p}^+_B(\mathbf{x},\omega) \rightarrow \mathbf{I}\delta(\mathbf{x}_{\mathrm{H}}-\mathbf{x}'_{\mathrm{H}})$ $\mathbf{p}^-_B(\mathbf{x},\omega) \rightarrow \mathbf{O}$

$n = 1$, this gives

$$\begin{aligned}
&\{\mathbf{G}^{+,+}_C(\mathbf{x}',\mathbf{x}_R,\omega)\}^t - \{\mathbf{F}^+_{1,A}(\mathbf{x}_R,\mathbf{x}',\omega) + \mathbf{r}^{\cap}\mathbf{F}^-_{1,A}(\mathbf{x}_R,\mathbf{x}',\omega)\}^* \\
&= \int_{\mathbb{S}_0} \mathbf{R}^{\cup}_C(\mathbf{x}_R,\mathbf{x},\omega)\mathbf{r}^{\cap}\{\mathbf{F}^+_{1,A}(\mathbf{x},\mathbf{x}',\omega)\}^*\mathrm{d}\mathbf{x} \\
&- \int_{\mathbb{S}_0} \mathbf{R}^{\cup}_C(\mathbf{x}_R,\mathbf{x},\omega)\{\mathbf{I} - (\mathbf{r}^{\cap})^{\dagger}\mathbf{r}^{\cap}\}^*\{\mathbf{F}^-_{1,A}(\mathbf{x},\mathbf{x}',\omega)\}^*\mathrm{d}\mathbf{x}, \qquad \text{(A.8.2)}
\end{aligned}$$

for $\mathbf{x}_R$ just above $\mathbb{S}_0$ and $\mathbf{x}'$ at $\mathbb{S}_1$. Equations (A.8.1) and (A.8.2) hold for the situation with or without free surface just above $\mathbb{S}_0$. Equation (A.8.2) can be further simplified for each of these situations. For the situation without free surface, with $\mathbf{r}^{\cap} = \mathbf{O}$, equation (A.8.2) becomes

$$\begin{aligned}
\{\mathbf{G}^{+,+}_C(\mathbf{x}',\mathbf{x}_R,\omega)\}^t - \{\mathbf{F}^+_{1,A}(\mathbf{x}_R,\mathbf{x}',\omega)\}^* \\
= -\int_{\mathbb{S}_0} \mathbf{R}^{\cup}_C(\mathbf{x}_R,\mathbf{x},\omega)\{\mathbf{F}^-_{1,A}(\mathbf{x},\mathbf{x}',\omega)\}^*\mathrm{d}\mathbf{x}.
\end{aligned} \qquad \text{(A.8.3)}$$

On the other hand, for the situation with free surface, with $(\mathbf{r}^{\cap})^{\dagger}\mathbf{r}^{\cap} = \mathbf{I}$ (equation (A.2.16)), we obtain

$$\begin{aligned}
&\{\mathbf{G}^{+,+}_C(\mathbf{x}',\mathbf{x}_R,\omega)\}^t - \{\mathbf{F}^+_{1,A}(\mathbf{x}_R,\mathbf{x}',\omega) + \mathbf{r}^{\cap}\mathbf{F}^-_{1,A}(\mathbf{x}_R,\mathbf{x}',\omega)\}^* \\
&= \int_{\mathbb{S}_0} \mathbf{R}^{\cup}_C(\mathbf{x}_R,\mathbf{x},\omega)\mathbf{r}^{\cap}\{\mathbf{F}^+_{1,A}(\mathbf{x},\mathbf{x}',\omega)\}^*\mathrm{d}\mathbf{x}. \qquad \text{(A.8.4)}
\end{aligned}$$

Response to the focusing function $\mathbf{F}^+_{1,A}$

We derive the response to the focusing function $\mathbf{F}^+_{1,A}(\mathbf{x},\mathbf{x}',\omega)$, when emitted into medium A from above. For state A in Table A.2 we place a source in medium A at $\mathbf{x}''$, just below $\mathbb{S}_1$. The flux-normalised upgoing field at $\mathbb{S}_1$ is the delta function $\mathbf{I}\delta(\mathbf{x}_{\mathrm{H}} - \mathbf{x}''_{\mathrm{H}})$, with its a singularity vertically above the source. There are no

Table A.5: *Quantities to derive the response to* $\mathbf{F}^-_{2,A}$.

	State A: Medium A Source at $\mathbf{x}''$ just above $\mathbb{S}_0$	State B: Medium A Focus at $\mathbf{x}'$ at $\mathbb{S}_0$
$\mathbb{S}_0$	$\mathbf{p}^+_A(\mathbf{x},\omega) \rightarrow \mathbf{I}\delta(\mathbf{x}_{\mathrm{H}} - \mathbf{x}''_{\mathrm{H}}) + \mathbf{r}^{\cap}\mathbf{R}^{\cup}_A(\mathbf{x},\mathbf{x}'',\omega)$	$\mathbf{p}^+_B(\mathbf{x},\omega) \rightarrow \mathbf{r}^{\cap}\mathbf{I}\delta(\mathbf{x}_{\mathrm{H}} - \mathbf{x}'_{\mathrm{H}})$
	$\mathbf{p}^-_A(\mathbf{x},\omega) \rightarrow \mathbf{R}^{\cup}_A(\mathbf{x},\mathbf{x}'',\omega)$	$\mathbf{p}^-_B(\mathbf{x},\omega) \rightarrow \mathbf{I}\delta(\mathbf{x}_{\mathrm{H}} - \mathbf{x}'_{\mathrm{H}})$
$\mathbb{S}_1$	$\mathbf{p}^+_A(\mathbf{x},\omega) \rightarrow \mathbf{T}^+_A(\mathbf{x},\mathbf{x}'',\omega)$	$\mathbf{p}^+_B(\mathbf{x},\omega) \rightarrow \mathbf{F}^+_{2,A}(\mathbf{x},\mathbf{x}',\omega)$
	$\mathbf{p}^-_A(\mathbf{x},\omega) \rightarrow \mathbf{O}$	$\mathbf{p}^-_B(\mathbf{x},\omega) \rightarrow \mathbf{F}^-_{2,A}(\mathbf{x},\mathbf{x}',\omega)$

other contributions to this upgoing field because the medium below $\mathbb{S}_1$ is homogeneous. The downgoing field at $\mathbb{S}_1$ is the reflection response of medium A from below, $\mathbf{R}^{\cap}_A(\mathbf{x},\mathbf{x}'',\omega)$. At $\mathbb{S}_0$, the upgoing field is the transmission response $\mathbf{T}^-_A(\mathbf{x},\mathbf{x}'',\omega)$ and the downgoing field is given by the downward reflected transmission response. The latter vanishes when the earth's surface is transparent. For state B we choose the same focusing function as in Table A.1. We substitute the quantities of Table A.2 into equation (A.2.1). Using equations (A.2.15) and (A.2.18), setting $m = 0$ and $n = 1$, this gives

$$\mathbf{I}\delta(\mathbf{x}''_{\mathrm{H}} - \mathbf{x}'_{\mathrm{H}}) = \int_{\mathbb{S}_0} \mathbf{T}^+_A(\mathbf{x}'',\mathbf{x},\omega)\mathbf{F}^+_{1,A}(\mathbf{x},\mathbf{x}',\omega)\mathrm{d}\mathbf{x}, \tag{A.8.5}$$

for $\mathbf{x}'$ at $\mathbb{S}_1$ and $\mathbf{x}''$ just below $\mathbb{S}_1$. Since $\mathbb{S}_1$ is transparent, $\mathbf{x}''$ may just as well be chosen at $\mathbb{S}_1$.

To derive the reflection response to the focusing function $\mathbf{F}^+_{1,A}$, we combine state A of Table 1 with state B of Table A.2. Substitution of these quantities into equation (A.2.1), using equations (A.2.10) and (A.2.15), setting $m = 0$ and $n = 1$, gives

$$\mathbf{F}^-_{1,A}(\mathbf{x}_R,\mathbf{x}',\omega) = \int_{\mathbb{S}_0} \mathbf{R}^{\cup}_A(\mathbf{x}_R,\mathbf{x},\omega)\mathbf{F}^+_{1,A}(\mathbf{x},\mathbf{x}',\omega)\mathrm{d}\mathbf{x}, \tag{A.8.6}$$

for $\mathbf{x}_R$ just above $\mathbb{S}_0$ and $\mathbf{x}'$ at $\mathbb{S}_1$.

Response to the focusing function $\mathbf{F}^-_{2,A}$

We derive the response to the focusing function $\mathbf{F}^-_{2,A}(\mathbf{x},\mathbf{x}',\omega)$, when emitted into medium A from below. For state A in Table A.3 we place a source in medium A at $\mathbf{x}''$, just above $\mathbb{S}_0$. This needs no further explanation, because this is very similar to state A in Table 1. State B represents the focusing function, which is defined in medium A. At $\mathbb{S}_1$, the upgoing field is given by the emitted focusing function $\mathbf{F}^-_{2,A}(\mathbf{x},\mathbf{x}',\omega)$. There are no other contributions to this upgoing field because the

medium below $\mathbb{S}_1$ is homogeneous. The downgoing field at $\mathbb{S}_1$ is given by the downgoing part of the focusing function. The quantities at $\mathbb{S}_0$ in state B represent the focusing conditions, formulated by equations (A.3.8) and (A.3.9).

We substitute the quantities of Table A.3 into equation (A.2.1). Using equations (A.2.15) and (A.2.18), setting $m = 0$ and $n = 1$, this gives

$$\mathbf{I}\delta(\mathbf{x}''_{\mathrm{H}} - \mathbf{x}'_{\mathrm{H}}) = \int_{\mathbb{S}_1} \mathbf{T}^-_A(\mathbf{x}'', \mathbf{x}, \omega)\mathbf{F}^-_{2,A}(\mathbf{x}, \mathbf{x}', \omega)\mathrm{d}\mathbf{x}, \tag{A.8.7}$$

for $\mathbf{x}'$ at $\mathbb{S}_0$ and $\mathbf{x}''$ just above $\mathbb{S}_0$. Since $\mathbb{S}_0$ is transparent, $\mathbf{x}''$ may just as well be chosen at $\mathbb{S}_0$.

To derive the reflection response to the focusing function $\mathbf{F}^-_{2,A}$, we combine state A of Table A.2 with state B of Table A.3. Substitution of these quantities into equation (A.2.1), using equations (A.2.11) and (A.2.15), setting $m = 0$ and $n = 1$, gives

$$\mathbf{F}^+_{2,A}(\mathbf{x}'', \mathbf{x}', \omega) = \int_{\mathbb{S}_1} \mathbf{R}^{\cap}_A(\mathbf{x}'', \mathbf{x}, \omega)\mathbf{F}^-_{2,A}(\mathbf{x}, \mathbf{x}', \omega)\mathrm{d}\mathbf{x}, \tag{A.8.8}$$

for $\mathbf{x}'$ at $\mathbb{S}_0$ and $\mathbf{x}''$ just below $\mathbb{S}_1$.

Relations between $\mathbf{F}^{\pm}_{1,A}$ and $\mathbf{F}^{\pm}_{2,A}$

To derive the relations between $\mathbf{F}^{\pm}_{1,A}$ and $\mathbf{F}^{\pm}_{2,A}$, we take for state A the quantities defined in Table A.3 for state B and replace $\mathbf{x}'$ by $\mathbf{x}''$. For state B we take the quantities defined in Table A.2 for state B. Substitution of these quantities into equation (A.2.1), using equation (A.2.15), setting $m = 0$ and $n = 1$, gives

$$\mathbf{F}^+_{1,A}(\mathbf{x}'', \mathbf{x}', \omega) = \{\mathbf{F}^-_{2,A}(\mathbf{x}', \mathbf{x}'', \omega)\}^t, \tag{A.8.9}$$

for $\mathbf{x}''$ at $\mathbb{S}_0$ and $\mathbf{x}'$ at $\mathbb{S}_1$. Substituting the same quantities into equation (A.2.2), using equation (A.2.15), setting $m = 0$ and $n = 1$, gives

$$\begin{aligned}\{\mathbf{I} - (\mathbf{r}^{\cap})^{\dagger}\mathbf{r}^{\cap}\}\mathbf{F}^-_{1,A}(\mathbf{x}'', \mathbf{x}', \omega) - (\mathbf{r}^{\cap})^*\mathbf{F}^+_{1,A}(\mathbf{x}'', \mathbf{x}', \omega) \\ = -\{\mathbf{F}^+_{2,A}(\mathbf{x}', \mathbf{x}'', \omega)\}^{\dagger}.\end{aligned} \tag{A.8.10}$$

Equations (A.8.9) and (A.8.10) hold for the situation with or without free surface just above $\mathbb{S}_0$. Equation (A.8.10) can be further simplified for each of these situations. For the situation without free surface, with $\mathbf{r}^{\cap} = \mathbf{O}$, equation (A.8.10) becomes

$$\mathbf{F}^-_{1,A}(\mathbf{x}'', \mathbf{x}', \omega) = -\{\mathbf{F}^+_{2,A}(\mathbf{x}', \mathbf{x}'', \omega)\}^{\dagger}. \tag{A.8.11}$$

On the other hand, for the situation with free surface, with $(\mathbf{r}^{\cap})^{\dagger}\mathbf{r}^{\cap} = \mathbf{I}$ (equation (A.2.16)), we obtain

$$(\mathbf{r}^{\cap})^*\mathbf{F}^+_{1,A}(\mathbf{x}'', \mathbf{x}', \omega) = \{\mathbf{F}^+_{2,A}(\mathbf{x}', \mathbf{x}'', \omega)\}^{\dagger}. \tag{A.8.12}$$

Using equation (A.8.9) this gives the following symmetry relation for $\mathbf{F}^{\pm}_{2,A}$

$$(\mathbf{r}^{\cap})^*\{\mathbf{F}^-_{2,A}(\mathbf{x}', \mathbf{x}'', \omega)\}^t = \{\mathbf{F}^+_{2,A}(\mathbf{x}', \mathbf{x}'', \omega)\}^{\dagger}. \tag{A.8.13}$$

A.8.2 Derivations for Section A.4

Equation for $\bar{\mathbf{G}}_B^{+,+}(\mathbf{x}, \mathbf{x}_S, \omega)$

To derive an equation for $\bar{\mathbf{G}}_B^{+,+}(\mathbf{x}, \mathbf{x}_S, \omega)$, we take for state A the quantities defined in Table A.2 for state A. For state B we take the quantities defined in Table 1 for state B, but with bars on these quantities. Substitution of these quantities into equation (A.2.1), using equations (A.2.11), (A.2.15) and (A.2.18), setting $m = 0$ and $n = 1$, gives

$$\begin{aligned}\mathbf{T}_A^+(\mathbf{x}'', \mathbf{x}_S, \omega) =& \bar{\mathbf{G}}_B^{+,+}(\mathbf{x}'', \mathbf{x}_S, \omega) \\ &- \int_{\mathbb{S}_1} \mathbf{R}_A^{\cap}(\mathbf{x}'', \mathbf{x}, \omega) \bar{\mathbf{G}}_B^{-,+}(\mathbf{x}, \mathbf{x}_S, \omega) \mathrm{d}\mathbf{x},\end{aligned} \tag{A.8.14}$$

for $\mathbf{x}_S$ just above $\mathbb{S}_0$ and $\mathbf{x}''$ just below $\mathbb{S}_1$. Since $\mathbb{S}_1$ is transparent, $\mathbf{x}''$ may just as well be chosen at $\mathbb{S}_1$. Next, we replace the integration variable $\mathbf{x}$ by $\mathbf{x}'$ and substitute equation (A.2.20) (but with bars on all quantities) into the right-hand side of equation (A.8.14). This gives

$$\begin{aligned}\mathbf{T}_A^+(\mathbf{x}'', \mathbf{x}_S, \omega) =& \bar{\mathbf{G}}_B^{+,+}(\mathbf{x}'', \mathbf{x}_S, \omega) \\ &- \int_{\mathbb{S}_1} \int_{\mathbb{S}_1} \mathbf{R}_A^{\cap}(\mathbf{x}'', \mathbf{x}', \omega) \bar{\mathbf{R}}_b^{\cup}(\mathbf{x}', \mathbf{x}, \omega) \bar{\mathbf{G}}_B^{+,+}(\mathbf{x}, \mathbf{x}_S, \omega) \mathrm{d}\mathbf{x} \mathrm{d}\mathbf{x}',\end{aligned} \tag{A.8.15}$$

for $\mathbf{x}_S$ just above $\mathbb{S}_0$ and $\mathbf{x}''$ at $\mathbb{S}_1$. We can rewrite this as

$$\mathbf{T}_A^+(\mathbf{x}'', \mathbf{x}_S, \omega) = \int_{\mathbb{S}_1} \bar{\mathbf{C}}_{Ab}(\mathbf{x}'', \mathbf{x}, \omega) \bar{\mathbf{G}}_B^{+,+}(\mathbf{x}, \mathbf{x}_S, \omega) \mathrm{d}\mathbf{x}, \tag{A.8.16}$$

with

$$\begin{aligned}\bar{\mathbf{C}}_{Ab}(\mathbf{x}'', \mathbf{x}, \omega) =& \mathbf{I} \delta(\mathbf{x}''_{\mathrm{H}} - \mathbf{x}_{\mathrm{H}}) \\ &- \int_{\mathbb{S}_1} \mathbf{R}_A^{\cap}(\mathbf{x}'', \mathbf{x}', \omega) \bar{\mathbf{R}}_b^{\cup}(\mathbf{x}', \mathbf{x}, \omega) \mathrm{d}\mathbf{x}',\end{aligned} \tag{A.8.17}$$

for $\mathbf{x}$ and $\mathbf{x}''$ at $\mathbb{S}_1$.

Representation for $\bar{\mathbf{T}}_B^+(\mathbf{x}'', \mathbf{x}_S, \omega)$

We derive a representation for $\bar{\mathbf{T}}_B^+(\mathbf{x}'', \mathbf{x}_S, \omega)$, in terms of the Green's function $\bar{\mathbf{G}}_B^{+,+}(\mathbf{x}, \mathbf{x}_S, \omega)$ and the transmission response of unit $\bar{b}$, $\bar{\mathbf{T}}_b^+(\mathbf{x}'', \mathbf{x}, \omega)$. Substituting the quantities of Table B.1 into equation (A.2.1), using equation (A.2.18), setting $m = 1$ and $n = 2$, gives

$$\bar{\mathbf{T}}_B^+(\mathbf{x}'', \mathbf{x}_S, \omega) = \int_{\mathbb{S}_1} \bar{\mathbf{T}}_b^+(\mathbf{x}'', \mathbf{x}, \omega) \bar{\mathbf{G}}_B^{+,+}(\mathbf{x}, \mathbf{x}_S, \omega) \mathrm{d}\mathbf{x}, \tag{A.8.18}$$

for $\mathbf{x}_S$ just above $\mathbb{S}_0$ and $\mathbf{x}''$ just below $\mathbb{S}_2$. Since $\mathbb{S}_2$ is transparent, $\mathbf{x}''$ may just as well be chosen at $\mathbb{S}_2$.

Table A.6: *Quantities to derive representation for* $\bar{\mathbf{T}}_B^+(\mathbf{x}'', \mathbf{x}_S, \omega)$.

	State A: Medium $\bar{b}$ Source at $\mathbf{x}''$ just below $\mathbb{S}_2$	State B: Medium $\bar{B}$ Source at $\mathbf{x}_S$ just above $\mathbb{S}_0$
$\mathbb{S}_1$	$\mathbf{p}_A^+(\mathbf{x}, \omega) \rightarrow \mathbf{O}$ $\mathbf{p}_A^-(\mathbf{x}, \omega) \rightarrow \bar{\mathbf{T}}_b^-(\mathbf{x}, \mathbf{x}'', \omega)$	$\mathbf{p}_B^+(\mathbf{x}, \omega) \rightarrow \bar{\mathbf{G}}_B^{+,+}(\mathbf{x}, \mathbf{x}_S, \omega)$ $\mathbf{p}_B^-(\mathbf{x}, \omega) \rightarrow \bar{\mathbf{G}}_B^{-,+}(\mathbf{x}, \mathbf{x}_S, \omega)$
$\mathbb{S}_2$	$\mathbf{p}_A^+(\mathbf{x}, \omega) \rightarrow \bar{\mathbf{R}}_b^{\cap}(\mathbf{x}, \mathbf{x}'', \omega)$ $\mathbf{p}_A^-(\mathbf{x}, \omega) \rightarrow \mathbf{I}\delta(\mathbf{x}_{\mathrm{H}} - \mathbf{x}''_{\mathrm{H}})$	$\mathbf{p}_B^+(\mathbf{x}, \omega) \rightarrow \bar{\mathbf{T}}_B^+(\mathbf{x}, \mathbf{x}_S, \omega)$ $\mathbf{p}_B^-(\mathbf{x}, \omega) \rightarrow \mathbf{O}$

Table A.7: *Quantities to derive equation for* $\bar{\mathbf{R}}_B^{\cap}(\mathbf{x}, \mathbf{x}', \omega)$.

	State A: Medium $\bar{B}$ Source at $\mathbf{x}_S$ just above $\mathbb{S}_0$	State B: Medium $\bar{B}$ Source at $\mathbf{x}'$ just below $\mathbb{S}_2$
$\mathbb{S}_0$	$\mathbf{p}_A^+(\mathbf{x}, \omega) \rightarrow \mathbf{I}\delta(\mathbf{x}_{\mathrm{H}} - \mathbf{x}_{\mathrm{H},S}) + \mathbf{r}^{\cap}\bar{\mathbf{R}}_B^{\cup}(\mathbf{x}, \mathbf{x}_S, \omega)$ $\mathbf{p}_A^-(\mathbf{x}, \omega) \rightarrow \bar{\mathbf{R}}_B^{\cup}(\mathbf{x}, \mathbf{x}_S, \omega)$	$\mathbf{p}_B^+(\mathbf{x}, \omega) \rightarrow \mathbf{r}^{\cap}\bar{\mathbf{T}}_B^-(\mathbf{x}, \mathbf{x}', \omega)$ $\mathbf{p}_B^-(\mathbf{x}, \omega) \rightarrow \bar{\mathbf{T}}_B^-(\mathbf{x}, \mathbf{x}', \omega)$
$\mathbb{S}_2$	$\mathbf{p}_A^+(\mathbf{x}, \omega) \rightarrow \bar{\mathbf{T}}_B^+(\mathbf{x}, \mathbf{x}_S, \omega)$ $\mathbf{p}_A^-(\mathbf{x}, \omega) \rightarrow \mathbf{O}$	$\mathbf{p}_B^+(\mathbf{x}, \omega) \rightarrow \bar{\mathbf{R}}_B^{\cap}(\mathbf{x}, \mathbf{x}', \omega)$ $\mathbf{p}_B^-(\mathbf{x}, \omega) \rightarrow \mathbf{I}\delta(\mathbf{x}_{\mathrm{H}} - \mathbf{x}'_{\mathrm{H}})$

Equation for $\bar{\mathbf{R}}_B^{\cap}(\mathbf{x}, \mathbf{x}', \omega)$

We derive an equation for $\bar{\mathbf{R}}_B^{\cap}(\mathbf{x}, \mathbf{x}', \omega)$. Substituting the quantities of Table B.2 into equation (A.2.2), using equations (A.2.10) and (A.2.18), setting $m = 0$ and $n = 2$, gives

$$\begin{aligned}\int_{\mathbb{S}_2} \{\bar{\mathbf{T}}_B^-(\mathbf{x}_S, \mathbf{x}, \omega)\}^* \bar{\mathbf{R}}_B^{\cap}(\mathbf{x}, \mathbf{x}', \omega) \mathrm{d}\mathbf{x} &= \mathbf{r}^{\cap}\bar{\mathbf{T}}_B^-(\mathbf{x}_S, \mathbf{x}', \omega) \\ &\quad - \int_{\mathbb{S}_0} \{\bar{\mathbf{R}}_B^{\cup}(\mathbf{x}_S, \mathbf{x}, \omega)\}^* \{\mathbf{I} - (\mathbf{r}^{\cap})^{\dagger}\mathbf{r}^{\cap}\} \bar{\mathbf{T}}_B^-(\mathbf{x}, \mathbf{x}', \omega) \mathrm{d}\mathbf{x},\end{aligned} \tag{A.8.19}$$

for $\mathbf{x}_S$ just above $\mathbb{S}_0$ and $\mathbf{x}'$ just below $\mathbb{S}_2$. Since $\mathbb{S}_2$ is transparent, $\mathbf{x}'$ may just as well be chosen at $\mathbb{S}_2$. For the situation without free surface, with $\mathbf{r}^{\cap} = \mathbf{O}$, this gives

$$\begin{aligned}\int_{\mathbb{S}_2} \{\bar{\mathbf{T}}_B^-(\mathbf{x}_S, \mathbf{x}, \omega)\}^* \bar{\mathbf{R}}_B^{\cap}(\mathbf{x}, \mathbf{x}', \omega) \mathrm{d}\mathbf{x} \\ = - \int_{\mathbb{S}_0} \{\bar{\mathbf{R}}_B^{\cup}(\mathbf{x}_S, \mathbf{x}, \omega)\}^* \bar{\mathbf{T}}_B^-(\mathbf{x}, \mathbf{x}', \omega) \mathrm{d}\mathbf{x}.\end{aligned} \tag{A.8.20}$$

On the other hand, for the situation with free surface, with $(\mathbf{r}^{\cap})^{\dagger}\mathbf{r}^{\cap} = \mathbf{I}$ (equation A.2.16), we obtain

$$\int_{\mathbb{S}_2} \{\bar{\mathbf{T}}_B^-(\mathbf{x}_S, \mathbf{x}, \omega)\}^* \bar{\mathbf{R}}_B^{\cap}(\mathbf{x}, \mathbf{x}', \omega) \mathrm{d}\mathbf{x} = \mathbf{r}^{\cap} \bar{\mathbf{T}}_B^-(\mathbf{x}_S, \mathbf{x}', \omega). \tag{A.8.21}$$

Bibliography

Alá'i, R., D. J. Verschuur, J. Drummond, S. Morris, and G. Haughey (2002), Shallow water multiple prediction and attenuation, case study on data from the Arabian Gulf, in *SEG Technical Program Expanded Abstracts 2002*, pp. 2229–2232, Society of Exploration Geophysicists.

Amundsen, L., L. T. Ikelle, and L. E. Berg (2001), Multidimensional signature deconvolution and free-surface multiple elimination of marine multicomponent ocean-bottom seismic data, *Geophysics*, *66*(5), 1594–1604.

Baardman, R. H., D. J. Verschuur, R. G. van Borselen, M. O. Frijlink, and R. F. Hegge (2010), Estimation of primaries by sparse inversion using dual-sensor data, in *SEG Technical Program Expanded Abstracts 2010*, pp. 3468–3472, Society of Exploration Geophysicists.

Bardan, V. (1987), Trace interpolation in seismic data processing, *Geophysical Prospecting*, *35*(4), 343–358.

Barnes, S., R. Hegge, R. van Borselen, and J. Owen (2014), Shallow reverberation prediction methodology with SRME, in *76th EAGE Conference and Exhibition 2014*, European Association of Geoscientists & Engineers.

Baysal, E., D. D. Kosloff, and J. W. Sherwood (1983), Reverse time migration, *Geophysics*, *48*(11), 1514–1524.

Behura, J., K. Wapenaar, and R. Snieder (2014), Autofocus imaging: Image reconstruction based on inverse scattering theory, *Geophysics*, *79*(3), A19–A26.

Belonosov, M., and R. van Borselen (2017), A comparison study for robust estimation of primaries by sparse inversion, in *SEG Technical Program Expanded Abstracts 2017*, pp. 4833–4837, Society of Exploration Geophysicists.

Belonosov, M., R. Baardman, J. Yoo, and R. Van Borselen (2019), Practical approach to Robust EPSI in shallow water data from the Middle East, in *81st EAGE Conference and Exhibition 2019*, European Association of Geoscientists & Engineers.

Berkhout, A., and D. Verschuur (1997), Estimation of multiple scattering by iterative inversion, Part I: Theoretical considerations, *Geophysics*, *62*(5), 1586–1595.

Brackenhoff, J. (2016), Rescaling of incorrect source strength using Marchenko redatuming: M.Sc. thesis, TU Delft Repository, Delft University of Technology.

Brackenhoff, J., J. Thorbecke, and K. Wapenaar (2019), Virtual sources and receivers in the real Earth: Considerations for practical applications, *Journal of Geophysical Research: Solid Earth*, *124*(11), 11, 802–11, 821.

Broggini, F., and R. Snieder (2012), Connection of scattering principles: a visual and mathematical tour, *European Journal of Physics*, *33*, 593–613.

Broggini, F., R. Snieder, and K. Wapenaar (2012), Focusing the wavefield inside an unknown 1D medium: Beyond seismic interferometry, *Geophysics*, *77*(5), A25–A28.

Broggini, F., R. Snieder, and K. Wapenaar (2014), Data-driven wavefield focusing and imaging with multidimensional deconvolution: Numerical examples for reflection data with internal multiples, *Geophysics*, *79*(3), WA107–WA115.

Brookes, D. (2011), Case studies in 3D interbed multiple attenuation, *The Leading Edge*, *30*(8), 914–918.

Castelan, A. R., C. Kostov, E. Saragoussi, F. X. De Melo, G. Miers, Z. Wu, K. Abdelaziz, O. Mataracioglu, P. Kristiansen, S. Slaton, et al. (2016), OBN multiple attenuation using OBN and towed-streamer data: Deepwater Gulf of Mexico case study, Thunder Horse Field, in *SEG Technical Program Expanded Abstracts 2016*, pp. 4513–4517, Society of Exploration Geophysicists.

Cypriano, L., F. Marpeau, R. Brasil, G. Welter, H. Prigent, H. Douma, M. Velasques, J. Boechat, P. de Carvalho, C. Guerra, et al. (2015), The impact of interbed multiple attenuation on the imaging of pre-salt targets in the Santos basin off-shore Brazil, in *77th EAGE Conference and Exhibition 2015*, European Association of Geoscientists & Engineers.

da Costa Filho, C. A., M. Ravasi, A. Curtis, and G. A. Meles (2014), Elastodynamic Green's function retrieval through single-sided Marchenko inverse scattering, *Physical Review E*, *90*(6), 063,201.

Davydenko, M., and D. Verschuur (2017), Full-wavefield migration: Using surface and internal multiples in imaging, *Geophysical Prospecting*, *65*(1), 7–21.

Dix, C. H. (1948), The existence of multiple reflections, *Geophysics*, *13*(1), 49–50.

Dragoset, B., E. Verschuur, I. Moore, and R. Bisley (2010), A perspective on 3D surface-related multiple elimination, *Geophysics*, *75*(5), 75A245–75A261.

Dukalski, M., and K. de Vos (2017), Marchenko inversion in a strong scattering regime including surface-related multiples, *Geophysical Journal International*, *212*(2), 760–776.

El-Emam, A., K. S. Al-Deen, A. Zarkhidze, and A. Walz (2011), Advances in interbed multiples prediction and attenuation: Case study from onshore Kuwait, in *SEG Technical Program Expanded Abstracts 2011*, pp. 3546–3550, Society of Exploration Geophysicists.

Elison, P., D. van Manen, F. Broggini, and J. O. Robertsson (2016), Using a Marchenko-redatumed reflection response as an exact boundary condition, in *78th EAGE Conference and Exhibition 2016*, pp. Th–SBT5–03, European Association of Geoscientists & Engineers.

Elison, P., M. Dukalski, C. Mildner, K. De Vos, C. Reinicke, D. Van Manen, and J. O. Robertsson (2019), Short-period internal multiple removal for a horizontally layered overburden using augmented Marchenko focusing, in *81st EAGE Conference and Exhibition 2019*, pp. 1–5, European Association of Geoscientists & Engineers.

Ellsworth, T. P. (1948), Multiple reflections, *Geophysics*, *13*(1), 1–18.

Esmersoy, C., and M. Oristaglio (1988), Reverse-time wave-field extrapolation, imaging, and inversion, *Geophysics*, *53*(7), 920–931.

Fishman, L., J. J. McCoy, and S. C. Wales (1987), Factorization and path integration of the Helmholtz equation: Numerical algorithms, *The Journal of the Acoustical Society of America*, *81*(5), 1355–1376.

Fomel, S. (2003), Seismic reflection data interpolation with differential offset and shot continuation, *Geophysics*, *68*(2), 733–744.

Fomel, S. (2009), Adaptive multiple subtraction using regularized nonstationary regression, *Geophysics*, *74*(1), V25–V33.

Foster, D. J., and C. C. Mosher (1992), Suppression of multiple reflections using the Radon transform, *Geophysics*, *57*(3), 386–395.

Griffiths, L., F. Smolka, and L. Trembly (1977), Adaptive deconvolution: A new technique for processing time-varying seismic data, *Geophysics*, *42*(4), 742–759.

Griffiths, M., J. Hembd, and H. Prigent (2011), Applications of interbed multiple attenuation, *The Leading Edge*, *30*(8), 906–912.

Guitton, A., and D. Verschuur (2004), Adaptive subtraction of multiples using the L1-norm, *Geophysical Prospecting*, *52*(1), 27–38.

Haines, A. J. (1988), Multi-source, multi-receiver synthetic seismograms for laterally heterogeneous media using FK domain propagators, *Geophysical Journal International*, *95*(2), 237–260.

Haines, A. J., and M. V. de Hoop (1996), An invariant imbedding analysis of general wave scattering problems, *Journal of Mathematical Physics*, *37*(8), 3854–3881.

Hampson, D. (1986), Inverse velocity stacking for multiple elimination, in *SEG Technical Program Expanded Abstracts 1986*, pp. 422–424, Society of Exploration Geophysicists.

Hampson, D. (1987), The discrete Radon transform: a new tool for image enhancement and noise suppression, in *SEG Technical Program Expanded Abstracts 1987*, pp. 141–143, Society of Exploration Geophysicists.

Hansen, R. F., and C. H. Johnson (1948), Multiple reflections of seismic energy, *Geophysics*, *13*(1), 58–85.

Hargreaves, N. (2006), Surface multiple attenuation in shallow water and the construction of primaries from multiples, in *SEG Technical Program Expanded Abstracts 2006*, pp. 2689–2693, Society of Exploration Geophysicists.

Hartstra, I., C. Almagro Vidal, and K. Wapenaar (2017), Full-field multidimensional deconvolution to retrieve body-wave reflections from sparse passive sources, *Geophysical Journal International*, *210*(2), 609–620.

Hatchell, P., and S. Bourne (2005), Rocks under strain: Strain-induced time-lapse time shifts are observed for depleting reservoirs, *The Leading Edge*, *24*(12), 1222–1225.

Herrmann, F. J., D. Wang, and D. J. Verschuur (2008), Adaptive curvelet-domain primary-multiple separation, *Geophysics*, *73*(3), A17–A21.

Herwanger, J. V., and S. A. Horne (2009), Linking reservoir geomechanics and time-lapse seismics: Predicting anisotropic velocity changes and seismic attributes, *Geophysics*, *74*(4), W13–W33.

Hubral, P., S. Treitel, and P. R. Gutowski (1980), A sum autoregressive formula for the reflection response, *Geophysics*, *45*(11), 1697–1705.

Hung, B., and M. Wang (2012), Internal demultiple methodology without identifying the multiple generators, in *SEG Technical Program Expanded Abstracts 2012*, pp. 1–5, Society of Exploration Geophysicists.

Hung, B., K. Yang, J. Zhou, and Q. L. Xia (2010), Shallow water demultiple, *ASEG Extended Abstracts*, *2010*(1), 1–4.

Ikelle, L. T. (2006), A construct of internal multiples from surface data only: the concept of virtual seismic events, *Geophysical Journal International*, *164*(2), 383–393.

Ikelle, L. T., G. Roberts, and A. B. Weglein (1997), Source signature estimation based on the removal of first-order multiples, *Geophysics*, *62*(6), 1904–1920.

Jakubowicz, H. (1998), Wave equation prediction and removal of interbed multiples, in *SEG Technical Program Expanded Abstracts 1998*, pp. 1527–1530, Society of Exploration Geophysicists.

Kabir, M. N., and D. Verschuur (1995), Restoration of missing offsets by parabolic Radon transform, *Geophysical Prospecting*, *43*(3), 347–368.

Keho, T. H., and P. G. Kelamis (2012), Focus on land seismic technology: The near-surface challenge, *The Leading Edge*, *31*(1), 62–68.

Kelamis, P. G., and D. Verschuur (2000), Surface-related multiple elimination on land seismic data—Strategies via case studies, *Geophysics*, *65*(3), 719–734.

Kennett, B. (1974), Reflections, rays, and reverberations, *Bulletin of the Seismological Society of America*, *64*(6), 1685–1696.

Kennett, B. (1979), The suppression of surface multiples on seismic records, *Geophysical Prospecting*, *27*(3), 584–600.

Kennett, B., K. Koketsu, and A. Haines (1990), Propagation invariants, reflection and transmission in anisotropic, laterally heterogeneous media, *Geophysical Journal International*, *103*(1), 95–101.

Kim, Y., Y. Cho, and C. Shin (2013), Estimated source wavelet-incorporated reverse-time migration with a virtual source imaging condition, *Geophysical Prospecting*, *61*(sup1), 317–333.

Krueger, J., D. Donno, R. Pereira, D. Mondini, A. Souza, J. Espinoza, and A. Khalil (2018), Internal multiple attenuation for four presalt fields in the Santos Basin, Brazil, in *SEG Technical Program Expanded Abstracts 2018*, pp. 4523–4527, Society of Exploration Geophysicists.

Larner, K., et al. (1981), Trace interpolation and the design of seismic surveys.

Leinbach, J. (1995), Wiener spiking deconvolution and minimum-phase wavelets: A tutorial, *The Leading Edge*, *14*(3), 189–192.

Lesnikov, V., J. Owusu, and S. Aramco (2011), Understanding the mechanism of interbed multiple generation using VSP data, in *SEG Technical Program Expanded Abstracts 2011*, pp. 4258–4262, Society of Exploration Geophysicists.

Lin, T. T., and F. J. Herrmann (2013), Robust estimation of primaries by sparse inversion via one-norm minimization, *Geophysics*, *78*(3), R133–R150.

Löer, K., A. Curtis, and G. Angelo Meles (2016), Relating source-receiver interferometry to an inverse-scattering series to derive a new method to estimate internal multiples, *Geophysics*, *81*(3), Q27–Q40.

Loewenthal, D., L. Lu, R. Roberson, and J. Sherwood (1974), The wave equation applied to migration and water bottom multiples. Presented at the 36th Mtg., Eur. Assn. Explo. Geophys.

Lokshtanov, D. (1999), Multiple suppression by data-consistent deconvolution, *The Leading Edge*, *18*(1), 115–119.

Meles, G. A., K. Wapenaar, and A. Curtis (2016), Reconstructing the primary reflections in seismic data by Marchenko redatuming and convolutional interferometry, *Geophysics*, *81*(2), Q15–Q26.

Meles, G. A., K. Wapenaar, and J. Thorbecke (2018), Virtual plane-wave imaging via Marchenko redatuming, *Geophysical Journal International*, *214*(1), 508–519.

Mildner, C., F. Broggini, J. O. Robertsson, D.-J. van Manen, and S. Greenhalgh (2017), Target-oriented velocity analysis using Marchenko-redatumed data, *Geophysics*, *82*(2), R75–R86.

Minato, S., T. Matsuoka, and T. Tsuji (2013), Singular-value decomposition analysis of source illumination in seismic interferometry by multidimensional deconvolution, *Geophysics*, *78*(3), Q25–Q34.

Moore, I., and B. Dragoset (2008), General surface multiple prediction: A flexible 3D SRME algorithm, *First Break*, *26*(9).

Nakata, N., R. Snieder, and M. Behm (2014), Body-wave interferometry using regional earthquakes with multidimensional deconvolution after wavefield decomposition at free surface, *Geophysical Journal International*, *199*(2), 1125–1137.

Owusu, J. C., O. Podgornova, M. Charara, S. Leaney, A. Campbell, S. Ali, I. Borodin, L. Nutt, and H. Menkiti (2016), Anisotropic elastic full-waveform inversion of walkaway VSP data from the Arabian Gulf, *Geophysical Prospecting*, *64*(1), 38–53.

Peacock, K., and S. Treitel (1969), Predictive deconvolution: Theory and practice, *Geophysics*, *34*(2), 155–169.

Pereira, R., D. Mondini, and D. Donno (2018), Efficient 3D Internal Multiple Attenuation in the Santos Basin, in *80th EAGE Conference and Exhibition 2018*, European Association of Geoscientists & Engineers.

Pereira, R., M. Ramzy, P. Griscenco, B. Huard, H. Huang, L. Cypriano, and A. Khalil (2019), Internal multiple attenuation for OBN data with overburden/target separation, in *SEG Technical Program Expanded Abstracts 2019*, pp. 4520–4524, Society of Exploration Geophysicists.

Ravasi, M. (2017), Rayleigh-Marchenko redatuming for target-oriented, true-amplitude imaging, *Geophysics*, *82*(6), S439–S452.

Ravasi, M., I. Vasconcelos, A. Kritski, A. Curtis, C. A. da Costa Filho, and G. A. Meles (2016), Target-oriented Marchenko imaging of a North Sea field, *Geophysical Supplements to the Monthly Notices of the Royal Astronomical Society*, *205*(1), 99–104.

Reinicke, C., and C. Wapenaar (2017), Elastodynamic single-sided homogeneous Green's function representation-theory and examples, in *79th EAGE Conference and Exhibition 2017*.

Reinicke, C., and K. Wapenaar (2019), Elastodynamic single-sided homogeneous Green's function representation: Theory and numerical examples, *Wave Motion*, *89*, 245–264.

Reinicke, C., M. Dukalski, and K. Wapenaar (2019), Do we need elastic internal de-multiple offshore Middle East, or will acoustic Marchenko suffice?, in *SEG/KOC Workshop: Seismic Multiples - The Challenges and the Way Forward, Kuwait*, Society of Exploration Geophysicists.

Resnick, J., I. Lerche, and R. Shuey (1986), Reflection, transmission, and the generalized primary wave, *Geophysical Journal International*, *87*(2), 349–377.

Robertsson, J. O., and C. H. Chapman (2000), An efficient method for calculating finite-difference seismograms after model alterations, *Geophysics*, *65*(3), 907–918.

Robinson, E. A. (1957), Predictive decomposition of seismic traces, *Geophysics*, *22*(4), 767–778.

Rønholt, G., O. Korsmo, S. Brown, A. Valenciano, D. Whitmore, N. Chemingui, S. Brandsberg, V. Dirks, J.-E. Lie, et al. (2014), High-fidelity complete wavefield velocity model building and imaging in shallow water environments – A North Sea case study, *First Break*, *32*(6), 127–131.

Rose, J. H. (2001), 'Single-sided' focusing of the time-dependent Schrödinger equation, *Physical Review A*, *65*(1), 012, 707.

Rose, J. H. (2002), 'Single-sided' autofocusing of sound in layered materials, *Inverse problems*, *18*(6), 1923.

Schneider, W. A., E. Prince Jr, and B. F. Giles (1965), A new data-processing technique for multiple attenuation exploiting differential normal moveout, *Geophysics*, *30*(3), 348–362.

Singh, S., and R. Snieder (2017), Source-receiver Marchenko redatuming: Obtaining virtual receivers and virtual sources in the subsurface, *Geophysics*, *82*(3), Q13–Q21.

Singh, S., R. Snieder, J. Behura, J. van der Neut, K. Wapenaar, and E. Slob (2015), Marchenko imaging: Imaging with primaries, internal multiples, and free-surface multiples, *Geophysics*, *80*(5), S165–S174.

Singh, S., R. Snieder, J. van der Neut, J. Thorbecke, E. Slob, and K. Wapenaar (2016), Accounting for free-surface multiples in Marchenko imaging, *Geophysics*, *82*(1), R19–R30.

Slob, E. (2016), Green's function retrieval and Marchenko imaging in a dissipative acoustic medium, *Physical Review Letters*, *116*(16), 164, 301.

Slob, E., and K. Wapenaar (2017), Theory for Marchenko imaging of marine seismic data with free surface multiple elimination, in *79th EAGE Conference and Exhibition 2017*.

Slob, E., K. Wapenaar, F. Broggini, and R. Snieder (2014), Seismic reflector imaging using internal multiples with Marchenko-type equations, *Geophysics*, *79*(2), S63–S76.

Snieder, R., A. Grêt, H. Douma, and J. Scales (2002), Coda wave interferometry for estimating nonlinear behavior in seismic velocity, *Science*, *295*(5563), 2253–2255.

Soubaras, R. (1996), Ocean bottom hydrophone and geophone processing, in *SEG Technical Program Expanded Abstracts 1996*, pp. 24–27, Society of Exploration Geophysicists.

Spitz, S. (1991), Seismic trace interpolation in the FX domain, *Geophysics*, *56*(6), 785–794.

Spitz, S. (1999), Pattern recognition, spatial predictability, and subtraction of multiple events, *The Leading Edge*, *18*(1), 55–58.

Staring, M., and K. Wapenaar (2020), 3D Marchenko internal multiple attenuation on narrow azimuth streamer data of the Santos Basin, Brazil, *Geophysical Prospecting*, *68*, 1864–1877.

Staring, M., R. Pereira, H. Douma, J. van der Neut, and C. Wapenaar (2017), Adaptive double-focusing method for source-receiver Marchenko redatuming on field data, in *SEG Technical Program Expanded Abstracts 2017*, pp. 4808–4812, Society of Exploration Geophysicists.

Staring, M., R. Pereira, H. Douma, J. van der Neut, and K. Wapenaar (2018a), Source-receiver Marchenko redatuming on field data using an adaptive double-focusing method, *Geophysics*, *83*(6), S579–S590.

Staring, M., J. van der Neut, and K. Wapenaar (2018b), Marchenko redatuming by adaptive double-focusing on 2D and 3D field data of the Santos basin, in *SEG Technical Program Expanded Abstracts 2018*, pp. 5449–5453, Society of Exploration Geophysicists.

Staring, M., M. Dukalski, M. Belonosov, R. Baardman, J. Yoo, R. Hegge, R. van Borselen, and K. Wapenaar (2019), Adaptive Marchenko multiple removal on Arabian Gulf OBC data, in *SEG/KOC Workshop: Seismic Multiples - The Challenges and the Way Forward, Kuwait*, Society of Exploration Geophysicists.

Staring, M., M. Dukalski, M. Belonosov, R. Baardman, J. Yoo, R. Hegge, R. van Borselen, and K. Wapenaar (2020), R-EPSI and Marchenko equation-based workflow for multiple suppression in the case of a shallow water layer and a complex overburden: A 2D case study in the Arabian Gulf, *Geophysics*.

Taner, M. (1980), Long period sea-floor multiples and their suppression, *Geophysical prospecting*, *28*(1), 30–48.

Telford, W. M., L. P. Geldart, and R. E. Sheriff (1990), *Applied Geophysics*, vol. 1, Cambridge university press.

ten Kroode, F. (2002), Prediction of internal multiples, *Wave Motion*, *35*(4), 315–338.

Thorbecke, J., E. Slob, J. Brackenhoff, J. van der Neut, and K. Wapenaar (2017), Implementation of the Marchenko method, *Geophysics*, *82*(6), WB29–WB45.

van der Neut, J., and K. Wapenaar (2016), Adaptive overburden elimination with the multidimensional Marchenko equation, *Geophysics*, *81*(5), T265–T284.

van der Neut, J., M. Tatanova, J. Thorbecke, E. Slob, and K. Wapenaar (2011), Deghosting, demultiple, and deblurring in controlled-source seismic interferometry, *International Journal of Geophysics*, *2011*.

van der Neut, J., I. Vasconcelos, and K. Wapenaar (2015a), On Green's function retrieval by iterative substitution of the coupled Marchenko equations, *Geophysical Journal International*, *203*(2), 792–813.

van der Neut, J., K. Wapenaar, J. Thorbecke, E. Slob, and I. Vasconcelos (2015b), An illustration of adaptive Marchenko imaging, *The Leading Edge*, *34*(7), 818–822.

van der Neut, J., M. Ravasi, Y. Liu, and I. Vasconcelos (2017), Target-enclosed seismic imaging, *Geophysics*, *82*(6), Q53–Q66.

van der Neut, J., J. Brackenhoff, M. Staring, L. Zhang, S. de Ridder, E. Slob, and K. Wapenaar (2018), Single-and Double-Sided Marchenko Imaging Conditions in Acoustic Media, *IEEE Transactions on Computational Imaging*, *4*(1), 160–171.

Van Groenestijn, G., and D. Verschuur (2009a), Estimating primaries by sparse inversion and application to near-offset data reconstruction, *Geophysics*, *74*(3), A23–A28.

Van Groenestijn, G., and D. Verschuur (2009b), Estimation of primaries and near-offset reconstruction by sparse inversion: Marine data applications, *Geophysics*, *74*(6), R119–R128.

van Manen, D.-J., J. O. Robertsson, and A. Curtis (2007), Exact wave field simulation for finite-volume scattering problems, *The Journal of the Acoustical Society of America*, *122*(4), EL115–EL121.

Vasmel, M., J. O. Robertsson, D.-J. van Manen, and A. Curtis (2013), Immersive experimentation in a wave propagation laboratory, *The Journal of the Acoustical Society of America*, *134*(6), EL492–EL498.

Verschuur, D. J. (2013), *Seismic multiple removal techniques: past, present and future*, EAGE publications.

Verschuur, D. J., A. Berkhout, and C. Wapenaar (1992), Adaptive surface-related multiple elimination, *Geophysics*, *57*(9), 1166–1177.

Vogel, H. U. (1993), The great well of China, *Scientific American*, *268*(6), 116–121.

Wang, M., and B. Hung (2014), 3D Inverse Scattering Series Method for Internal Multiple Attenuation, in *76th EAGE Conference and Exhibition 2014*, European Association of Geoscientists & Engineers.

Wang, P., and K. Nimsaila (2014), Fast progressive sparse Tau-P transform for regularization of spatially aliased seismic data, in *SEG Technical Program Expanded Abstracts 2014*, pp. 3589–3593, Society of Exploration Geophysicists.

Wang, P., S. Ray, C. Peng, Y. Li, and G. Poole (2013), Premigration deghosting for marine streamer data using a bootstrap approach in Tau-P domain, in *SEG Technical Program Expanded Abstracts 2013*, pp. 4221–4225, Society of Exploration Geophysicists.

Wang, Y., Y. Luo, and G. T. Schuster (2009), Interferometric interpolation of missing seismic data, *Geophysics*, *74*(3), SI37–SI45.

Wapenaar, K. (1996), One-way representations of seismic data, *Geophysical Journal International*, *127*(1), 178–188.

Wapenaar, K. (2014), Single-sided Marchenko focusing of compressional and shear waves, *Physical Review E*, *90*(6), 063, 202.

Wapenaar, K., and J. Grimbergen (1996), Reciprocity theorems for one-way wavefields, *Geophysical Journal International*, *127*(1), 169–177.

Wapenaar, K., D. J. Verschuur, and P. Herrmann (1992), Amplitude preprocessing of single and multicomponent seismic data, *Geophysics*, *57*(9), 1178–1188.

Wapenaar, K., J. Fokkema, M. Dillen, and P. Scherpenhuijsen (2000), One-way acoustic reciprocity and its applications in multiple elimination and time-lapse seismics, in *SEG Technical Program Expanded Abstracts 2000*, Society of Exploration Geophysicists.

Wapenaar, K., J. Thorbecke, and D. Draganov (2004), Relations between reflection and transmission responses of three-dimensional inhomogeneous media, *Geophysical Journal International*, *156*(2), 179–194.

Wapenaar, K., F. Broggini, E. Slob, and R. Snieder (2013), Three-dimensional single-sided Marchenko inverse scattering, data-driven focusing, Green's function retrieval, and their mutual relations, *Physical Review Letters*, *110*(8), 084, 301.

Wapenaar, K., J. Thorbecke, J. Van Der Neut, F. Broggini, E. Slob, and R. Snieder (2014a), Marchenko imaging, *Geophysics*, *79*(3), WA39–WA57.

Wapenaar, K., J. Thorbecke, J. van der Neut, F. Broggini, E. Slob, and R. Snieder (2014b), Green's function retrieval from reflection data, in absence of a receiver at the virtual source position, *The Journal of the Acoustical Society of America*, *135*(5), 2847–2861.

Wapenaar, K., J. van der Neut, and E. Slob (2016a), Unified double- and single-sided homogeneous Green's function representations, in *Proc. R. Soc. A*, vol. 472, p. 20160162, The Royal Society.

Wapenaar, K., J. Thorbecke, and J. van der Neut (2016b), A single-sided homogeneous Green's function representation for holographic imaging, inverse scattering, time-reversal acoustics and interferometric Green's function retrieval, *Geophysical Supplements to the Monthly Notices of the Royal Astronomical Society*, *205*(1), 531–535.

Wapenaar, K., J. Brackenhoff, J. Thorbecke, J. van der Neut, E. Slob, and E. Verschuur (2018), Virtual acoustics in inhomogeneous media with single-sided access, *Scientific Reports*, *8*(1), 2497.

Wapenaar, K., M. Staring, J. Brackenhoff, L. Zhang, J. Thorbecke, and E. Slob (2020), An overview of Marchenko methods, *82nd EAGE Conference and Exhibition 2020*.

Ware, J. A., and K. Aki (1969), Continuous and discrete inverse-scattering problems in a stratified elastic medium. I. Plane waves at normal incidence, *The journal of the Acoustical Society of America*, *45*(4), 911–921.

Waterman, J. C. (1948), Multiple-reflection evidence, *Geophysics*, *13*(1), 41–44.

Weglein, A. B., F. A. Gasparotto, P. M. Carvalho, and R. H. Stolt (1997), An inverse-scattering series method for attenuating multiples in seismic reflection data, *Geophysics*, *62*(6), 1975–1989.

Wiggins, J. W. (1988), Attenuation of complex water-bottom multiples by wave-equation-based prediction and subtraction, *Geophysics*, *53*(12), 1527–1539.

Wu, X., and B. Hung (2015), High-fidelity adaptive curvelet domain primary-multiple separation, *First Break*, *33*(1), 53–59.

Xue, Y., J. Yang, J. Ma, and Y. Chen (2016), Amplitude-preserving nonlinear adaptive multiple attenuation using the high-order sparse Radon transform, *Journal of Geophysics and Engineering*, *13*(3), 207–219.

Yanez, M., C. Tyagi, M. Steiger-Jarvis, J. Bailey, M. Shadrina, and S. Dingwall (2018), Addressing the challenges of heritage surface seismic data in a complex shallow water environment for improved overburden imaging and reservoir characterization, in *SEG Technical Program Expanded Abstracts 2018*, pp. 1123–1127, Society of Exploration Geophysicists.

Zhang, L., and E. Slob (2019), Free-surface and internal multiple elimination in one step without adaptive subtraction, *Geophysics*, *84*(1), A7–A11.

Zhang, L., and E. Slob (2020a), A fast algorithm for multiple elimination and transmission compensation in primary reflections, *Geophysical Journal International*.

Zhang, L., and E. Slob (2020b), A field data example of Marchenko multiple elimination, *Geophysics*, *85*(2), S65–S70.

Zhang, L., and M. Staring (2018), Marchenko scheme based internal multiple reflection elimination in acoustic wavefield, *Journal of Applied Geophysics*, *159*, 429–433.

Zhang, L., J. Thorbecke, K. Wapenaar, and E. Slob (2019), Transmission compensated primary reflection retrieval in the data domain and consequences for imaging, *Geophysics*, *84*(4), Q27–Q36.

Zhou, B., and S. A. Greenhalgh (1994), Wave-equation extrapolation-based multiple attenuation: 2-D filtering in the fk domain, *Geophysics*, *59*(9), 1377–1391.

Acknowledgements

This research was performed in the framework of the project 'Marchenko imaging and monitoring of geophysical reflection data', which is part of the Dutch Open Technology Programme with project number 13939, and financially supported by NWO Domain Applied and Engineering Sciences. I would like to thank the project sponsors and their representatives: Elisa Guasti (NWO-TTW), Peter Mesdag (CGG), Rob Hegge (Aramco Overseas Company), Marcin Dukalski (Aramco Overseas Company), Roald van Borselen (Aramco Overseas Company), Koos de Vos (Shell), Arie Verdel (TNO), Vsevolod Kovalenko (Fugro), Jesper Spetzler (KNMI) and Alex Kirichek (Deltares). I am very grateful for the feedback from the sponsors throughout my PhD project and the internship opportunities that they offered me.

Kees Wapenaar has been of invaluable help during the PhD process. He provided me with the right amount of freedom and supervision, and would always be there if I needed his advice or help. Also, he helped me to keep my focus and always had my back. I am very grateful that he opened doors for me, for example, by recommending me for the technical committee of the KOC/SEG workshop on multiples and by allowing me to visit many conferences.

I am also very grateful for the help of Joost van der Neut. He helped me to start up and shape the PhD. He introduced me to the Marchenko method and the academic world in general. I will never forget the roadtrip in our first year, visiting multiple academic institutions and staying in hostels. It was useful and a lot of fun. Also, Joost arranged the internship with CGG Brazil for me. He even traveled to Rio de Janeiro and joined me for some traveling in Brazil. Thank you for all your ideas and initiatives, I would not know what I would have done without those.

Another important person in shaping my professional life is Huub Douma. We met in Rio de Janeiro, where he was the manager of the R&D team that I interned with. He helped me to get started on arrival and taught me a lot during my time there. Also, he would often pick me up or drop me off by car to make sure that I would get to and from work safely. Since my time in Brazil, we have kept in touch and he has been a valuable mentor. In the past months, he has been giving me advice regarding post-PhD life and how to find my way, I am very grateful for that.

Other people that made my stay in Rio de Janeiro special are Roberto Pereira and Natacha Rocha. Roberto, it was a pleasure to work with you on Marchenko. I miss the lunch breaks and your humour. I hope that we will meet again in the future. And Natacha, my stay in Rio would not have been fun without you. All the dinners, trips, nail treatments, sushi lunches, and new year on Copacabana beach. You made my stay unforgettable. Also, thank you CGG for this opportunity to test

my method on field data and to experience Brazilian life. The travel, the housing, the permits, everything was smoothly arranged.

After the internship in Brazil, I asked CGG for permission to continue working on their 3D field data. Peter Mesdag helped me to get permission and I started another internship in their office in Den Haag. Thank you Peter and CGG for that opportunity. And thank you Jouke for setting up a (complicated) link to get access to the Brazilian processing software and data. Thank you Maartje, Ali, Barbara and Shyla for the chats and support.

Next, Aramco Overseas Company in Delft provided me with the opportunity to work on their field data. I mostly worked with Marcin Dukalski, Rolf Baardman, Mikhail Belonosov, Rob Hegge, Jewoo Yoo and Roald van Borselen. Thank you very much for your support and advice in handling this challenging dataset. I would also like to thank the other colleagues who were always available for a nice chat at the coffee machine and fun/interesting discussions during lunch: Janny, Hannes, Diego, Apostolos, Paul and Yimin.

Then my fellow Marchenko people: Joeri, Lele, Chris, Giovanni, Jan, Evert and Ivan. Thank you for the valuable discussions and your support. And my other colleagues at TU Delft: Karlien, Lisanne, Florencia, Niels, Max, Billy, Reuben, Jan-Willem, Johno, Auke, Femke, Deyan, Wim, Kees, Sixue, Shan, Aparajita, Martha, Matteo, Dieter, Timo, Ranjani, Iris, Carlos, Koen, Thais, Kevin, Santosh, Aukje, Hamed, Menno, Aydin, Nicolas, Musab, Gerrit, Guy, Shohei, Milad, Aayush, Samantha, Shahar, Olivier, Nelson, Diego, Sara, Quinten, Baptiste, Guus, Joost, Gil, Bingkun and Atsushi. Thank you very much for making my PhD time unforgettable. Especially the road trips after the conferences in California and Texas were special, thank you for all the fun Joeri, Matteo, Jan-Willem, Shan, Paloma, Laura and Johno. The support staff was always there when I needed them: thank you Ralf, Lydia, Marlijn, Myrthe and Margot. A special thanks goes to Pieter Smets, for providing me with the latex template for this thesis. I would also like to thank Eric Verschuur for providing me with books and the dataset used in chapter 5 of this thesis.

In the past 4 years, the following people have had an impact on my non-academic developments. The Imperial Barrel Award team: Joeri, Ella, Bas, Mohammed and of course Gerhard. From Thrive PhD Academy: Daphne, Han, Maud, Stephan, Taavi and Abe. Ilaria and Alexandra from EAGE who assisted me in setting up Women in Geoscience & Engineering Netherlands. The EAGE/GAIA Women in Geoscience & Engineering team: Florencia, Angie, Jerney, Swarna and Konstantina. Being part of these teams has enriched my PhD experience and shaped me as a professional, so thank you all very much. Also, thank you Aletta for providing me with advice for WGE and my career.

Lastly, I would like to thank my family and friends. My parents Liesbeth and Tsjeert and their dog Doedel, for always supporting me, listening to my complaints and sharing my wins. My friends Mirjam, Jacky, Aya, Gabriella, Isabelle, Alex, Francoise, Marijse, Eline, Hyein and Rosanne, for always being ready for some fun.

Curriculum Vitæ

Myrna Staring

15-10-1990 Vlissingen, The Netherlands.

Education

2015 – 2020 Ph.D. project in Applied Geophysics
Delft University of Technology, Delft, The Netherlands.
Thesis: Adaptive Marchenko internal multiple attenuation
Promotor: Prof. dr. ir. C.P.A. Wapenaar

2018 – 2019 Participant Thrive Ph.D. Academy
Thrive Institute, Rotterdam, The Netherlands.

2013 – 2015 M.Sc. in Applied Geophysics
Delft University of Technology, Delft, The Netherlands.
Eidgenössische Technische Hochschule, Zürich, Switzerland.
Rheinisch-Westfälische Technische Hochschule, Aachen, Germany.

2010 – 2013 B.Sc. in Liberal Arts & Sciences
University College Roosevelt, Middelburg, The Netherlands.

2003 – 2009 Secondary School
SSG Nehalennia, Middelburg, The Netherlands.

Professional Experience

2020–present	Technologist, Fugro, Nootdorp, The Netherlands.
2015 – 2020	Ph.D. project in Applied Geophysics, Delft University of Technology, Delft, The Netherlands.
2018 – 2019	Visiting Researcher, Aramco Overseas Company, Delft, The Netherlands.
2017 – 2018	Visiting Researcher, CGG, The Hague, The Netherlands.
2016 – 2017	Research & Development Intern, CGG, Rio de Janeiro, Brazil.

Grants and Awards

2019	Exxon Mobil Student Education Program Travel Grant
2018	Nominee Best Paper Award of the faculty Civil Engineering & Geosciences
2018	Chevron Student Leadership Symposium Travel Grant
2013 – 2015	Shell Comprehensive Scholarship
2012	SIRIUS Scholarship

Other Activities

2019–present	Founder/President EAGE Women in Geoscience & Engineering Netherlands
2018–present	Reviewer Geophysics
2019	Member Technical Committee of the SEG/KOC Workshop on Seismic Multiples
2019	Member of the SEG Europe Regional Advisory Committee
2018 – 2019	Vice-President of the Delft Organization of Geophysics Students
2018	Participant American Association of Petroleum Geologists Imperial Barrel Award
2018	Secretary of the Delft Organization of Geophysics Students
2016 – 2018	General board member of the Delft Organization of Geophysics Students

List of publications

Journal Papers

[6] **Staring, M.**, M., Dukalski, M., Belonosov, M., Baardman, R.F., Yoo, J., Hegge, R.F., van Borselen, R. & Wapenaar, K. (2020), *R-EPSI and Marchenko equation-based workflow for multiple suppression in the case of a shallow water layer and a complex overburden: A 2D case study in the Arabian Gulf*, under review.

Chapter 4 of this thesis

[5] **Staring, M.**, and Wapenaar K. (2020), *3D Marchenko internal multiple attenuation on narrow azimuth streamer data of the Santos Basin, Brazil*, Geophysical Prospecting, 68, 1864–1877. Chapter 3 of this thesis

[4] Zhang, L. and **M. Staring**, (2018), *Marchenko scheme based internal multiple reflection elimination in acoustic wavefield*, Journal of Applied Geophysics, 159, 429–433.

[3] Wapenaar, K and **M. Staring**, (2018), *Marchenko-based target replacement, accounting for all orders of multiple reflections*, Journal of Geophysical Research: Solid Earth, 123(6), 4942–4964. Appendix A of this thesis

[2] van der Neut, J., J. Brackenhoff, **M. Staring**, L. Zhang, S. de Ridder, E. Slob, and K. Wapenaar (2018), *Single-and Double-Sided Marchenko Imaging Conditions in Acoustic Media.*, IEEE Transactions on Computational Imaging, 4(1), 160–171.

[1] **Staring, M.**, R. Pereira, H. Douma, H., J. van der Neut and K. Wapenaar, (2017), *Source-receiver Marchenko redatuming on field data using an adaptive double-focusing method*, Geophysics, 83(6), S579–S590. Chapter 2 of this thesis

Conference proceedings

Staring, M., Zhang, L., Thorbecke, J., and Wapenaar, K., (2020), *A new role for adaptive filters in Marchenko equation-based methods for the attenuation of internal multiples (invited)*, 82nd annual EAGE Conference and Exhibition 2020, Amsterdam.

Wapenaar, K., **Staring, M.**, Brackenhoff, J., Zhang, L., Thorbecke, J. and Slob, E., (2020), *An overview of Marchenko methods*, 82nd annual EAGE Conference and Exhibition 2020, Amsterdam.

Staring, M, Dukalski, M., Belonosov, M., Baardman, R.F., Yoo, J., Hegge, R.F., van Borselen, R.G. and Wapenaar, K. (2019), *Adaptive Marchenko multiple removal on Arabian Gulf OBC data* (invited), SEG/KOC Workshop: Seismic Multiples - The Challenges and the Way Forward, Kuwait, 3–5 December 2019.

Staring, M, and K. Wapenaar (2019), *Interbed demultiple using Marchenko redatuming on 3D field data of the Santos Basin*, The sixteenth International Congress

of the Brazilian Geophysical Society & EXPOGEF, Rio de Janeiro, Brazil, 19–22 August 2019.

Wapenaar, K., Brackenhoff, J., **Staring, M.**, and Thorbecke, J. (2019), *Green's theorem in seismic imaging across the scales*, EGU, General Assembly 2019, Vienna.

Wapenaar, K., Brackenhoff, J., **Staring, M.**, Thorbecke, J., and Slob, E., (2018), *Virtual seismology: from hydrocarbon reservoir imaging to induced earthquake monitoring*, American Geophysical Union, 2018 Fall Meeting, Washington.

Staring, M., and Wapenaar, K., (2018), *Marchenko redatuming for multiple prediction and removal in situations with a complex overburden*, American Geophysical Union, 2018 Fall Meeting, Washington.

Staring, M., van der Neut, J., and Wapenaar, K., (2018), *Marchenko redatuming by adaptive double-focusing on 2D and 3D field data of the Santos Basin (invited)*, 88th annual SEG meeting, Anaheim, Workshop W-4: The business value of multiple identification and removal - Status, challenges and road ahead. In SEG Technical Program Expanded Abstracts 2018 (pp. 5449–5453).

Staring, M., Pereira, R., Douma, H., van der Neut, J., and Wapenaar, K., (2017), *Applying source-receiver Marchenko redatuming to field data, using an adaptive double-focusing method*, SIAM Houston Imaging Sciences Symposium, Houston.

Staring, M., Pereira, R., Douma, H., van der Neut, J., and Wapenaar, K., (2017), *Adaptive double-focusing method for source-receiver Marchenko redatuming on field data*, 87th annual SEG meeting, Houston. In SEG Technical Program Expanded Abstracts 2017 (pp. 4808–4812).

Staring, M., Pereira, R., Douma, H., van der Neut, J., and Wapenaar, K., (2017), *An adaptive method for source-receiver Marchenko redatuming*, The fifteenth International Congress of the Brazilian Geophysical Society & EXPOGEF, Rio de Janeiro, Brazil, 31 July–3 August 2017 (pp. 1323–1328).

Staring, M., van der Neut, J., Grobbe, N., and Wapenaar, K., (2017), *Sparse inversion for solving the coupled Marchenko equations including free-surface multiples*, 79th annual EAGE Conference and Exhibition 2017, Paris.

Zhang, L., Slob, E., van der Neut, J., **Staring, M.**, Wapenaar, K., (2016), *Electromagnetic Marchenko imaging in 1D for dissipative media*, 86th annual SEG meeting, Dallas, In SEG Technical Program Expanded Abstracts 2016 (pp. 2479-2483).

Staring, M., van der Neut, J., and Wapenaar, K., (2016, *An interferometric interpretation of Marchenko redatuming including free-surface multiples*, 86th annual SEG meeting, Dallas, In SEG Technical Program Expanded Abstracts 2016 (pp. 5172-5176).

Afanasiev, M., Ermert, L., **Staring, M.**, Trampert, J., and Fichtner, A. (2016), *Full seismic waveform inversion of the African crust and Mantle-Initial Results.* In EGU General Assembly Conference Abstracts (Vol. 18).